STELLAR ATMOSPHERE MODELING AND SUBSYSTEM DEVELOPMENT FOR THE ACCESS PROGRAM

by

Matthew Morris

A dissertation submitted to Johns Hopkins University in conformity with the requirements for the degree of Doctor of Philosophy

Baltimore, Maryland

July, 2018

Abstract The goal of the ACCESS program (Absolute Color Calibration Experiment for Standard Stars) is to enable greater discrimination between theoretical astrophysical models and observations, where the comparison is limited by systematic errors associated with the relative flux calibration of the targets. To achieve these goals, ACCESS has been designed as a sub-orbital rocket borne payload and ground calibration program, to establish absolute flux calibration of stellar targets at <1 % precision, with a resolving power of 500 across the 0.35 to 1.7 micron (μm) bandpass.

In order to obtain higher resolution spectroscopy in the optical and near-infrared range than either the ACCESS payload or CALSPEC observations provide, the ACCESS team has conducted a multi-instrument observing program at Apache Point Observatory. Using these calibrated high resolution spectra in addition to the HST/CALSPEC data, I have generated stellar atmosphere models for ACCESS flight candidates, as well as a selection of A and G stars from the CALSPEC database. I developed a system of iterative, chi-squared minimization, model fitting for these targets in this population. Using ATLAS9 and ATLAS12 Kurucz stellar atmosphere code result in models, converging to within 20 K effective temperature, 0.05 log(g), and 0.02 log[M/H] for the majority of targets.

Key components of my contribution to the experiment are control software I wrote for the detector controller for flight and ground operations, and also for the ACCESS data reduction pipeline. We have been able to perform characterization tests with a modified ground cryogenic dewar system, yielding comparable dark currents to Goddard's Detector Characterization Lab. Additionally, I performed characterization tests on the ruggedized detector controller and added a heat sink interface, enabling vacuum operations beyond the duration of our rocket flight.

Contents

List of Figures

Thesis Road-map The scientific emphasis of my thesis is the observation, modeling, and analysis of candidate standard stars for the ACCESS program. To extend the utility of this sample, all potential JWST calibrator stars encompassing spectral type A and G stars have been included in the modeling and analysis. One of the prime goals is to test the robustness of the ATLAS12 stellar modeling software. The ATLAS12 software provides greater flexibility in stellar parameter selection. This comes at the expense of longer run times and potentially model execution fragility. It is our goal to test whether the ATLAS12 modeling code is fragile, whether the increased control over parameter space yields more accurate models (smaller chi square for model fits to the stellar spectra) and why, whether models generated directly from either ATLAS9 or ATLAS12 provide better fits to the stellar spectra than models generated from existing model grids, and a benchmark of ATLAS9 versus ATLAS12 versus model interpolation run times. The model results will also be assessed in the context of other methods for determining fundamental stellar parameters such as the effective temperature.

My thesis also includes software development in support of the ACCESS program. In particular, I have written modules for detector data acquisition, the ACCESS data reduction pipeline, and software to control and measure components of the ground-based calibration system.

Chapter 1 outlines the scientific motivation behind the ACCESS program.

Chapter 2 discusses the selection of the ACCESS candidate stellar targets and the extended sample that includes JWST calibrator stars.

Chapter 3 discusses the Apache Point Observatory observing program and observations in support of the planned ACCESS observations and stellar modeling effort. The data reduction, error propagation and analysis are discussed.

Chapter 4 focuses on the development of the stellar atmospheres models and the ATLAS9 and ATLAS12 modeling software used to generate the models.

Chapter 5 compares the results of the ATLAS9 and ATLAS12 modeling software used to generate the models. Also discussed are the ACCESS stellar model fits that I have generated in comparison with model fits and model grids used in the literature.

Chapter 6 presents a brief overview of the ACCESS instrument – the telescope and spectrograph.

Chapter 7 presents the ACCESS detector and the software data acquisition modules that I have developed. Also presented are dark current and read noise measurements undertaken using this software with the detector mounted in a lab cryogenic dewar that incorporates shutter and baffle modifications that I designed to enable these measurements.

Chapter 8 presents LabVIEW software modules that I developed or enhanced for control of the ground-based calibration hardware.

Chapter 9 summarizes the observations and stellar models.

Chapter 1

Introduction

1.1 Dark Energy Discovery, Characterization, and the ACCESS Program

In the late 1990's, it was discovered that the expansion of the universe is not slowing (as previously believed) but rather accelerating outwards [Riess et al. (1998); Perlmutter et al. (1999)]. The initial evidence for this accelerated expansion of the universe comes from observations of supernovae type Ia (SNe Ia) (see sec. 1.1.2). Initially proposed as a "cosmological constant" by Albert Einstein, dark energy provides a negative vacuum pressure and accounts for about 70% of the energy density of the universe at the present epoch [Planck Collaboration (2014)]. As such, understanding and characterizing dark energy is one of the most compelling problems in current cosmology and in astrophysics in general. Although the discovery of dark energy has been corroborated by measurements of the Cosmic Microwave Background (CMB) [Lange et al. (2001); Spergel et al. (2007); Sherwin et al. (2011)] and baryon acoustic oscillations [Eisenstein et al. (2005)], SNe Ia remain an important method for discrimination between cosmological models that describe the evolution of the universe. To make dis-

criminations between dark energy models, the supernova brightness is determined in the rest frame blue band and plotted as a function of distance (represented by redshift).

This curve, comprised of the brightness determination of numerous SNe Ia as a function of the distance (represented by redshift) is known as the Hubble supernova diagram (fig. 1.2). It is the shape of this distribution that is compared to the different cosmological models to discriminate between them and contribute to the characterization of dark energy.

SNe Ia are found by observing a field of the sky and measuring any differences in absolute brightness between subsequent images. By fitting the brightness of transient objects as a function of time, it is possible to determine whether that transient is in fact a SNe Ia (see sec. 1.1.2) These images are taken for a series of filter bandpasses, as more distant SNe Ia are redshifted from their rest frame velocity. In order to determine the absolute brightness and therefore the distance of the SNe Ia, the image must be converted back into the rest frame (see sec. 1.2). The filter efficiency must be known precisely to perform this conversion.

The primary goal of the ACCESS program is to reduce the uncertainties associated with these photometric measurements across the bandpass of 0.35 to 1.7 μm. This is achieved through a series of rocket-borne observations of standard stars, in which the end-to-end efficiency of the instrument is determined using NIST calibrated photodiode detectors (see sec. 1.2.4 and fig. 1.5). stellar atmosphere modeling of these standard stars provides an important cross-check and extend the ACCESS observations beyond the payload bandpass (see Chapters 2, 4, and 5). The key science component of my thesis is the generation of these stellar atmosphere models for the set of ACCESS stars and the set of potential JWST calibration stars of the same spectral type (A and G main sequence) as the ACCESS stars.

1.1.1 Interstellar Distances

Understanding and quantifying astrophysical distances, specifically extragalactic distances, is important for the determination of the evolution of the universe as a whole. Depending on the distance to the source, different methods are used to achieve an accurate measurement. The entire system of distance measurement techniques is collectively known as the cosmic distance ladder.

The first astronomical distance measurements, both within and beyond the solar system, were performed through the use of parallax [Short (1763); Bessel (1838)]. Parallax is determined by measuring the proper motion of an astronomical object relative to distant background sources, as the earth orbits the sun [Short (1763); Bessel (1838)]. This process is only viable for nearby stars and objects within the solar system.

Cepheid variable stars vary in brightness in a periodic manner. The length of that period is directly related to its absolute luminosity [Leavitt & Pickering (1912); Shapley (1918)]. Having knowledge of the absolute brightness and observed brightness, one can determine the distance to this star, as the observed flux of any spherically symmetric body will drop off at the rate of the square of its distance from the observer:

$$F = \frac{L}{4\pi D_L^2} \tag{1.1}$$

Here, F is the observed flux, L is the absolute luminosity of the object, and D_L is the distance from the object to the observer. The distance modulus d can be determined from the absolute magnitude M and the apparent magnitude m:

$$m - M = 5log_{10}\left(\frac{d}{10parsec}\right) \tag{1.2}$$

Because of the great distances involved, very few sources are luminous enough to provide an accurate measure of distances between galaxies. Currently one of the best extragalactic distance measurements come from Type Ia supernovae [Riess et al. (1998); Perlmutter et al. (1999)].

1.1.2 Supernovae Ia

A type Ia supernova begins as a white dwarf, a star in the late stages of its life cycle. The majority of a star's life is spent as a "main sequence star". During this phase, the vast majority of the composition of the star is hydrogen. The intense pressure and temperature at the core of the star results in the hydrogen being fused into helium. The star, during this time, is pulled inwards towards collapse by gravity, but radiation pressure (a byproduct of nuclear fusion) counteracts this, creating a stable equilibrium. As it runs out of hydrogen in the core, the helium may fuse into heavier and heavier elements, forming an onion like structure within the star, with heavier elements towards the core. However, if the star is not massive enough, the pressures and temperatures may not reach a tipping point, capable of fusing carbon or oxygen. As the outer layers of the star are shed by the star, only the white dwarf remains [Bohm-Vitense (1992); Arnett (1996)].

Composed mostly of carbon and oxygen, by-products of the nuclear fusion that occurred within the earlier stages of the star, a white dwarf is no longer supported by radiation pressure from continued nuclear fusion. Electron degeneracy pressure, the inability of electrons to occupy the same space simultaneously, now maintains the structure of the white dwarf. The density of white dwarfs reach 10^6 kg/m^3[Chandrasekhar (1931)]. Once a white dwarf exceeds $\sim$ 1.38 solar masses (either from accretion of mass from a companion star or merging with another white dwarf), the pressure and temperature become great enough to finally allow for carbon fusion [Chandrasekhar (1931); Nomoto et al. (1984)]. The carbon fusion process leads to a runaway fusion reaction across the entire white

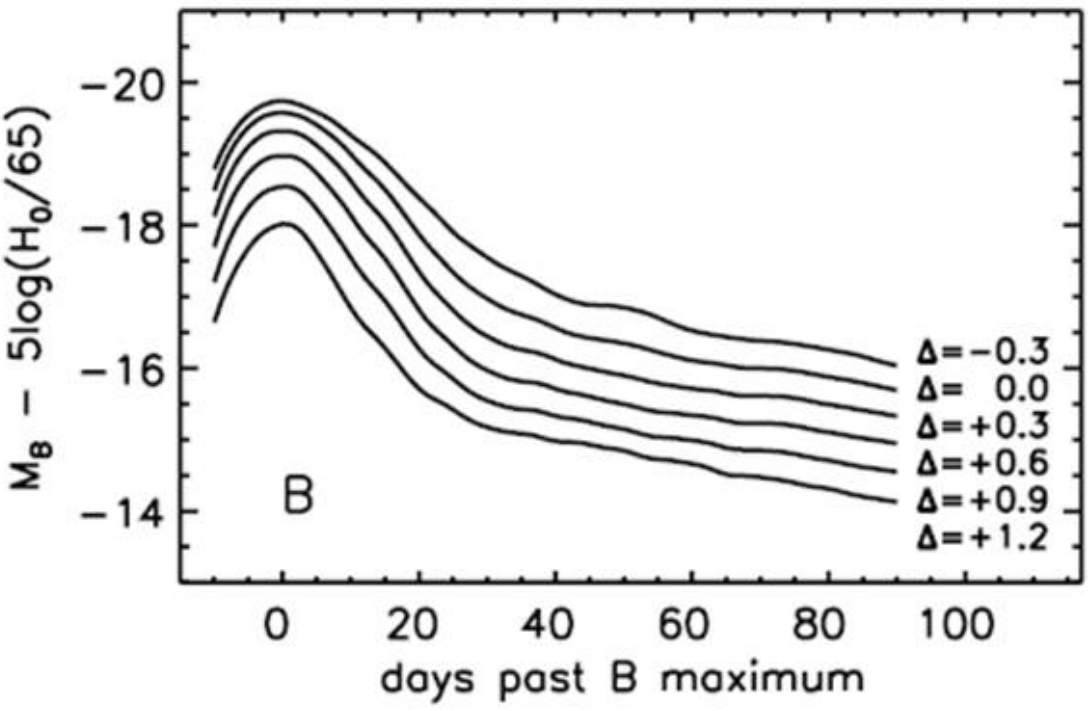

Figure 1.1: A series of B-Band light curves for a type Ia supernova [Jha et al. (2007)]. $\triangle$ here refers to the relative luminosity of a given supernova, relative to a fiducial (e.g. observed V band maximum relative to the theoretical V band maximum determined from a host galaxy redshift).

dwarf, faster than the speed of sound within the star. About $\sim$1-2x10^{44} Joules are released during this reaction. A large majority of the light seen in the supernova light curve comes not from the initial explosion, but from the radioactive decay of the fusion products ^{56}Ni $\rightarrow$ ^{56}Co $\rightarrow$ ^{56}Fe (^{56}Ni has a half-life of about 6 days, and ^{56}Co has a half-life of about 77 days) [Truran et al. (1967); Colgate & McKee (1969)]. The light from this type of supernova is bright enough that it can be seen in another galaxy.

A supernova can drop by two magnitudes from peak brightness on the order of months (see Figure 1.1). With current technology and scientific understanding, it isn't possible to know where a supernova will occur before it happens. Rather, when looking for supernovae, one must look at a large section of the sky, with many galaxies within, over a period of time. By comparing subsequent images of the same field of view, and subtracting one from the other, a supernova can be found if the supernova

brightens or dims within the timeframe between exposures.

By measuring the light of the supernovae over a months-long time span, a lightcurve can be created for that supernovae. Type Ia supernovae have well-modeled lightcurves that can be an excellent indicator of their distance from us. Though a supernova, itself, is not a perfect standard candle, its light curve allows it to be a "standardizable" candle. If one can match an observed supernova to a lightcurve model (see Figure 1.1), the absolute brightness of the supernova can be determined, and the one can determine its distance via equation 1.1.

This type of supernova occurs less than once per galaxy per century ($\sim 0.47\text{x}10^{-4}$ yr^{-1} MPc^3) [Neill et al. (2006)]. By observing a large population of galaxies across many redshifts, many supernova can be discovered at different lookback times. By plotting the distance of the SNe Ia as a function of redshift, an expansion history of the universe may be deduced (see fig. 1.2). This expansion history can then be compared to various cosmological models, thereby characterizing the properties of dark energy (see fig. 1.3).

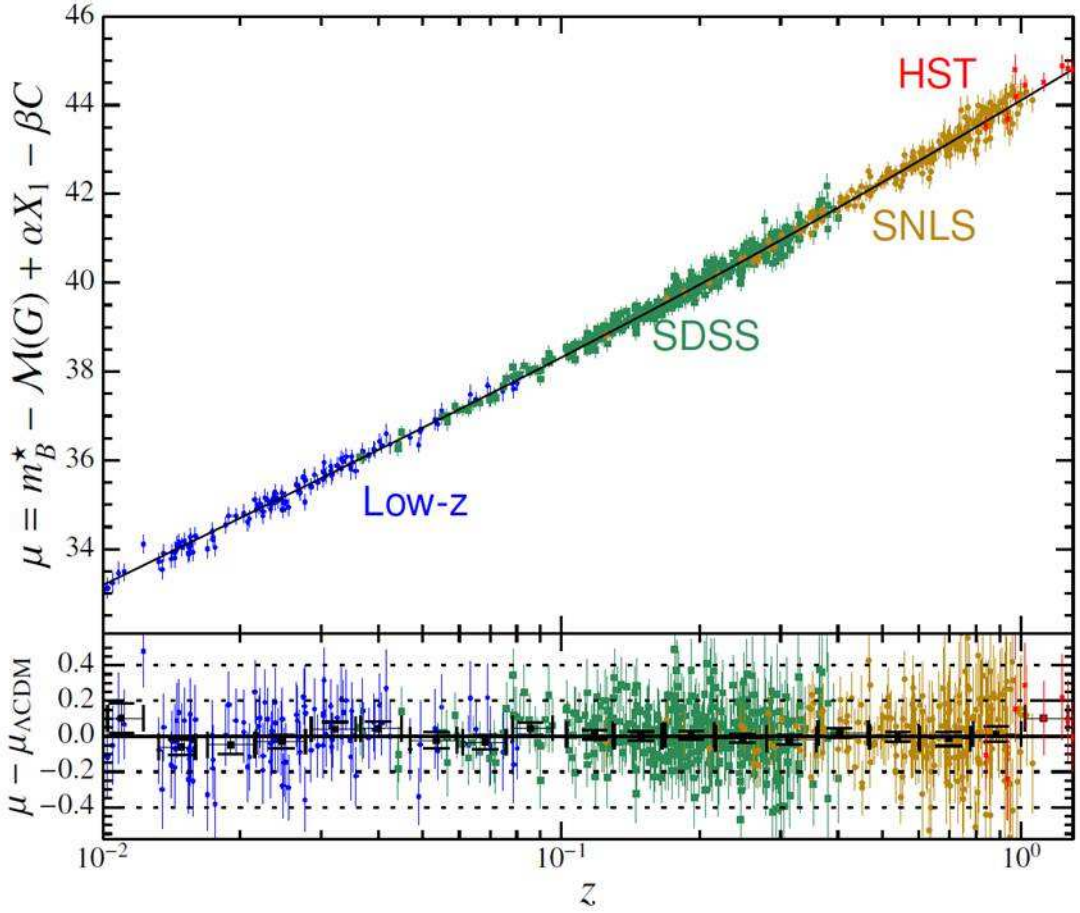

Figure 1.2: Hubble diagram of redshift versus distance modulus, from several large surveys, spanning a range of redshifts. [Betoule et al. (2013)]

The energy density of dark energy is constant when observed at low redshifts, but in order to determine whether this holds true throughout the history of the universe (see Figure 1.3), it is necessary to study galaxies from a time period before the present day.

By observing distant galaxies, one can discover distant SNe Ia galaxy that can be used to probe the expansion history of the universe. Modern supernova surveys span a wide range of redshifts. These supernovae need to be directly compared to each other in order to correlate distances between galaxies. The light curve models, which are used to determine the absolute brightness of a given supernova, can only be fit to supernova data in its own rest frame, rather than the observer's rest frame. In order to do this, they must be converted to the rest wavelength.

Spectroscopy of supernovae can be taken as a supplementary measure, to probe the chemical content of the supernova or confirm supernova identification. Type I and Type II supernovae are differentiated by the absence or presence of hydrogen lines, respectively [Carroll & Ostlie (1996); Arnett (1996)]. Spectra of the supernova host galaxy can be taken afterwards, in order to determine galactic characteristics. It has been found that there is a slight correlation between host galaxy characteristics (such as metallicities and star formation rates) and the absolute brightness of the supernova [D'Andrea et al. (2011)].

However, it is often not feasible to use high resolution spectroscopy to determine the light curve properties of the supernova over the entire, often months long, observation window. Supernova spectra can only be obtained near its peak brightness, and thus it is logistically difficult to dedicate observing time for SNe Ia targets of opportunity. For large surveys, broadband photometry is taken, in which the brightness of an observed target is measured for large bins, spanning a wide section of the electromagnetic spectrum.

Improving the accuracy and precision of these photometric measurements is a primary goal of

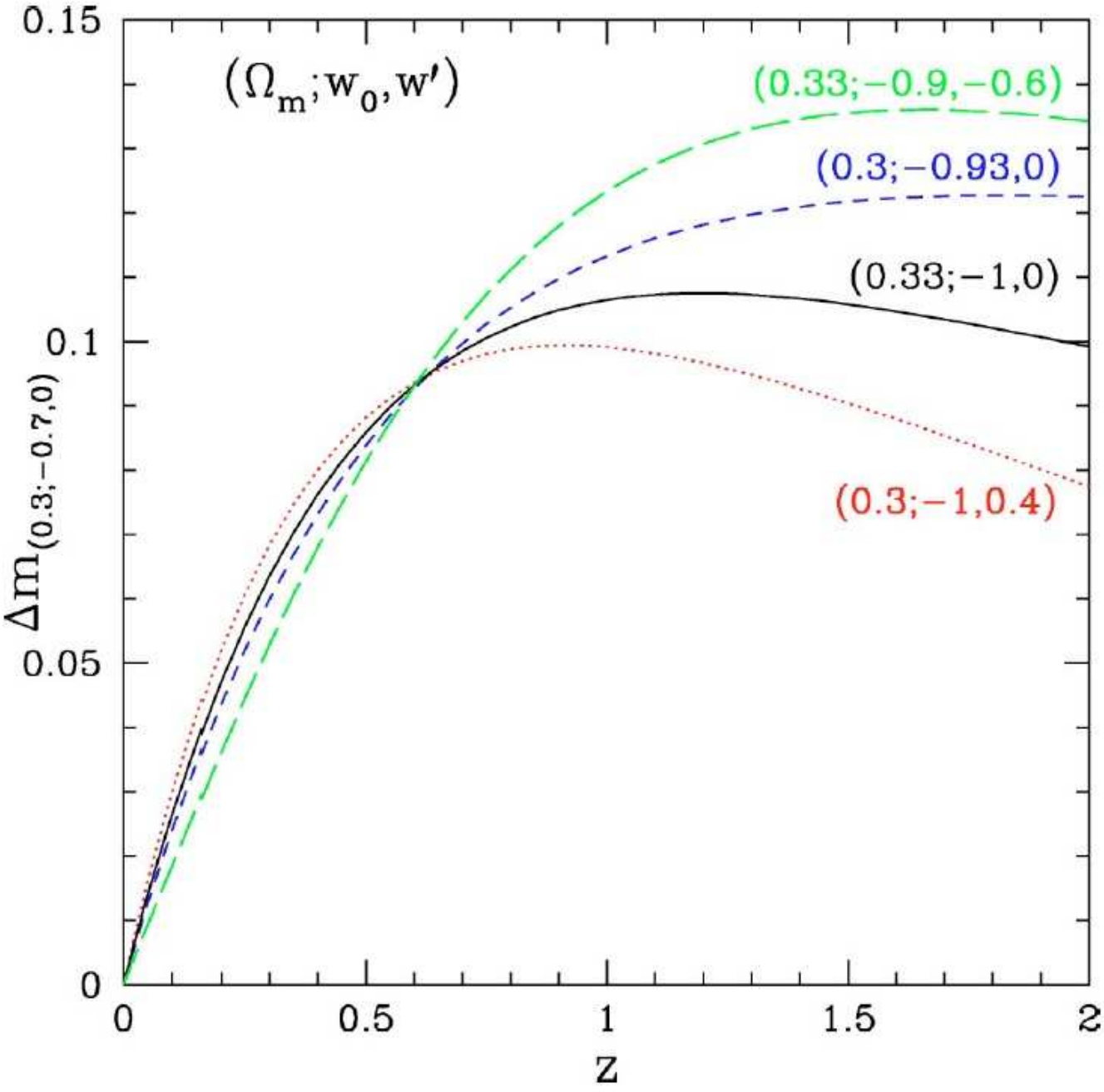

Figure 1.3: Degeneracy of dark energy models relative to redshift [Linder & Huterer (2003)].

the ACCESS program. This is achieved through the reduction of calibration uncertainty from the observation of standard stars.

1.2 Absolute Calibration

1.2.1 Photometry

Photometry (sometimes more generally referred to as radiometry) is the measurement and quantification of the absolute flux levels of an emitting body [Friedman & Miller (2004)]. Commonly, wavelength regions of light (bandpasses) are selected using filters, gratings, or prisms.

Standardized filter bandpasses are used across the discipline, typically denoted by a single letter (see table 1.1).

In some studies, U B and V magnitudes are used in measuring lightcurves of supernovae, and models are applied to determine their absolute peak magnitude, and thereby, their distance modulus. Three quarters of the light emitted from a type Ia supernova is in the optical band, when the supernova is viewed at rest [Howell et al. (2009)]. However, as supernovae are studied at greater distances, their spectra become redshifted into other filters.

Modern surveys can extend to z $\sim$ 1.5 (due to detection limits of the supernovae), and supernovae have been discovered at as far as z=1.91 [Jones et al. (2013)]. As shown by Fig. 1.3, determining the magnitude, and therefore distance, of supernovae at higher redshifts is necessary to break the degeneracy between competing dark energy models.

The B bandpass in the Johnson-Cousins photometric system has a central wavelength of 4361 Angstroms (Å), with a full-width-half-maximum of 890 Å ($\sim$ 3500 to 5300 Å) (Fig.1.4). The B-band is the normalization factor used in supernova Hubble diagrams, which is a graphical representation

Photometric Band	**Central λ (Å)**	**FWHM**	**Central λ at Z=1**	$\lambda > 1\%$
U	3663	650	7326	3200-4100
B	4361	890	8722	3750-5700
V	5448	840	10896	4800-6800
R	6407	1580	12814	5500-8450
I	7980	1540	15960	7000-9200
J	12200	2130	24400	10400-14400
H	16300	3070	32600	14600-24800
K	21900	3900	43800	19400-38400
L	34500	4720	69000	30400-38000

Table 1.1: Central wavelengths for the Johnson UBVRI system [Bessel (2005); Bessell (1990)], and those wavelengths at a redshift of Z=1. NIR filter data from [Binney & Merrifield (1998); Bessell & Brett (1988)].

of the relationship between luminosity derived distance and recessional velocity (i.e. redshift). Thus, a 3500-16000 Å calibration could yield transformations into the B-band all the way to z=1.8 (a z of 0 indicates the rest frame with no redshift, and a z of 1.85 would amount to $\sim$.78c). Emitted light at the 5700 Å edge of the B-band, would be observed as light at 16000 Å. Color terms (e.g. B-V) may also be used to infer supernova luminosity [Mandel et al. (2017)]. A 3500-16000 Å calibration could enable this procedure up to a redshift of z $\sim$ 1.3 (the edge of the V-band being at 6800 Å).

1.2.2 Zeropoint Calibration

The instrumental sensitivity across photometric bands must be precisely known to accurately convert flux measurements between photometric bands or instruments. For a given instrument, measuring relative flux between separate science targets in the same band can be done without knowledge of the instrumental zeropoint. However, converting flux between different photometric bands is required to obtain the flux value of a redshifted target in the rest frame. In addition, by calibrating a telescope's zeropoint, it may be cross correlated with programs using different instruments.

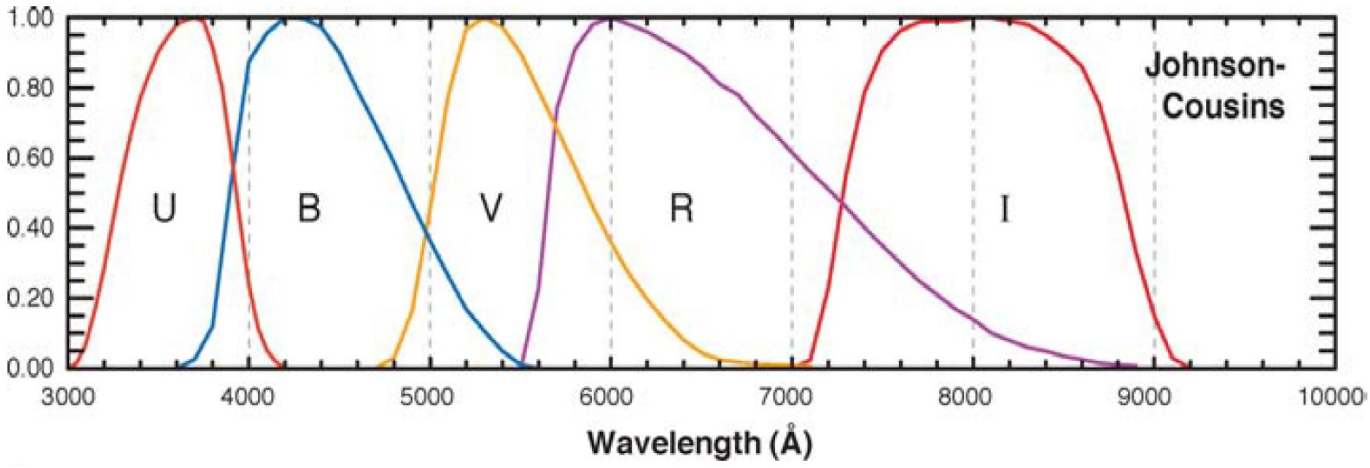

Figure 1.4: Normalized photometric filter transmission functions for the Johnson UBVRI system [Bessel (2005)].

An instrument's photometric zeropoint is defined as the flux at which the instrument detects one count per second. By using the relative flux formula:

$$m1 - m2 = -2.5log(f1/f2) \tag{1.3}$$

And stating that m2 is zero and f2 is 1 count per second, one can see that:

$$m = -2.5log(DN/t) + ZEROPOINT \tag{1.4}$$

where m is the apparent magnitude, DN/t is an instrument's count rate, and ZEROPOINT is the correction term [Voit (1997)]. That correction term is the magnitude of an object that produces one count per second. As long as the instrumental response is linear in flux, this will allow one to convert relative count rates into a known photometric system, such as AB magnitudes, the UBVRI system, or even natural flux units, like ergs cm^{-2} s^{-1} $Å^{-1}$.

In order to determine a telescope's zeropoints, one needs a source of known flux. A standard star is a star with accurate and precise flux measurements. Historically, the determination of flux was

done by comparing the star's observed flux with the flux of a laboratory source, such as a melting-point blackbody, typically copper or platinum [Hayes (1985)]. The first standard star observation was performed by Hayes in 1985, by observing a chamber of copper at its melting point, and subsequently observing the star Vega. Copper, at its melting point, is a well known and studied blackbody source in the laboratory, transitioning between liquid and solid phases at 1358 K [Coates & Andrews (1978)]. A blackbody has a spectral energy distribution solely dependent on temperature. This is expressed by Planck's law of radiation:

$$B_\lambda(\lambda, T) = \frac{2hc^2}{\lambda^5} \frac{1}{e^{\frac{hc}{\lambda k_B T}} - 1} \tag{1.5}$$

Where B_λ is the spectral radiance, λ is the wavelength of light, and T is the temperature of the object. For a melting-point copper blackbody, this would produce a flux distribution peaked at 2.1 μm. No object is a pure blackbody, as emission and absorption features at specific wavelengths are intrinsic to all elements and materials. By controlling for source stability and purity, the deviance from a perfect blackbody can be observed and quantified in the laboratory [Ahmed et al. (2013); Gogolev et al. (1994); O'Brian et al. (1995)].

Using these laboratory flux sources, an observer is capable of determining the observing efficiency of the telescope, as a function of wavelength. The same telescope can then used to observe a bright star. By accounting for the attenuation of light due to the optical components within the telescope, one can then calculate the flux incident on the telescope from the star [Smith et al. (2009)]. Once this calibration of a star is established, other telescopes may now simply use that star to calibrate their telescope. Rather than attempting to repeat the precise conditions in which a blackbody source is used, future observers can use a standard star as a stable, constant flux source.

Vega is a primary standard, having been directly compared to a NIST laboratory melting black-

body source. A secondary standard is then calibrated relative to the primary standard. This is done to establish standards at fainter magnitudes. Primary standards such as Sirius and Vega are too bright to be observed in conjunction with a science target. Many modern telescopes are too sensitive to observe primary standards without saturating the detector. For instance, the IR channel of the WFC3 instrument aboard HST requires 2.93 seconds to read out its full array, a saturation level of 77,900 electrons, and a gain of 2.3 e^{-}/DN [Dressel et al. (2017)]. The zeropoints for the IR channel range from 23-27 magnitudes (in the AB magnitude system [Oke (1974)]), depending on the filter used [Kalirai et al. (2009)]. Therefore, using eqn. 1.4, a target between -0.4 and 3.6 magnitudes in the AB system would saturate a field image before it could be read out. Star similar in brightness to Vega are therefore not suitable as calibrator stars for this instrument.

Having standard stars at the appropriate flux levels and at low airmass for various observing campaigns requires a distributed network of standard stars.

The observing conditions between the laboratory blackbody source and the star can often be different enough to be a significant error contribution, in large part due to the atmospheric variability between the target and the telescope. It is technologically difficult to establish a laboratory flux source for real-time observations using space-based telescopes [Price et al. (2004)]. It is not routinely performed for ground-based observations.

Currently, calibration uncertainty is a dominant source of systematic uncertainty in supernova surveys. As supernova surveys grow, in terms of number of supernovae found and observed, statistical uncertainty of derived cosmological parameters becomes lower; statistical uncertainty of the matter density of the universe has gone from $\sim$30% in 1998 to $\sim$3.5% in 2014 [Riess et al. (1998); Scolnic et al. (2014)].Calibration uncertainty can be thought of as the error inherent in targets used to calibrate an instrument, and the instruments themselves. Depending on the supernova survey, sources of error

can include the extinction from the milky way galaxy itself, the accuracy of the lightcurve models, the properties of the host galaxy, Malmquist bias (the bias in which brighter objects are found more often than fainter objects), properties of the telescope, observation methods. among many others. Calibration uncertainty – the combined uncertainty of the spectral energy distribution of the standard star, and the instrumental precision of the standard star measurement – tends to be the greatest source of systematic uncertainty [Scolnic et al. (2014)]. For the Supernova Legacy Survey, the systematic uncertainty of the standard star's magnitude and spectral energy distribution is an order of magnitude greater than the other sources of systematic uncertainty in the near-infrared [Regnault et al. (2009)].

1.2.3 Vega as a Historical Standard Star

Vega has been studied extensively throughout the history of astronomy, and was one of the first stars aside from the Sun to have its spectrum recorded [Draper (1877)], calibrated [Hayes (1985)], and modeled [Kurucz (1979)]. The Vega magnitude system is a commonly used photometry system, defining the zeropoint as the flux of Vega [Johnson & Morgan (1955)]. However, Vega is not perfectly ideal, and it has been shown that it is rapidly rotating at 93% of breakup speed (274 km/second at the equator), with its pole pointed along earth's line of sight, which can create a 2400 K temperature gradient from pole to equator [Aufdenberg et al. (2006); Peterson et al. (2006); Yoon et al. (2008)]. This can affect the line and continuum shapes relative to stars of similar type. In addition, Vega is surrounded by a warm debris disk, which can cause excess spectral emission in the infrared [Su et al. (2013)]. For these reasons, efforts have shifted towards establishing other stars as standards (see section 2.2 for examples and discussion).

1.2.4 NIST-calibrated Photodiodes

The blackbody flux source has already been established as a laboratory standard, but advances in technology are enabling their replacement with standard detectors. These detectors are photodiodes which have very precise and accurate responsivity with low error, from 200 to 1800 nanometers (nm) [Larason & Houston (2008)] (see Figure 1.5). These detectors exhibit long term stability of less than 0.05% for photodiodes in the visible range (405-920 nm) and less than 0.5% for photodiodes in the NIR (700-1500 nm) [Larason & Houston (2008)]. The photodiodes being used by ACCESS have been previously calibrated at a NIST facility.

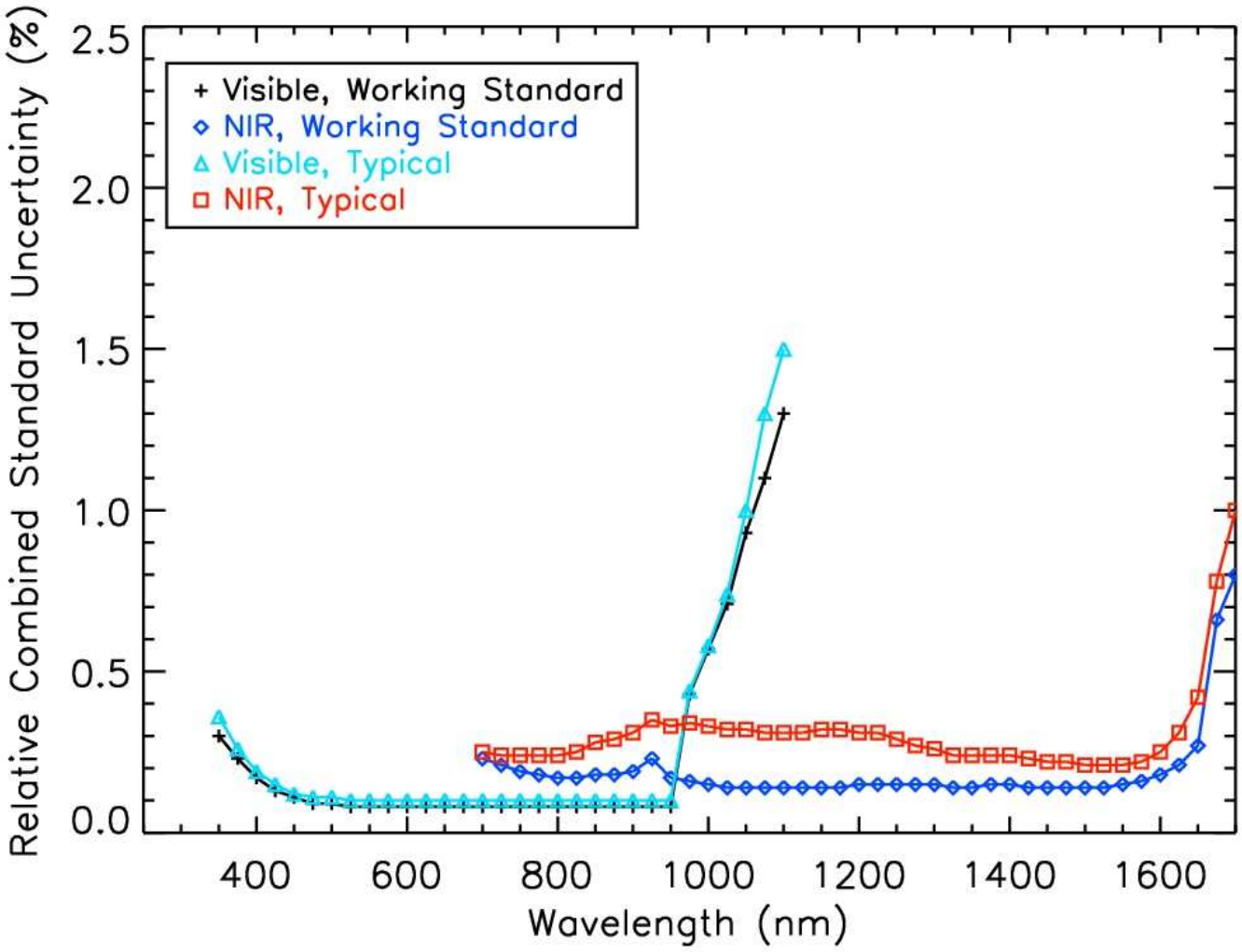

Figure 1.5: Absolute uncertainty of NIST photodiode calibrations, in Visible and NIR [Larason & Houston (2008)].

1.2.5 Atmospheric Contamination

Initial standard star calibration efforts were executed using ground-based telescopes. This approach cannot be used for observations that extend into the near infrared, however. In wavelengths redder than about 6800 Å, OH, molecular oxygen, and water in the atmosphere can have both absorptive and emissive properties that either eliminate extended spectral regions from use or introduce noise into ground based observations for stellar targets [Meinel (1950); Catanzaro (1998)]. Not only does the atmosphere absorb strongly, but it is highly variable on the scale of 10-15 minutes, with large seasonal variability as well [Dayton et al. (2010)]. The OH emission occurs at high enough altitudes ($\sim$70 km) that even using a balloon for observations would not sufficiently eliminate this spectral contamination. A balloon borne observation, typically observing longer wavelengths [Pascale et al. (2008); Gandilo et al. (2016)], will typically reach an altitude of 30 km.

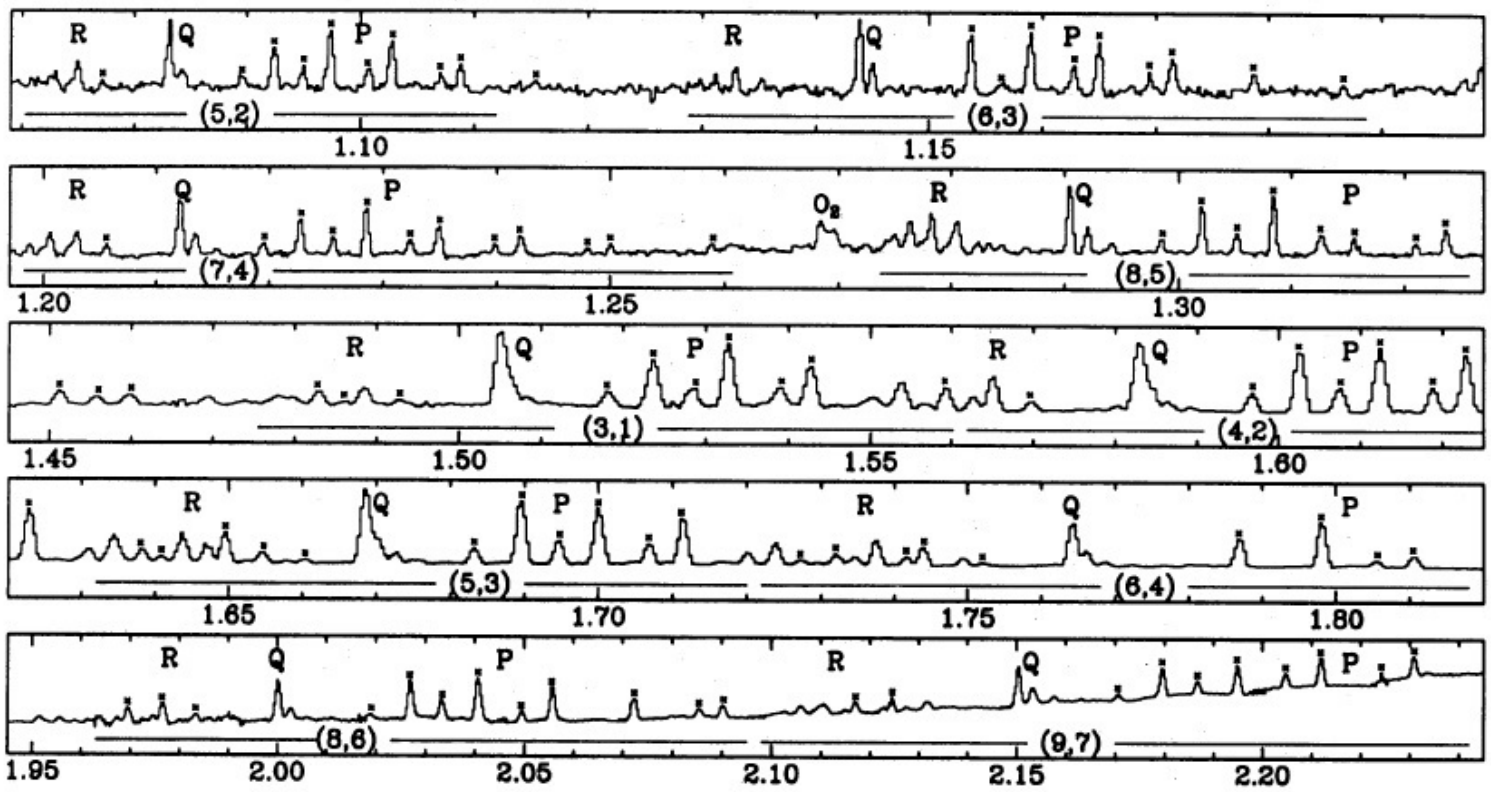

Figure 1.6: Spectrum of the IR airglow from [Oliva & Origlia (1992)]. Wavelength Scale is in μm, flux scale is arbitrary. R, Q, and P markers denote OH transitions in which the change in rotational quantum number ΔJ=+1,0, and -1, respectively. Numbers in parenthesis denote the initial and final states of the vibrational quantum number. O_2 line is noted at 1.27 μm.

.

A sounding rocket program, though short-lived with observing times on the scale of 6-10 minutes, can observe above the atmosphere. It can be characterized and recalibrated directly before and after flight, as the payload is recovered after the end of its flight. It can also be monitored during its flight, for any changes in payload sensitivity. NIST calibrated photodiodes can be used to determine the efficiency of the payload before flight to a high level. We will use a Si photodiode for the visible (0.35-1.1 μm). An InGaAs photodiode will be used for the NIR (0.8-1.7 μm). The InGaAs photodiode will be moderately cooled for the purpose of background reduction, instrument stability, and to bring the instrument close to – but above – the atmospheric dew-point while under nitrogen gas purge. Transferring this precision NIST calibrated detector standard to a stellar source is a primary motivation for the ACCESS program.

ACCESS will launch its payload with a sounding rocket, specifically a two-stage rocket, consisting of a Terrier and Black Brandt IX. This will be done at White Sands Missile Range, with the support and assistance of the NASA Sounding Rocket Program. The NASA Sounding Rocket Program has been performing rocket launches since 1959. The payload will fly above 120 km for approximately 380 seconds, reaching a nominal apogee of 283 km, observing one of the ACCESS targets continuously throughout. It flies on a parabolic arc, and will then return to the ground in the White Sands Desert, where it will be recovered, for future flights.

Chapter 2

The ACCESS Stellar Targets

A necessary component to the ACCESS program that I have performed is the initial analysis of the ACCESS flight targets and a selection of JWST calibrator stars of A and G stellar type. This is achieved through the ground-based observation of candidate stars at Apache Point Observatory, and the subsequent fitting of stellar atmosphere models to the targets selected for the ACCESS program. The model fits are performed using both APO data and HST data.

2.1 ACCESS Calibration Strategy

ACCESS, the Absolute Color Calibration Experiment for Standard Stars, is a sub-orbital rocket payload and ground calibration program designed to transfer NIST calibrated detector standards to stellar targets across the bandpass of 3500 to 17000 Å with greater than 1% precision with a resolving power of $\lambda/\Delta\lambda$=500 [Kaiser et al. (2013b)]. We will achieve this goal through the minimization of calibration uncertainties.

1. We will observe above the atmosphere, so as to not introduce any atmospheric contamination into the observation.

2. We will use a single optical path to eliminate cross-calibration systematic uncertainties. The ACCESS telescope and spectrograph will disperse and cross disperse the incoming light, such that the entire bandpass in three orders (0.9 to 1.9 μm, 0.45 to 0.95 μm, and 0.3 to 0.63 μm) falls on the sole ACCESS detector (Ch. 6).

3. We will perform NIST-traceable subsystem and end-to-end payload calibration, before and after the ACCESS flights. We will use NIST-traceable calibration standard detectors, to transfer an absolute flux scale with low uncertainty to the stars. ACCESS will use a silicon photodiode in the visible range, and an InGaAs photodiode in the infrared [Kaiser et al. (2007)].

4. We will monitor and track payload performance in-flight, to monitor any calibration drift ([Kruk et al. (2008)], sec. 6.9).

5. An error budget will be made and maintained, before and throughout the calibration process, to quantify and track sources of uncertainty [Kaiser et al. (2008)].

6. Finally, and most importantly to this work, we select and perform analysis – prior to the ACCESS observations – on standard stars that can fulfill the conditions stated above with an individual observation within an ACCESS flight.

2.2 Standard Star Selection

In order to have a calibration that is transferable to other telescopes, a primary standard will be observed while in flight by the ACCESS payload. The standard stars chosen by ACCESS must satisfy stringent requirements.

1. In order to confirm the accuracy of an individual measurement from flight, ACCESS plans on observing a given target on multiple flights [Kaiser et al. (2007)]. Due to this, the standard star

chosen must not exhibit variability. Approximately 25% of all stars exhibit intrinsic photometric variability at or above 1% rms [Howell et al. (2005)]. A planetary system, as it transits in front of or behind a star, can cause a variance in the flux observed. With the revelation that nearly all late-type main sequence stars are likely to host at least one planet[Batalha (2014)], selecting a suitable candidate becomes more difficult. Even without a planetary system, circumstellar dust has been shown to create an IR flux excess [Wu et al. (2013)] which complicates modeling efforts.

2. To provide further confirmation of the findings by ACCESS, the chosen star must have previous space-based observation heritage. Even if the multiple ACCESS flights agree with each other, concurrent measurements made by other observers will provide further validation. The targets chosen have heritage with CALSPEC, a calibration database system consisting of a library of flux standards compiled on the HST system. In addition, many of them are primary standards for other instruments and surveys. The extended list of non-flight candidates included in this analysis consists of proposed JWST flux calibration standards [Gordon & Bohlin (2012)], of A and G type.

3. The star must be bright enough to obtain a signal-to-noise of 200 across the ACCESS bandpass of 3500 to 17000 Å in a single flight [Kaiser et al. (2008)]. Because flights will be compared to each other to confirm the data gathered from an individual flight, the precision of each flights data must be of a sub-percent level. Though in low flux regimes, the data may have to be binned up to obtain this, the limiting magnitude for this is about 9.5 V magnitudes. White dwarf targets have been used as standard stars owing to a well modeled structure[Bohlin (2003)]. However, there are no white dwarfs bright enough to be ACCESS candidates.

4. ACCESS has selected stars of spectral type A and G. A star's spectral type is associated with

the blackbody temperature of the star's photosphere, although it is also correlated with mass and spectral features. G stars are the same spectral type as the sun (G2V), and are typically in the temperature range of 5,200 to 6,000 K [Habets & Heintze (1981)]. Because the sun is the most well studied star by far, similar spectral types make good candidates for modeling. A stars are the same spectral type as Vega (A0V), a commonly used primary standard (see Sec. 1.2.3) with a temperature of 7,500 to 10,000 K [Habets & Heintze (1981)]. Both stars are main-sequence stars (i.e., stars that are in the stage of their life cycle in which they are primarily burning hydrogen in their core [Bohm-Vitense (1992)]).

5. Future observations of Vega and Sirius are part of the ACCESS flight strategy, and so the selected targets are required to be within 45^{o} of the zenith for flights observing Vega or Sirius [Kaiser et al. (2016)].

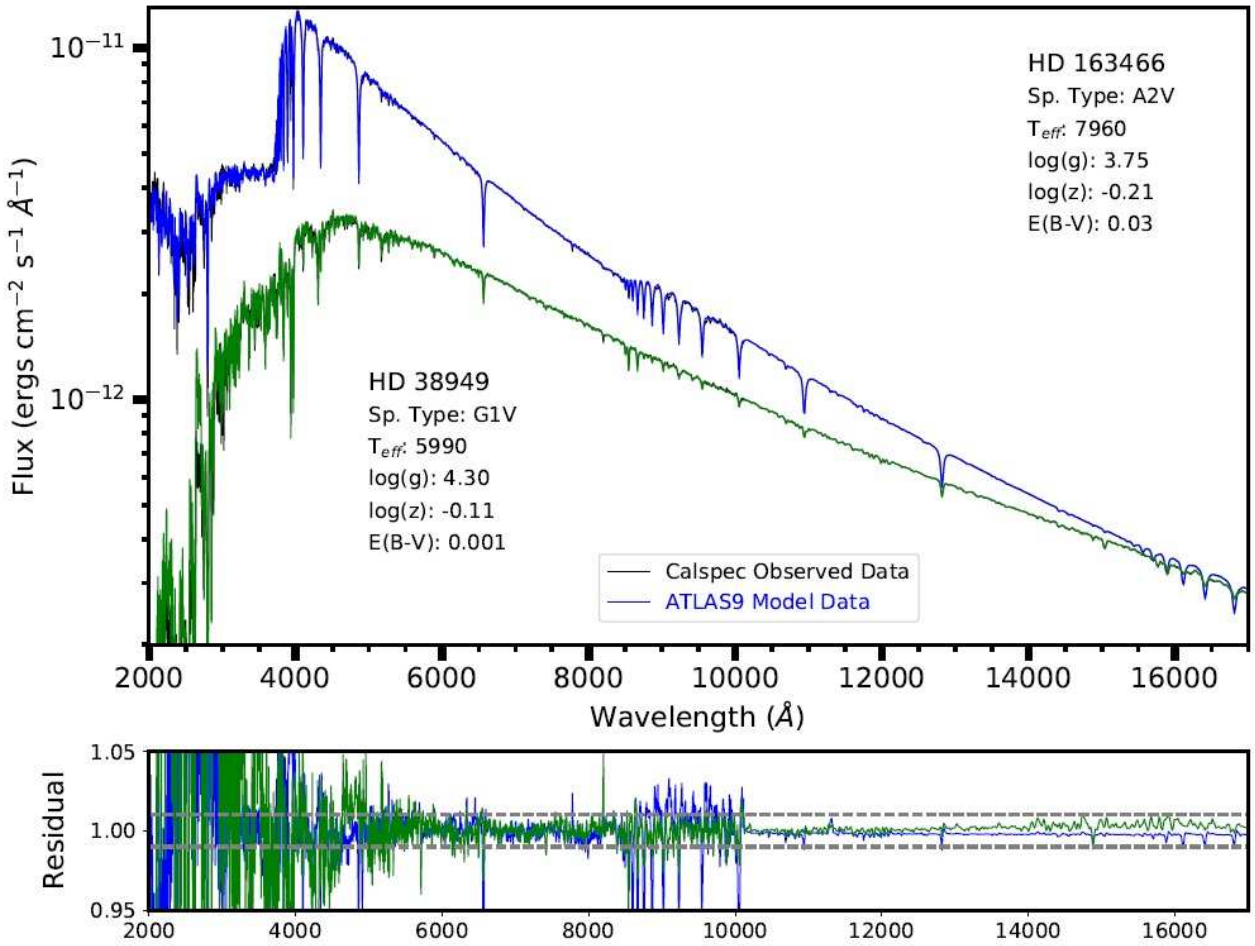

Figure 2.1: Comparison plots of spectra from ACCESS candidate stars, compared to ATLAS generated model spectra. Spectra taken from the CALSPEC database.

2.2.1 HD 38949

HD 38949 is a primary target for the ACCESS program. It is of spectral type G1V [Houk & Smith-Moore (1988)], similar in spectral type to the sun. HD 38949 has a relatively low rotational velocity (vsini) of 3.46 km/sec [Soubiran et al. (2013)], which can allow its spectrum to provide a cross check of the instrumental broadening for the ACCESS ground-based observing campaign. The absorption lines would be broadened by approximately 0.2 Å (according to equation 3.3), which is similar in

magnitude to the instrumental broadening for the ARCES instrument at Apache Point Observatory (R=33,000 [Wang et al. (2003)], see Sec. 3.1.1 for further discussion). Its low, stable radial velocity has made HD 38949 a radial velocity standard for the GAIA Radial Velocity Spectrograph [Soubiran et al. (2013)]. The GAIA project has determined the trigonometric parallax of HD 38949 to be 22.32 milliarcseconds, which corresponds to a distance of approximately 45 parsecs [Gaia Collaboration et al. (2016)]. It is part of the CALSPEC HST calibration standard data base [Bohlin et al. (2017)], and is a Spitzer standard as well [Engelbracht et al. (2007)]. It is sufficiently bright for the ACCESS program with a V magnitude of 7.80 [Høg et al. (2000)], and an H magnitude of 6.481 [Cutri et al. (2003)].

2.2.2 HD 163466

HD 163466 is the primary A star target for the ACCESS program, similar in spectral type to Vega. This will assist in developing and comparing stellar atmosphere models to HD 163466, as the stellar spectrum of A stars is already well modeled and understood. As with HD 38949, it is a CALSPEC standard [Bohlin et al. (2017)] and a Spitzer calibrator star [Engelbracht et al. (2007)]. It has a V magnitude of 6.85 [Høg et al. (2000)], and an H magnitude of 6.348 [Cutri et al. (2003)]. Though not a GAIA radial velocity standard (as hotter stars tend to have greater radial velocities [Fukuda (1982)]), HD 163466 has been observed by GAIA, and has a trigonometric parallax of 3.74 milliarcseconds ($\sim$267 parsecs) [Gaia Collaboration et al. (2016)]. Spitzer data exists for a long baseline for HD 163466 on the NASA/ IPAC Infrared Science Archive. It has shown photometric stability in the infrared, varying with a standard deviation of 2-4% across $\sim$4 years of observations (see Fig. 2.2).

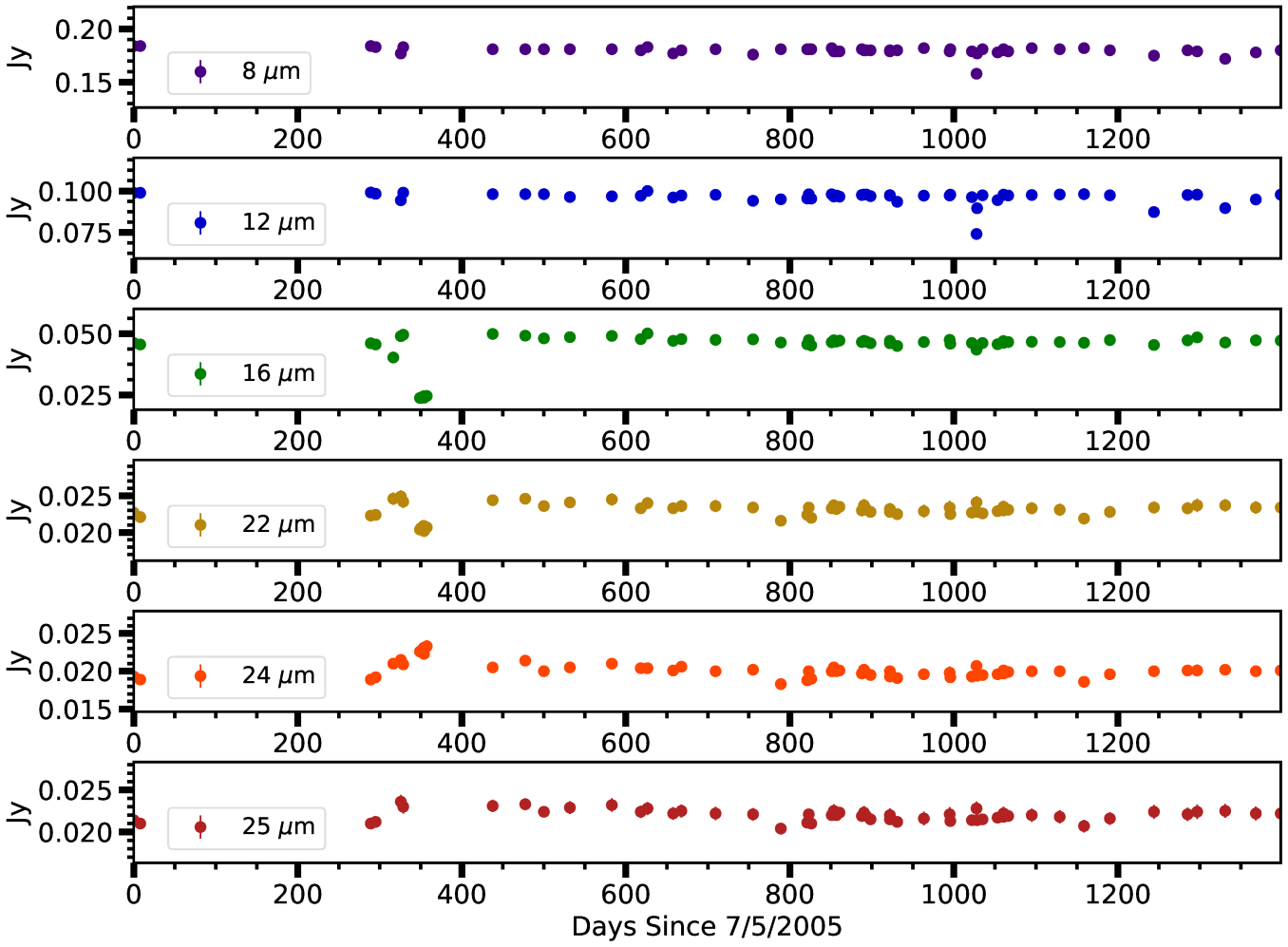

Figure 2.2: Spitzer observations in 6 photometric bands, across the span of 4 years, demonstrating the photometric stability of HD 163466.

2.2.3 Vega

In future flights, ACCESS will observe Vega (see Sec. 1.2.3), as confirmation of the methods used to calibrate the target stars. It is an A0V star [Gray et al. (2003)], with a V magnitude of 0.03 [Ducati (2002)] and an H magnitude of -0.03 [Cutri et al. (2003)]. Vega is approximately 7.7 parsecs away [van Leeuwen (2007)].

Vega is much brighter than the other targets and needs special observational considerations to prevent saturation of the detector. Sub-second integration times are required, in order to prevent saturation of the ACCESS detector. This can be accomplished by reading out a subsection of the detector array. Additionally, the aperture of the telescope can be reduced to limit the amount of flux seen by the spectrograph.

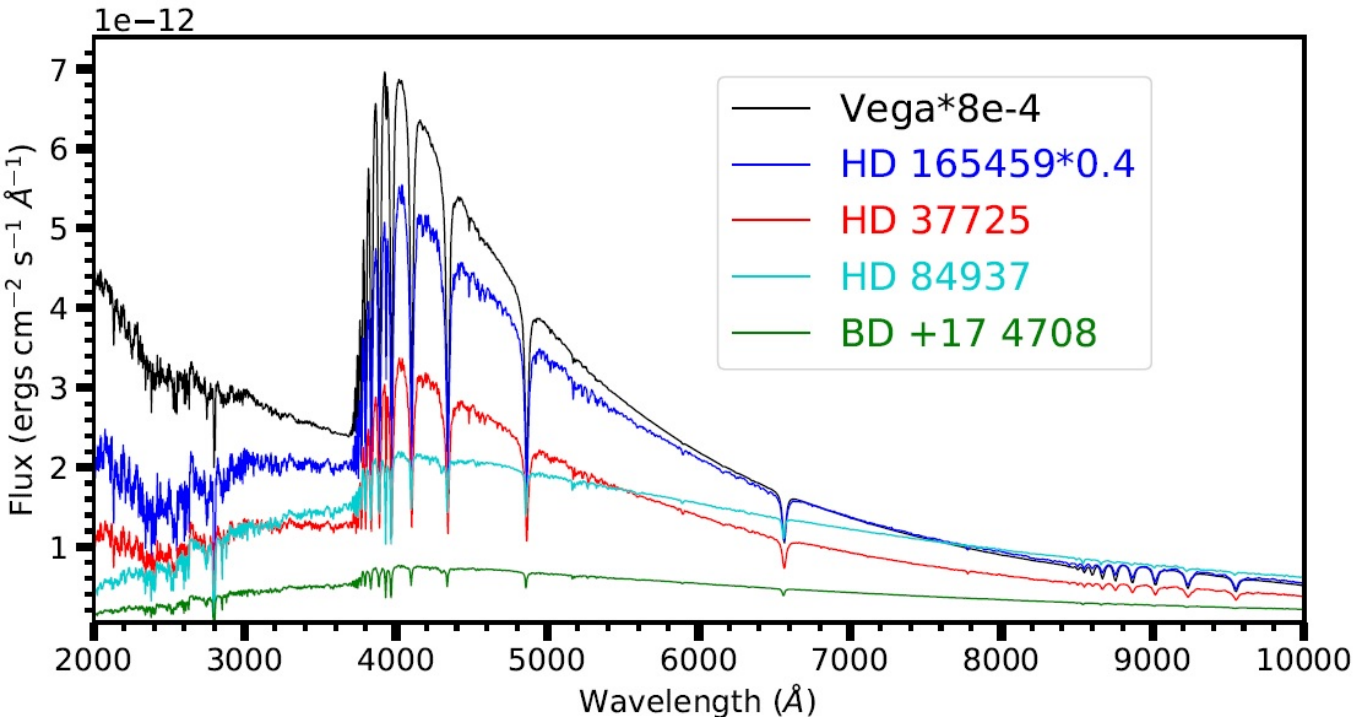

Figure 2.3: Comparison plots of spectra from previous ACCESS candidate stars. Spectra taken from the CALSPEC database; HD 84937 is not on the CALSPEC database, and the BD +17 4708 spectrum is scaled to the brightness of HD 84937 .

2.2.4 Previous ACCESS candidates

HD 37725

HD 37725, an A3V star, was one of ACCESS's primary targets. It is an IRAC standard for the Spitzer Space telescope [Reach et al. (2005)]. It has been observed by CALSPEC, and has a brightness of 8.31 magnitudes in the V band [Pancino et al. (2012)] and 7.9 magnitudes in the H band [Cutri et al. (2003)], which is practical for the $\sim$ 400 seconds we have for observation in the ACCESS rocket. It was vetted by the GAIA ground-based calibration selection and monitoring program (pre-launch) [Pancino et al. (2012)]. However, as part of the GAIA ground-based calibration selection program, it was found that HD 37725 exhibits noticeable variability, on the timescales of about a half hour, and signs point to it being a δ Scuti variable star [Marinoni et al. (2016)].

BD +17 4708

BD 17 +4708 is another target with standard star observing heritage, being a primary standard for the Sloan Digital Sky Survey [Betoule et al. (2013)], GAIA [Pancino et al. (2012)], the Supernova Legacy Survey [Regnault et al. (2009)], and the Hubble Space Telescope [Bohlin & Gilliland (2004)]. Its rotational velocity is much lower, giving the absorption lines a much lower gaussian width. BD +17 4708 exhibits a V magnitude of 9.46 [Ducati (2002)] and an H magnitude of 8.108 [Cutri et al. (2003)], which is at the faint limits of what the ACCESS payload can observe, while still achieving the goal of S/N of 200. However, BD +17 4708 exhibits variation in radial velocity, with a period of about 220 days, which suggests that it has a faint companion that can contribute to the flux and affect efforts to fit a model spectrum to it [Ramirez et al. (2006)]. BD +17 4708 is a metal poor star of spectral type F8, having an effective temperature of 6000 degrees [Mishenina et al. (2000)]. Additionally, it has been found that BD +17 4708 is increasing in brightness as a function of time; the GAIA survey found that it increased by a factor of 0.03 magnitudes in the B, V, and R filters, over a time scale of several years [Marinoni et al. (2016)]. [Bohlin & Landolt (2015)] found similar results, seeing a 0.04 mag increase in brightness over a period of 5 years.

HD 165459

HD 165459 is, like HD 37725, an IRAC and HST standard [Reach et al. (2005)]. The added benefit of HD 165459 is that, in addition to having strong observing heritage and no known variability, it is one of our brightest targets, with a V magnitude of 6.86 [Høg et al. (2000)] and an H magnitude of 6.626 [Cutri et al. (2003)]. This would help us gain the highest signal-to-noise in the limited time that the rocket flight allows. BD +17 4708, pictured in Fig. 2.3, is at the magnitude limit for achieving a signal to noise of 200 in one flight. This target is over ten times as bright in absolute flux (2.6 V

mags brighter). According to the Hipparcos catalog, the rotational velocity of HD 165459 is -19.2 kilometers per second, with an error of 5.7 kilometers per second [Grenier et al. (1999)]. However, a later survey puts its radial velocity at -24.1 kilometers per second, with an error of 3.5 kilometers per second [Gontcharev (2006)]. The resolution for HST/STIS data is approximately 50 km/sec, and the resolution for APO ARCES data is approximately 10 km/sec. It has been observed that HD 165459 has an excess flux in the infrared regime – observed by Spitzer at 22, 24 and 70 μm – indicative of a circumstellar disk [Rieke et al. (2005); Su et al. (2006); Wu et al. (2013)], which complicates modeling in that bandpass. The JWST bandpass is from 5 to 28.5 μm with the MIRI instrument [Rieke et al. (2015)], and so this effect would be visible.

HD 84937

HD 84937 is a commonly used standard, of similar spectral type to BD +17 4708, being a metal-poor sub-dwarf, of spectral type F8. It is, however, much brighter than BD +17 4708, having a V magnitude of 8.32 [Ducati (2002)]. HD 84937 has been selected as a benchmark star by GAIA for the calibration and validation of spectra for F, G, or K stars [Blanco-Cuaresma et al. (2014)]. Additionally, HD 84937 is one of the standards chosen by the Sloan Digital Sky Survey as a star directly calibrated in their photometric system against Vega [Fukugita et al. (1996)]. HD 84937's modeling is complicated by it being extremely metal-poor ([Fe/H]=-2.32 [Sneden et al. (2016)]), putting it at the extreme end of many model grids[Castelli & Kurucz (2004); Bohlin et al. (2017)]. Its stability is impacted by a high proper motion (∼860 milliarcseconds/year [van Leeuwen (2007)]). However, the CALSPEC database and selection of potential JWST calibrator late type stars are selected to be solar analogs. HD 84937, as a F8 subdwarf, is not a solar analog and has not been observed by HST/STIS. For these reasons, it was excluded as an ACCESS flight candidate.

Target	Alt. Name	Rank	R.A. (2000)	Dec. (2000)	Sp. Type	V mag	H mag
HD 37725		L[a]	5 41 54	29 17 51	A3V	8.31	7.92
HD 38949		P	5 48 20	-24 27 50	G1V	7.80	6.48
Sirius	Sirius	P	6 45 09	-16 42 58	A1V	-1.46	-1.33
HD 84937		L[b]	9 48 56	13 44 39	F8V	8.32	7.12
HD 163466		P	17 52 25	60 23 47	A2	6.85	6.35
HD 165459		L[c]	18 02 31	58 37 38	A1V	6.86	6.63
HD 172167	Vega	P	18 36 56	38 47 01	A0V	0.03	-0.03
BD +17 4708		L[d]	22 11 31	18 05 34	sdF8	9.46	8.11

[a] HD 37725 lien: variable
[b] HD 84937 lien: sdF5 spectral luminosity class. Only AV and GV stars were ultimately included.
[c] HD 165459 lien: IR excess, circumstellar disk
[d] BD +17 4708 lien: variable, multiple star system.

Table 2.1: List of Current and Former ACCESS candidate stars. Targets with rank "L" have been excluded as ACCESS candidates due to liens against them.

2.3 JWST Calibrator Stars

In addition to the ACCESS flight candidates, a set of A and G stars that are included as potential JWST calibrator stars [Gordon & Bohlin (2012)] have been analyzed as part of the ground-based observation campaign (Ch. 3) and the stellar atmosphere modeling efforts (Ch. 4).

Target	Alt. Name	R.A. (2000)	Dec. (2000)	Sp. Type	V mag	H mag
HD 37962		05 40 51.97	-31 21 03.99	G2V	7.85	6.343
HD 159222		17 32 00.99	+34 16 16.13	G1V	6.56	5.076
HD 106252		12 13 29.51	+10 02 29.89	G0	7.36	6.02
P330E	GSC 02581-02323	16 31 33.82	+30 08 46.50	G2V	12.917	11.454
HD 205905		21 39 10.15	-27 18 23.67	G1.5IV-V	6.74	5.387
HD 38949		05 48 20.06	-24 27 49.85	G1V	7.8	6.481
1743045	2MASS J17430448+6655015	17 43 04.48	+66 55 01.60	A5V	13.525	12.88
1757132	TYC 4212-455-1	17 57 13.23	+67 03 40.76	A3V	12.01	11.219
1812095	TYC 4205-1677-1	18 12 09.57	+63 29 42.27	A3V	12.01	11.312
1808347	TYC 4433-1800-1	18 08 34.74	+69 27 28.73	A3V	11.69	11.596
HD 14943		02 22 54.68	-51 05 31.66	A5V	5.898	5.491
HD 163466		17 52 25.37	+60 23 46.95	A2	6.85	6.348
HD 37725		05 41 54.37	+29 17 50.96	A3V	8.31	7.915
HD 180609		19 12 47.20	+64 10 37.18	A0V	9.42	9.141
HD 165459		18 02 30.74	+58 37 38.16	A1V	6.86	6.626
1805292	TYC 4209-1396-1	18 05 29.28	+64 27 52.10	A4V	12.74	12.031
HD 158485		17 26 04.84	+58 39 06.83	A4V	6.494	6.163
1732526	TYC 4207-219-1	17 40 34.69	+65 27 14.79	A6V	12.12	12.022
1802271	2MASS J18022716+6043356	18 02 27.17	+60 43 35.70	A2V	11.985	11.85
BD+60 1753		17 24 52.28	+60 25 50.75	A1V	9.65	9.651
HD 116405		13 22 45.12	+44 42 53.90	A0V	8.34	8.486

Table 2.2: ACCESS Stellar Analysis Sample. Order is in effective temperature derived in table 5.1.

Chapter 3

Ground-Based Observation at Apache Point Observatory

In order to provide a noiseless spectrum for usage in the future and extend the ACCESS spectra beyond our observed bandpass, stellar atmosphere models are generated and will be fit to the ACCESS data. In order to provide constraints on those models (and also to monitor the fidelity of the ACCESS targets), a multi-epoch observing program has been conducted at Apache Point Observatory. Apache Point Observatory (APO) is an observatory in southern New Mexico. The ACCESS program performed observations using the ARC 3.5 m telescope, as Johns Hopkins University is a member of ARC (the Astronomical Research Consortium). Spectral observations at APO were obtained at a much greater resolution than will be obtained by the ACCESS spectrograph, and thus are useful for determining line profiles across the ACCESS bandpass.

I have observed and reduced data from three different instruments at APO: ARCES, a permanently mounted high-resolution, echelle spectrograph covering 3200-10000 Å with a resolving power of 33,000, Triplespec, a near-infrared spectrograph covering the wavelength region extending from 0.92 to 2.46

Target observed	# ARCES nights	# Tspec nights
HD 38949	3	0
HD 163466	2	2
HD 37725	5	5
BD +17 4708	5	6
HD 165459	5	6
HD 84937	6	5
HD 159222	2	1
HD 158485	3	2

Table 3.1: List of APO observations undertaken by the ACCESS program, nights listed are only counted if the signal-to-noise for a given targets exceeds 100 across the faint blue region (∼4800 Å) for ARCES and 200 across the full wavelength range of 0.95 to 2.3 μm for Triplespec.

μm with a resolving power of 3500 (using the default 1.1 arcsecond slit), and DIS (Dual Imaging Spectrometer), a two channel, lower resolution spectrograph observing – in our configuration – 3660-5140 Å and 6720-7880 Å with R $\sim$ 1200, used with a wide slit to obtain photometric data.

We have been awarded a total of 33 half nights on the 3.5 m telescope. Though about half of all nights were not clear enough to observe due to poor weather, humidity, forest fires, etc., we have observed the majority of our targets with a signal-to-noise greater than 200 (4000-9500 Å for ARCES, 0.95 to 2.3 μm for Triplespec) at 2 or more epochs. On any given night, the target stars were observed with two instruments when available. This was typically ARCES and TripleSpec, to enable observations in the visible and near-infrared.

In addition to our primary targets and a flux calibration standard, each observing night we observe a star with known low vsini (rotational velocity, and therefore line width), so that we may measure the instrumental line spread function.

The seeing disk of the observed targets can range on a typical night from 0.9 to 2.0 arcseconds. The default slit size for the ARCES instrument is 1.6 by 3.2 arcseconds, and so the observations with this instrument are not photometric. ARCES consists of about 100 orders in which apertures can reliably be extracted for the targets observed by ACCESS. Each order spans about 100-200 Å, with

an order overlap of a similar scale.

3.1 ARCES Data Reduction

The reduction steps for the ARCES echelle data are done mostly in IRAF as per the reduction guide, and are performed as follows:

1. An error array for the science data (SCI) is initialized. This is done prior to any reduction steps, and the formula for the CCD error is outlined in the WFC3 data handbook [Deustua & et al. (2016)]:

$$\sigma_{CCD} = \sqrt{(SCI - bias)/(gain) + (readnoise/gain)^2} \tag{3.1}$$

   The bias is determined by a bias frame taken on the night of observations, and the gain and readnoise for the ARCES instrument are 3.8 $e^- DN^{-1}$ and 7 e^-RMS, respectively [Wang et al. (2003)] , and for Triplespec, 3.5 $e^- DN^{-1}$ and 18 e^-RMS/$\sqrt{N_{fowler}}$, where $N_{fowler}$is the number of Fowler samples taken [Wilson et al. (2004)]. Fowler sampling is the technique of performing several non-destructive reads of an image at the beginning and end of the integration, for the purpose of reducing the read noise [Fowler & Gatley (1990)]. These error arrays are overscan trimmed, magnified in the Y-direction (for the ARCES images), and extracted using the same apertures as the science data.

2. Remove cosmic rays from both blue and red flat field exposures. Two images with the same exposure time, light source, and filter optics are divided by each other, and a bad pixel mask is created with **CRMEDIAN** by marking the pixels that are two standard deviations above the median value of surrounding pixels. The task **CRFIX** takes the mask and linearly interpolates over the bad pixels marked

3. Flat field exposures are co-added using **IMSUM** Two types of flat images are used on ARCES. The red exposures are taken with no filter, as the QTH lamps used for flat images emit predominantly in the red region. However, in order to get sufficient signal in the blue, longer exposures must be taken. A filter composed of copper sulfate is inserted in the system to attenuate the red light. On a typical night, ten red exposures (taken with no filter) at seven seconds each, and ten blue exposures (taken with the CuSO4 filter) at 240 seconds are taken. An error array similar to the array created for the science data is created and propagated for the flat field exposures.

4. Thorium Argon line lamp exposures are obtained for wavelength identification, as they have many lines throughout the observed spectral bandpass. These exposures are co-added using **IMSUM**. The ThAr exposures consist of a mix of both 30 and 7 second exposures. The 7 second exposures provide data for the bright lines, which are saturated in the 30 second exposures. The NOAO has an atlas of ThAr lines that is used to correlate the lines to their laboratory measured wavelengths [Palmer & Engleman (1983)].

5. The bias voltage is subtracted, the overscan region is removed, and a bad pixel mask is applied to the ThAr data, flat field, and object exposures using **CCDPROC**. The bias is removed via a median from the image section [2100:2068,2:2027]. A table of known bad pixels is provided by APO.

6. Cosmic rays are removed from the science data, using the same method as for the flat field exposures. As cosmic rays are corrected, those pixels are flagged in a separate array. Those pixels are not used in the error propagation. A cosmic ray mask is also provided as an intermediate output during this step.

7. To avoid aliasing in the next step when identifying and extracting signal apertures, **MAGNIFY**

is used on all exposures to increase the Y scale by a factor of four. Total flux is preserved with rebinning and a linear interpolation in this step.

8. **APALL** is used on object spectra to define image apertures and aperture traces for all data. **APALL** can be set to automatically find apertures, although if automatic aperture finding does not work properly, these should be identified manually (which is often the case). Though most of the extraction is done automatically, aperture identifications and traces are inspected visually, to ensure no apertures are skipped over or counted twice. Object spectra are also used to extract the apertures for the flat field data (i.e. the flat field apertures were not recentered or resized) to ensure the same pixels are used to remove pixel-to-pixel sensitivity variations in the detector. If the apertures are defined using the filled slit of the flat field exposures, the extracted spectrum is offset in the cross-dispersion direction by 2 pixels (this is also the reason why flat fielding is done on 1-d data, rather than the typical 2-d method).

9. Background subtraction of dark current, sky, and scattered light is performed using **APSCATTER** The lower envelope of the inter-order light is fit and removed from the data. This is done to the data before aperture extraction, but the apertures are defined first, so that this step does not interfere with aperture definition.

10. Spectra of stars, flat field, and ThAr exposures are extracted using **APALL** and the previously defined apertures.

11. Line identification of emission lines is performed using **ECIDENTIFY** on the extracted ThAr spectra. For several orders, this must be done manually (referencing the NOAO ThAr Atlas), before an automatic line identification and dispersion fit can be applied. After the fit, lines can be found automatically. Outliers from the fit are rejected, and the automatic fit is iterated on,

until the RMS error is < 0.025 Å (less than 1 pixel).

12. The flats are then normalized using an eight piece spline in **CONTINUUM**, and the science data is divided by the flat field. When the science data is flat fielded, the error array for the science data and flat field are added in quadrature. They are summed as percent error:

$$\frac{\delta_{SCI/flat}}{(SCI/Flat)} = \sqrt{(\frac{\delta_{SCI}}{SCI})^2 + (\frac{\delta_{flat}}{flat})^2} \tag{3.2}$$

13. The wavelength reference and dispersion correction found from the ThAr exposures are then added to the object spectra.

14. If the image is being used for line data alone, the spectral continuum is normalized with **CONTINUUM**. Through trial and error, it has been found that an eight piece, cubic spline fit produces the best automated fit, though manual inspection and correction is still necessary, especially around strong absorption lines such as the Balmer lines. Within orders that contain Balmer lines, or very little continuum, a three piece spline fit tends to work better, in order to avoid biasing the fit.

    However, in orders with very little to no continuum, it becomes a highly subjective matter to fit any sort of continuum to the data. Orders with broad lines are of particular interest, such as orders containing Balmer lines and the calcium Fraunhofer lines. To mitigate this, a five pixel tall median filter is applied to the data, in the cross dispersion direction. Assuming the continuum varies monotonically throughout the spectrum, the orders directly adjacent to the orders without continuum can provide an accurate continuum estimate. Using this methodology, the line shape and profiles are dramatically improved. This method introduces a systematic shift in regions with highly varying flux, and thus is only applied in the context of measuring the

characteristics of broad lines.

15. If the stellar spectrum is to be compared directly with another stellar spectrum, it is flux calibrated relative to a standard star.

    A continuum fit is applied to the flux calibrator spectrum with **CONTINUUM**. This continuum fit is an eight piece spline, which in general works well throughout the spectrum.

    A similar continuum fit is applied to the spectrum of a standard within a database, such as CALSPEC. A 20 piece cubic spline is fit to the data; smooth enough to remove wide absorption features, but flexible enough to fit closely to the continuum.

    The smoothed absolute continuum is then mapped directly to the points from the desired spectra, matching in wavelength space, using IDL's function INTERPOL. The calibration spectrum is shifted slightly, to correct for the heliocentric velocity of the target spectrum (the target spectrum will be shifted to the rest frame after it is flux calibrated).

    One can then directly divide the smoothed absolute continuum by the continuum fit of the observed flux calibrator. The result is an instrument sensitivity spectrum that, when multiplied by the target spectra, yields a flux calibrated solution.

16. For direct comparison relative to an ATLAS generated model, it is important to consider the flux normalization step carefully. In the blue region of the spectrum, line blanketing is so severe that the highest peaks of the spectrum sit below the model continuum by 5-10 %. Additionally, ATLAS continuum data includes the effects of photo-ionization edges, and is therefore discontinuous at points across the APO bandpass. In order to correct for this, the ATLAS model is convolved with a gaussian to fit to either the line spread function of the APO instrument, or the vsini of the star (whichever is greater). The residual between the continuum normalized APO

data and the smoothed ATLAS model is then convolved with another gaussian, such that the quadrature sum of the FWHM of both smoothing gaussians comes out to 120 pixels of APO data. This provides a smooth correction function for the APO data that is periodic at the rate of the APO orders. Once this correction is applied, the χ^2 value can be computed between the model and the data.

17. For either continuum fitting, a heliocentric correction is then applied to that data as a final step.

Though a common method for removing cosmic rays is a sigma rejection of a pixel compared to its surrounding neighbors, this can lead to missed CR's in areas of high signal, or grazing incidence cosmic rays, which expose many pixels in an area. We adopted a method in which each exposure is compared to an exposure of the same target, scaled to the same exposure time.

3.1.1 Determining the line spread function (LSF)

Using the higher resolution (R=33,000) spectra from APO, we can measure the equivalent widths of lines in the ACCESS targets that would be blended with adjacent lines at the ACCESS payload resolution (R=500). The equivalent width is a measure of how much energy is removed from a spectrum via a specific absorption line. The absorption depth of an individual line is a poor measure of its strength, because stellar absorption lines are broadened due to the rotation of the star (line depth ratios may be used [Gray (1992)] to determine stellar parameters, however) (see sec. 3.5).

If a stellar atmosphere model is generated at a higher resolution than the observed data, it must be deresolved to the spectrograph resolution, which is performed by convolving the model data with the LSF of the spectrograph.

The line spread function was measured using the Thorium Argon lamp exposures, and confirmed

HD 159222 λ (Å)	HD 159222 FWHM (Å)	HD 159222 Species	ThAr λ (Å)	ThAr FWHM
4507.47	0.142	Fe II	4515.22	0.137
5089.86	0.140	Fe I	5096.56	0.146
5500.50	0.152	Fe I	5504.38	0.157
6015.60	0.166	Mn I	6049.19	0.174
7120.90	0.183	Ni I	7000.91	0.187
8083.67	0.244	Fe I	8093.71	0.251
9053.05	0.295	C I	8868.93	0.272

Table 3.2: A comparison of the FWHM of spectral lines across the ARCES bandpass for a low vsini star (HD 159222, vsini=3-5 km/sec [Martínez-Arnáiz et al. (2010)]), and a ThAr line lamp taken on the same date.

using a star with low vsini. The Thorium Argon exposures provide for a high number of strong lines throughout all spectral regions.

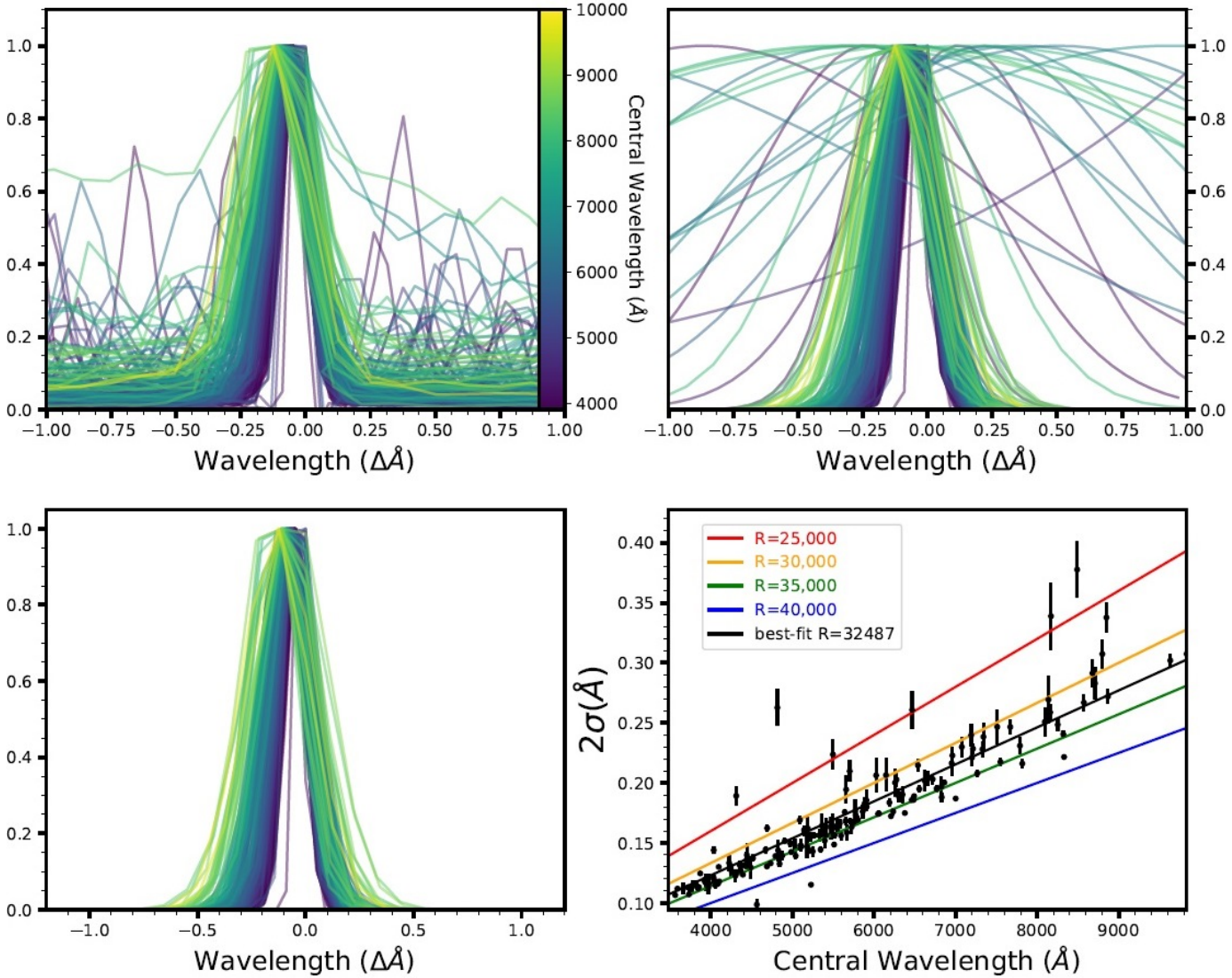

Figure 3.1: The process by which the line spread function is fit to a thorium argon lamp exposure. **Top Left:** All lines found within the ThAr data that exceed 100 DN's, normalized to a peak value of 1. **Top Right:** Gaussian profile fits to all lines found, interpolated to the resolution of the ARCES data. **Bottom Left:** Removal of poor fits (correlation coefficient < 0.9) to the lines. **Bottom Right:** The final fit, using $\sim$160 lines across the ARCES bandpass.

In order to determine the line spread function using a star, the effects of stellar rotation were removed from the line. The broadening effects of stellar rotation are not of a gaussian form, as the distribution of velocities cannot exceed the equatorial speed. Rather, it takes the form described in [Gray (1992)]:

$$G(\Delta\lambda) = \frac{2(1-\varepsilon)[1-(\Delta\lambda/\Delta\lambda_L)^2]^{\frac{1}{2}} + \frac{1}{2}\pi\varepsilon[1-(\Delta\lambda/\Delta\lambda_L)^2]}{\pi\Delta\lambda_L(1-\varepsilon/3)} \tag{3.3}$$

where ε is the limb darkening coefficient,

$$I_c/I_c^0 = 1 - \varepsilon + \varepsilon cos\theta \tag{3.4}$$

and $\Delta\lambda_L$ is the vsini of the star. The limb darkening coefficient for the low vsini star HD 159222 was assumed to be 0.5, a typical value for stars with low B-V color index [Gray (1992)]. HD 159222 has published vsini values of 3-5 kilometers per second [Martínez-Arnáiz et al. (2010)]. Using an adopted value of 4 km/sec, the width of the stellar rotation profile is only 3 pixels wide at the resolution of the ARCES data. The results of the thorium argon lamp fitting and the stellar fitting are within the 95% confidence interval of each other (see table 3.2 for a few examples lines), and agree with ARCES's published resolving power of R=33,000 [Wang et al. (2003)]. The scatter of values for FWHM in the lines of the low vsini star is much greater than the ThAr lamp exposures. The lines measured in a stellar spectra are broadened by several physical mechanisms, such as pressure broadening and thermal broadening. These effects are dependent not just on the wavelength of emitted light, but on the intrinsic qualities of the emitter particle, such as mass and ionization level [Gray (1992)].

According to the prescription of [Nidever et al. (2015)], a Gauss-Hermite polynomial was tested on the data as well. No skew was detected in the lines. Using a Gauss-Hermite polynomial resulted

in a wider spread of σ. Therefore, it was determined that a gaussian was the optimal shape to apply to achieve a wavelength dependent LSF. A traditional "R" value (gaussian in which $\sigma = R/\lambda$) was applied to stellar atmosphere models of higher resolution, when compared to the APO data.

3.2 DIS

DIS (Dual Imaging Spectrograph) is a two-channel spectrograph that observes in the red and blue regions of the spectrum simultaneously. The red and blue spectral regions are separated by a dichroic beam splitter, with a transition edge around 5350 Å. ACCESS has used gratings for DIS that provide a resolution of R $\sim$ 6,000 in the blue spectral region of 3660-5140 Å, and R $\sim$ 12,000 in the red spectral region of 6720-7880 Å. Though this is not as high resolution as the ARCES instrument, DIS has a wide slit mode (5 arcseconds) designed to collect all spectral light and mitigate slit losses. The reduction of DIS data follows a similar format to the ARCES echelle data reduction, albeit with a much larger aperture extraction window, as there are no cross dispersed orders of light. DIS was only used on nights in which the atmospheric disturbances and variations were low, so as to ensure that atmospheric effects contributed as little as possible to the data. For this reason, very few nights granted to the ACCESS program qualified for DIS observations.

3.3 TripleSpec

TripleSpec [Wilson et al. (2004)] can be mounted onto the port opposite the ARCES instrument, thus both instruments can be used on the same observing night. The advantage of Triplespec is that it provides spectra from 0.92 to 2.46 μm, extending the ground-based observations much further into the near-infrared. Though lower resolution than ARCES at R=3,500, it still observes at a

higher resolution than the ACCESS instrument. Triplespec is a cross dispersed echelle spectrograph consisting of five orders.

The majority of steps for data reduction with the TripleSpec instrument were performed with TripleSpecTool, a modified version of Spextool [Vacca et al. (2003); Cushing et al. (2004)]. These steps are performed as follows:

1. Flat fields are constructed. For each night of TripleSpec observations, a series of images are taken with the bright truss lamps (a QTH style lamp) on and the telescope covers closed. At least 10 60-second exposures are taken per night. These images are averaged together and normalized.

2. A wavelength solution is determined, using science images. By offsetting the extraction aperture from a stellar spectrum in a science image, the sky background is extracted. Telluric lines are strong and numerous within the sky background in the TripleSpec bandpass (see sec. 1.2.5 and fig. 1.6), and are used to determine the wavelength scale of the night's exposures.

3. The stellar targets observed by ACCESS are point-sources, and are observed in an ABBA dither pattern. Within an AB pair, the images are normalized by the flat, and exposure A is subtracted from exposure B (or B from A, depending on the pair).

4. Within the subtracted image, spatial profiles in the cross-dispersion direction are defined, by performing a median across the full order. This is performed for all five TripleSpec orders for both A and B exposures.

5. The width of the apertures are defined. This width is dependent on the seeing of the particular night, but the suggested value of ± 2 pixels is typically sufficient. Additionally the background apertures are also defined. Similar to the aperture definition, the suggested values of ± 3 pixels

for the minimum distance from the aperture center with a width of 2 pixels.

6. The apertures are traced across the orders, and extracted according to the defined width. The background is extracted in the same manner and subtracted from the stellar signal.

7. All extracted exposures are scaled to the same count level. This is typically done in the range of 1.55 to 1.75 μm, as this bandpass has high signal-to-noise, and is predominantly continuum. All exposures are then combined using the robust weighted mean, excluding outliers from the combination.

8. An A0V calibrator star is fit to a Vega spectrum, stellar features are removed, and a telluric correction spectrum is produced [Vacca et al. (2003)]. This method applies a flux calibration solution to the data, but is not precise enough for the ACCESS program, showing disagreement with the CALSPEC database on the order of $\backsim$5%.

9. For flux calibration, the most dependable method has been through a custom written program, as the flux calibration from the previous step is not sufficient for the ACCESS group. This program performs a continuum fit on the TripleSpec data and CALSPEC data for the same star. It then multiplies the TripleSpec continuum by ratio between the two continuum. The TripleSpec line data may now be directly compared to the CALSPEC data or stellar atmosphere models as outlined in Chapter 4.

3.4 Selected Results

3.4.1 ARCES and Triplespec

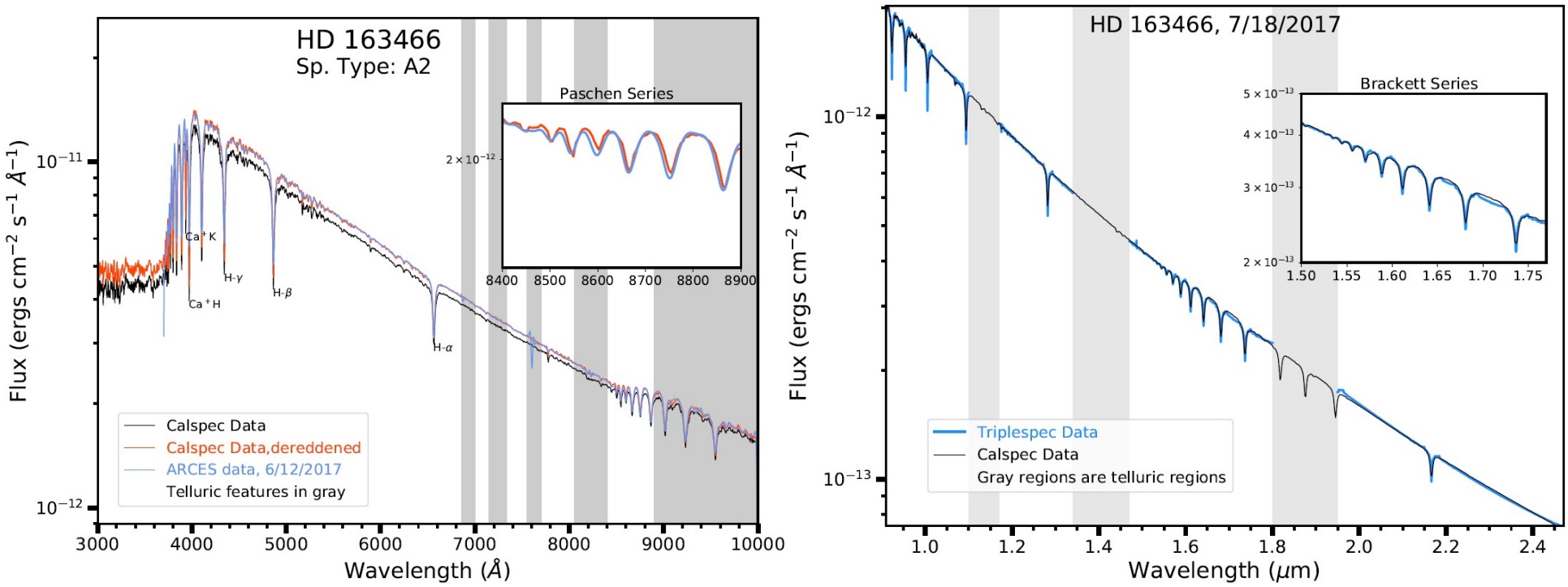

Figure 3.2: ARCES (left) and Triplespec data (right) for primary ACCESS target HD 163466, overplotted with CALSPEC data. ARCES data is smoothed for readability.

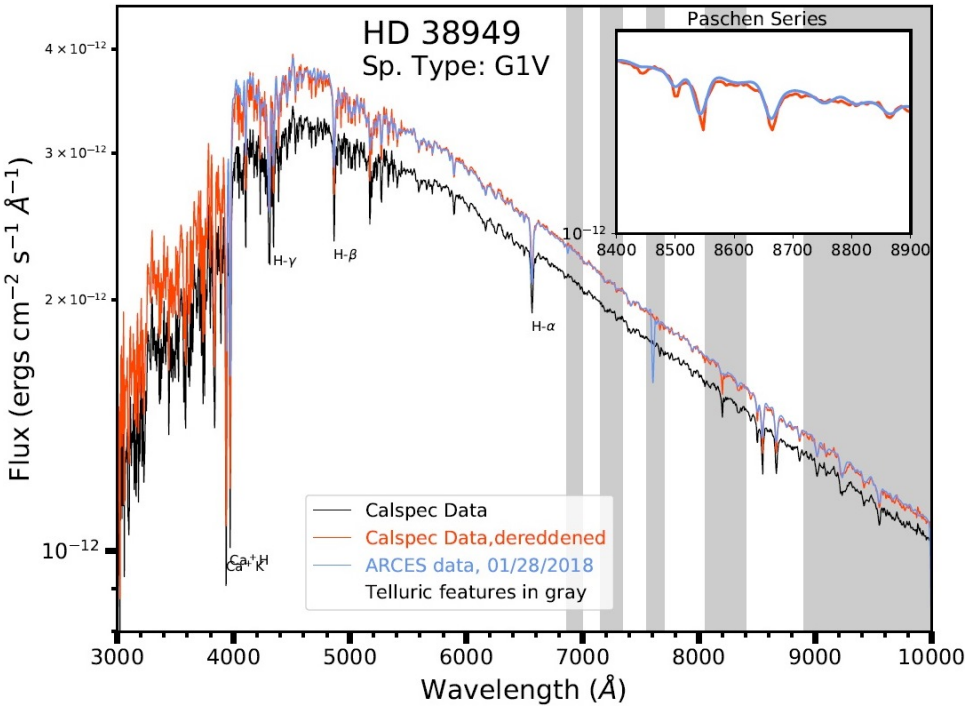

Figure 3.3: ARCES data for Primary ACCESS target HD 38949, overplotted with CALSPEC data. ARCES data is smoothed for readability. Triplespec data of HD 38949 was of poor quality, and thus was not used.

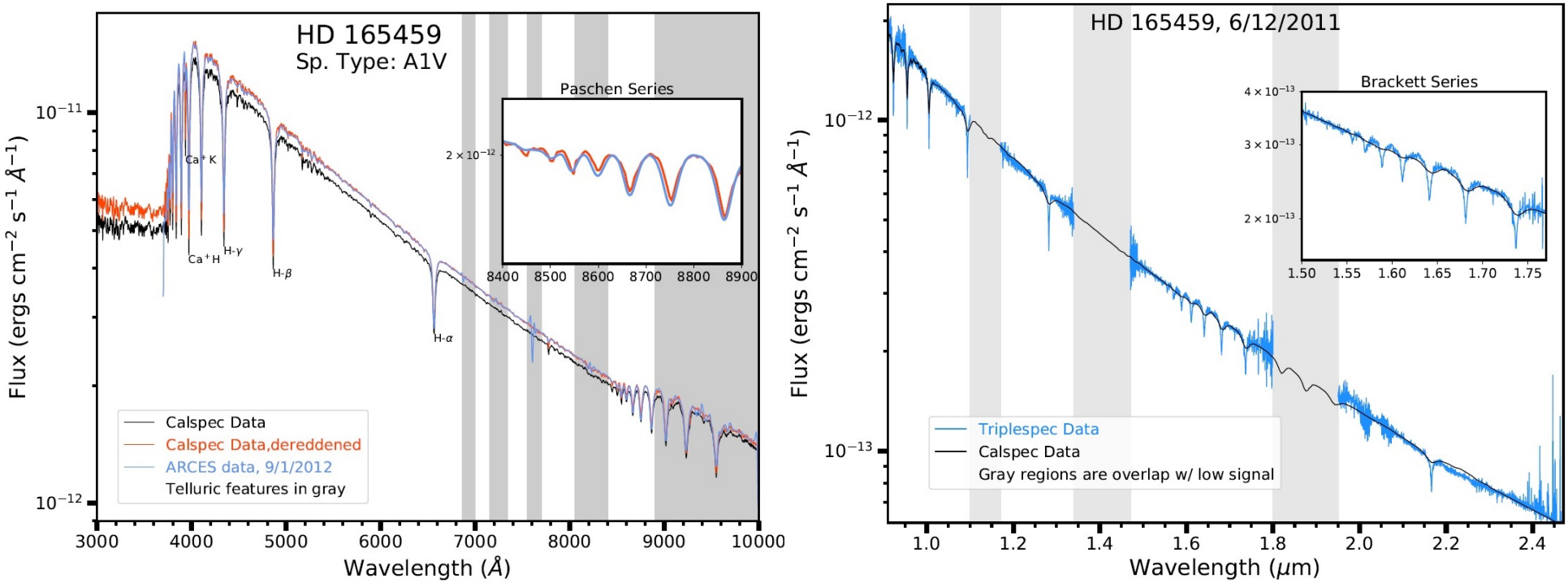

Figure 3.4: ARCES (left) and Triplespec data (right) for previous secondary ACCESS target HD 165459, overplotted with CALSPEC data. ARCES data is smoothed for readability.

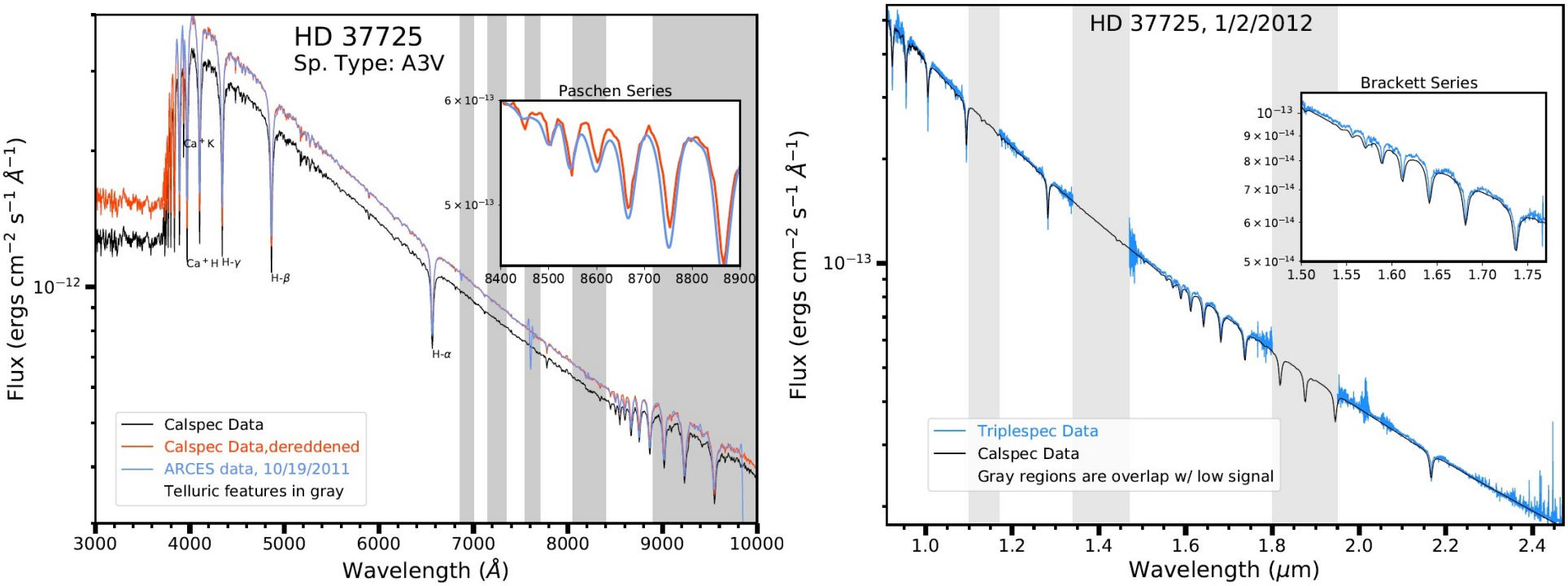

Figure 3.5: ARCES (left) and Triplespec data (right) for previous secondary ACCESS target HD 37725, overplotted with CALSPEC data. ARCES data is smoothed for readability.

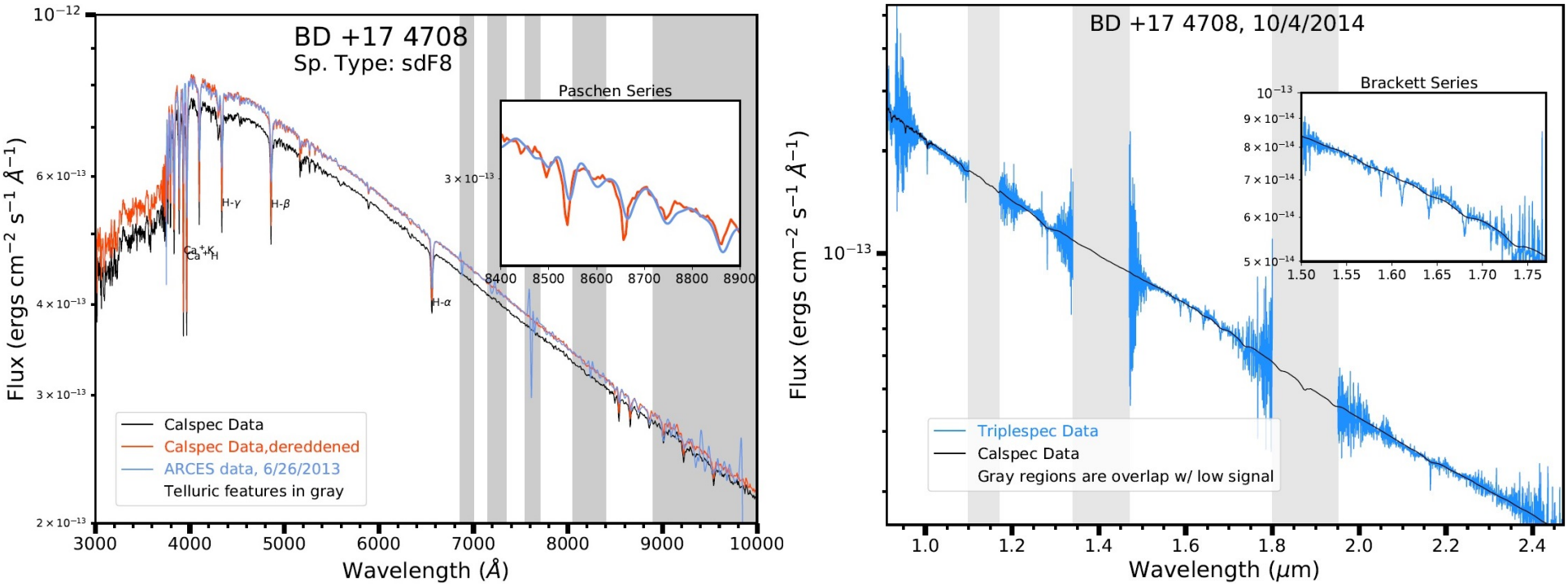

Figure 3.6: ARCES (left) and Triplespec data (right) for previous secondary ACCESS target BD +17 4708, overplotted with CALSPEC data. ARCES data is smoothed for readability.

3.4.2 DIS: BD +17 4708

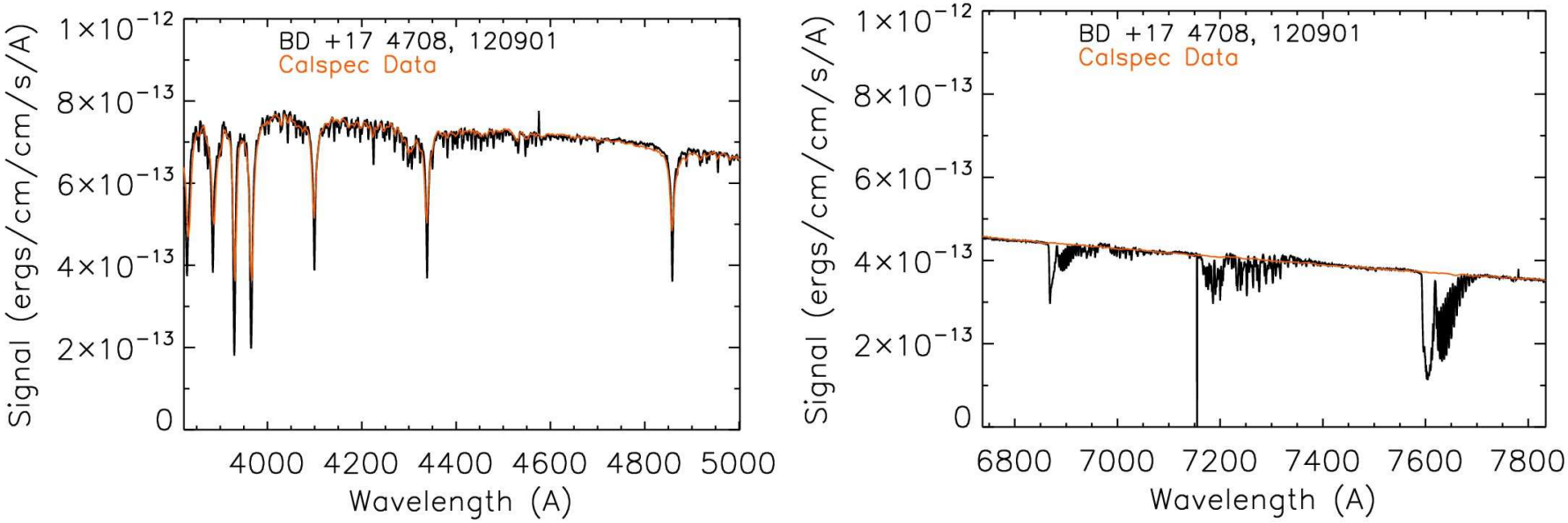

Figure 3.7: The results of an exposure taken at APO with the blue channel (left) and red channel (right) of DIS on 09/12/2012 of BD +17 4708, overlayed with data from the CALSPEC database. Prominent features in the red channel are telluric lines.

3.5 Effective Temperature Confirmation from EW Ratios

To optimize the quality of fits that are achievable between the observed spectra and models, the ACCESS team sought to use individual line profiles to determine the stellar temperature for a sample of G stars.

3.5.1 Absorption line structure

The shape and size of various absorption lines within the stellar spectra can be used to determine important stellar parameters, as mentioned above [Gonzalez & Lambert (1996)]. Absorption lines are caused by photon absorption by an atom and a subsequent transition of an electron to a higher energy level (emission lines occurring in the opposite process). For example, Balmer lines are absorption lines formed by hydrogen transitions that begin or end at $n = 2$ [Balmer (1885)]. An exception to this is the 1→2 or 2→1 transition (Lyman-α), part of the Lyman ($n = 1$) transition series, found in the UV spectral region[Lyman (1906)]. In the infrared region, $n = 3$ transitions are known as the Paschen series[Paschen (1908)], and $n = 4$ are known as the Brackett series [Brackett (1922)]. The wavelength of light absorbed or emitted in the Balmer series depends on the final or initial state of the electron **n**, following the formula [Balmer (1885)]:

$$\frac{1}{\lambda} = R\left[\frac{1}{2^2} - \frac{1}{n^2}\right] \tag{3.5}$$

With the Rydberg constant R=1.097 x 10^7 m^{-1}, in SI units. Therefore, the transition of 2→3 would emit light at the wavelength of 6562.8 Å (Hα).

In weaker lines, (i.e. lines with equivalent widths between 10 mÅ and 200 mÅ [Sousa et al. (2010)]) the relative strength of lines at different energy levels is correlated to the effective temperature:

$$\frac{N_n}{N_m} = \frac{g_n}{g_m} e^{-(\chi_n - \chi_m)/kT} \tag{3.6}$$

The equivalent width (EW) of a line is a measure of how much flux was removed from the spectrum. Equivalent width is defined as the width, in wavelength space, that the absorption line would be if *all* the flux were removed from the spectral region centered around the transition wavelength. Equivalent width allows one to quantify the strength of an absorption effect regardless of broadening effects. The equivalent width is maintained as constant due to broadening from instrumental resolution as well.

The spread of the measured shape of an absorption line can be described as a Voigt profile [Gray (1992)], which is a combination of a Gaussian profile and a Lorentz profile. The Gaussian profile comes from the physical mechanism of doppler broadening:

$$G(\omega; \sigma) \equiv \frac{e^{-(\omega - \omega_0)^2 \backslash (2\sigma^2)}}{\sigma\sqrt{2\pi}} \tag{3.7}$$

where ω is the frequency, and ω_0 is the central frequency of the transition. The standard deviation of the Gaussian, σ, can be expressed as:

$$\sigma \equiv \sqrt{\frac{kT}{mc^2}} \omega_0 \tag{3.8}$$

where k is the Boltzmann constant, m is the mass of the particle, and c is the speed of light. The Lorentz profile is due to two effects: collisional broadening, from gases at high pressure, and natural broadening from the uncertainty principle. Low-mass (and therefore low-temperature) stars have higher pressures at the photospheric layers, and therefore stronger collisional broadening than high-mass stars [Carroll & Ostlie (1996)]. It takes the form:

$$L(f;\gamma) \equiv \frac{\gamma}{\pi((\omega-\omega_0)^2+\gamma^2)} \tag{3.9}$$

In which γ is either a function of the time interval between particle collisions or the energy uncertainty of the transition. The Voigt profile combination of the Lorentzian and the Gaussian would take the form of:

$$V(\omega;\sigma,\gamma) = \int_{-\infty}^{\infty} G((\omega)';\sigma)L(\omega-\omega';\gamma)d\omega' \tag{3.10}$$

The analytical solution to this is:

$$V(x;\sigma,\gamma) = \frac{Re[w(z)]}{\sigma\sqrt{2\pi}} \tag{3.11}$$

where:

$$z = \frac{x+i\gamma}{\sigma\sqrt{2}} \tag{3.12}$$

and Re[w(z)] is the real part of the Faddeeva function:

$$w(z) = e^{-z^2}\left(1+\frac{2i}{\sqrt{\pi}}\int_0^z e^{t^2}dt\right) \tag{3.13}$$

The ratio of equivalent widths, between disparate elements, have a correlation, that can be fit via a polynomial, to effective temperature [Sousa et al. (2010)]. There is a correlation between the equivalent width (divided by its central wavelength) and the abundance of the element that caused the line. This is typically known as a "curve of growth" (see Fig. 3.8).

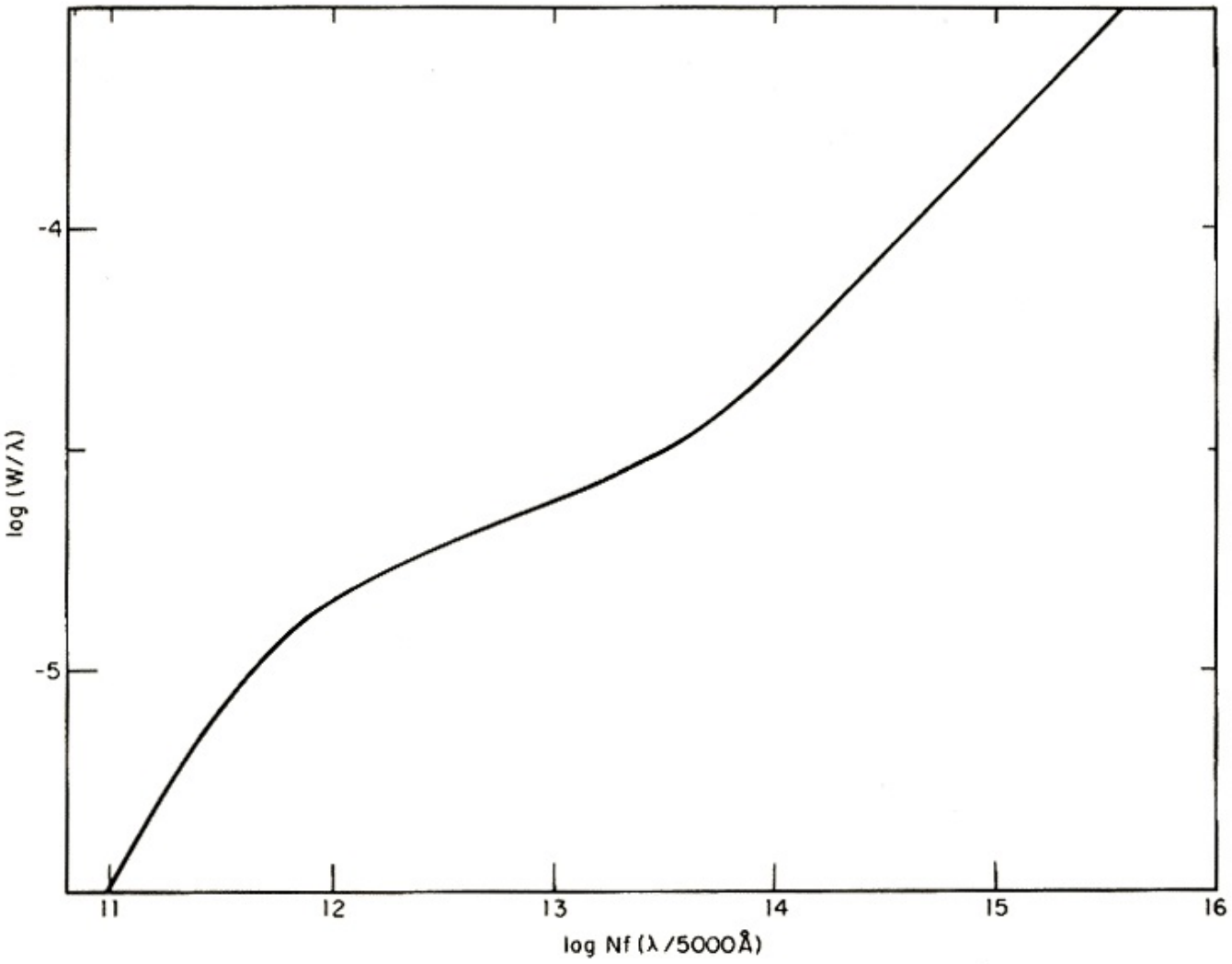

Figure 3.8: A generalized curve of growth for the sun. N is number density (atoms cm^{-2}), f is the oscillator strength of the transition, and W is the equivalent width. [Aller (1971)]. The curve of growth shows three regimes. On the left end exists the "linear" regime, in which optical depths are small ($\tau_0 \ll 1$), and the equivalent width grows proportional to number density, by increasing the line core depth. Within the central "flat" regime ($10 \leq \tau_0 \leq 10^3$), the line depth begins to saturate, and the equivalent width grows proportional to the logarithm of number density, by widening the wings of the line profile. The right "square root" regime ($\tau_0 > 10^4$) occurs when the the line is saturated at the core. The optical depth of the line wings become comparable to the optical depth of the line core and equivalent width grows as the square root of number density [Gray (1992)].

3.5.2 EW ratios to G stars

[Teixeira et al. (2016)], building on the work of [Sousa et al. (2010)], produced a set of 322 polynomial functions, using EW line-ratios as inputs, that can be used to determine the effective temperature of a star. The line ratios are derived from a series of 135 absorption lines in the 4950-6800 Å bandpass. The majority of the stellar calibration sample in [Teixeira et al. (2016)] was provided by the High Accuracy Radial velocity Planet Searcher (HARPS) instrument at the ESO La Silla 3.6m telescope (R∼110,000). The lower resolution of the ARCES spectra prevents many of the 322 ratios from being used, due to one or both lines being too weak or blended with adjacent lines.

Within the ACCESS stellar targets sample, the flight target HD 38949 is the most suitable candidate. It has been observed multiple times at APO, it is within the temperature range of the calibration, and its surface gravity is close to the peak of the gravity distributions within the [Teixeira et al. (2016)] sample (see Fig. 3.9).

A series of discriminants was used to determine which lines were suitable to use. Firstly, if the Voigt profile fit has a correlation coefficient less than 0.8, it indicates that the line is not fit well, and these lines are not used. If the line's equivalent width is less than 0.01 Å at a S/N of 100, it indicates that the line is too weak to be reliably measured. If the equivalent width is greater than 1 Å or the central peak is offset by more than 0.02 Å, it indicates either a poor fit, or that the line is blended. Finally, if the calculated temperature from the EW ratio is out of the range of the applicability within [Teixeira et al. (2016)] (∼4500-6500), one or both lines in the ratio may be blended, and that ratio is excluded.

For a suitable target, only about 20 or so line ratios were determined to be acceptable for effective temperature determination. The majority of G stars in the ACCESS stellar analysis sample have log(g) in the range of 3.5-3.7, of which there are very few in the [Teixeira et al. (2016)] calibration

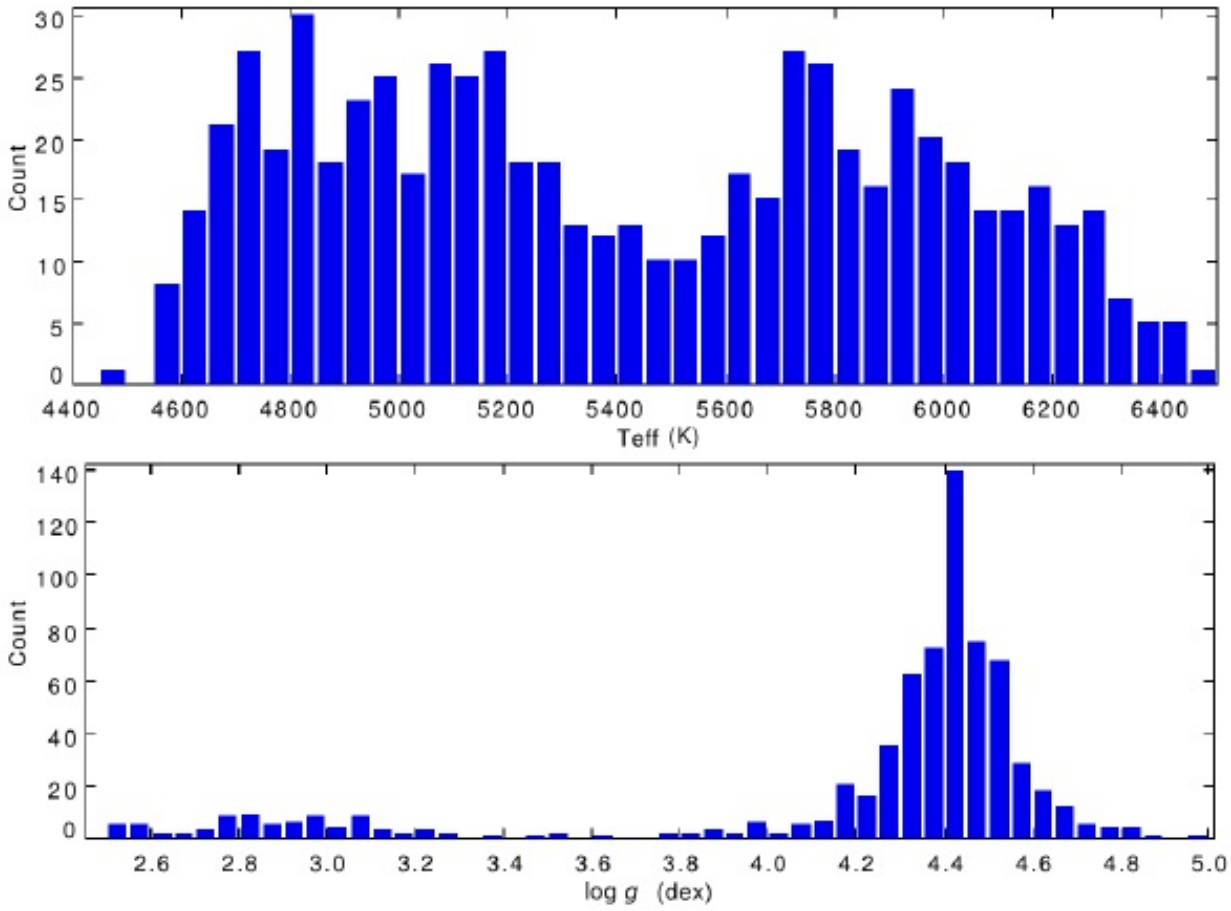

Figure 3.9: The temperature and gravity distribution for the [Teixeira et al. (2016)] sample.

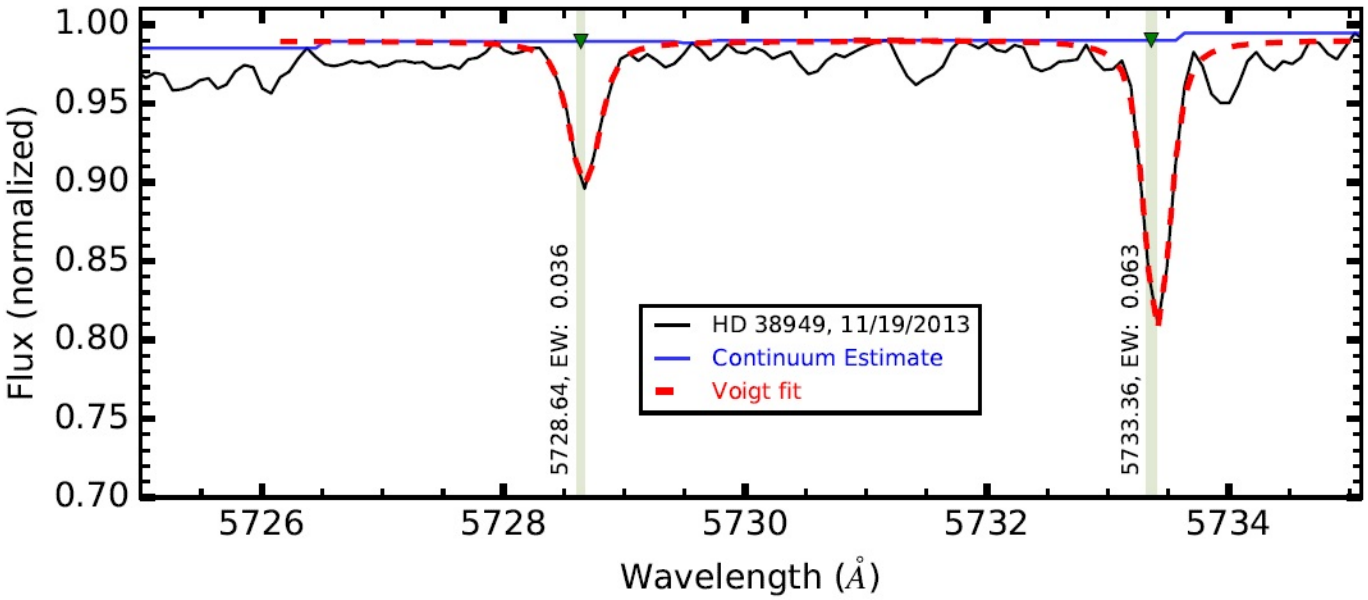

Figure 3.10: Example of an EW line-ratio used for effective temperature determination for HD 38949. The left line is a vanadium line, and the right line is iron.

Star	**Obs. Date**	**# of ratios used**	**mean T_{eff} (K)**	**ΔT_{eff} (K)**
HD 38949	11/19/2013	23	6012	22
HD 38949	12/10/2017	25	5991	1
HD 38949	1/28/2018	21	6041	51
HD 106252	4/10/2012	24	5890	60
HD 106252	1/23/2013	32	5870	40
HD 37962	12/10/2017	36	5698	52
HD 37962	1/28/2018	34	5694	56
HD 159222	6/28/2013	54	5812	12
HD 159222	6/12/2017	57	5808	8

Table 3.3: Effective temperature determinations from APO observations, compared to the effective temperature for these targets determined by [Bohlin et al. (2017)].

sample. Stars that were in the temperature range of (∼4500-6500) show agreement within 100 K or better with the parameters derived from model fits within this work or derived parameters within [Bohlin et al. (2017)].

3.6 ATLAS12 Fits to APO data

The APO data taken by the ACCESS group was also fit to ATLAS12 stellar atmosphere models, using a chi-squared minimization method described in Chapter 4. The primary ACCESS targets HD 38949 and HD 163466 were observed, as well as the previous ACCESS target HD 165459. Each of these targets has two nights of observations with signal-to-noise of over 200 per night across the bandpass of 4500-8000 Å, making them good candidates to test the consistency of the fits. HD 38949 has three nights of observations. Only effective temperature, surface gravity and metallicity were used in these fits. The data was continuum normalized, rather than flux calibrated, owing to the non-photometric circumstances under which most of the APO data was taken. This precludes any fitting to interstellar extinction.

Furthermore, because the data is continuum normalized, we performed a point-to-point fit between data and model. Broad bin fitting is used to measure the overall shape of the spectrum, which is only appropriate for flux calibrated data. Additionally, a point-to-point fit captures the resolved line profiles of the APO data.

stellar atmosphere models are generated with vacuum wavelengths. For comparison with ground based observation, the conversion to air wavelengths is performed according to the parameters presented in [Ciddor (1996)].

The ARCES data used for this fit has poor continuum fitting in the region of ∼3800-4200 Å. Flux is at its lowest in this region (achieving a S/N of 100 within our acceptable targets), and the photo-ionization edge at 3645 nm leads to heavy line blanketing in this region. Because the error array generated during reduction is applied to the reduced chi-squared statistic, fits in this region are particularly poor. The line blanketing is much more irregular for G stars in this region, and this may affect the quality of the fits for HD 38949.

In order to compare the APO data directly to the CALSPEC data, the continuum normalized data can be multiplied by the continuum of the best-fit model, and then scaled by an absolute value to the CALSPEC data. Agreement is within 1% for the majority of the spectrum, with agreement reaching 5% in wavelengths shorter than 5500 Å. Strong hydrogen lines can have high residuals up to 10% in the line cores. Additionally, regions of strong telluric contamination are excluded from the fits, and are clearly in disagreement with CALSPEC data.

The maximum disagreement between nights is 60 K effective temperature, 0.15 logarithm of surface gravity, and 0.04 logarithm of metallicity for all three targets. There is some disagreement between these fits and fits using CALSPEC data. There is a particular disagreement in temperature, with a mean disagreement of -40 ± 122 K.

At the STIS resolution, the residual between best-fit models for CALSPEC data and best-fit models for APO data is less than 1% from 500 nm out to 1000 nm. For HD 163466 and HD 165459, the residual exceeds 2% only at the Balmer lines at 486, 434 and 410 nm. For HD 38949 there is 2% disagreement between these models at H-alpha and lines within the Paschen series, and the fits disagree up to 10% between 400 and 500 nm.

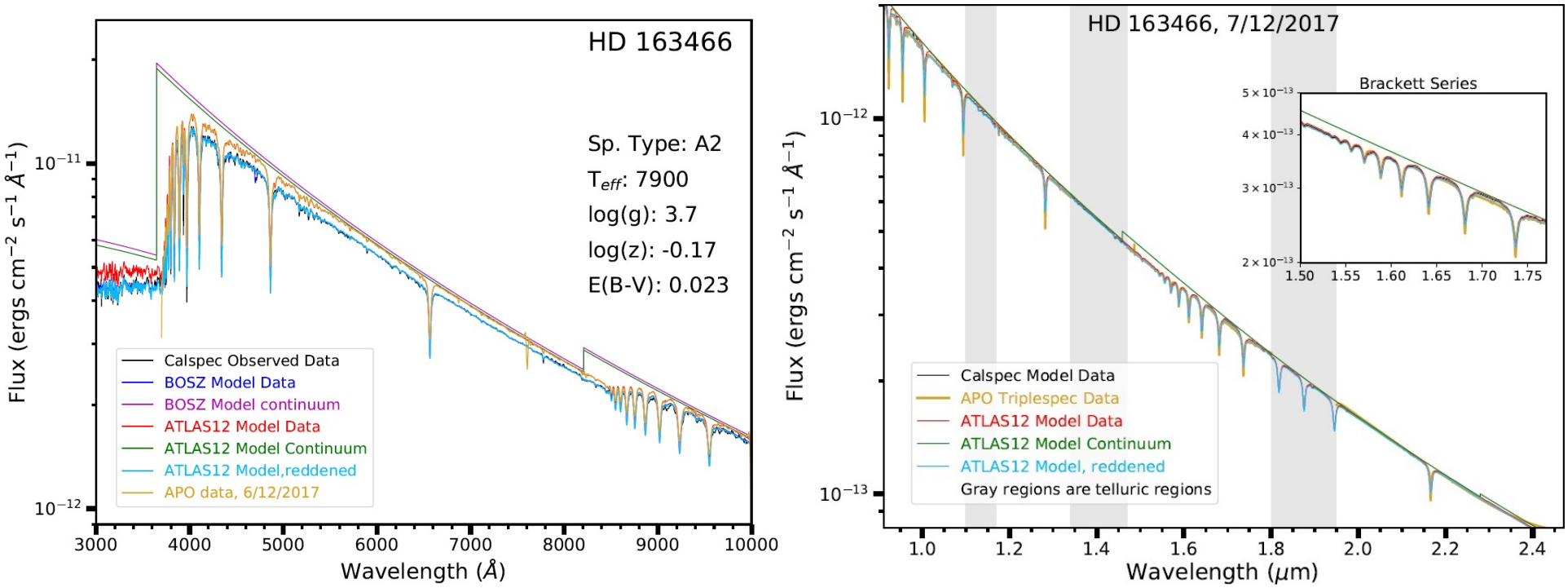

Figure 3.11: The result for the the primary ACCESS target, HD 163466, overplotted with the CALSPEC data and models. The ARCES data (left) and Triplespec data (right) on each row are fit to models with the same stellar parameters, though they were not taken on the same night.

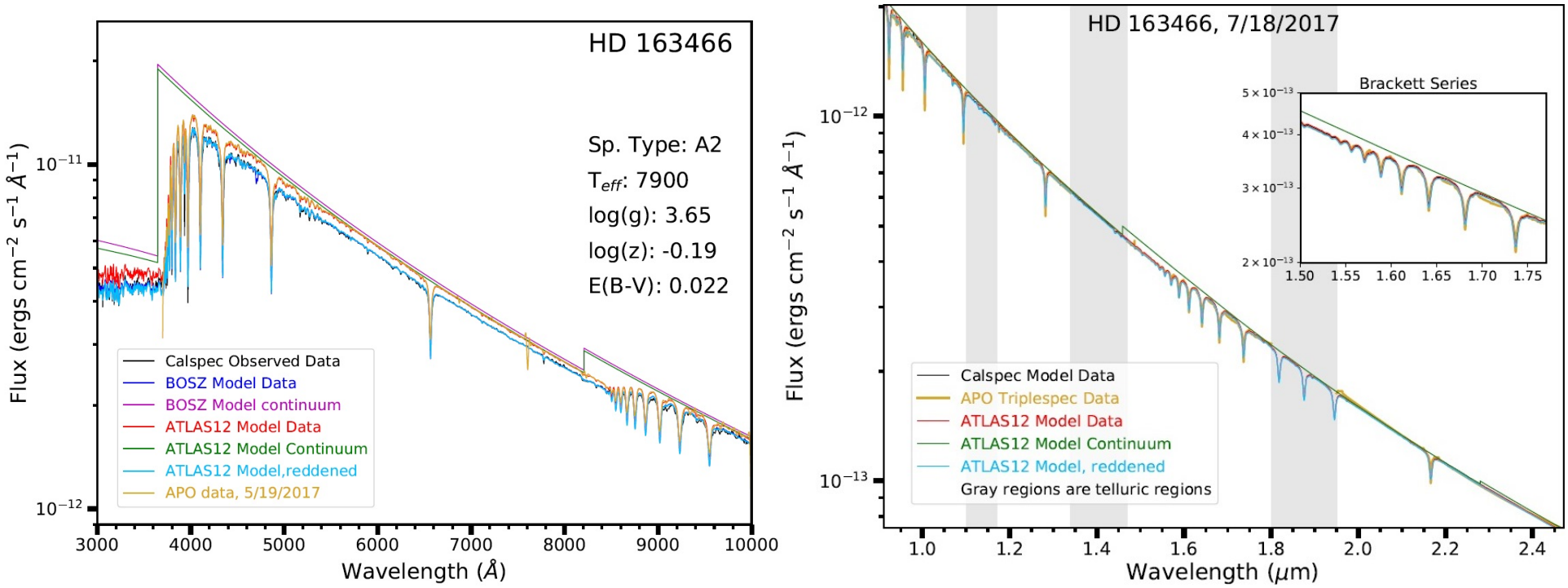

Figure 3.12: The result for the the primary ACCESS target, HD 163466, overplotted with the CALSPEC data and models. The ARCES data (left) and Triplespec data (right) on each row are fit to models with the same stellar parameters, though they were not taken on the same night.

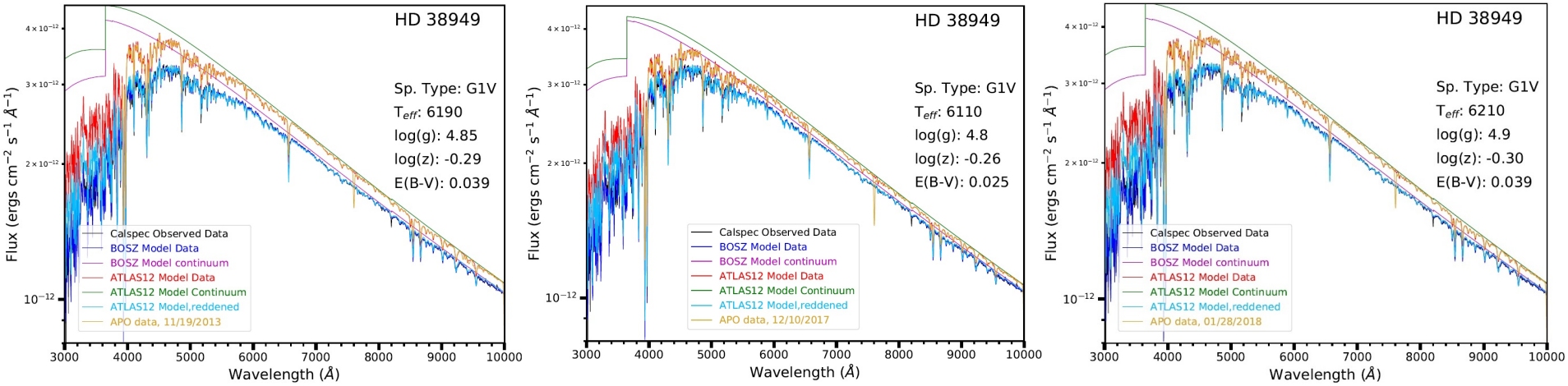

Figure 3.13: The result for the the primary ACCESS target HD 38949, taken on 11/19/2013, 12/10/2017, and 1/28/2018, overplotted with the CALSPEC data and models. One night of Triplespec data was taken, but not of a high enough quality to be used for the fits.

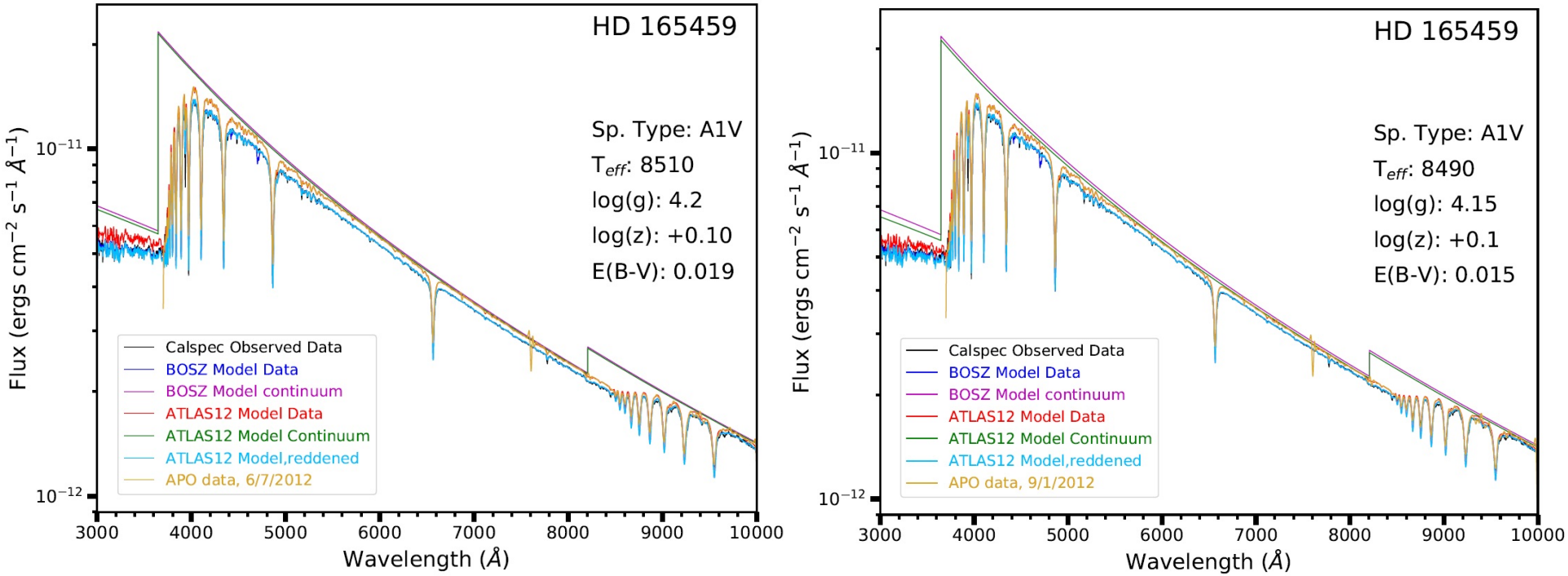

Figure 3.14: The result for the the secondary ACCESS targets, HD 165459, overplotted with the CALSPEC data and models.

Chapter 4

Stellar Atmosphere Modeling

An important component of the ACCESS program is to fit a stellar atmosphere model to the spectra obtained, both by the ACCESS payload, and the ground based data obtained at Apache Point Observatory. This model spectrum will be a noiseless spectrum, allowing weak lines to be differentiated from noise. In addition, a model spectrum can extend much further in wavelength space than is obtainable by the ACCESS payload. The ATLAS modeling program [Kurucz (1979, 1993)] will be used to fit a spectrum to each stellar target, using the spectral data from the payload, and the high resolution line data from Apache Point Observatory (see sec. 3.6).

4.1 Existing stellar atmosphere model generation software

This work focuses on the stellar atmosphere model generation software of ATLAS9 and ATLAS12, as well as the spectral synthesis software SYNTHE ([Kurucz (2005a)], see Sec's 4.4,4.5). However, there are several other stellar atmosphere model generation codes that are publicly available to the community.

The MARCS model grid [Gustafsson et al. (2008)] has updated from an "opacity distribution

function" to an "opacity sampling" method of opacity calculation (see Sec. 4.4 for a discussion of the two methods). The temperature range of the model grid ranges from 2,500 to 8,000 K, with a [Fe/H] range of +1.00 to -5.00. Additionally, the majority of atmospheric calculations are performed assuming spherically symmetric geometry, rather than the plane-parallel geometry used by the ATLAS software. Plane parallel geometry is sufficient for main sequence stars, but the atmospheres of giant stars are much more extended. Regions of the stellar atmosphere observed at an oblique angle produce a non-negligible contribution to the flux calculations [Bessel & Scholz (1989)]. MARCS models treat convection in a similar fashion to the ATLAS software packages, using the mixing-length theory, an approximation of convective flux based on the temperature gradient of the atmosphere [Carroll & Ostlie (1996)]. The mixing length parameter is set as the ratio of the pressure scale height and the distance a fluid "bubble" will travel before equilibrating with its surroundings. The MARCS model grid has been compared with ATLAS9 generated models previously [Gustafsson et al. (2008); Mészáros et al. (2012); Bohlin et al. (2017)] and shows good agreement.

Tlusty [Hubeny & Lanz (1995)] is a stellar atmosphere model generation software that uses opacity distribution functions and plane-parallel geometry, but allows for departure from local thermodynamic equilibrium. LTE assumptions break down in hot stars such as O and B type (<15,000 K) [Gray (1992)], which have atmospheres of high flux and low density. Therefore, the grids generated for public use by the Tlusty group are that of O type stars (T=27,500 K - 55,000 K) [Lanz & Hubeny (2003)] and B stars (15,000 K - 30,000 K) [Lanz & Hubeny (2007)]. Tlusty also uses a mixing-length theory of approximating convection.

PHOENIX [Hauschildt et al. (1997)] uses spherically symmetric geometry and allows for departure from local thermodynamic equilibrium. It is designed to be able to generate model atmospheres for more unique astronomical objects such as supernovae, brown dwarfs, and white dwarfs. One

of the benefits of the PHOENIX software package is an implementation of parallel computing for faster atmospheric calculations. This is especially necessary for models in which the atmospheric layers are moving relative to one another, such as with novae and supernovae. Multiple model grids have been generated by the PHOENIX code [Hauschildt et al. (1999); Husser et al. (2013)], with a temperature range of 2,300 to 12,000 K. Comparisons of the PHOENIX-generated and ATLAS9-generated model grids show that they are both capable of reproducing a stellar spectral energy distribution of $\sigma_{flux} \sim 2 - 5\%$, with both grids performing worse with cooler stars of spectral type K [Bertone et al. (2004)].

4.2 Derived Properties of a Stellar Atmosphere Model

To generate a stellar atmosphere model for a specific star, the properties of the photosphere (the surface of last scattering on the star) must be known, or deduced. This will inform both the overall structure of the spectrum, and the various absorption lines throughout. These parameters may be iterated upon to match to specific spectral features. The typical organization of stellar type is a function of temperature, but this is one of several free variables in the ATLAS model generation codes, including chemical abundance, surface gravity, and microturbulent velocity.

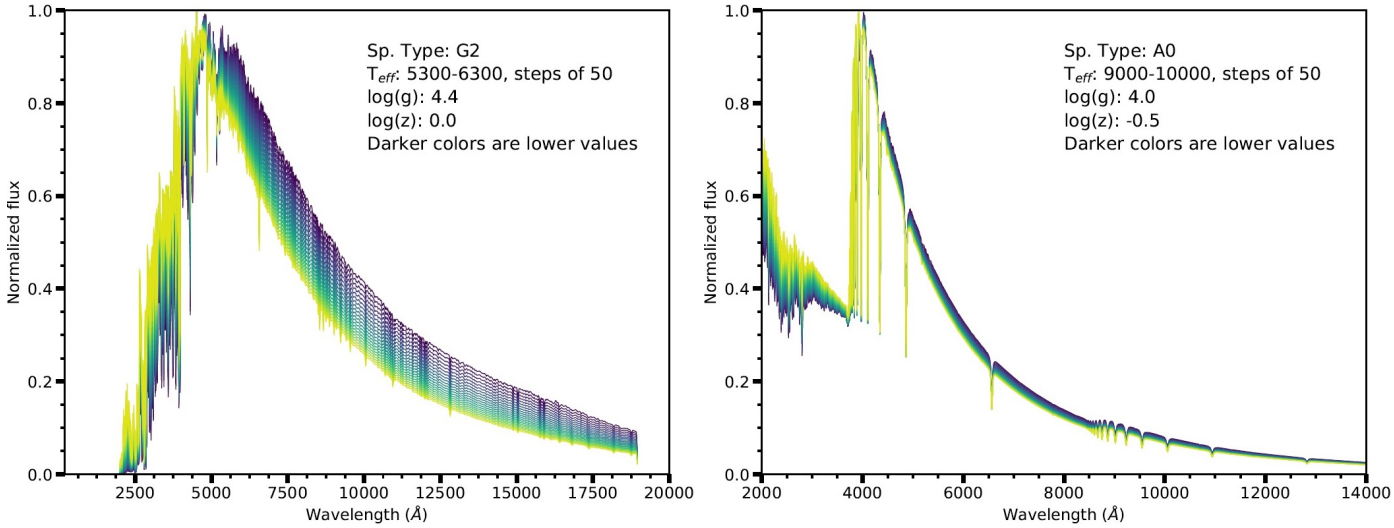

(a) Fixed Parameters for a typical G2 Star

(b) Fixed Parameters for a typical A0 star

Figure 4.1: The results of modulating temperature on a stellar atmosphere model, keeping surface gravity and metallicity at fixed values.

4.2.1 Effective Temperature

The effective temperature describes the temperature that would most closely reproduce a blackbody shape and peak seen within the spectrum. The temperature of a gas is a determinant in the population of energy levels for a given element, and thus will inform the relative strengths of different absorption lines. The probability distribution of kinetic energy (and by extension energy levels) of the atoms is determined by the Maxwell-Boltzmann distribution:

$$f(v) = \sqrt{\left(\frac{m}{2\pi kT}\right)^3} 4\pi v^2 e^{-\frac{mv^2}{2kT}} \tag{4.1}$$

Where T is the temperature in LTE, m is the mass of the atom, and v is the velocity of the particle.

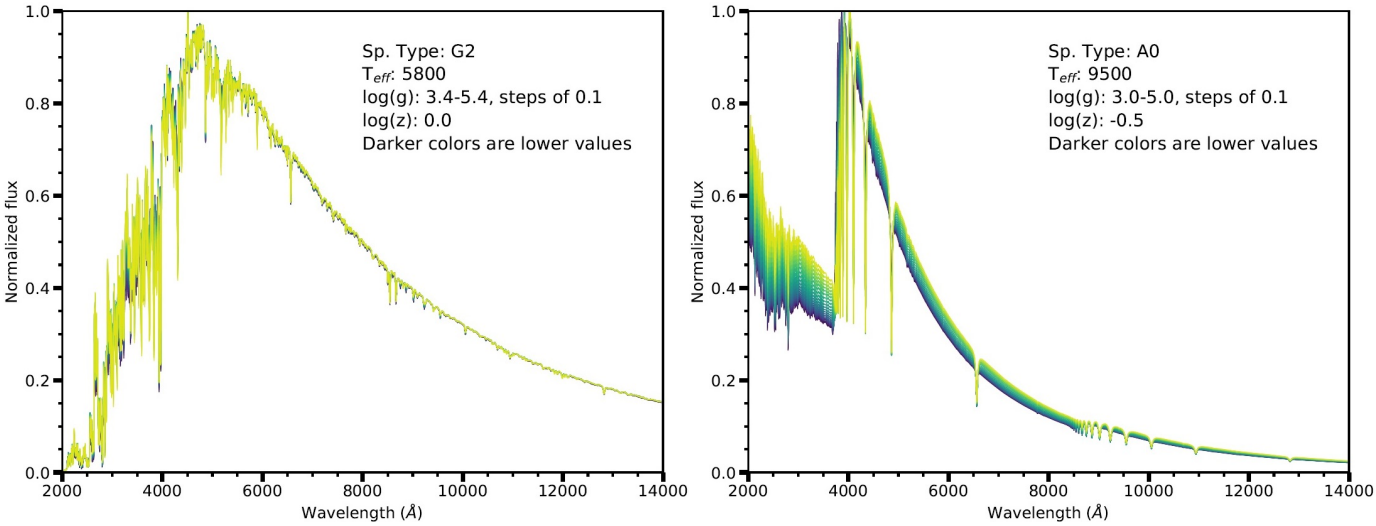

(a) Fixed Parameters for a typical G2 Star

(b) Fixed Parameters for a typical A0 star

Figure 4.2: The results of modulating surface gravity on a stellar atmosphere model, keeping effective temperature and metallicity at fixed values.

4.2.2 Surface Gravity

Surface gravity (typically expressed as **log g**, the logarithm of the ratio between the object's gravity and Earth gravity). The gravity at the photosphere effects the electron pressure, which is a factor in the population density of ions of given elements, relative to its neutral element. The relative distribution of ionized states of a collection of atoms is computed from the Saha equation:

$$\frac{n_{i+1}n_e}{n_i} = \frac{2}{\left(\frac{h^2}{2\pi m_e k_b T}\right)^{3/2}}\left(\frac{g_{i+1}}{g_i}\right) exp\left[-\frac{(\epsilon_{i+1}-\epsilon_i)}{k_b T}\right] \tag{4.2}$$

where n_i is the number density of atoms in the i^{th} state, g_i is the degeneracy of the i^{th} state, and ϵ_i is the energy required to create an ion of the i^{th} state. m_e and n_e are the mass and number density of electrons, respectively.

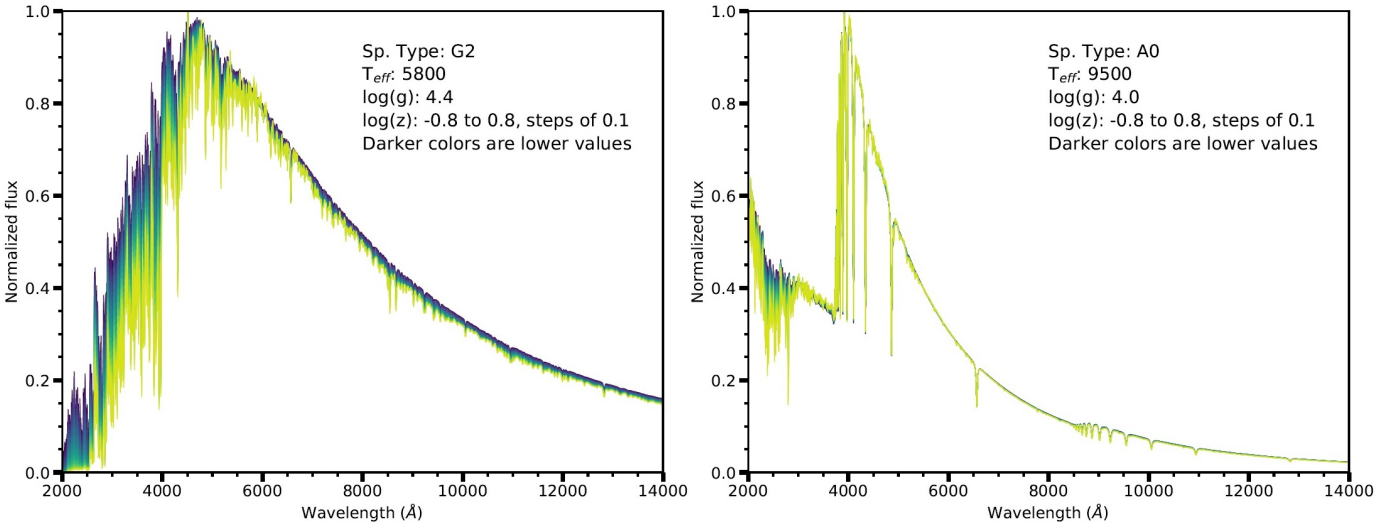

(a) Fixed Parameters for a typical G2 Star

(b) Fixed Parameters for a typical A0 star

Figure 4.3: The results of modulating metallicity on a stellar atmosphere model, keeping effective temperature and surface gravity at fixed values.

4.2.3 Metallicity

Metallicity, typically expressed as either **[M/H]**, the logarithmic proportion of non-hydrogenic elements to hydrogen, or **[Fe/H]**, the logarithmic proportion of iron to hydrogen. Though other elements can provide a better correlation of equivalent width and abundance of non-hydrogenic abundances, iron lines are especially numerous and strong within the optical range. This gives iron the distinct advantage of reducing statistical uncertainty in abundance measurements, relative to other elements. **[Fe/H]** and **[M/H]** tend to closely mirror each other. This is also often expressed as relative to logarithmic solar metallicity, i.e. **[Fe/H]=0** is solar metallicity. The abundance of a specific element can be calculated by measuring the equivalent width of the absorption lines, using a curve of growth.

4.2.4 Interstellar Extinction

Though not an intrinsic property of a star, the extinction along the line of sight, between star and observer [Trumpler (1930)], is a necessary factor in fitting the proper model to the star in flux calibrated data. This effect is caused by scattering and absorption of stellar light by regions of interstellar medium. Because extinction is wavelength dependent and affects the overall continuum shape, it is typically expressed as a color term E[B-V]. Fortunately, interstellar extinction is smoothly varying, well-modeled, and straightforward to apply, or remove, from a spectrum.. The [Cardelli et al. (1989)] extinction law was used by [Bohlin et al. (2017)] below 2 μm, and was used within this work to compare results (Fig. 4.4c). Several other curves exist (e.g. [O'Donnell (1994); Chiar & Tielens (2006); Fitzpatrick & Massa (2007)], see Fig. 4.4c). These extinction laws agree to within 1% across the majority of the spectrum. The exception to that is the [Fitzpatrick & Massa (2007)], which achieves disagreement with [Cardelli et al. (1989)] up to 2% in the ultraviolet at an extinction value of E(B-V)=0.05. This extinction value is higher than any of the values found within this work (see Ch. 5), with the mean extinction value being E(B-V)=0.019. Thus, the choice of extinction law is unlikely to produce a strong bias between studies.

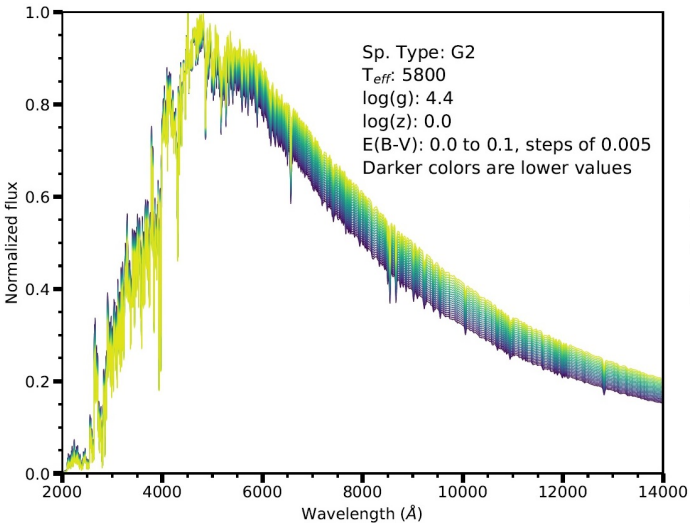

(a) Fixed Parameters for a typical G2 Star

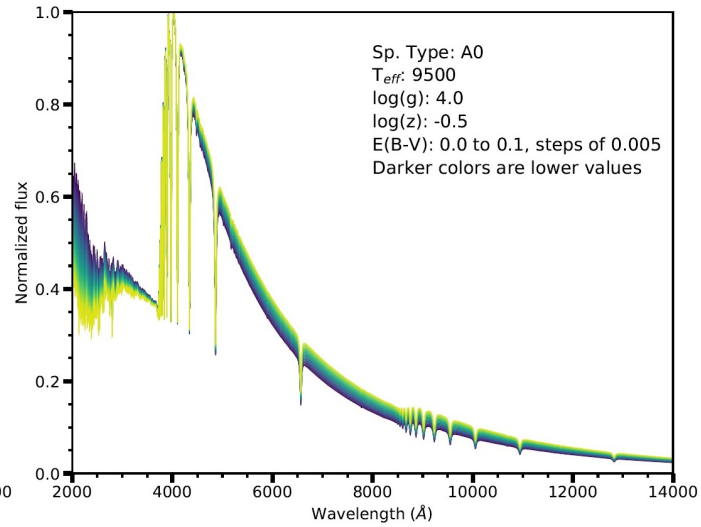

(b) Fixed Parameters for a typical A0 star

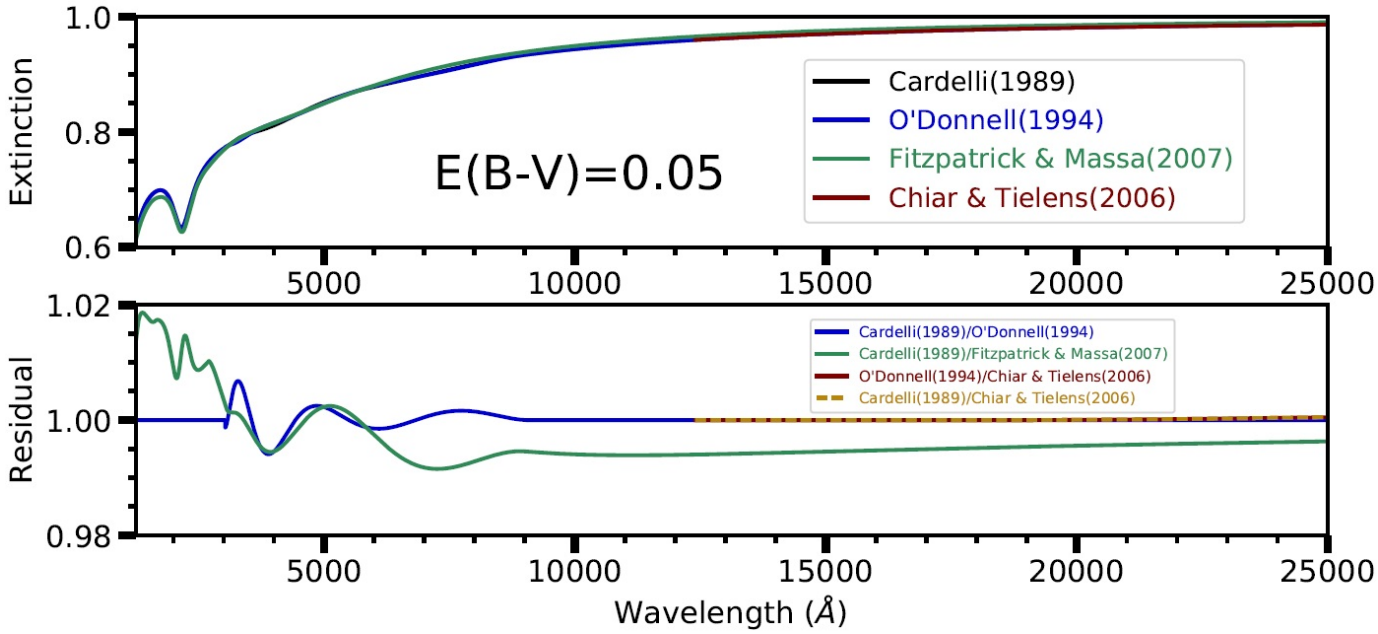

(c) Comparison of Extinction laws at E(B-V)=0.05

Figure 4.4: The results of modulating interstellar extinction on a stellar atmosphere model, keeping effective temperature, surface gravity, and metallicity at fixed values.

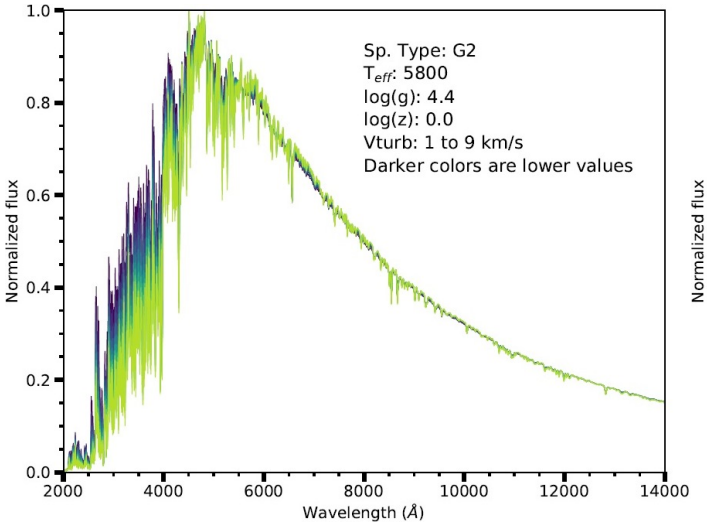

(a) Fixed Parameters for a typical G2 Star

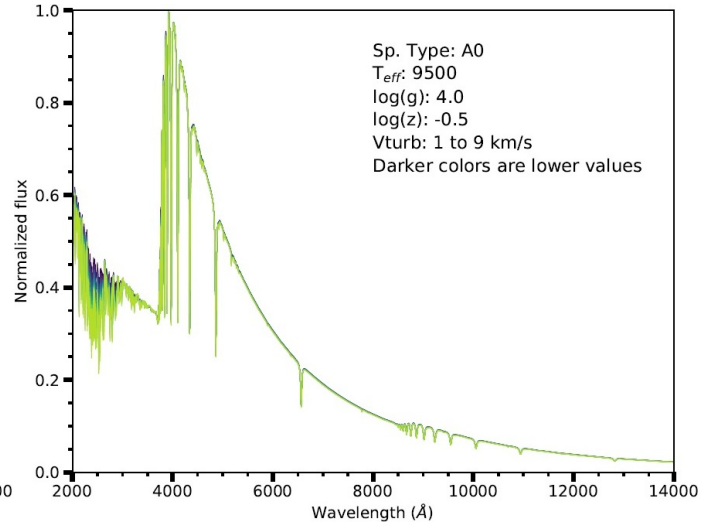

(b) Fixed Parameters for a typical A0 star

Figure 4.5: The results of modulating microturbulent velocity on a stellar atmosphere model, keeping effective temperature, surface gravity, and metallicity at fixed values.

4.2.5 Microturbulence

Microturbulence, expressed in kilometers per second, is the small scale turbulence in a stellar atmosphere. Thermal broadening and macroturbulence do not always fully describe the observed line profiles, and so a microturbulence component is added to the model. This tends to be much smaller than the vsini of the star. For the majority of the fits, microturbulence was set to 2 km/sec. It was found that modulation of the microturbulence parameter in either direction (i.e. 1 or 3 km/sec) yielded a higher chi-squared value for all targets in the sample.

4.2.6 α-element Abundance

The abundance of α-elements refers to elements of atomic mass less than Fe that are formed from helium capture, including oxygen, neon, magnesium, silicon, sulfur, calcium and titanium. Carbon is also considered an α element, but we have treated it separately within the context of this study. There is evidence that stars with host exoplanets are more likely to have overabundances in α-elements (in particular Mg) [Adibekyan & others. (2012)]. Older studies had indicated that the position of galactic birth has some correlation with α-abundance, with a higher abundance found in stars formed closer to the galactic center [Wallerstein (1962); McWilliam & Rich (1994)]. A possible explanation for these differences may be due to these elements not occurring through the chemical processes within the observed stars, but rather from the differing abundances, ages, and galactic location of type I (relative overabundance of iron) vs type II supernovae (overabundance of α-elements) vs planetary nebulae (overabundance of carbon) [Tinsley (1979); Woosley & Weaver (1995)]. The APOGEE pipeline for stellar parameters determines specific windows that are sensitive to changes for alpha and carbon, and holds temperature and gravity constant while searching these windows for a best fit on those parameters [García Pérez et al. (2016)]. However, the APOGEE instrument obtains spectra in the wavelength region from 1.51 to 1.70 μm at a much higher resolution ($R \approx 22,500$) than NICMOS data ($R \approx 200$) , so they cannot be used for this analysis.

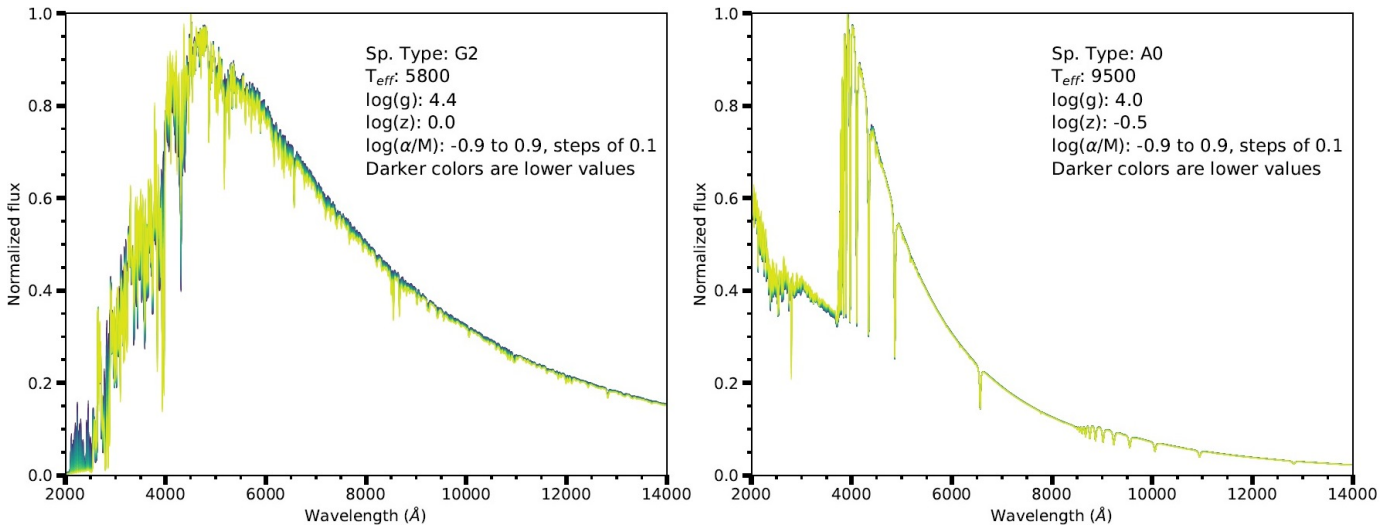

(a) Fixed Parameters for a typical G2 Star

(b) Fixed Parameters for a typical A0 star

Figure 4.6: The results of modulating α-element abundance on a stellar atmosphere model, keeping effective temperature, surface gravity, and metallicity at fixed values.

4.3 Model Assumptions

The ATLAS stellar atmosphere modeling software assumes local thermodynamic equilibrium (LTE). This means that the photosphere observed is in a state where it's temperature is in an equilibrium with the radiation observed, which would allow the observed temperature to be used to compute the energy level of atoms and the amount of atoms in each ionized states.

For most stars on the main sequence, the temperature is a slowly varying function of stellar radius, and so this is a safe assumption.

It is generally assumed that, when creating a stellar atmosphere model, the light source surface may be approximated as plane parallel. As one looks at a star from a close distance, it can be observed that the edges are fainter than the center (known as limb darkening), but this effect is too small to affect the model in stars which are seen as point sources, and the shape on the detector is dominated by the optical characteristics of the observing instrument.

The ATLAS software assumes a static atmosphere, in that the layers are not in relative motion,

and ignores structure such as magnetic fields, granulation, spicules, cells and spots.

4.4 ATLAS9 and ATLAS12

As a component of this work, the ACCESS group sought to determine whether the stellar atmosphere model generation code ATLAS9 or ATLAS12 produces higher fidelity results when fitting to stellar spectra. ATLAS9 is more commonly used, due to ease of use and heritage (see Sec. 4.6). The advantages and disadvantages of ATLAS9 and ATLAS12 were also studied.

In the ATLAS9 software, the various parameters within the stellar atmosphere model are computed using a series of opacity distribution functions (ODF) as input. The opacity of the photosphere is converted into smoothly varying functions, along sections of the spectrum. Taking a small section of frequency and a given temperature, metallicity, microturbulence, and electron number density, one can calculate the optical depth, source function, and radiation moments in that section. A normal section of frequency would have high variances of optical depth, due to the monochromatic quantities of particular elements. However, the calculation requires an integration over frequency regardless. In order to reduce computational complexity, the opacities in that frequency interval can be ordered by opacity, and normalized. These opacity distribution functions are then converted into coarse step functions, and pretabulated prior to model generation (see Fig. 4.7). During model generation, the frequency intervals are then computed together, to determine the photospheric opacity as a whole [Kurucz (1979)]. The initial solar abundance for the ATLAS model generation code was from [Grevesse & Sauval (1998)]. For the ATLAS9 models generated here, metallicity was determined by the solar abundances of [Asplund et al. (2005)].

However, in the ATLAS12 software, the latest version of the models, the spectrum is calculated via opacity sampling. This is a process in which a random selection of points in frequency space (i.e.,

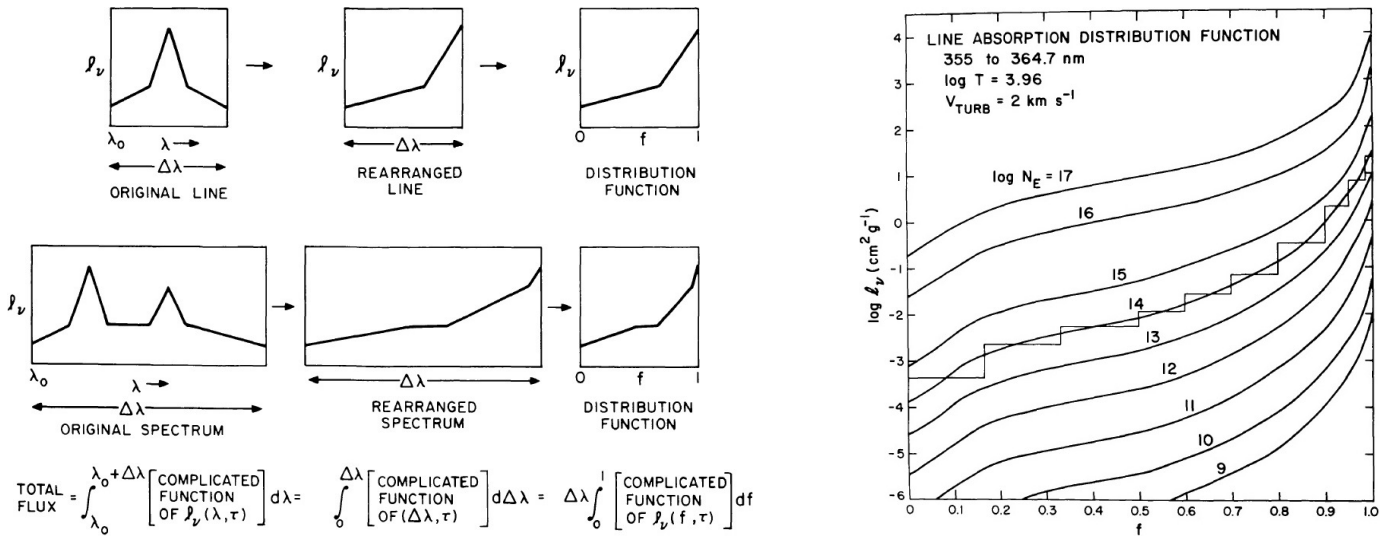

Figure 4.7: From [Kurucz (1979)], **Left:** schematic demonstration of the process by which opacity distribution functions are created. **Right:** Sample distribution functions for a wavelength region, showing one temperature and nine different electron densities. The step function for log N_e=14 shows how the ODF's are actually represented in the software.

they may be evenly spaced, but not intentionally centered on lines) are each individually integrated, incorporating the absorption strength of line blanketing (bound-bound absorption), scattering effects (free-free absorption), and true absorption effects (bound-free absorption) [Kurucz (1993)]. As long as the frequency points are sufficiently random and numerous, the statistical uncertainty of this process should be sufficiently low for comparison to observed data. ATLAS12 performs this calculation at 30,000 frequency points, evenly spaced in logarithm of wavelength [Castelli (2005)].

The advantage of ATLAS9 over ATLAS12 is that it only takes a few minutes to generate a model. However, one cannot specify specific elemental abundances or the microturbulence parameter, aside from the values already generated within the ODF files. ATLAS12 can specify abundances for each individual element, but takes approximately 30 minutes to compute a stellar atmosphere model, using a Dell Precision T3500 running a 64-bit version of Ubuntu Linux, with 12 GB of RAM, and an Intel Xeon CPU. Therefore, as a first pass, to check the models against our data, ATLAS9 is the better choice, and once the values have been determined more specifically, ATLAS12 may be used.

The ATLAS program outputs are not a flux spectrum, but rather a mathematical model of the photosphere, detailing temperature (K), pressure (dyne cm^{-2}), electron number density (cm^{-3}), Rosseland opacity (g^{-1} cm^2), turbulent velocity (km sec^{-1}), convective flux (ergs cm^{-2} sec^{-1}), convective velocity (cm sec^{-1}), and the velocity of sound (cm sec^{-1}) for 72 different layers of the photosphere, organized by RHOX, the mass depth variable:

$$M(j) = \int_0^x \rho(x)dx \quad [gm\ cm^{-2}] \tag{4.3}$$

4.4.1 Rosseland Mean Opacity

In the early steps of the calculation of a stellar atmosphere model, an approximation of the total flux in a given layer must be made. A typical method is the Rosseland approximation [Rybicki & Lightman (1986)]. First we define the radiative transfer equation in an isotropically scattering medium at local thermodynamic equilibrium as:

$$\mu \frac{dI_\upsilon}{dz} = -\alpha_\upsilon(I_\upsilon - B_\upsilon) + \sigma_\upsilon(J_\upsilon - I_\upsilon) \tag{4.4}$$

Where I_υ is the frequency-dependent specific intensity, dz is the depth in the surface, μ is $cos\theta$, α_υ is the frequency-dependent absorption coefficient, σ_υ is the frequency-dependent scattering coefficient, B_υ is the blackbody function, and $J_\upsilon$is the mean intensity.

The source function:

$$S_\upsilon = \frac{\alpha_\upsilon B_\upsilon + \sigma_\upsilon J_\upsilon}{\alpha_\upsilon + \sigma_\upsilon} \tag{4.5}$$

May be substituted:

$$\mu \frac{dI_\upsilon}{dz} = -(\alpha_\upsilon + \sigma_\upsilon)(I_\upsilon - S_\upsilon) \tag{4.6}$$

And rearranged:

$$I_\upsilon(z, \mu) = S_\upsilon - \frac{\mu}{\alpha_\upsilon + \sigma_\upsilon} \frac{dI_\upsilon}{dz} \tag{4.7}$$

If the LTE assumption is made that the source function is equivalent to the blackbody function, $I_\upsilon \approx S_\upsilon \approx B_\upsilon$,

$$I_\upsilon(z, \mu) = B_\upsilon(T) - \frac{\mu}{\alpha_\upsilon + \sigma_\upsilon} \frac{dB_\upsilon}{dz} \tag{4.8}$$

We can use this relationship in the formula for flux:

$$F_\upsilon(z) = 2\pi \int_{-1}^{+1} I_\upsilon(z, \mu) \mu d\mu \tag{4.9}$$

$$F_\upsilon(z) = -\frac{2\pi}{\alpha_\upsilon + \sigma_\upsilon} \frac{dB_\upsilon}{dz} \int_{-1}^{+1} \mu^2 d\mu = -\frac{4\pi}{3(\alpha_\upsilon + \sigma_\upsilon)} \frac{dB_\upsilon(T)}{dT} \frac{dT}{dz} \tag{4.10}$$

If we then integrate over frequency:

$$F(z) = -\frac{4\pi}{3} \frac{dT}{dz} \int_0^\infty \frac{1}{(\alpha_\upsilon + \sigma_\upsilon)} \frac{dB_\upsilon(T)}{dT} d\upsilon \tag{4.11}$$

It is established that the integrated planck function is:

$$\int_0^\infty \frac{dB_\upsilon(T)}{dT} d\upsilon = \frac{4\sigma_{sb} T^3}{\pi} \tag{4.12}$$

Where σ_{sb} is the stefan-boltzmann constant. Therefore, if we then define the Rosseland mean absorption coefficient as:

$$\frac{1}{\alpha_R} = \frac{\int_0^\infty \frac{1}{(\alpha_\upsilon + \sigma_\upsilon)} \frac{dB_\upsilon(T)}{dT} d\upsilon}{\int_0^\infty \frac{dB_\upsilon(T)}{dT} d\upsilon} \tag{4.13}$$

The integrated flux then becomes:

$$F(z) = -\frac{16\sigma_{sb}T^3}{3\alpha_R}\frac{dT}{dz} \tag{4.14}$$

As part of the ATLAS programs, α_R is output for every depth of the atmosphere. Tables of this variable are used as an initial input; an initial gas pressure, temperature, metallicity, and microturbulence value provides a specific Rosseland mean opacity ($\tau_R = \alpha_R \rho$) , which is used to determine an initial gray temperature distribution, dependent only on τ_R :

$$T(\tau_R) = T_{eff} * (0.75 * (0.710 + \tau_R - 0.1331 * e^{(-3.4488 * \tau_R)}))^{0.25} \tag{4.15}$$

This gray temperature distribution is then used to convert T as a function of τ_R to T as a function of RHOX [Kurucz (1970)].

4.5 SYNTHE

The SYNTHE program, another Fortran program written by [Kurucz (2005a)], takes as an input the model photosphere generated by one of the two ATLAS programs, as well as all absorption line information in a given bandpass, and generates an intensity spectrum at several angles. This intensity can be integrated to create an overall flux spectrum. Though it is initially computed with a user-chosen resolution, various broadening effects are inserted into the spectrum to match the line

spread of an observed stellar target. Both rotational and instrumental broadening may be separately specified by the ROTATE and BROADEN subroutines. The output is a set of three data: wavelength, line data and continuum, and continuum alone. A catalog of photo-ionization edges are included as discontinuities in the continuum data, to simplify modeling the numerous lines leading up to the edge.

4.6 Existing Model Grids

Model grids exist for ATLAS9 generated model atmospheres and synthetic flux spectra [Castelli & Kurucz (2004); Bohlin et al. (2017)], and have been used to fit stellar parameters to a selection of fundamental standard stars. Using bins specifically excluding strong line profiles (e.g. Balmer lines, CaII H&K, etc.), the continuum is fit using a χ^2 minimization technique. However, these model grids exist in parameter space of 250 K effective temperature, 0.25 log metallicity, and 0.5 log surface gravity. The difference between generating a model between these parameters and interpolation can exceed 1 %, in particular in short wavelength regions with heavy wavelength blanketing (see Fig. 4.8). This is likely due to the fact that many line characteristics do not change at a strictly linear rate with these parameters. Additionally, the entire grid was calculated at 2 km/s microturbulent velocity.

Therefore, the ACCESS group undertook a program to determine the similarities between an interpolated fit and individual model generations, using the same χ^2 minimization technique.

4.7 ACCESS and ATLAS: Fitting Procedure

The original ATLAS9, ATLAS12, and SYNTHE software was written for the OPENVMS operating system. A port to GNU/Linux was developed, using an Intel Fortran Compiler [Sbordone (2005)], as OPENVMS is proprietary and rarely used. Once the infrastructure for stellar atmosphere model and

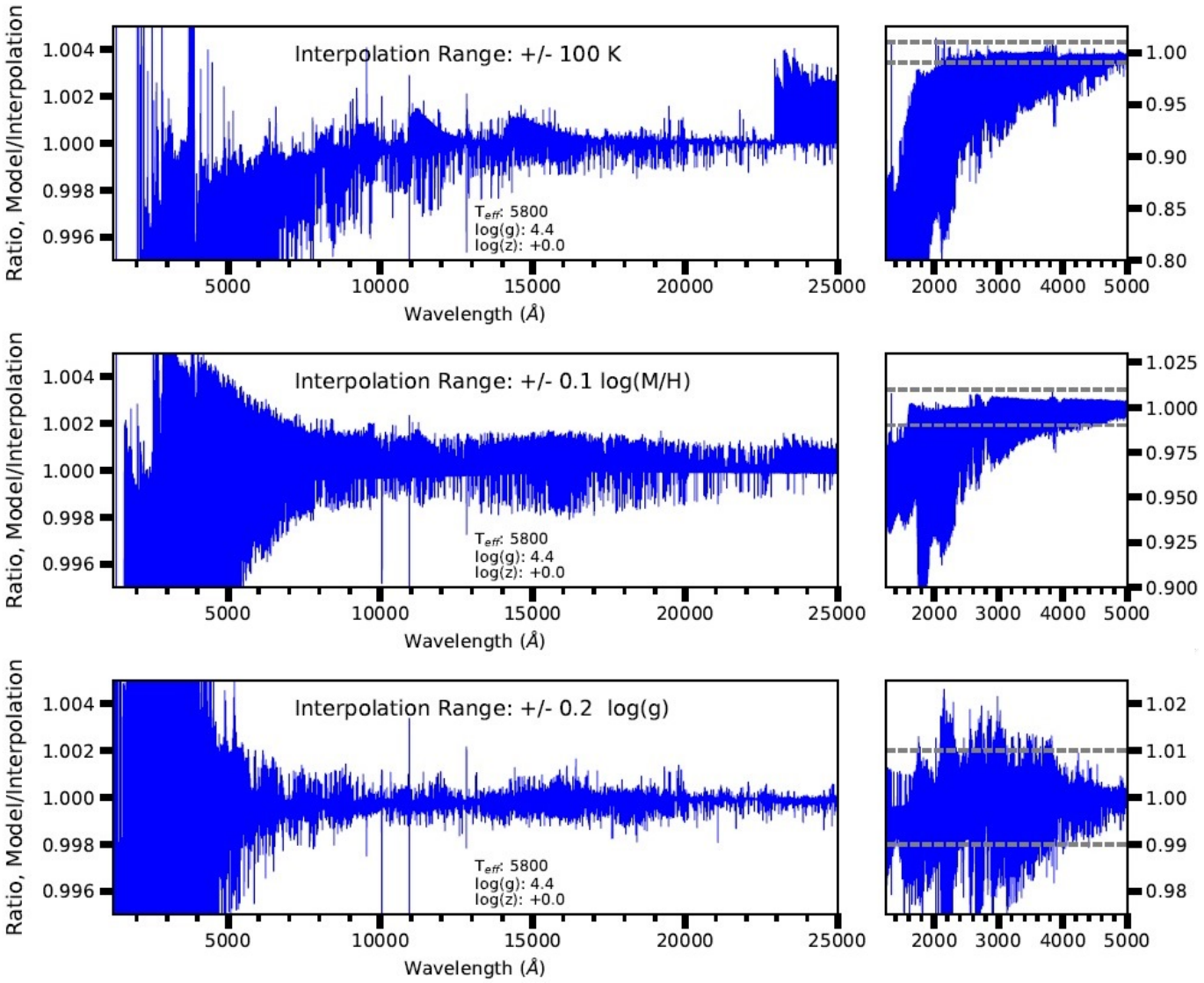

Figure 4.8: A comparison between independently generated models, compared to models interpolated at a coarseness of parameters for the commonly available model grids. **Right:** A zoom out of the blue end of the spectrum, which shows the greatest disagreement.

synthetic flux spectrum generation was developed, using a specified effective temperature, effective gravity, and metallicity, the stellar extinction could be fit to that particular model. Using these tools, a process was developed, for the purpose of iterating through many models in order to find the best fit to all four parameters.

The line list for SYNTHE is from Bob Kurucz's webpage, and was the most recent version at the time, updated on December 2016. Molecular lines included in the fits are also from Bob Kurucz's webpage, and include the molecular linelists for C_2, CH, CN, CO, H_2, H_2O, MgH, NH, OH, SiH, and SiO. [Bohlin et al. (2017)] use TiO as well, but only for stars cooler than 4500 K, which are not part of our sample.

For the fits to CALSPEC data, a reduced chi squared statistic was used. Using the formula:

$$\chi^2_\upsilon = \frac{\chi^2}{\upsilon} \tag{4.16}$$

in which υ is the number of observation in the fit minus the number of free parameters and χ^2 is:

$$\chi^2 = \sum_i \frac{(O_i - E_i)^2}{\sigma_i^2} \tag{4.17}$$

where σ_i is the uncertainty of the observations, O_i is observed data (in this case, either the CALSPEC or APO data), and E_i is the model data in a given wavelength bin i. Background correction uncertainty and observational repeatability uncertainty for the HST datasets were provided by Ralph Bohlin (see Figs. 4.9 & 4.10). The scatter for the CALSPEC instruments is scaled to the stellar flux of the target being compared. The background uncertainty was determined by the average of the background seen in a series of long exposure images taken by HST. This was performed for each grating configuration. The background correction uncertainty scaling factor was determined

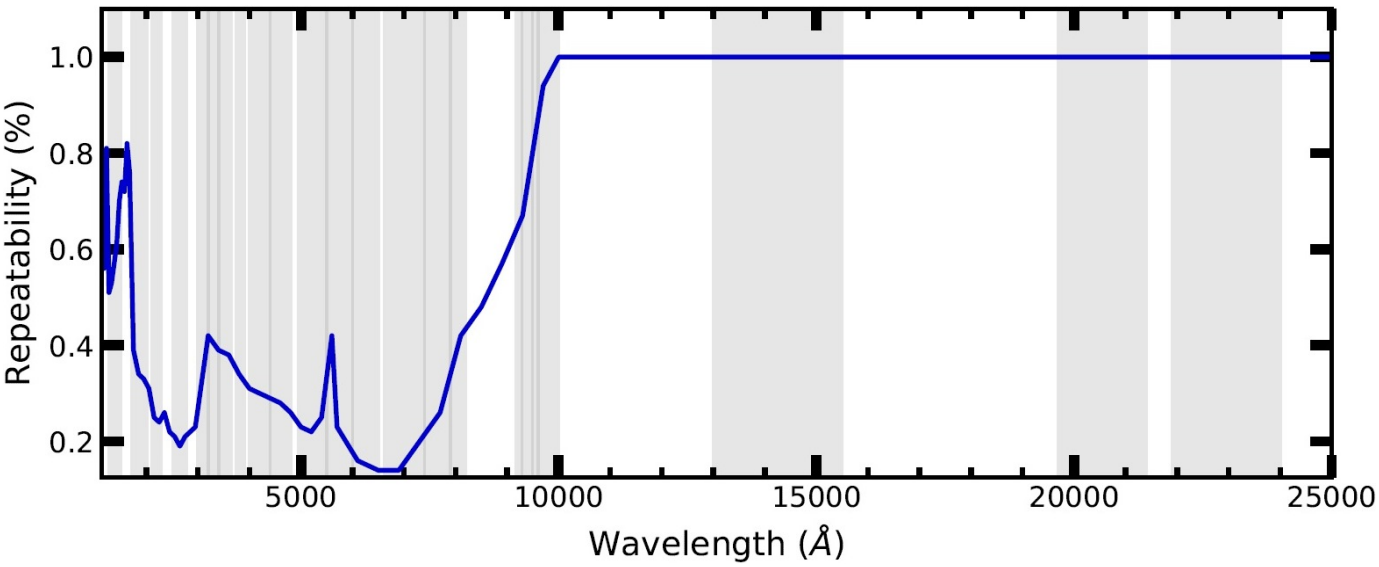

Figure 4.9: Systematic error uncertainty contribution from scatter in the measurement repeatability for CALSPEC observations, provided by Ralph Bohlin. Repeatability for NICMOS was estimated to be 1%. Overlayed are the bins used when fitting to the models, for an A star (see table 4.2).

empirically by Ralph Bohlin, using the stellar target 1732526. The model uncertainty is captured by a line blanketing factor. Areas with high line blanketing, in particular in the UV, are deemphasized by adding a "line blanketing factor" to the quadrature sum of errors. It takes the form:

$$0.1 * (1 - \frac{Flux}{Continuum}) \tag{4.18}$$

Using the flux and continuum outputs from the ATLAS model. This factor is then subsequently multiplied by the scaled model flux. The scatter is mulitiplied by the CALSPEC data flux. The background, scattering, and line-blanketing-factor are interpolated to the same wavelength scale (that of the CALSPEC observations) and added in quadrature sum to form the σ_i in the chi-squared equation.

The data points between model and data fluxes are the mean of a series of wavelength bins described within [Bohlin et al. (2017)] (see tables 4.2 & 4.3). These bins were used here to allow for direct comparison between the two studies. Wavelength bins were excluded in cases where the bin

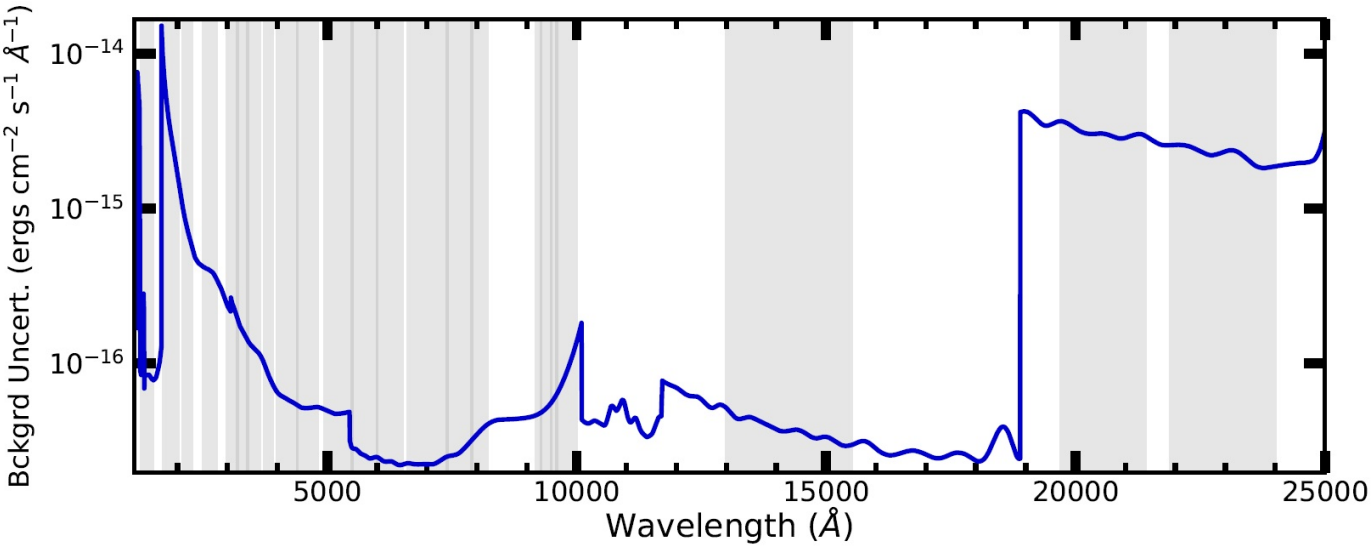

Figure 4.10: Systematic error uncertainty contribution from background flux for CALSPEC observations, provided by Ralph Bohlin. Overlayed are the bins used when fitting to the models, for an A star (see table 4.2).

contained less than 1% of the peak flux of the spectrum. This imposes a necessary constraint on the UV fluxes for G stars, as the fluxes are not stable. Observations of the sun show that G star UV fluxes can vary several percent day-to-day [Donnelly et al. (1983)]. The models are computed at a resolution of R=600,000. When compared to the CALSPEC data, they are converted to STIS and NICMOS resolution via gaussian convolution of FWHM λ/R, and fit to the wavelength scale of the CALSPEC data by way of linear interpolation. Models were computed without convective overshooting and a mixing length parameter of 1.25.

For spectra containing NICMOS data, the region of 1 - 1.3 μm was excluded from the fits due to NICMOS count-rate dependent non-linearity at shorter wavelengths [Bohlin et al. (2006)].

Beginning with an initial guess, the fit is performed. Afterwards a new model, with a slightly different metallicity, is generated. This continues until a local minima in χ^2 is found. Once the minima is found, the system then iterates over effective temperature, and subsequently log surface gravity. This cycle may occur several times, before finding a minimum in all four parameters. The process for fitting extinction is fast relative to model generation, and is extrinsic to the stellar properties of the

model. Because of this, extinction fitting is performed every time a new model is generated, with the best fit Chi-squared value being the one reported. Because of the long computational times required, the iteration is first performed with steps every 100 K T_{eff} and 0.1 log g, and 0.05 [M/H]. After a minimum is found, T_{eff} step size is reduced to 10 K, 0.05 log g and 0.01 [M/H], in order to provide the best fit parameters at the desired resolution.

In order to confirm that these fits are not constrained to a local minimum, tests were performed with different initial guesses. Additionally, the order that parameters were fit in was changed as well. Typically, metallicity is iterated on first, followed by effective temperature, and finally surface gravity. Fits were performed on targets starting with surface gravity, and thereafter effective temperature. These tests resulted in the same final fit.

Parameter	**T_{eff} (K)**	**log g**	**[M/H]**	**[α/M]**	**[C/M]**	**E(B-V)**
Step size	10	0.05	0.01	0.05	0.05	0.001

Table 4.1: Final resolution for parameters for the model fitting processes

Wavelength Range (Å)
1280-1510
1725-2020
2110-2280
2520-2780
3000-3200
3200-3400
3400-3640
3750-4400
4400-4800
4950-5500
5500-6000
6000-6500
6620-7400
7400-7900
7900-8200
9182-9282
9290-9480
9499-9599
9600-10000
13000-15500
19700-21400
21900-24000

Table 4.2: Wavelength bins for A stars, used when fitting the ATLAS models to the CALSPEC data. Wavelengths greater than 10,000 Å are excluded for targets that did not have NICMOS data.

Wavelength Range (Å)
3000-3850
4000-4260
4380-4800
4950-5500
5500-6000
6000-6500
6620-7400
7400-8400
8800-9400
9400-10000
13000-15500
15500-19000
19000-24000

Table 4.3: Wavelength bins for G stars, used when fitting the ATLAS models to the CALSPEC data. Wavelengths greater than 10,000 Å are excluded for targets that did not have NICMOS data.

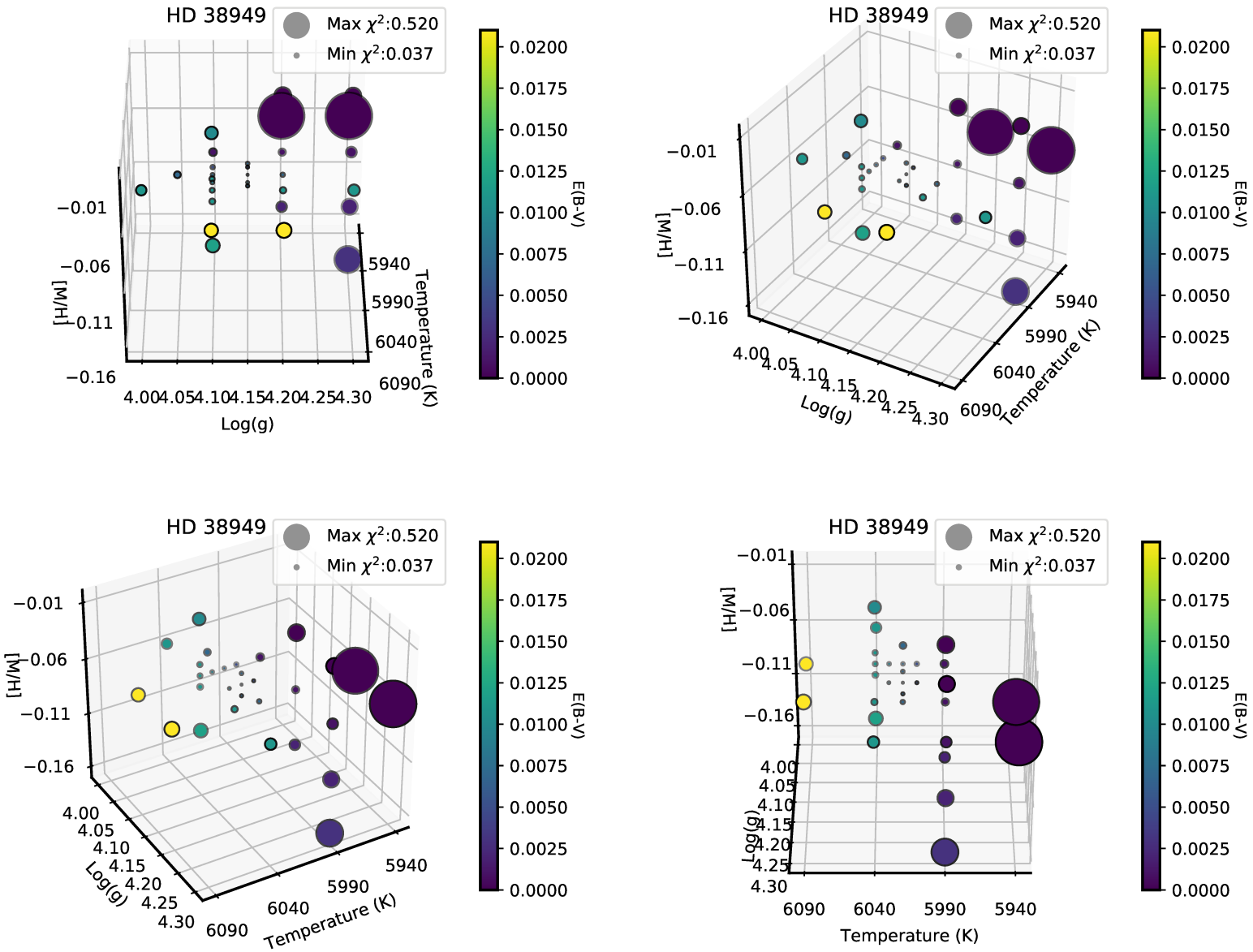

Figure 4.11: Visualization of the fitting process for the primary target HD 38949. The 3D plot is rotated by 30 degrees in each subsequent plot. The size of the dot is an indicator of the chi-squared value, and is scaled here for readability.

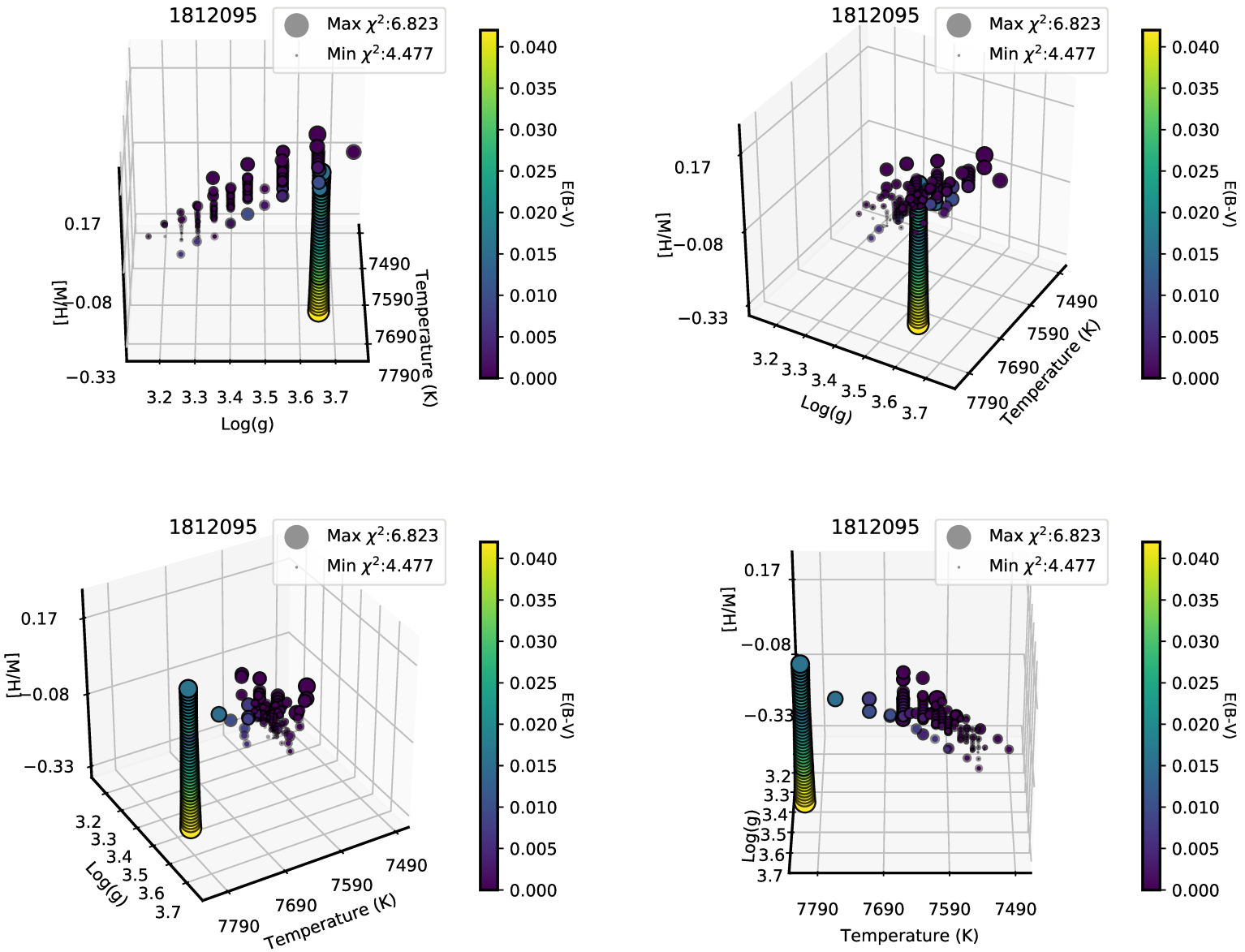

Figure 4.12: Shown here is an early test, inputting a poor initial guess for the star 1812095. The result is a moderately directed route toward a best fit solution.

4.7.1 Convergence Tests for ATLAS9

In order to test for convergence, the errors on flux conservation and flux derivative error are computed for an ATLAS9 model. This computation is performed at all levels of the atmospheric model. If the mean values are below 1% and 10% respectively, the model is considered converged. For a given optical depth layerτ, the flux error is computed to be:

$$\Delta H = (H_{BB} - H_{rad}(\tau) - H_{conv}(\tau)) \tag{4.19}$$

The variable here being the blackbody flux, radiative flux, and convective flux. The total flux per steradian for a blackbody is:

$$H_{BB} = \frac{\sigma T_{eff}^4}{4\pi} \tag{4.20}$$

σ here representing the Stefan-Boltzmann constant. The radiative flux is a matrix integration over optical depth and frequency, as prescribed in [Kurucz (1969)]. The convective flux is calculated using the mixing length theory, and is described in [Kurucz (1970)]:

$$H_{conv}(\tau) = \rho C_p v_{conv} \Delta T \tag{4.21}$$

Where ΔT is the temperature differential in a convective cell, $\rho$is the density of the layer (a function of the pressure and average molecular weight), C_p is the specific heat at that pressure, and v_{conv} is the convective velocity. The layers of a convective cell in the ATLAS code are defined as 0.1% above and below the rosseland opacity for each individual layer.

Chapter 5

Modeling Results

5.1 ATLAS9 vs ATLAS12

Parameters and χ^2 results for the ATLAS9 and ATLAS12 models were compared. The two methods are in good agreement and converge on similar answers: within a mean of -3 K ± 22 effective temperature, -0.02 ± 0.04 logarithm of surface gravity, -0.02 ± 0.03 logarithm of metallicity, and -0.001 ± 0.004 E(B-V) for the target list (ATLAS9-ATLAS12, see fig. 5.1). For G stars, the agreement is -8 K ± 35 effective temperature, -0.03 ± 0.07 logarithm of surface gravity, -0.02 ± 0.04 logarithm of metallicity, and -0.002 ± 0.005 E(B-V) (fig. 5.9), and for A stars it is -1 K ± 14 effective temperature, -0.01 ± 0.02 logarithm of surface gravity, -0.02 ± 0.02 logarithm of metallicity, and -0.001 ± 0.001 E(B-V) (fig. 5.10). Even among targets with the highest disagreement in stellar parameters between ATLAS9 and ATLAS12, the flux residual between models is below 1% across the 0.3-2 µm bandpass (see figs 5.11-5.23). For some targets, the blue end of the spectrum exceeds this and reaches a few percent. This region has very heavy line blanketing, and centers on the photo-ionization edge for Balmer transitions at 364.6 nm. For HD 38949, the RMS flux residual across the 200-1000 nm bandpass is 1.9% (see fig. 5.15). However, the dominant source of this discrepancy comes from the

blue end of the spectrum and the residual from 300-1000 nm is only 0.3%. For HD 163466, the RMS flux residual is 0.7% across the 200-1000 nm bandpass (see fig. 5.18).

Star	Sp. Type	ATLAS9 T_{eff}	ATLAS12 T_{eff}	ΔT_{eff}	ATLAS9 Log(g)	ATLAS12 Log(g)	ΔLog(g)	ATLAS9 [M/H]	ATLAS12 [M/H]	Δ[M/H]	ATLAS 9 E(B-V)	ATLAS12 E(B-V)	ΔE(B-V)
HD 37962	G2V	5780	5750	30	3.45	3.45	0	-0.23	-0.25	0.02	0.018	0.012	0.006
P330E	G2V	5810	5840	-30	3.85	3.9	-0.05	-0.18	-0.14	-0.04	0.031	0.036	-0.005
HD 159222	G1V	5810	5850	-40	3.3	3.35	-0.05	0.07	0.12	-0.05	0.003	0.01	-0.007
HD 106252	G0V	5840	5870	-30	3.55	3.65	-0.1	-0.12	-0.07	-0.05	0	0.006	-0.006
HD 205905	G2V	5900	5850	50	3.55	3.45	0.1	0.08	0.02	0.06	0.011	0.002	0.009
HD 38949	G1V	5990	6020	-30	4.05	4.15	-0.1	-0.1	-0.06	-0.04	0.002	0.007	-0.005
1743045	A5V	7380	7370	10	3.55	3.55	0	-0.25	-0.25	0	0.013	0.013	0
1757132	A3V	7620	7650	-30	3.75	3.8	-0.05	0.36	0.4	-0.04	0.03	0.035	-0.005
1812095	A5V	7770	7760	10	3.75	3.75	0	0.37	0.38	-0.01	0	0	0
HD 14943	A5V	7870	7860	10	3.9	3.9	0	0.21	0.22	-0.01	0.001	0.001	0
1808347	A3V	7890	7890	0	3.85	3.85	0	-0.65	-0.66	0.01	0.023	0.024	-0.001
HD 163466	A2V	7930	7920	10	3.75	3.75	0	-0.16	-0.15	-0.01	0.025	0.025	0
HD 37725	A3V	8280	8260	20	4.25	4.25	0	-0.02	-0.02	0	0.034	0.033	0.001
HD 165459	A4V	8440	8420	20	4.2	4.2	0	0.16	0.15	0.01	0.008	0.008	0
HD 180609	A0V	8560	8560	0	4.05	4.05	0	-0.33	-0.32	-0.01	0.037	0.038	-0.001
1805292	A4V	8570	8570	0	4	4	0	0.05	0.07	-0.02	0.032	0.033	-0.001
HD 158485	A4V	8580	8590	-10	4.2	4.2	-0.05	-0.28	-0.25	-0.03	0.046	0.048	-0.002
1732526	A4V	8630	8630	0	4.05	4.1	-0.05	-0.35	-0.35	0	0.032	0.033	-0.001
1802271	A2V	8980	8990	-10	4	4.05	-0.05	-0.48	-0.47	-0.01	0.01	0.012	-0.002
BD +60 1753	A1V	9370	9380	-10	3.95	3.95	0	-0.04	-0.01	-0.03	0.013	0.014	-0.001
HD 116405	A0V	10770	10780	-10	4.1	4.1	0	-0.22	-0.19	-0.03	0	0.001	-0.001

Table 5.1: The resultant best-fit stellar parameters for the full ACCESS target list. Comparing ATLAS9 and ATLAS12. Fits performed without the [Bohlin et al. (2017)] χ^2 formalism (sec. 5.4)

Star	Sp. Type	ATLAS9 T_{eff}	AT9interp T_{eff}	ΔT_{eff}	ATLAS9 Log(g)	AT9interp Log(g)	ΔLog(g)	ATLAS9 [M/H]	AT9interp [M/H]	Δ[M/H]	ATLAS9 E(B-V)	AT9interp E(B-V)	ΔE(B-V)
HD 37962	G2V	5780	5820	-40	3.45	3.6	-0.15	-0.23	-0.17	-0.06	0.018	0.027	-0.009
P330E	G2V	5810	5860	-50	3.85	3.95	-0.1	-0.18	-0.11	-0.07	0.031	0.041	-0.01
HD 159222	G1V	5810	5890	-80	3.3	3.45	-0.15	0.07	0.17	-0.1	0.003	0.019	-0.016
HD 106252	G0V	5840	5850	-10	3.55	3.65	-0.1	-0.12	-0.09	-0.03	0	0.003	-0.003
HD 205905	G2V	5900	5870	30	3.55	3.5	0.05	0.08	0.05	0.03	0.011	0.007	0.004
HD 38949	G1V	5990	5980	10	4.05	4.05	0	-0.1	-0.12	0.02	0.002	0	0.002
1743045	A5V	7380	7470	-90	3.55	3.7	-0.15	-0.25	-0.16	-0.09	0.013	0.025	-0.012
1757132	A3V	7620	7640	-20	3.75	3.8	-0.05	0.36	0.39	-0.03	0.03	0.033	-0.003
1812095	A5V	7770	7770	0	3.75	3.75	0	0.37	0.36	0.01	0	0	0
HD 14943	A5V	7870	7910	-40	3.9	3.95	-0.05	0.21	0.25	-0.04	0.001	0.006	-0.005
1808347	A3V	7890	7880	10	3.85	3.85	0	-0.65	-0.62	-0.03	0.023	0.022	0.001
HD 163466	A2V	7930	7940	-10	3.75	3.8	-0.05	-0.16	-0.11	-0.05	0.025	0.026	-0.001
HD 37725	A3V	8280	8280	0	4.25	4.25	0	-0.02	-0.01	-0.01	0.034	0.034	0
HD 165459	A4V	8440	8530	-90	4.2	4.2	0	0.16	0.13	0.03	0.008	0.016	-0.008
HD 180609	A0V	8560	8510	50	4.05	4.05	0	-0.33	-0.43	0.1	0.037	0.033	0.004
1805292	A4V	8570	8500	70	4	4	0	0.05	-0.03	0.08	0.032	0.026	0.006
HD 158485	A4V	8580	8540	40	4.2	4.2	0	-0.28	-0.27	-0.01	0.046	0.041	0.005
1732526	A4V	8630	8590	40	4.05	4.05	0	-0.35	-0.35	0	0.032	0.028	0.004
1802271	A2V	8980	9000	-20	4	4.05	-0.05	-0.48	-0.47	-0.01	0.01	0.012	-0.002
BD +60 1753	A1V	9370	9350	20	3.95	3.95	0	-0.04	-0.07	0.03	0.013	0.011	0.002
HD 116405	A0V	10770	10770	0	4.1	4.1	0	-0.22	-0.26	0.04	0	0	0

Table 5.2: The resultant best-fit stellar parameters for the full ACCESS target list. Comparing ATLAS9, using uniquely generated models and interpolated from a grid of ATLAS9 models. Fits performed without the [Bohlin et al. (2017)] χ^2 formalism (sec. 5.4)

This process was performed using both ATLAS9 and ATLAS12 as the model generation codes. SYNTHE is agnostic to which model code was used prior to its computations, therefore it was used for both iterative processes. Seven targets within this target list also had NICMOS observations within the CALSPEC database: P330E, HD 165459, 1743045, 1732526, 1802271, 1805292, and 1812095. Only one of these seven, P330E, is a G star; the other 6 are all A stars.

Within the fits, strong hydrogen lines show residuals of 5-10%. Strong lines are not well modeled under the assumption of local thermodynamic equilibrium (LTE) [Kurucz (2005b)]. Because the ATLAS9 and ATLAS12 codes use LTE calculations, most of the Balmer, Paschen, and Brackett hydrogen lines are excluded from the fitting bandpasses. Hydrogen lines residuals are seen in both STIS data as well as NICMOS data. Within the NICMOS data, the residual for a given hydrogen line is typically only on the order of 1%, but spans a greater bandpass (500-1000 Å). This can be attributed to the lower resolution of NICMOS data (R=200) relative to STIS (R=500-1,000). In particular, the n=5 to n=3 transition at 1281 nm and the n=10 to n=4 transition at 1735 nm reach 1-3% ratios.

The targets with NICMOS data were fit with and without NICMOS data, and showed a mean agreement of 4 K ± 25 effective temperature, 0.01 ± 0.02 logarithm of surface gravity, 0.00 ± 0.03 logarithm of metallicity, and 0.001 ± 0.025 E(B-V) for the seven targets ((with NICMOS) - (without NICMOS)).

The target with the highest temperature discrepancy from [Bohlin et al. (2017)] was that of HD 165459. In addition, HD 165459 had NICMOS data and also shows the greatest temperature and extinction differential between fits performed with and without NICMOS data. Visible within the NICMOS data of HD 165459 is a particular flux excess relative to the fit models. This feature spans the bandpass of approximately 1.55-1.65 µm. This feature is not seen within other targets with

Target	Alternative Name	STIS Obs.	NICMOS Obs.	Potential JWST Calibrator
HD 37962		Yes		Yes
HD 159222		Yes		Yes
HD 106252		Yes		Yes
P330E	GSC 02581-02323	Yes	Yes	Yes
HD 205905		Yes		Yes
HD 38949		Yes		Yes
1743045	2MASS J17430448+6655015	Yes	Yes	Yes
1757132	TYC 4212-455-1	Yes		Yes
1812095	TYC 4205-1677-1	Yes	Yes	Yes
1808347	TYC 4433-1800-1	Yes		Yes
HD 14943		Yes		Yes
HD 163466		Yes		Yes
HD 37725		Yes		
HD 180609		Yes		Yes
HD 165459		Yes	Yes	
1805292	TYC 4209-1396-1	Yes	Yes	Yes
HD 158485		Yes		Yes
1732526	TYC 4207-219-1	Yes	Yes	Yes
1802271	2MASS J18022716+6043356	Yes	Yes	Yes
BD+60 1753		Yes		Yes
HD 116405		Yes		Yes

Table 5.3: ACCESS Stellar Atmosphere Modeling Sample

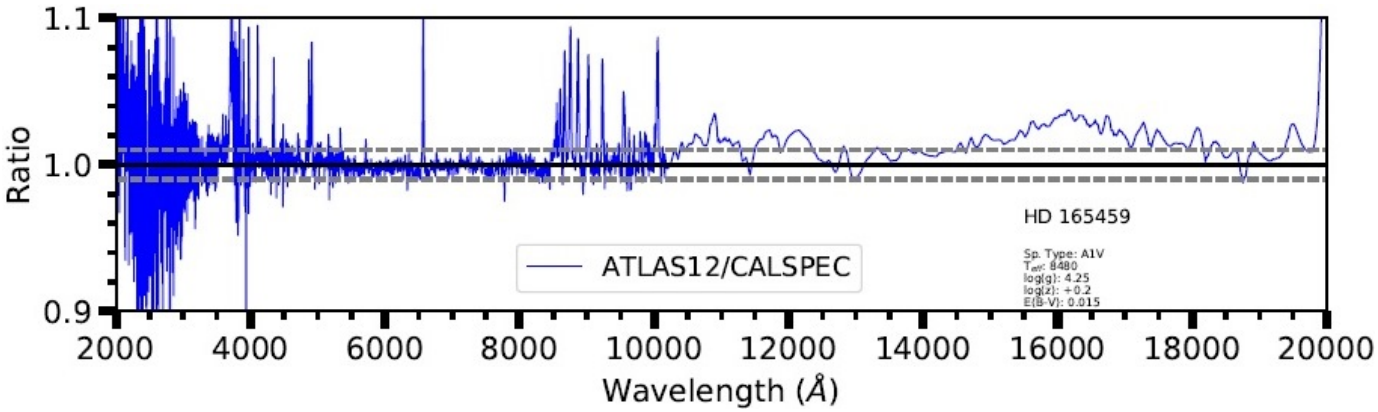

Figure 5.1: Ratio between the best-fit model for HD 165459 and the CALSPEC data. Visible within the NICMOS region is a flux excess centered around 1.6 µm. Excess IR flux of 46.7% in Spitzer data provides evidence of a circumstellar disk about this star [Rieke et al. (2005); Su et al. (2006); Wu et al. (2013)].

Star	Teff	Teff	Log(g)	Log(g)	[M/H]	[M/H]	E(B-V)	E(B-V)
	NIC	NO NIC	NIC	NO NIC	NIC	NO NIC	NIC	NO NIC
P330E	5850	5840	3.95	3.90	-0.12	-0.14	0.037	0.036
1743045	7370	7400	3.55	3.60	-0.25	-0.20	0.013	0.016
1812095	7760	7760	3.75	3.75	0.37	0.38	0.000	0.000
HD 165459	8480	8420	4.25	4.20	0.20	0.15	0.015	0.008
1805292	8570	8570	4.00	4.00	0.07	0.07	0.034	0.033
1732526	8620	8630	4.10	4.10	-0.36	-0.35	0.032	0.033
1802271	8990	8990	4.05	4.05	-0.47	-0.47	0.012	0.012

Table 5.4: The result of fits performed with ATLAS12, while either including NICMOS data in the fit, or excluding the NICMOS data.

NICMOS data, and could be a likely source of bias. The resultant fit including NICMOS is in greater agreement with [Bohlin et al. (2017)], which is to be expected, as it is included in their fits. HD 165459 is already known to have a circumstellar disk [Rieke et al. (2005); Su et al. (2006); Wu et al. (2013)], causing an IR excess of 0.45 magnitudes relative to Vega at 22 μm [Rieke et al. (2005); Su et al. (2006); Wu et al. (2013)].

The mean agreement for all targets [Bohlin et al. (2017)] is -15 K ± 39 effective temperature, -0.04 ± 0.18 logarithm of surface gravity, 0.06 ± 0.07 logarithm of metallicity, and -0.003 ± 0.008 E(B-V) (ATLAS-BOSZ). For G stars, this comes out to 15 K ± 22 effective temperature, -0.3 ± 0.11 logarithm of surface gravity, 0.01 ± 0.03 logarithm of metallicity, and 0.003 ± 0.004 E(B-V). For A stars, this comes out to 36 K ± 42 effective temperature, 0.05 ± 0.10 logarithm of surface gravity, 0.08 ± 0.07 logarithm of metallicity, and -0.006 ± 0.006 E(B-V). The discrepancy may be due to the difference between models interpolated on a grid, and models generated with a unique set of parameters. Additionally, we use the Kurucz line list from December 2016, and [Bohlin et al. (2017)] uses a line list from April 2015. The standard deviation of log surface gravity is four times that of the standard deviation (0.05 ± 0.2 log(g)), greater than the other parameters. There may be several reasons for this. It may have the least linear response compared to the other parameters, and therefore has the greatest difference between an interpolated model and a uniquely generated one. In

the [Bohlin et al. (2017)] grid, the logarithm of surface gravity is computed in steps of 0.5, whereas logarithm of metallicity is computed in steps of 0.25. The difference in parameter grid step size may be the explanation for this discrepancy. Finally, this discrepancy primarily comes from G-type stars, which are particularly insensitive to changes within surface gravity (see fig. 4.2), and thus it would serve to reason that this parameter would vary by the largest amount with changes to the line list, interpolation, calculation of chi-squared, etc.

In order to test whether interpolation was the primary driver of the discrepancy, a series of models were generated using ATLAS9 at the same grid points as the [Bohlin et al. (2017)] work. Only the points necessary to encapsulate the candidate stars were generated. The same fitting procedure was applied to the CALSPEC stars, generating interpolated models from the grid points as necessary (see Fig. 5.2). The results show a mean agreement of 14 K $\pm$ 39 effective temperature, 0.02 $\pm$ 0.16 logarithm of surface gravity, 0.06 $\pm$ 0.06 logarithm of metallicity, and 0.002 $\pm$ 0.008 E(B-V). The continued discrepancy is likely from the difference in input files for atomic and molecular data. HD 165459 shows an improved agreement with [Bohlin et al. (2017)], with the interpolated best-fit model disagreeing by 40 K (ATLAS9 disagreed by 130 K when using uniquely generated models).

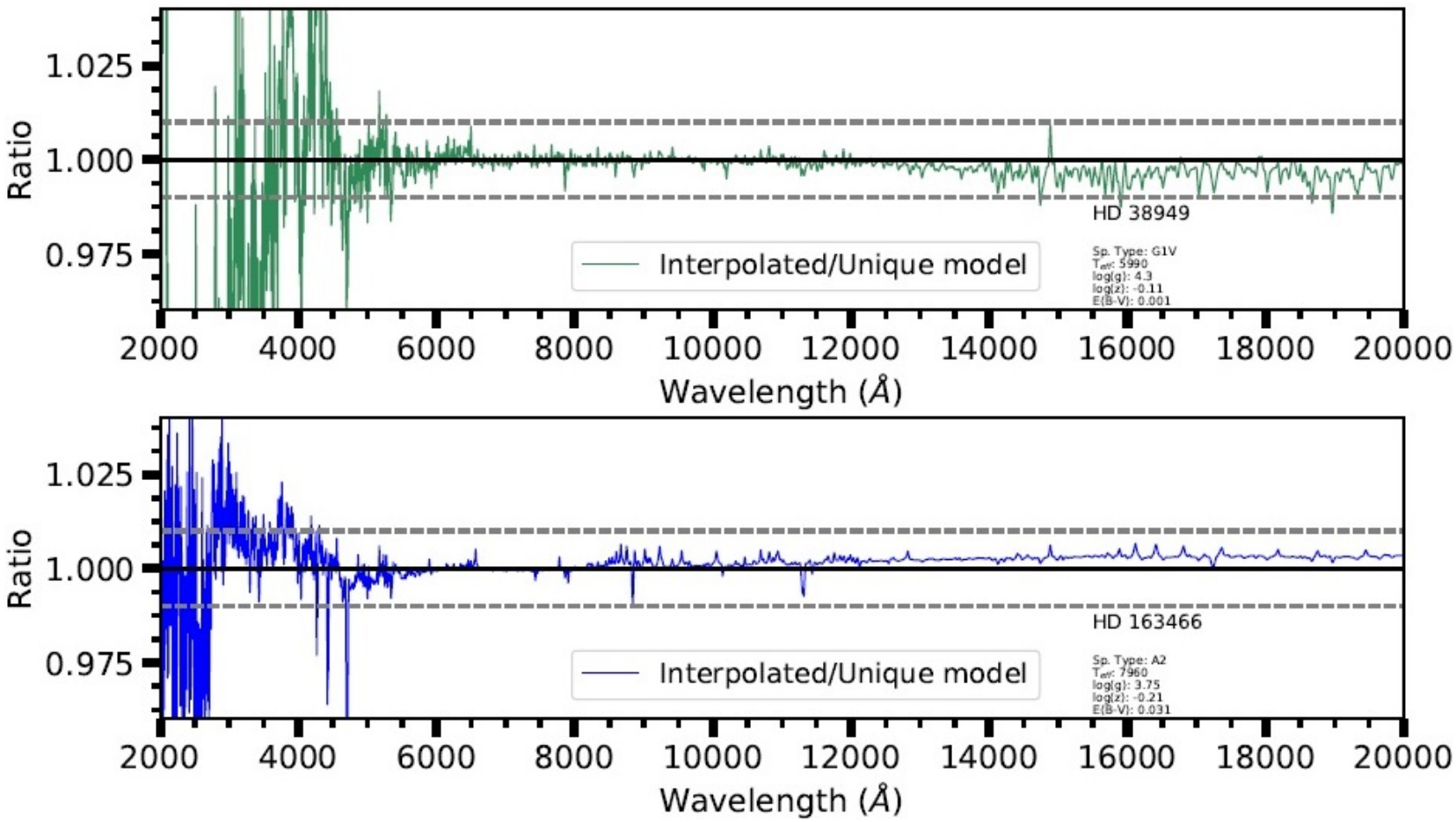

Figure 5.2: The ratio between models with the same stellar parameters, one the result of interpolation from a model grid, the other a uniquely generated model. The interpolated models were created by generating model spectra at step sizes of 250 K, 0.5 log(g) and 0.25 [M/H] and interpolating between them. The unique model and the model grid points were both generated using ATLAS9. The two targets are the primary ACCESS targets; HD 38949 is a G star, and HD 163466 is an A star.

We checked the ratio between two models with the same stellar parameters, one generated using interpolation and the other generated as a unique model with the ATLAS9 code (fig. 5.2). The discrepancy between these two models is on the same order as the difference between the ACCESS group's best-fit models and the best-fit models of [Bohlin et al. (2017)]. Similar to the fits between ATLAS9 and ATLAS12, the agreement is at its worst in the blue end of the spectrum, in regions with heavy line blanketing.

It can be seen from plotting the fitting algorithm results for a given target that a higher effective temperature is associated with a higher value of interstellar reddening for any individual target. The plots in which only one of these variables is modified shows that the behavior between these two is very similar, in particular for an A star. G stars exhibit similar behavior, but are more sensitive to temperature redward of the peak flux value than an A star. Interstellar reddening, by its nature, affects the blue end of the spectrum more strongly.

Overall, the results of these tests demonstrate that similar results will be achieved in using ATLAS9 or ATLAS12, for the purpose of fitting stellar models to flux calibrated data. The primary benefit of ATLAS9 is that it is faster to generate models, whereas the flexibility of parameter space is the strength of ATLAS12. SYNTHE, however, is used to generate a synthetic flux spectrum for both ATLAS9 and ATLAS12. Running SYNTHE can take longer than the generation of an ATLAS12 model, depending on the bandpass and resolution desired. A typical ATLAS9 stellar atmosphere model takes less than a minute to generate, using a Dell Precision T3500 running a 64-bit version of Ubuntu Linux, with 12 GB of RAM, and an Intel Xeon CPU. An ATLAS12 stellar atmosphere model takes approximately 13 minutes to generate, compared to the sub-minute ATLAS9 time. It takes approximately 20 additional minutes to compute a SYNTHE synthetic flux spectrum from 0.125 to 2.5 μm with a resolution of 600,000. This resolution was chosen to be sufficiently above both

CALSPEC data (R=200-1,000) and APO data (R=31,500), while allowing for the potential to be used with higher resolution without regenerating a synthetic flux spectrum. SYNTHE computation time is independent of whether ATLAS9 or ATLAS12 was used to generate the input model.

The atmospheric models between ATLAS9 and ATLAS12 agree well in terms of temperature, pressure, and electron density as a function of optical depth. The differences result in spectral energy distributions that disagree to a value less than 0.1% from 5000 Å through 20,000 Å. From 2000 Å to 5000 Å, the differences do not exceed 1%. For A stars, there is disagreement between ATLAS9 and ATLAS12 models at low optical depths, but these differences occur at $\tau < 0.01$, and weak spectral lines and continuum form at higher optical depths. These differences do not result in flux differences greater than 0.5% throughout the same bandpass.

An ATLAS9 or ATLAS12 model will have, as an output, the flux error and the flux derivative error (see sec. 4.7.1). These can be used to ensure convergence. The prescription for this in ATLAS9 is to input a model that values similar to the expected parameter values. For the ACCESS group, the [Mészáros et al. (2012)] grid was used as a starting point. If the mean flux error is above 1% or the mean flux derivative error is above 10% for a generated model, the generated model can then be used as an input model, and the process iterated upon until convergence is achieved. This usually only requires one or two iterations. In order to reduce the time required for ATLAS12 to compute a model while still ensuring convergence, ATLAS9 can be used to input an already converged model. This model should have similar stellar properties (i.e. temperature, metallicity, gravity), and ATLAS12 can then be used to further refine the model in other parameters. It was only necessary to run the ATLAS12 model generation procedure once for an individual model.

We tested convergence on the final fit ATLAS12 models for all the selected targets. For all targets, the mean flux error (see sec. 4.7.1) was well below 1%, with no targets exceeding 0.02% mean flux

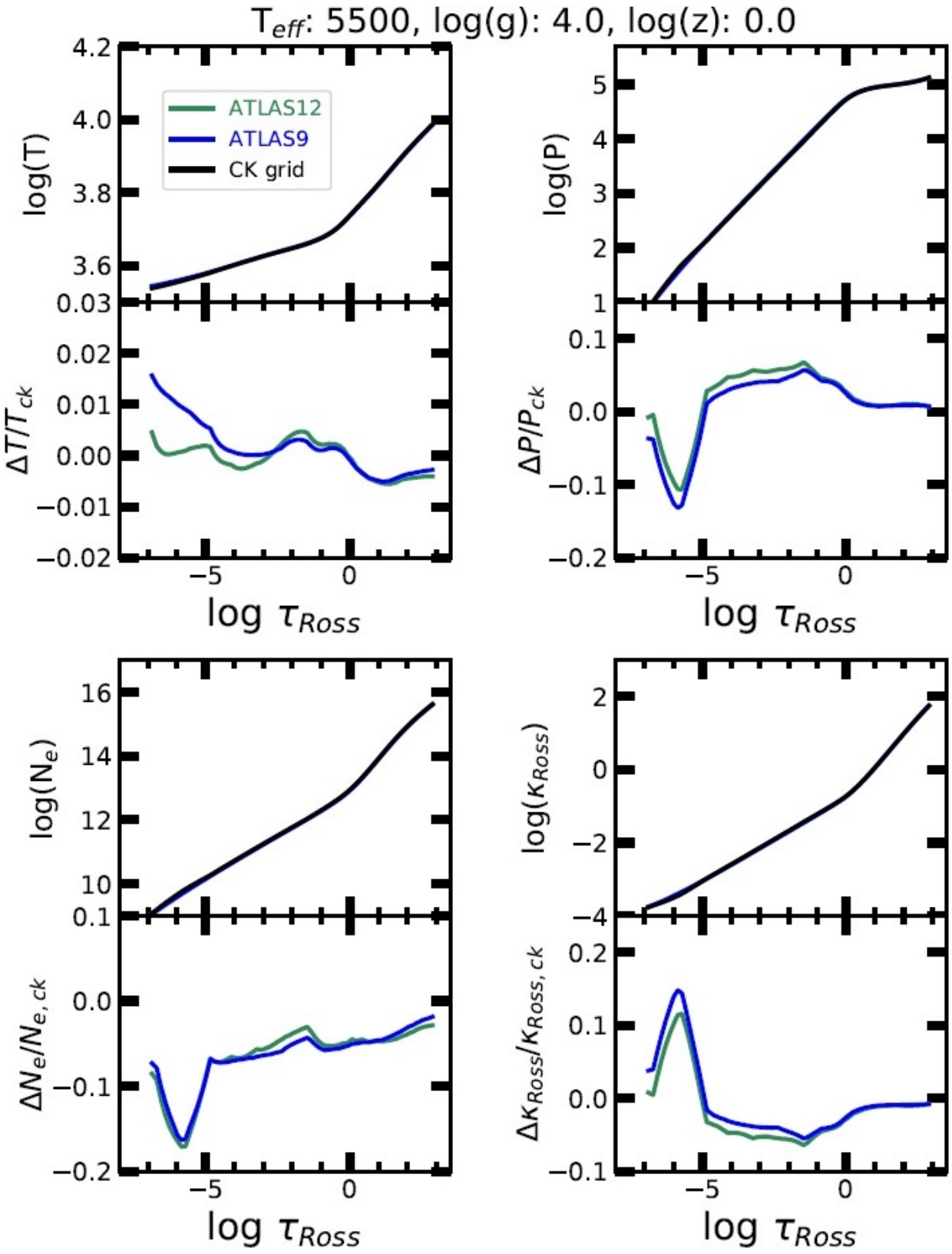

Figure 5.3: Four plots demonstrating a comparison between ATLAS9 models, ATLAS12 models, and models taken from the Castelli-Kurucz model grid [Castelli & Kurucz (2004)]. From the top left clockwise, these show temperature, pressure, rosseland absorption coefficient, and electron number density, as a function of the optical depth. The bottom sections of the plots show the difference between ACCESS generated models and the models from the CK grid. The parameters here are for a typical G star.

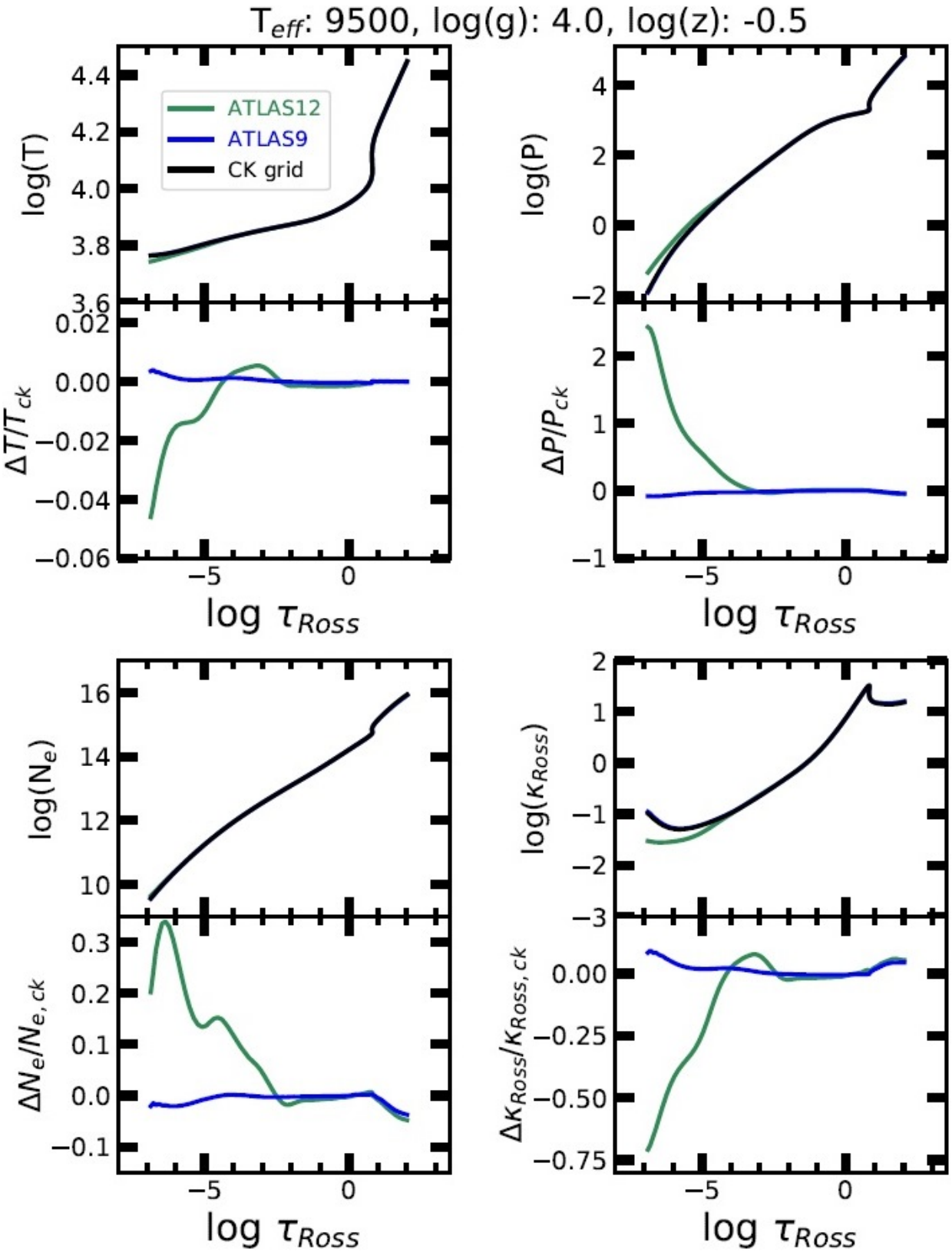

Figure 5.4: The same plots as Figure 5.3, using parameters for a typical A star.

error. 1757132, the target with the highest metallicity, was the only target that had a non-converged mean flux derivative error, at 12.3%. However, this was wholly due to the flux derivative error for the top most layer ($\tau_R \sim 10^{-7}$). Removing this layer, and taking the mean of the remaining 71 layers, yielded mean derivative flux error of 0.48% for 1757132. Mean flux derivative error was below 1% for all targets, when the mean was performed in this manner. This top layer is so optically thin that its contribution to the stellar flux is very low [Mészáros et al. (2012)]. ATLAS12 has shown robustness for the parameter space within the selected targets. This test was also performed when targets were fit with carbon and α-abundance as free parameters (Sec. 5.2), with all ATLAS12 models converging, including 1757132.

The only parameter consistent throughout the fits was microturbulent velocity. We find a best-fit parameter for microturbulent velocity to be 2 km/sec. It was found that modulation of the microturbulence parameter in either direction (i.e. 1 or 3 km/sec) yielded a higher chi-squared value for all targets in the sample. After confirming this across all targets in ATLAS12, microturbulence was left fixed, so as to reduce the convergence time of the fitting algorithm.

5.2 Fits to Carbon and α

After the fits with ATLAS9 and ATLAS12 were performed, ATLAS12 was used to fit to the spectrum, allowing α-element abundance to vary as a free parameter. The previously mentioned stellar parameters were allowed to vary as well. The agreement between these fits and fits with the α-elements fixed to scaled solar values was a mean of -14 K ± 63 effective temperature, 0.08 ± 0.16 logarithm of surface gravity, 0.004 ± 0.11 logarithm of metallicity, and 0.004 ± 0.007 E(B-V). α-abundance had a mean value of -0.05 ± 0.33 log[α/M] for the targets in this sample (for G stars 0.00 ± 0.36 log[α/M]; for A stars, -0.07 ± 0.38 log[α/M]).

Star	Sp. Type	ATLAS12 T_{eff}	ATLAS12 Log(g)	ATLAS12 Log[M/H]	ATLAS12 Log[α/M]	ATLAS12 E(B-V)
HD 37962	G2V	5740	4.05	-0.16	0.05	0.005
P330E	G2V	5750	3.9	-0.22	0.05	0.018
HD 159222	G1V	5830	3.55	0.2	-0.1	0.003
HD 106252	G0V	5840	3.8	-0.08	0.05	0
HD 205905	G2V	5880	3.8	0.1	-0.1	0.004
HD 38949	G1V	6000	3.95	-0.14	0.05	0.006
1743045	A5V	7520	3.75	-0.04	0.15	0.028
1757132	A3V	7640	3.8	0.4	0.1	0.033
1812095	A5V	7780	3.75	0.47	0.15	0
HD 14943	A5V	7860	3.9	0.21	0.2	0
HD 163466	A3V	7910	3.75	-0.06	-0.2	0.019
1808347	A2V	7920	3.85	-0.54	0.2	0.024
HD 37725	A3V	8250	4.25	0.08	-0.05	0.028
HD 165459	A4V	8380	4.2	0.19	0.05	0.002
1732526	A0V	8430	4.1	-0.15	-1.15	0.01
HD 180609	A4V	8560	4.1	-0.29	-0.25	0.038
1805292	A4V	8570	4.1	0.05	-0.25	0.036
HD 158485	A4V	8590	4.3	-0.07	-0.6	0.044
1802271	A2V	9020	4	-0.5	0.1	0.015
BD+60 1753	A1V	9310	4	-0.11	0	0.009
HD 116405	A0V	10780	4.1	-0.41	0.5	0

Table 5.5: Results for the fitting algorithm, allowing α-abundance as an additional free parameter

These fits were not performed by minimizing the chi-squared value of broad bins, but rather a point-to-point fit between model and data. Because the ATLAS12 synthetic flux spectra are at a much higher resolution than the CALSPEC data, the ATLAS12 data are interpolated onto the wavelength scale of the CALSPEC data. This interpolation was performed after the ATLAS12 data was deresolved to the CALSPEC resolution. This was achieved by convolving the ATLAS12 spectra with a normalized gaussian window (σ of $\sim$470 pixels for STIS).

Both broad bin and point-to-point fits were attempted initially. It was found using a point-to-point fit reduces the mean and variance of log[α/M] by 43% and 35%, respectively. Targets with the highest absolute values of log[α/M] also showed a very high disagreement in metallicity in the opposite direction. This suggests degeneracy between metallicity and α-abundance, which is why we chose to perform a point-to-point fitting. Even at the STIS resolution there is enough line blending that this may remain.

The ACCESS group performed fits to the data, allowing carbon abundance to vary. The agreement between these fits and the initial ATLAS12 fits was a mean of -28 K $\pm$ 67 effective temperature, 0.10 $\pm$ 0.18 logarithm of surface gravity, 0.09 $\pm$ 0.18 logarithm of metallicity, and 0.006 $\pm$ 0.009 E(B-V). α-abundance had a mean value of -0.10 $\pm$ 0.40 log[α/M], and carbon abundance had a mean value of -0.31 $\pm$ 0.52 log [C/M], for the targets in this sample (for G stars 0.02$\pm$ 0.07 log[α/M], 0.04 $\pm$ 0.06 log[C/M]; for A stars, -0.09$\pm$ 0.40 log[α/M], -0.41 $\pm$ 0.49 log[C/M]). Similar to the α-abundance tests, there seems to be degeneracy with carbon+alpha and metallicity. Temperature is also sensitive to modulating carbon, when fit to spectra with a broad bandpass. Small changes in metallicity lead to large flux differences, relative to either alpha or carbon. When there is a metallicity difference between the two fitting procedures, the resultant carbon abundance can be quite different.

Particularly high or low values for carbon and α-abundance seem to be exclusive to the A stars

Star	Sp. Type	ATLAS12 T_{eff}	ATLAS12 Log(g)	ATLAS12 [M/H]	ATLAS12 [α/M]	ATLAS12 [C/M]	ATLAS12 E(B-V)
HD 37962	G2V	5740	4.05	-0.16	0.05	0	0.005
P330E	G2V	5750	3.9	-0.22	0.05	0	0.018
HD 159222	G1V	5850	3.55	0.2	-0.05	0.1	0.008
HD 106252	G0V	5870	3.8	-0.09	0.1	-0.15	0.007
HD 205905	G2V	5880	3.8	0.1	-0.1	0	0.004
HD 38949	G1V	6000	3.95	-0.14	0.05	0	0.006
1743045	A5V	7540	3.8	0.04	0	-0.05	0.029
1757132	A3V	7640	3.8	0.4	0.1	-0.05	0.033
1812095	A5V	7780	3.75	0.47	0.15	-0.1	0
HD 14943	A5V	7880	3.95	0.29	0.1	-0.7	0
HD 163466	A3V	7910	3.75	-0.06	-0.2	0	0.019
1808347	A2V	7920	3.85	-0.54	0.25	0.5	0.024
HD 37725	A3V	8250	4.25	0.08	-0.05	-0.15	0.028
HD 165459	A4V	8380	4.2	0.21	0	-0.55	0.001
1732526	A0V	8390	4.2	0.19	-1.25	-1.55	0
1805292	A4V	8530	4.15	0.27	-0.45	-0.65	0.027
HD 180609	A4V	8570	4	-0.42	0	-0.15	0.039
HD 158485	A4V	8620	4.4	0.13	-0.6	-0.65	0.044
1802271	A2V	9040	4.05	-0.39	0.05	-0.4	0.016
BD +60 1753	A1V	9300	4.05	-0.07	0	-1.25	0.008
HD 116405	A0V	10780	4.15	-0.39	0.5	-0.4	0

Table 5.6: Results for the fitting algorithm, allowing carbon abundance as an additional free parameter

Star	Spectral Type	Spitzer $\lambda's$ (μm)	# of datasets
HD 106252	G0	12,16,22,24,25	1
HD 38949	G1V	12,16,22,24,25	1
HD 159222	G1V	12,16,22,24,25	1
HD 37962	G2V	12,16,22,24,25	1
HD 205905	G2V	12,16,22,24,25	1
HD 165459	A1V	8,12,16,22,24,25	2
HD 163466	A2	8,12,16,22,24,25	63

Table 5.7: Subset of the stellar sample, with corresponding Spitzer data

of this sample, likely due to the weak spectral dependence on these characteristics in A stars (see figs. 5.6). The most extreme value for α-abundance within G stars is -0.1. Seven out of ten of the A stars had more extreme value, either greater than 0.1 or less than -0.1. It is visible from plotting A stars, and only varying these abundances, that A stars are relatively insensitive to changes in carbon and α-abundances. In particular, there is very little difference in A star spectra with differing carbon abundances. About 0.97% of the spectrum between 0.2 and 2 μm exceed a 1% ratio for an order of magnitude difference in carbon abundance for a typical A star. 77% of a G star exceeds 1% ratio in the same bandpass. Individual line fitting from higher resolution spectra may be needed to measure these abundances in A stars.

5.3 Incorporating Spitzer data

Seven stars in the target list have Spitzer photometric data and corresponding uncertainties for 12, 16, 22, 24, and 25 μm (see Fig. 5.7). Five of these stars are G stars (having been observed as part of the Spitzer legacy program [Meyer et al. (2006)]), and two are A stars observed as part of calibration campaigns [Rieke et al. (2008); Bohlin et al. (2011)]. These datasets were incorporated with the CALSPEC data, to provide further constraints in the infrared wavelength range.

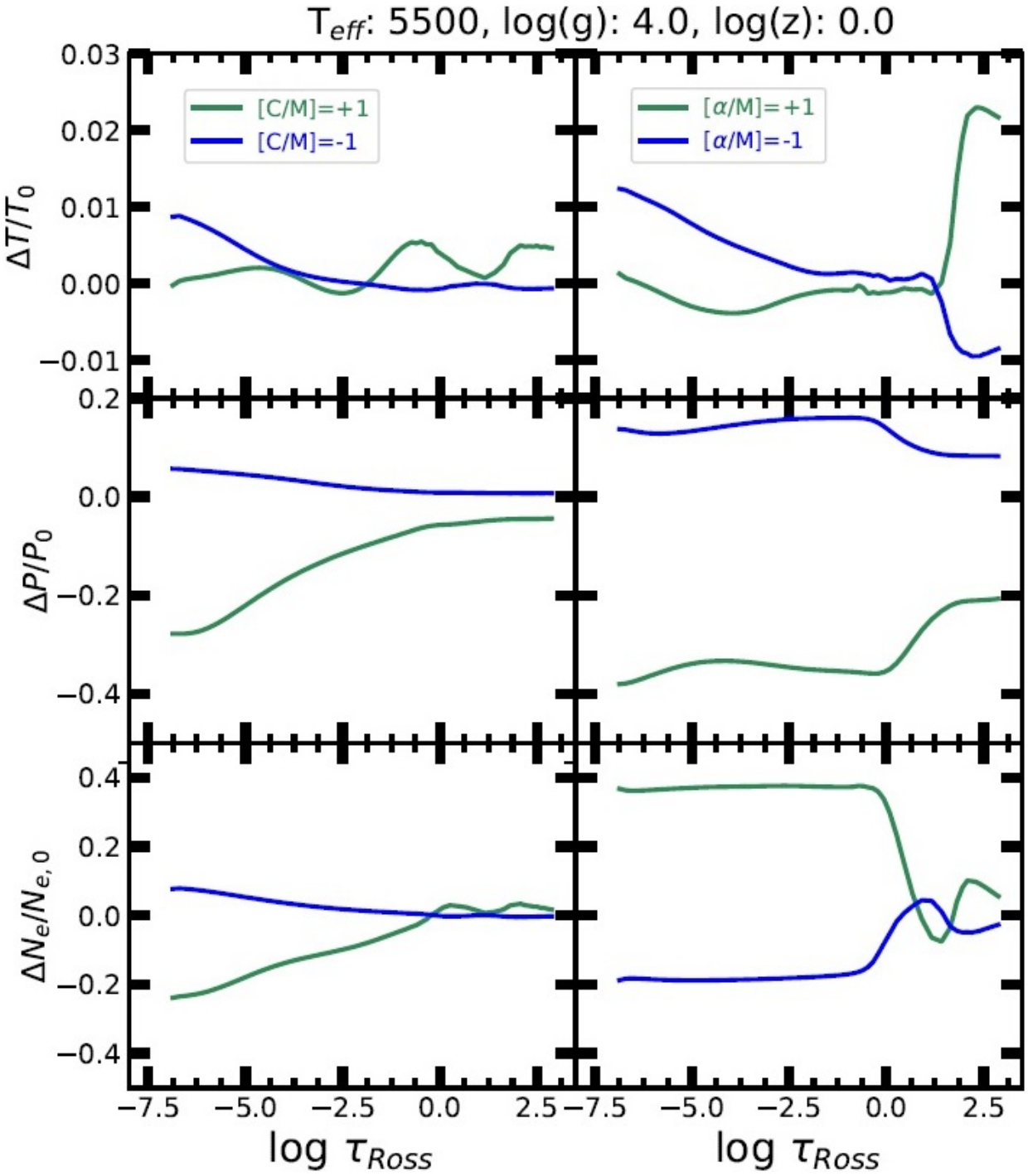

Figure 5.5: ATLAS12 models, compared to models with differing Carbon and α abundance values. From the top, these show temperature, pressure, and electron number density, as a function of the optical depth. The parameters here are for a typical G star.

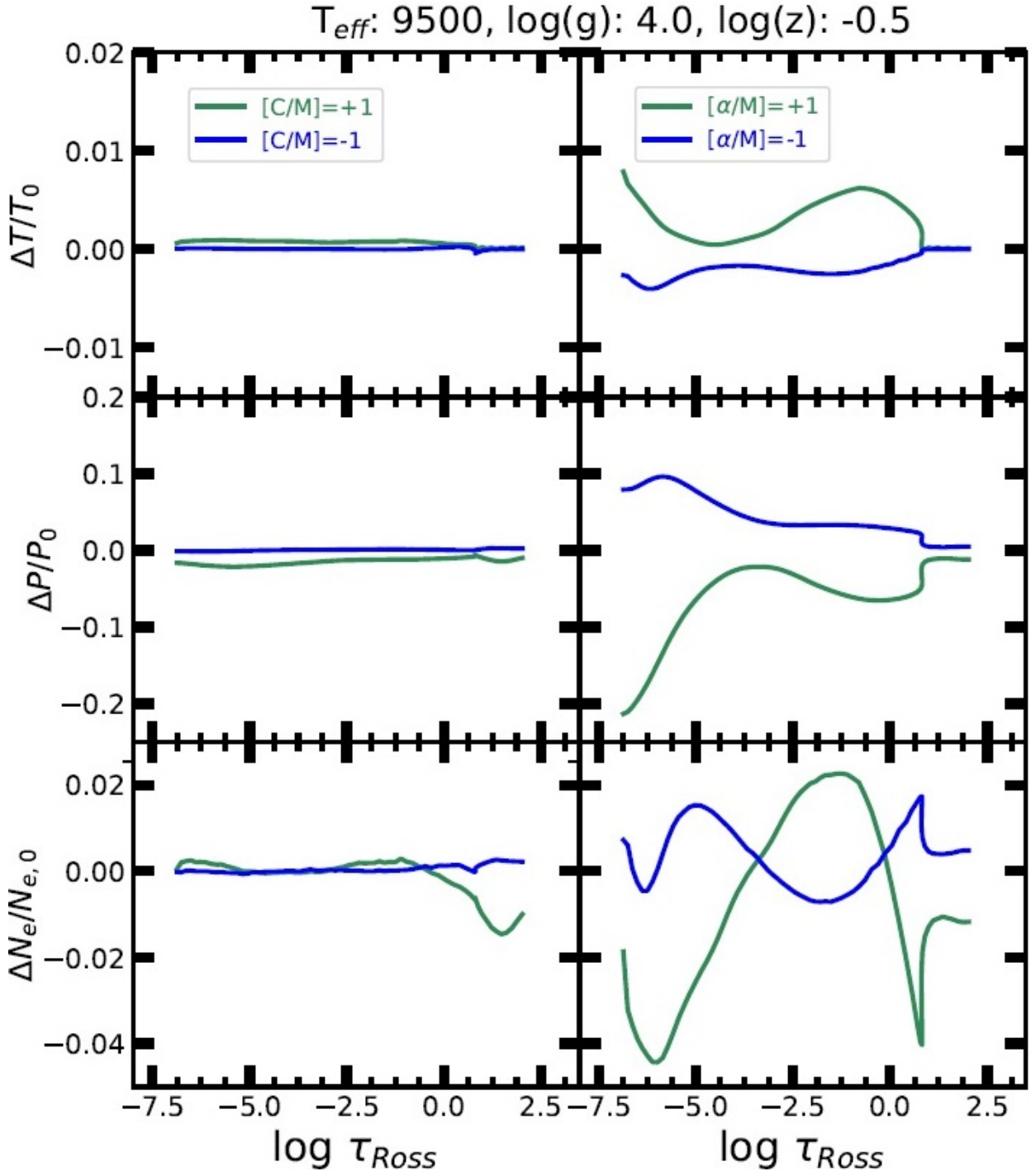

Figure 5.6: The same plot as Figure 5.5 using parameters for a typical A star.

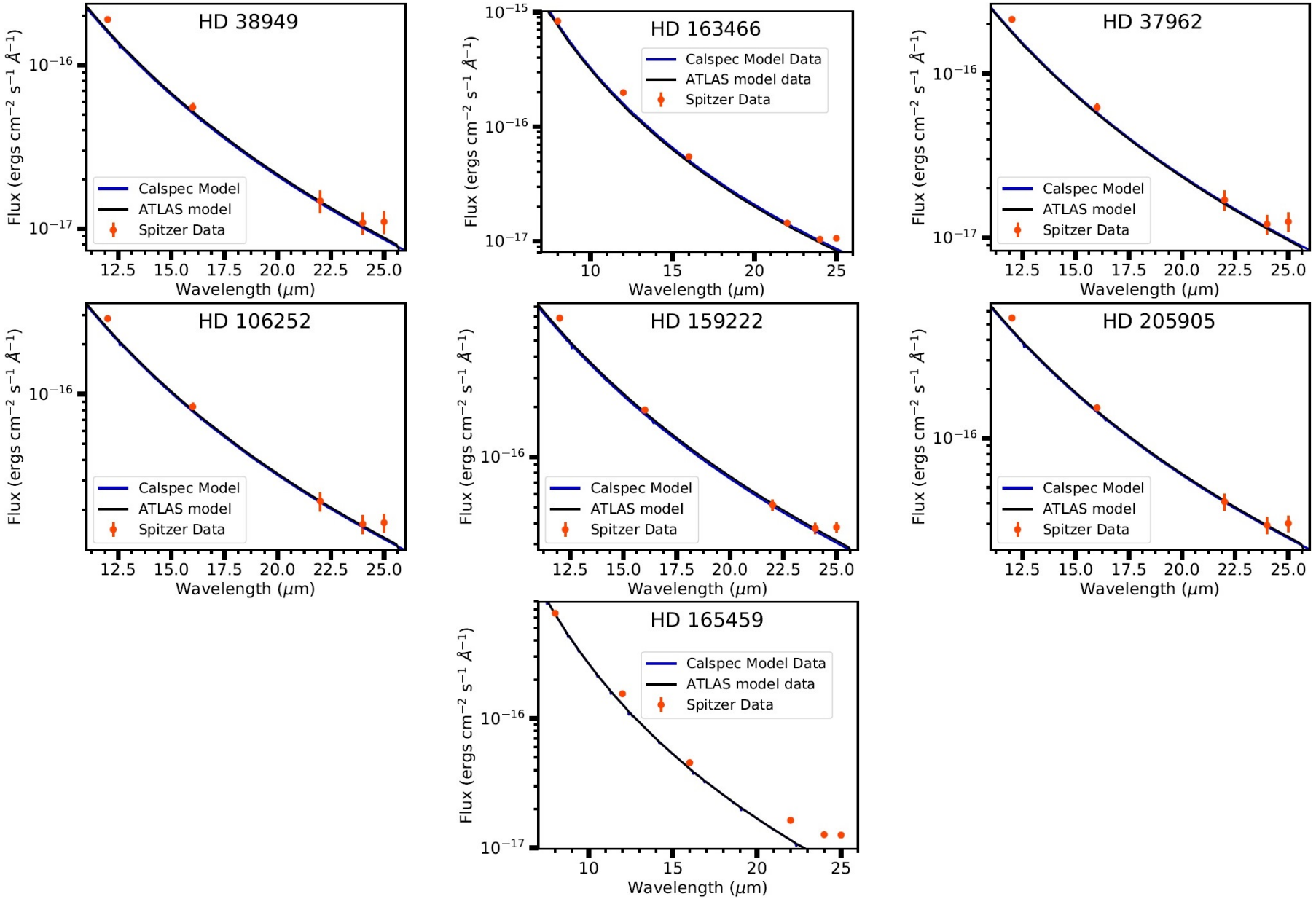

Figure 5.7: Comparison of the 12, 16, 22, 24 and 25 μm Spitzer data from the NASA/ IPAC Infrared Science Archive, compared to the CALSPEC models at the same wavelength. Spitzer data is converted from Janskys to ergs cm^{-2} s^{-1} Å^{-1}according to [Skinner (1996)]. ATLAS12 was used to perform these fits. The 25 μm band is systematically high by nearly 25% for all target stars; the calibration constants for that band have varied by up to 6%, depending on the campaign [Beichman et al. (1988); Cohen et al. (1992); Rieke et al. (2008)]. Of particular note is the infrared excess in the 22, 24 and 25 μm bandpasses for HD 165459.

Star	Sp. Type	ATLAS12 T_{eff}	ATLAS12 Log(g)	ATLAS12 Log[M/H]	ATLAS12 E(B-V)
HD 159222	G1V	5800	3.3	0.06	0.001
HD 37962	G2V	5800	3.55	-0.2	0.022
HD 106252	G0V	5840	3.6	-0.11	0.0
HD 205905	G2V	5860	3.45	0.02	0.004
HD 38949	G1V	5980	4.05	-0.12	0.0
HD 163466	A3V	7920	3.75	-0.18	0.026
HD 165459	A4V	8370	4.15	0.08	0.003

Figure 5.8: Results for the fitting algorithm, adding Spitzer infra-red data to the fits

The uncertainty model for applying the reduced χ^2 follows the same prescription as the CALSPEC data using broad bin fitting, utilizing the published uncertainty in place of the CALSPEC repeatability and background uncertainty values. The resultant fits produce similar parameters, while weighting the χ^2 such that the contributions of the Spitzer data and the CALSPEC data are on the same order.

5.4 Comparison to Previous Works

These ATLAS9 and ATLAS12 best-fit models were ultimately determined using wavelength regions (see tables 4.2 & 4.3), uncertainties and χ^2 formalism following [Bohlin et al. (2017)] for the purpose of comparing the custom best-fit models generated by these two software programs with the BOSZ ATLAS9 model interpolations. This study shows agreement with a mean of -16 K ± 43 effective temperature, -0.09 ± 0.18 logarithm of surface gravity, 0.06 ± 0.07 logarithm of metallicity, and -0.004 ± 0.005 E(B-V) (ATLAS-BOSZ) (see tables 5.8-5.11). For G stars, this came out to 14 K ± 21 effective temperature, -0.3 ± 0.08 logarithm of surface gravity, -0.01 ± 0.03 logarithm of metallicity, and -0.003 ± 0.003 E(B-V). For A stars, this came out to -35 K ± 44 effective temperature, 0.04 ± 0.05 logarithm of surface gravity, 0.09 ± 0.05 logarithm of metallicity, and -0.005 ± 0.005 E(B-V). A typical indicator of disagreement was either fainter targets (e.g. 1757132, Vmag=12.01) or targets

that have been found to have non-standard characteristics (e.g. HD 165459 having a circumstellar disk).

Although initially, the ATLAS9 and ATLAS12 models were not generated with the same χ^2 fitting minimizations as the BOSZ models (tables 5.8-5.11), the results of the earlier fits (tables 5.1 & 5.2) are consistent with those obtained using the BOSZ formalism. For 12 of the stars modeled and fit with both formalisms, the results agree to within 20 K, 0.05 log(g), 0.02 [M/H] and 0.005 E(B-V). P330E, the faintest G star in this target list by 5 magnitudes in the V band, and the only G star with NICMOS data, showed a higher disagreement with [Bohlin et al. (2017)]: 50 K, 0.05 log(g), and 0.04 [M/H]. The spectra were compared between models with best-fit parameters for each method, and the ratio between model spectra was better than 1% from 0.25 to 2 μm at the STIS resolution, with ratios between 0.2 to 0.25 μm reaching 2-5% in some cases (see figs 5.11-5.23).

For G stars, this work showed a systematic difference in surface gravity relative to the results within [Bohlin et al. (2017)]. The mean underestimate was -0.3 log(g). G-type stars are particularly insensitive to changes within surface gravity (see figure 4.2a), and thus it would serve to reason that this parameter would vary by the largest amount with changes to the line list, interpolation, calculation of χ^2 , etc. To confirm that this was not due to local minima, we performed additional fits for a selection of G stars. The initial guess for the fitting algorithm was set to the parameters of the sun. For stars in which log(g) literature values existed (HD 37962, HD 15922, and HD 38949), these were also used as initial guesses. The final best-fit parameter results were the same. When the values for log(g) were fixed to the literature values, the resultant best-fit parameters were much higher in effective temperature (70-300 K) and metallicity (0.09-0.46). The chi-squared value was 2-3 times higher as well.

For A stars, there was a similar disagreement with [Bohlin et al. (2017)] within metallicity. A type

stars are relatively insensitive to metallicity (see figure 4.3b). The mean overestimate for metallicity was 0.07 [M/H]. There are two targets within the A star list that have lower values than in [Bohlin et al. (2017)].

Comparing the results herein to fits performed by [Bohlin et al. (2017)] using the Castelli-Kurucz grid [Castelli & Kurucz (2004)] and the MARCS grid tended to show higher disagreement than with the [Bohlin et al. (2017)] grid, in particular with metallicity (see tables 5.8-5.11). This may be in part due to the fact that the CK04 and MARCS grids use different sources for solar abundance: CK04 uses [Grevesse & Sauval (1998)] and MARCS uses [Grevesse et al. (2007)]. The abundances of [Asplund et al. (2005)] were used for this work and for [Bohlin et al. (2017)]. The MARCS model grid has a temperature range from 2,500 to 8,000 K, and therefore is only appropriate for cooler stars, such as the G stars. The agreement with the MARCS grid is -6 K $\pm$ 27 effective temperature, -0.77 $\pm$ 0.12 logarithm of surface gravity, 0.14 $\pm$ 0.03 logarithm of metallicity, and -0.006 $\pm$ 0.005 E(B-V) (ATLAS-MARCS). The higher disagreement with surface gravity and metallicity may suggest that spherically symmetric stellar atmosphere model calculations produce very different synthetic flux spectra at this temperature range.

Star	Teff	Teff	Teff	Teff	Log(g)	Log(g)	Log(g)	Log(g)	[M/H]	[M/H]	[M/H]	[M/H]	E(B-V)	E(B-V)	E(B-V)	E(B-V)
	AT9	Bosz	CK04	MARCS	AT9	Bosz	CK04	MARCS	AT9	Bosz	CK04	MARCS	AT9	Bosz	CK04	MARCS
HD37962	5760	5750	5690	5790	3.45	3.75	3.35	4.35	-0.23	-0.20	-0.41	-0.31	0.013	0.012	0.002	0.024
P330E	5860	5840	5900	5900	3.95	4.40	4.10	4.75	-0.12	-0.16	-0.25	-0.29	0.04	0.036	0.049	0.052
HD159222	5800	5800	5790	5780	3.25	3.55	3.30	4.10	0.05	0.08	-0.09	-0.07	0.001	0.000	0.001	0.001
HD106252		5830	5820	5810		3.85	3.50	4.20		-0.11	-0.28	-0.27		0.000	0.000	0.000
HD205905	5900	5850	5830	5870	3.55	3.75	3.45	4.30	0.08	0.03	-0.14	-0.08	0.011	0.003	0.001	0.011
HD38949	5980	5990	5980	5990	4.05	4.30	4.00	4.60	-0.11	-0.11	-0.25	-0.26	0	0.001	0.001	0.005

Table 5.8: Comparison of the best-fit parameters for ATLAS9, using [Bohlin et al. (2017)] χ^2 formulations. Compared to the fits results from [Bohlin et al. (2017)], using the BOSZ grid, the CK04 grid [Castelli & Kurucz (2004)], and the MARCS grid [Gustafsson et al. (2008)].

Star	χ^2	χ^2	χ^2	χ^2
	AT9	Bosz	CK04	MARCS
HD37962	0.218	0.28	0.18	0.35
P330E	0.313	0.32	0.49	0.52
HD159222	0.151	0.16	0.12	0.19
HD106252		0.17	0.16	0.21
HD205905	0.184	0.18	0.14	0.18
HD38949	0.195	0.08	0.07	0.18

Table 5.9: Comparison of the best-fit χ^2 for ATLAS9, using [Bohlin et al. (2017)] χ^2 formulations. Compared to the fits results from [Bohlin et al. (2017)], using the BOSZ grid, the CK04 grid [Castelli & Kurucz (2004)], and the MARCS grid [Gustafsson et al. (2008)].

Star	Teff	Teff	Teff	Log(g)	Log(g)	Log(g)	[M/H]	[M/H]	[M/H]	E(B-V)	E(B-V)	E(B-V)
	AT9	Bosz	CK04	AT9	Bosz	CK04	AT9	Bosz	CK04	AT9	Bosz	CK04
1743045		7470	7460		3.65	3.65		-0.29	-0.31		0.026	0.026
1757132	7610	7640	7660	3.75	3.75	3.80	0.34	0.19	0.18	0.034	0.036	0.041
1812095	7780	7810	7830	3.70	3.65	3.70	0.37	0.22	0.22	0.000	0.008	0.013
HD 14943		7940	7930		3.90	3.90		0.09	0.07		0.011	0.012
1808347		7910	7890		3.85	3.85		-0.61	-0.62		0.024	0.022
HD 163466	7940	7960	7950	3.75	3.75	3.75	-0.16	-0.21	-0.24	0.026	0.031	0.031
HD 37725		8350	8380		4.25	4.30		-0.10	-0.08		0.041	0.045
HD 165459	8430	8570	8540	4.20	4.20	4.20	0.17	0.10	0.07	0.006	0.023	0.021
HD 180609		8560	8600		3.95	4.00		-0.44	-0.45		0.037	0.042
1805292	8570	8570	8540	4.00	4.00	4.00	0.05	-0.07	-0.11	0.032	0.034	0.032
HD 158485	8580	8580	8640	4.20	4.15	4.20	-0.28	-0.39	-0.35	0.046	0.046	0.052
1732526		8630	8670		4.10	4.15		-0.32	-0.25		0.036	0.039
1802271	8980	9040	9070	4.00	4.00	4.00	-0.48	-0.48	-0.47	0.010	0.017	0.020
BD +60 1753	9360	9370	9410	3.95	3.90	3.90	-0.05	-0.09	-0.06	0.011	0.013	0.017
HD 116405	10780	10790	10790	4.15	4.00	4.05	-0.20	-0.35	-0.37	0.000	0.000	0.000

Table 5.10: Comparison of the best-fit parameters for ATLAS9, using [Bohlin et al. (2017)] χ^2 formulations. Compared to the fits results from [Bohlin et al. (2017)], using the BOSZ grid and the CK04 grid [Castelli & Kurucz (2004)].

Star	χ^2 AT9	χ^2 Bosz	χ^2 CK04
1743045		1.38	1.59
1757132	0.579	0.83	1.23
1812095	1.732	0.88	0.95
HD 14943		0.76	1.04
1808347		2.46	2.80
HD 163466	1.045	2.21	2.53
HD 37725		1.17	1.43
HD 165459	0.264	0.53	0.64
HD 180609		0.59	0.75
1805292	0.991	0.80	0.90
HD 158485	0.689	1.47	1.72
1732526		2.92	2.99
1802271	0.475	0.94	0.98
BD +60 1753	0.392	0.84	1.01
HD 116405	1.093	0.61	0.42

Table 5.11: Comparison of the best-fit χ^2 for ATLAS9, using [Bohlin et al. (2017)] χ^2 formulations. Compared to the fits results from [Bohlin et al. (2017)], using the BOSZ grid and the CK04 grid [Castelli & Kurucz (2004)].

Star	Sp. Type	Teff	Teff	Log(g)	Log(g)	[M/H]	[M/H]	E(B-V)	E(B-V)	χ^2	χ^2
		AT9 B	AT12 B	AT9 B	AT12 B	AT9 B	AT12 B	AT9 B	AT12 B	AT9 B	AT12 B
HD 37962	G2V	5760	5750	3.45	3.4	-0.23	-0.25	0.013	0.011	0.218	0.219
P330E	G2V	5860	5860	3.95	3.95	-0.12	-0.12	0.04	0.04	0.313	0.309
HD 159222	G1V	5800	5830	3.25	3.35	0.05	0.11	0.001	0.006	0.151	0.158
HD 106252	G0V										
HD 205905	G2V	5900	5850	3.55	3.4	0.08	0.01	0.011	0.002	0.184	0.179
HD 38949	G1V	5980	5980	4.05	4.1	-0.11	-0.08	0	0.001	0.195	0.196
1743045	A5V										
1757132	A3V	7610	7640	3.75	3.8	0.34	0.39	0.034	0.034	0.579	0.602
1812095	A5V	7780	7760	3.7	3.7	0.37	0.36	0	0	1.732	1.743
HD 14943	A5V										
1808347	A3V										
HD 163466	A2V	7940	7930	3.75	3.75	-0.16	-0.15	0.026	0.026	1.045	1.105
HD 37725	A3V										
HD 165459	A4V	8430		4.2		0.17		0.006		0.264	
HD 180609	A0V										
1805292	A4V	8570	8570	4	4	0.05	0.07	0.032	0.033	0.991	1.093
HD 158485	A4V	8580	8590	4.2	4.25	-0.28	-0.26	0.046	0.048	0.689	0.771
1732526	A4V										
1802271	A2V	8980	8990	4	4.05	-0.48	-0.46	0.01	0.012	0.475	0.449
BD +60 1753	A1V	9360	9370	3.95	3.95	-0.05	-0.02	0.011	0.013	0.392	0.443
HD 116405	A0V	10780	10780	4.15	4.15	-0.2	-0.2	0	0	1.093	1.139

Table 5.12: Comparison of the best-fit χ^2 for ATLAS9 and ATLAS12, using [Bohlin et al. (2017)] χ^2 formulations.

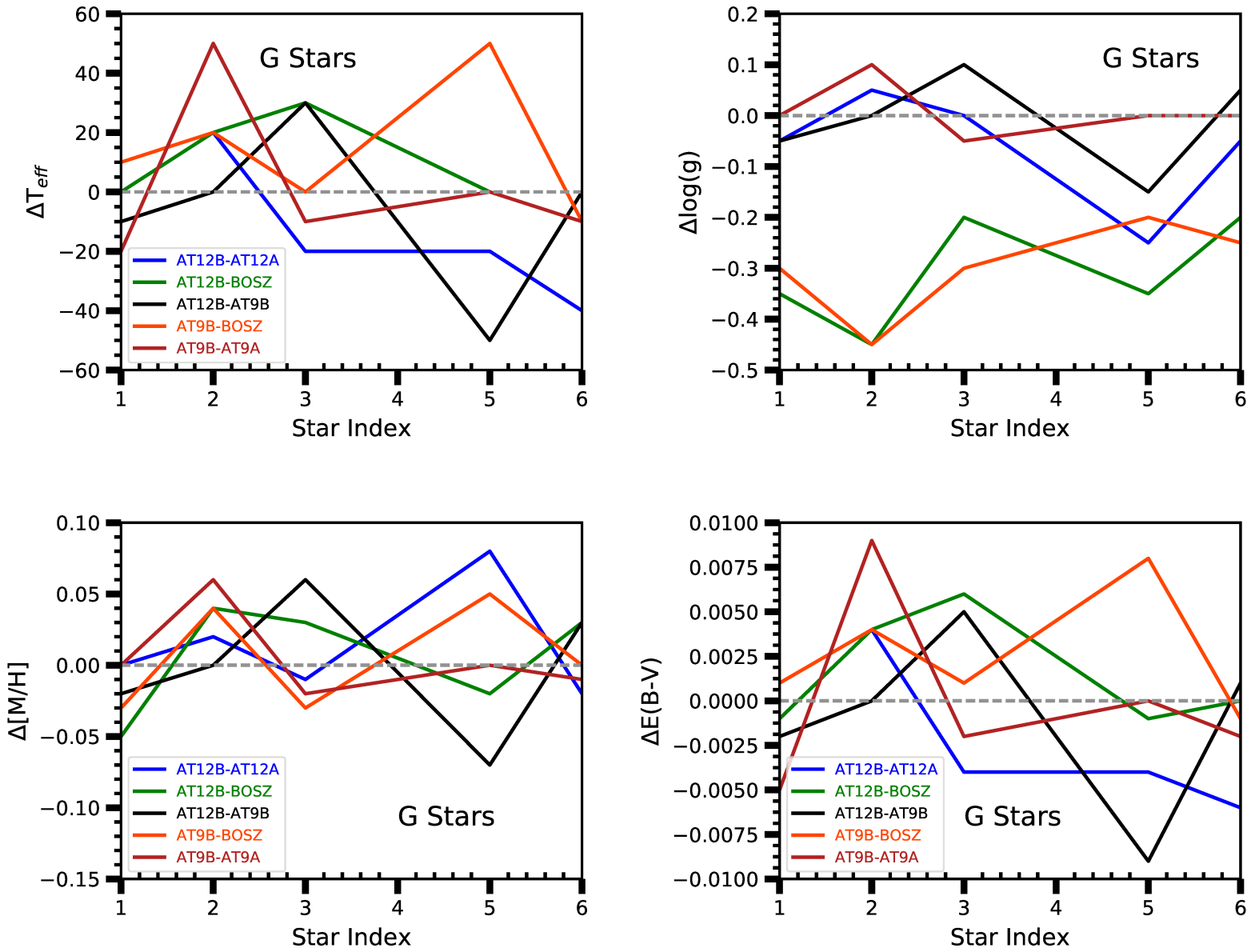

Figure 5.9: Comparison of individual G star parameters for ATLAS9 and ATLAS12, with and without [Bohlin et al. (2017)] χ^2 formulations. AT9B and AT12B are fits with the BOSZ formalism, AT9A and AT12A are those without. Star index is that of table 5.13.

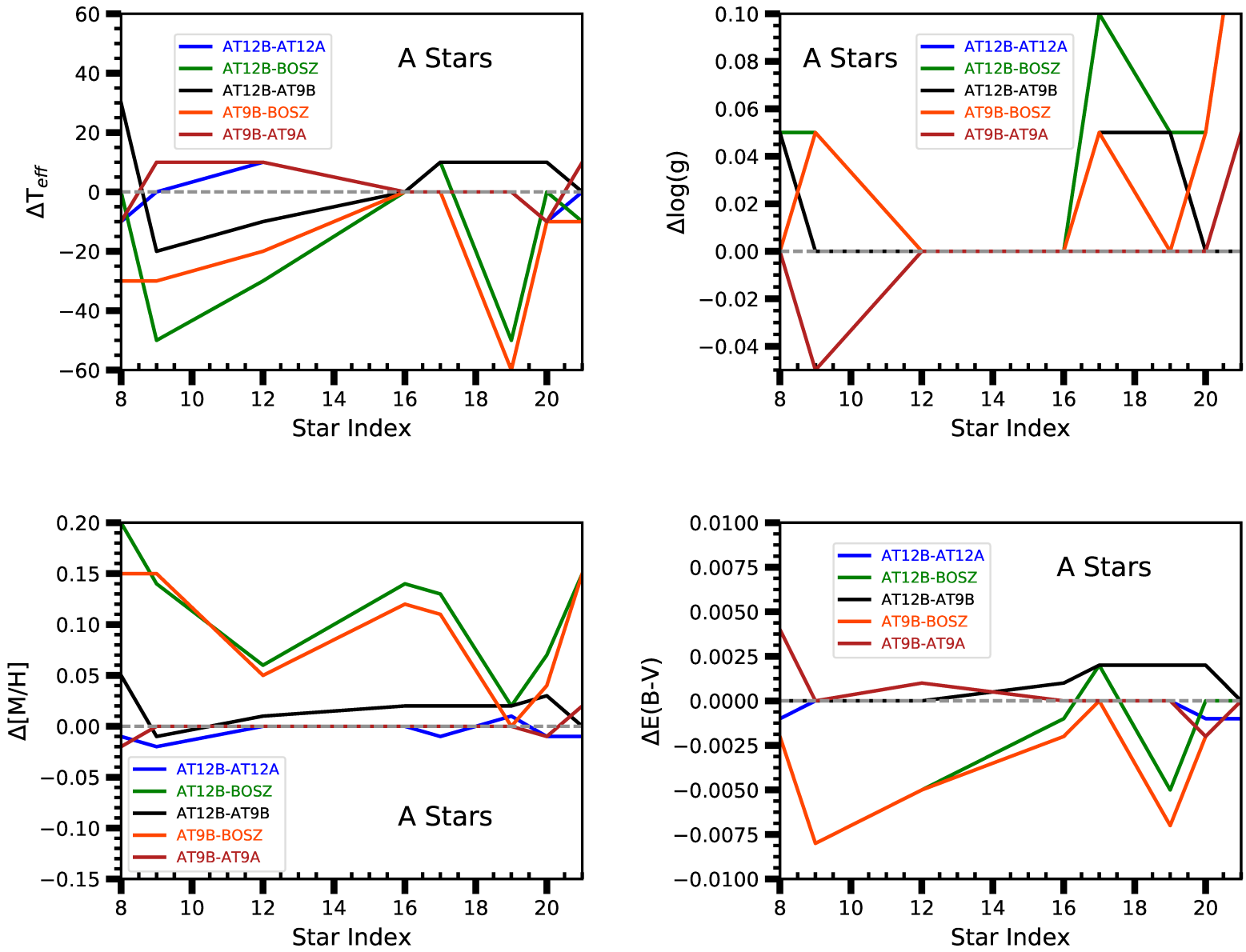

Figure 5.10: Comparison of individual A star parameters for ATLAS9 and ATLAS12, with and without [Bohlin et al. (2017)] χ^2 formulations. AT9B and AT12B are fits with the BOSZ formalism, AT9A and AT12A are those without. Star index is that of table 5.13.

Star Index	Target	Sp. Type
1	HD 37962	G2V
2	HD 159222	G1V
3	HD 106252	G0
4	P330E	G2V
5	HD 205905	G1.5IV-V
6	HD 38949	G1V
7	1743045	A5V
8	1757132	A3V
9	1812095	A3V
10	1808347	A3V
11	HD 14943	A5V
12	HD 163466	A2
13	HD 37725	A3V
14	HD 180609	A0V
15	HD 165459	A1V
16	1805292	A4V
17	HD 158485	A4V
18	1732526	A6V
19	1802271	A2V
20	BD+60 1753	A1V
21	HD 116405	A0V

Table 5.13: ACCESS stellar targets, for reference to figures 5.9 & 5.10.

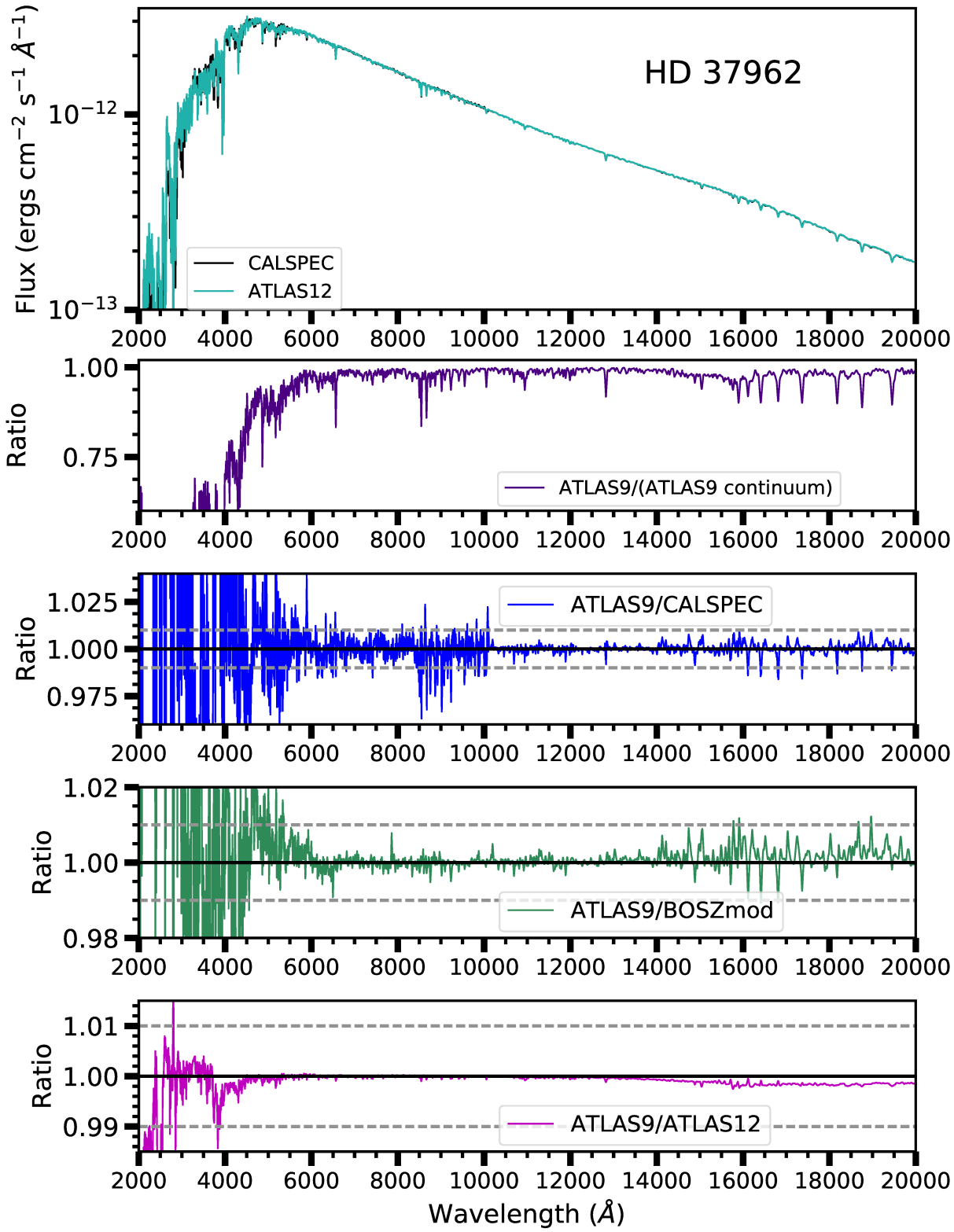

Figure 5.11: Comparison of Model spectra to CALSPEC data, for stellar target HD 37962. From top to bottom: **1.** Overplot of CALSPEC data with best-fit ATLAS9 model. **2.** Best-fit ATLAS9 model, continuum normalized. **3.** Ratio between best-fit ATLAS9 model and CALSPEC data. **4.** Ratio between best-fit ATLAS9 model and best-fit BOSZ model from [Bohlin et al. (2017)]. **5.** Ratio between best-fit ATLAS9 model and best-fit ATLAS12 model.

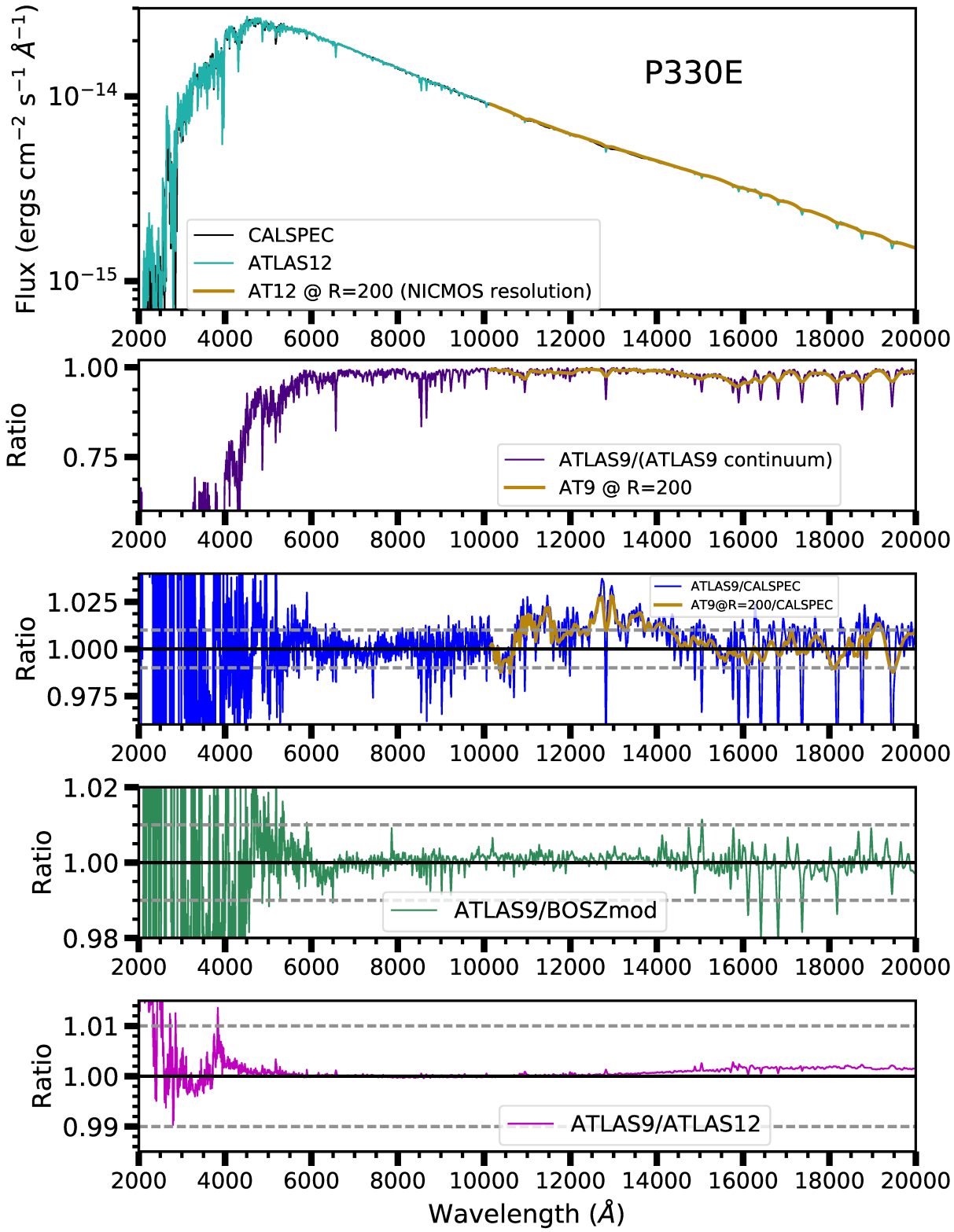

Figure 5.12: Comparison of Model spectra to CALSPEC data, for stellar target P330E. From top to bottom: **1.** Overplot of CALSPEC data with best-fit ATLAS9 model. **2.** Best-fit ATLAS9 model, continuum normalized. **3.** Ratio between best-fit ATLAS9 model and CALSPEC data. **4.** Ratio between best-fit ATLAS9 model and best-fit BOSZ model from [Bohlin et al. (2017)]. **5.** Ratio between best-fit ATLAS9 model and best-fit ATLAS12 model. **NB:** Gold data in plots 1,2, and 3 are the same dataset smoothed to the NICMOS resolution.

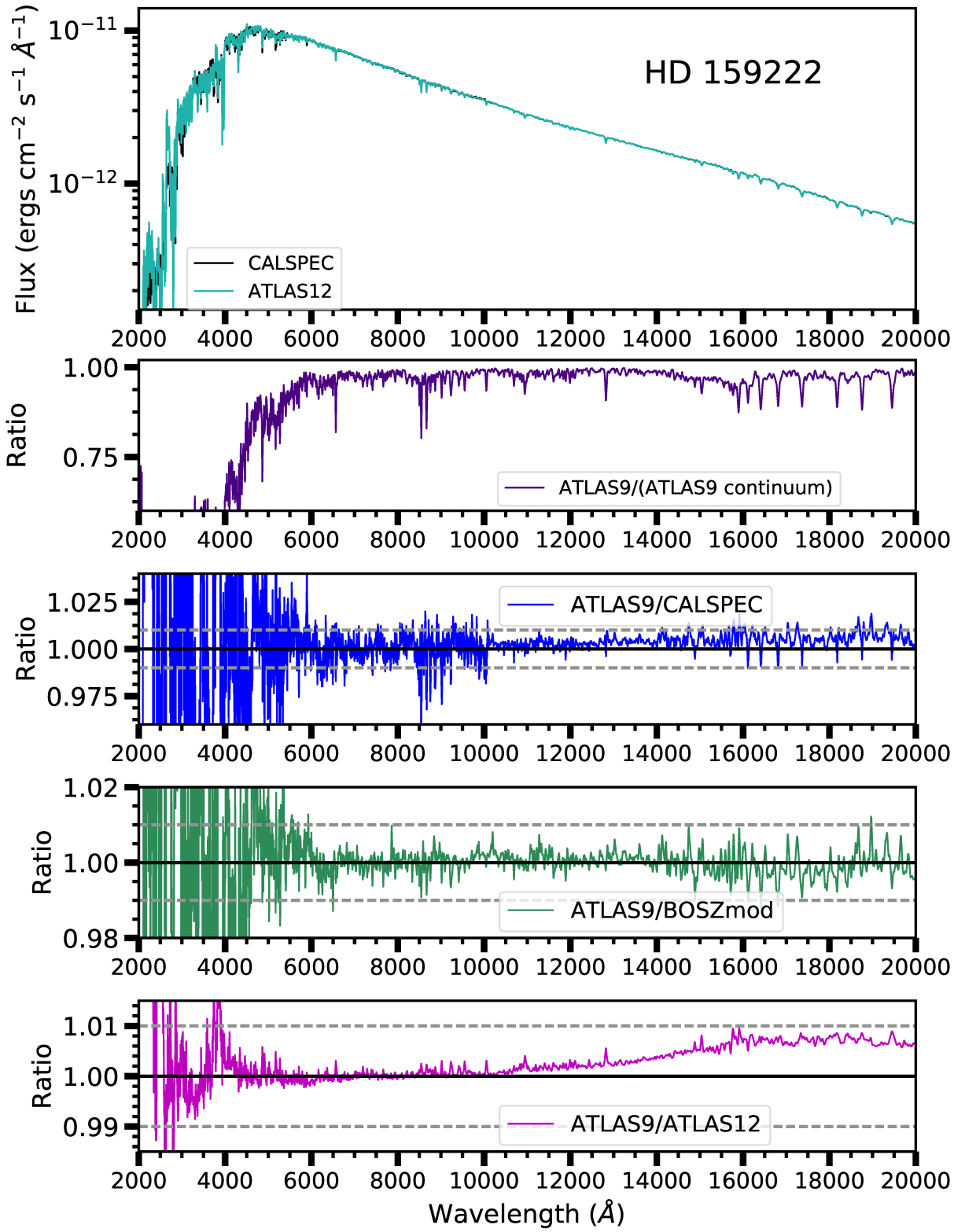

Figure 5.13: Comparison of Model spectra to CALSPEC data, for stellar target HD 159222. From top to bottom: **1.** Overplot of CALSPEC data with best-fit ATLAS9 model. **2.** Best-fit ATLAS9 model, continuum normalized. **3.** Ratio between best-fit ATLAS9 model and CALSPEC data. **4.** Ratio between best-fit ATLAS9 model and best-fit BOSZ model from [Bohlin et al. (2017)]. **5.** Ratio between best-fit ATLAS9 model and best-fit ATLAS12 model.

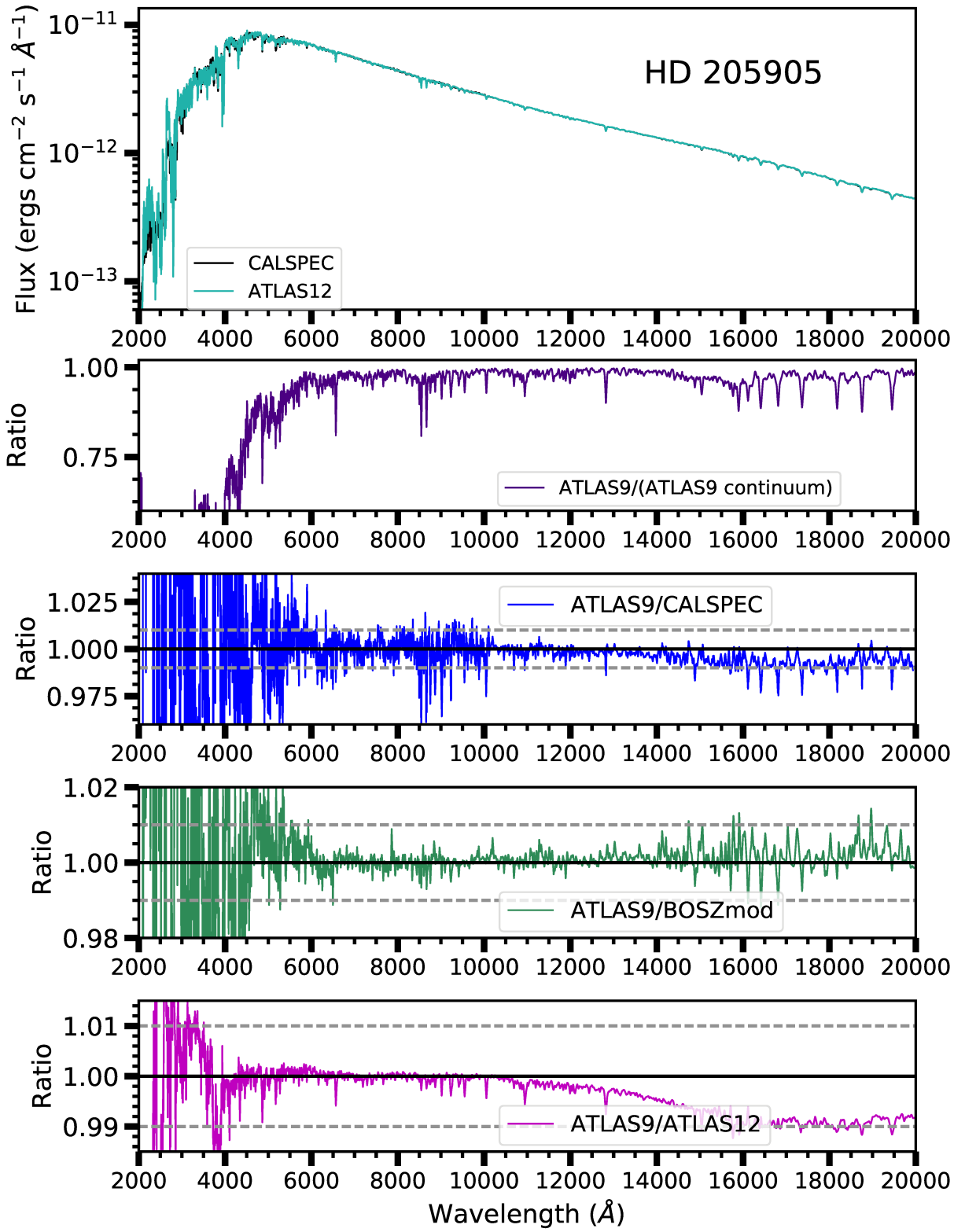

Figure 5.14: Comparison of Model spectra to CALSPEC data, for stellar target HD 205905. From top to bottom: **1.** Overplot of CALSPEC data with best-fit ATLAS9 model. **2.** Best-fit ATLAS9 model, continuum normalized. **3.** Ratio between best-fit ATLAS9 model and CALSPEC data. **4.** Ratio between best-fit ATLAS9 model and best-fit BOSZ model from [Bohlin et al. (2017)]. **5.** Ratio between best-fit ATLAS9 model and best-fit ATLAS12 model.

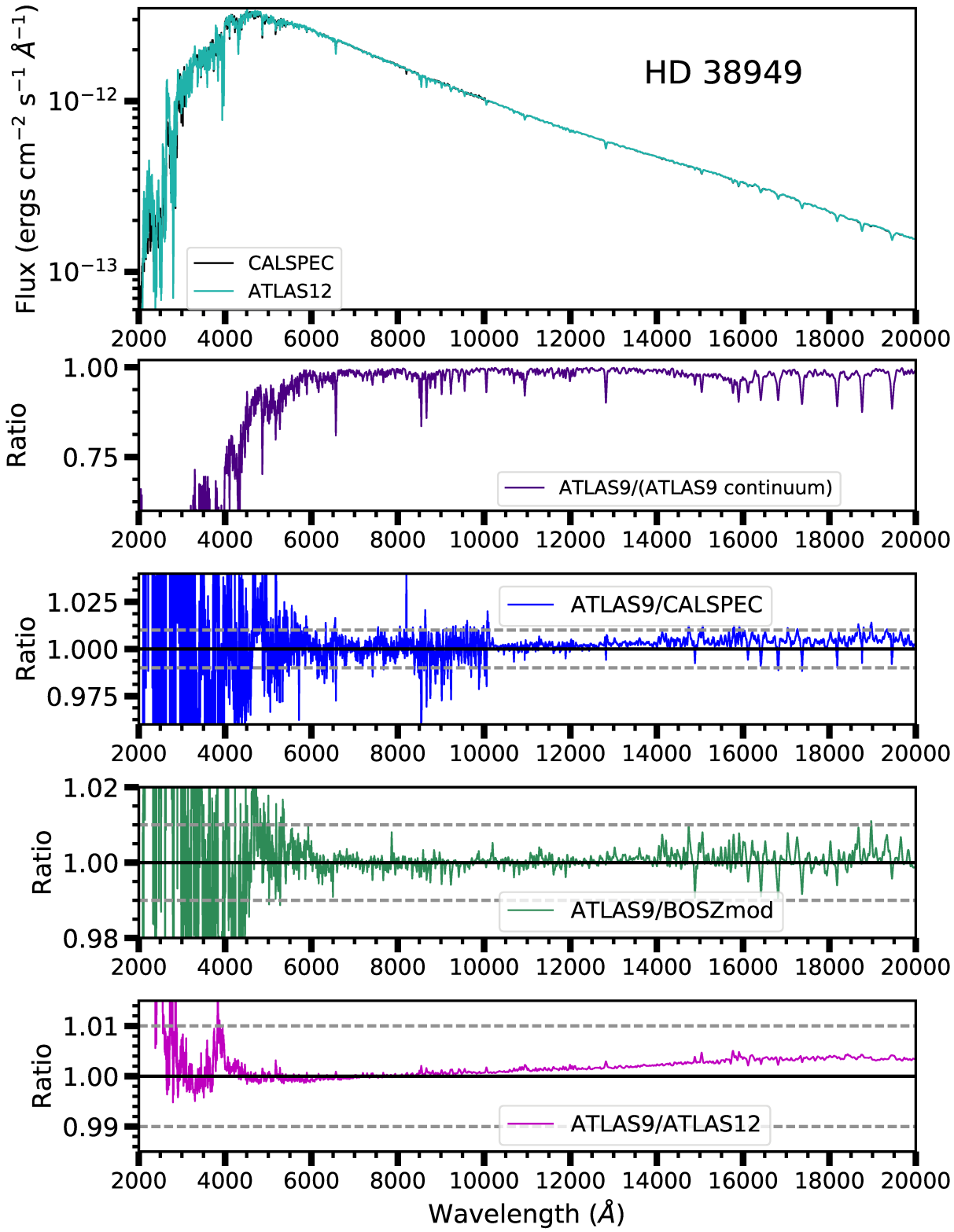

Figure 5.15: Comparison of Model spectra to CALSPEC data, for stellar target HD 38949. From top to bottom: **1.** Overplot of CALSPEC data with best-fit ATLAS9 model. **2.** Best-fit ATLAS9 model, continuum normalized. **3.** Ratio between best-fit ATLAS9 model and CALSPEC data. **4.** Ratio between best-fit ATLAS9 model and best-fit BOSZ model from [Bohlin et al. (2017)]. **5.** Ratio between best-fit ATLAS9 model and best-fit ATLAS12 model.

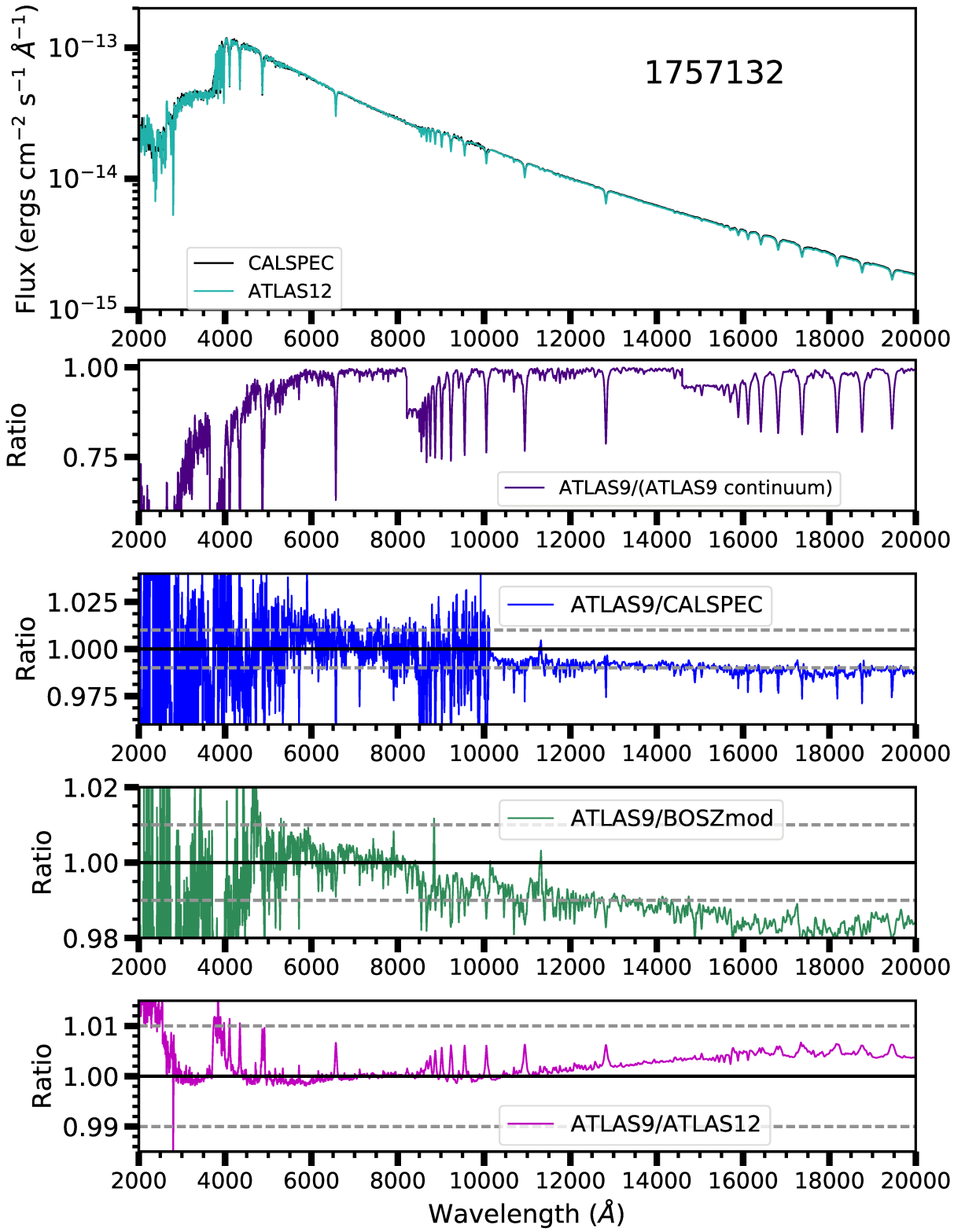

Figure 5.16: Comparison of Model spectra to CALSPEC data, for stellar target 1757132. From top to bottom: **1.** Overplot of CALSPEC data with best-fit ATLAS9 model. **2.** Best-fit ATLAS9 model, continuum normalized. **3.** Ratio between best-fit ATLAS9 model and CALSPEC data. **4.** Ratio between best-fit ATLAS9 model and best-fit BOSZ model from [Bohlin et al. (2017)]. **5.** Ratio between best-fit ATLAS9 model and best-fit ATLAS12 model.

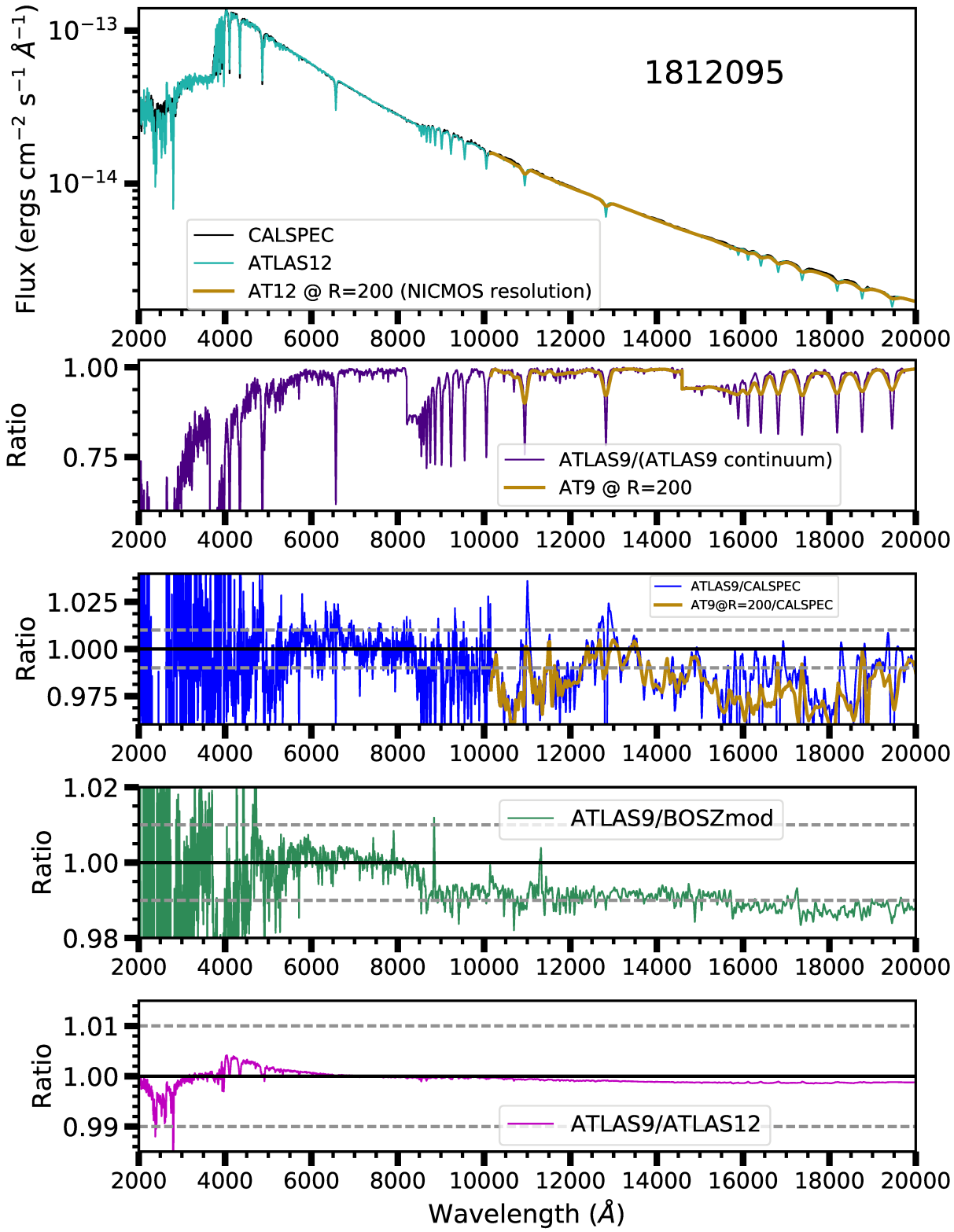

Figure 5.17: Comparison of Model spectra to CALSPEC data, for stellar target 1812095. From top to bottom: **1.** Overplot of CALSPEC data with best-fit ATLAS9 model. **2.** Best-fit ATLAS9 model, continuum normalized. **3.** Ratio between best-fit ATLAS9 model and CALSPEC data. **4.** Ratio between best-fit ATLAS9 model and best-fit BOSZ model from [Bohlin et al. (2017)]. **5.** Ratio between best-fit ATLAS9 model and best-fit ATLAS12 model. **NB:** Gold data in plots 1,2, and 3 are the same dataset smoothed to the NICMOS resolution.

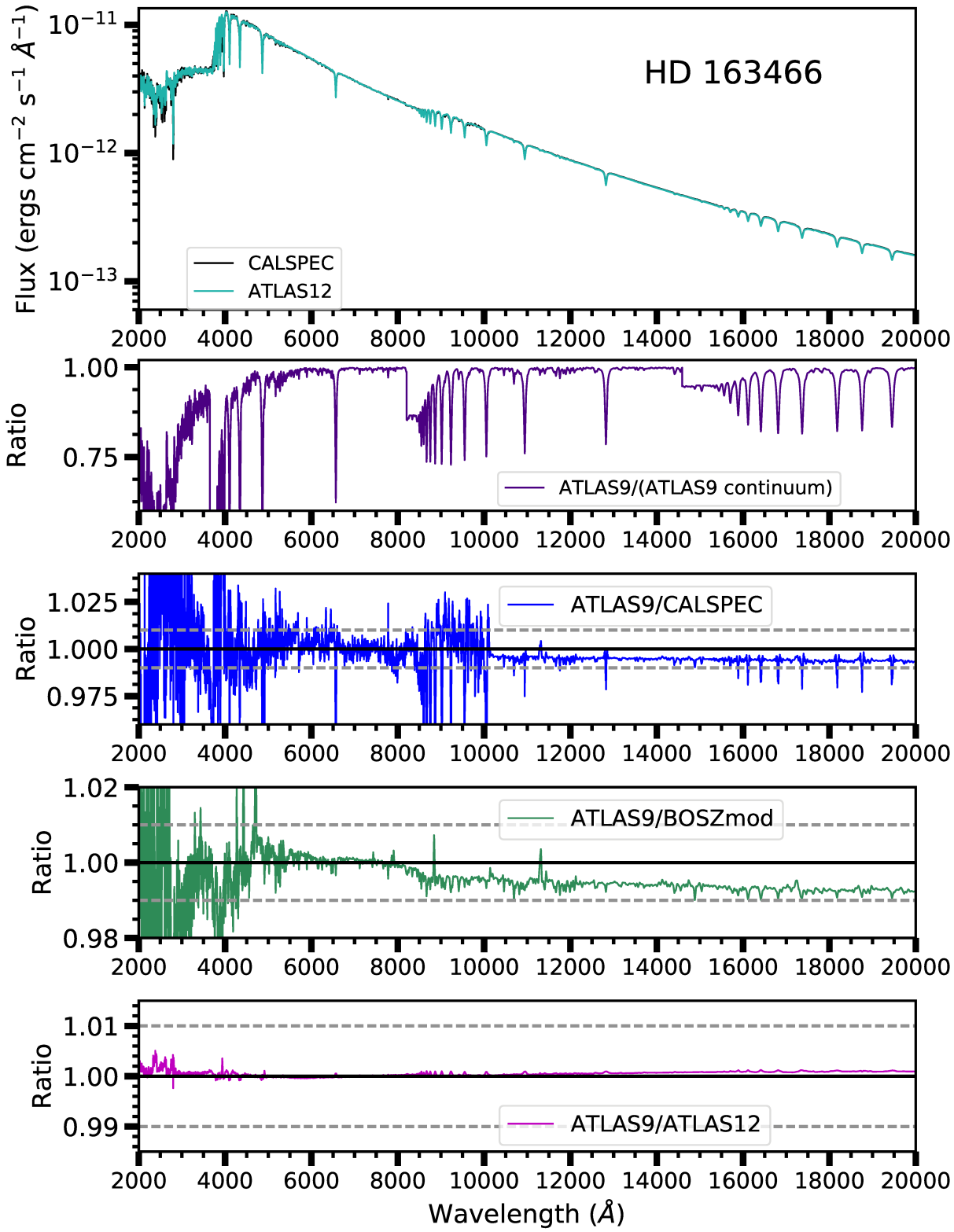

Figure 5.18: Comparison of Model spectra to CALSPEC data, for stellar target HD 163466. From top to bottom: **1.** Overplot of CALSPEC data with best-fit ATLAS9 model. **2.** Best-fit ATLAS9 model, continuum normalized. **3.** Ratio between best-fit ATLAS9 model and CALSPEC data. **4.** Ratio between best-fit ATLAS9 model and best-fit BOSZ model from [Bohlin et al. (2017)]. **5.** Ratio between best-fit ATLAS9 model and best-fit ATLAS12 model.

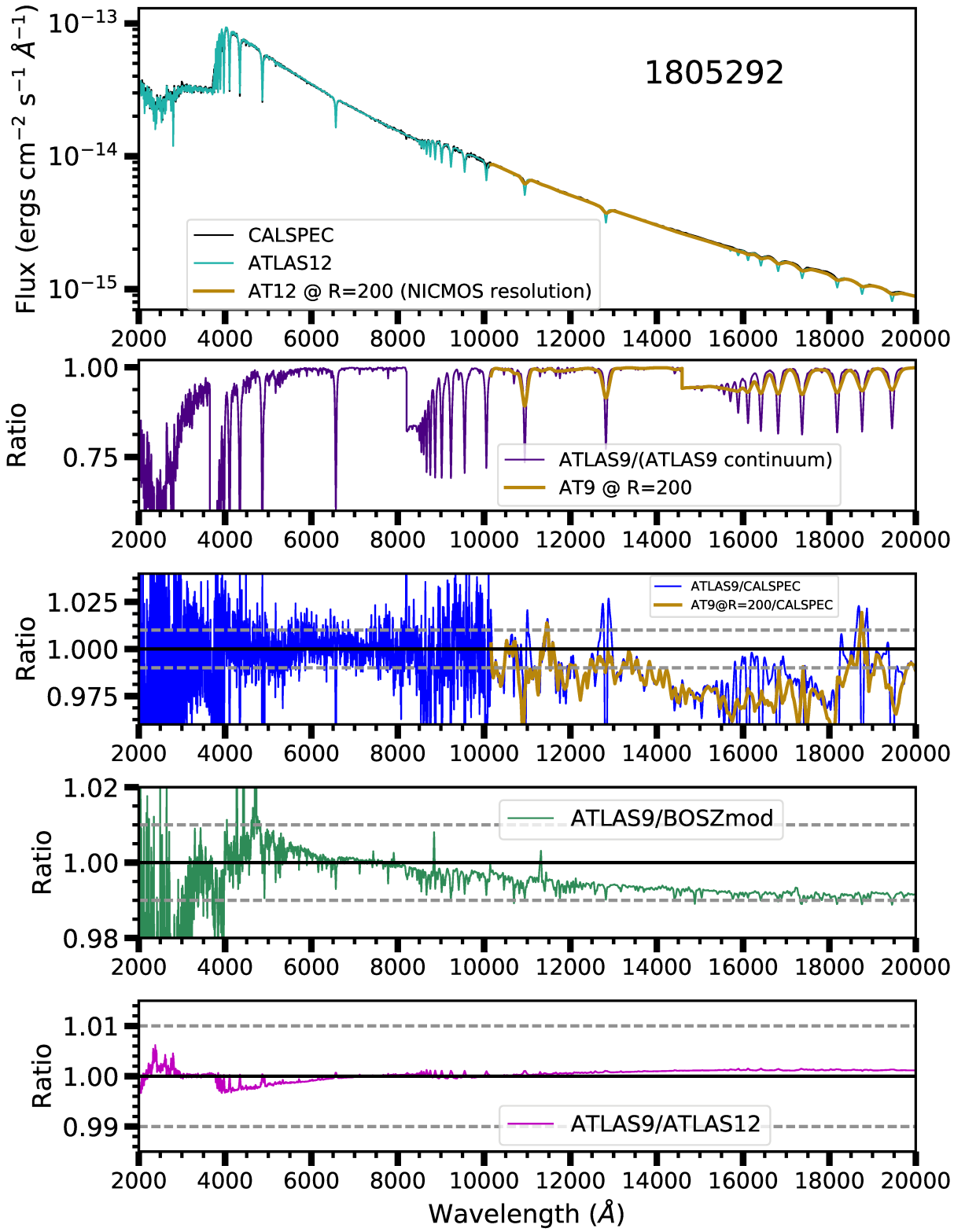

Figure 5.19: Comparison of Model spectra to CALSPEC data, for stellar target 1805292. From top to bottom: **1.** Overplot of CALSPEC data with best-fit ATLAS9 model. **2.** Best-fit ATLAS9 model, continuum normalized. **3.** Ratio between best-fit ATLAS9 model and CALSPEC data. **4.** Ratio between best-fit ATLAS9 model and best-fit BOSZ model from [Bohlin et al. (2017)]. **5.** Ratio between best-fit ATLAS9 model and best-fit ATLAS12 model. **NB:** Gold data in plots 1,2, and 3 are the same dataset smoothed to the NICMOS resolution.

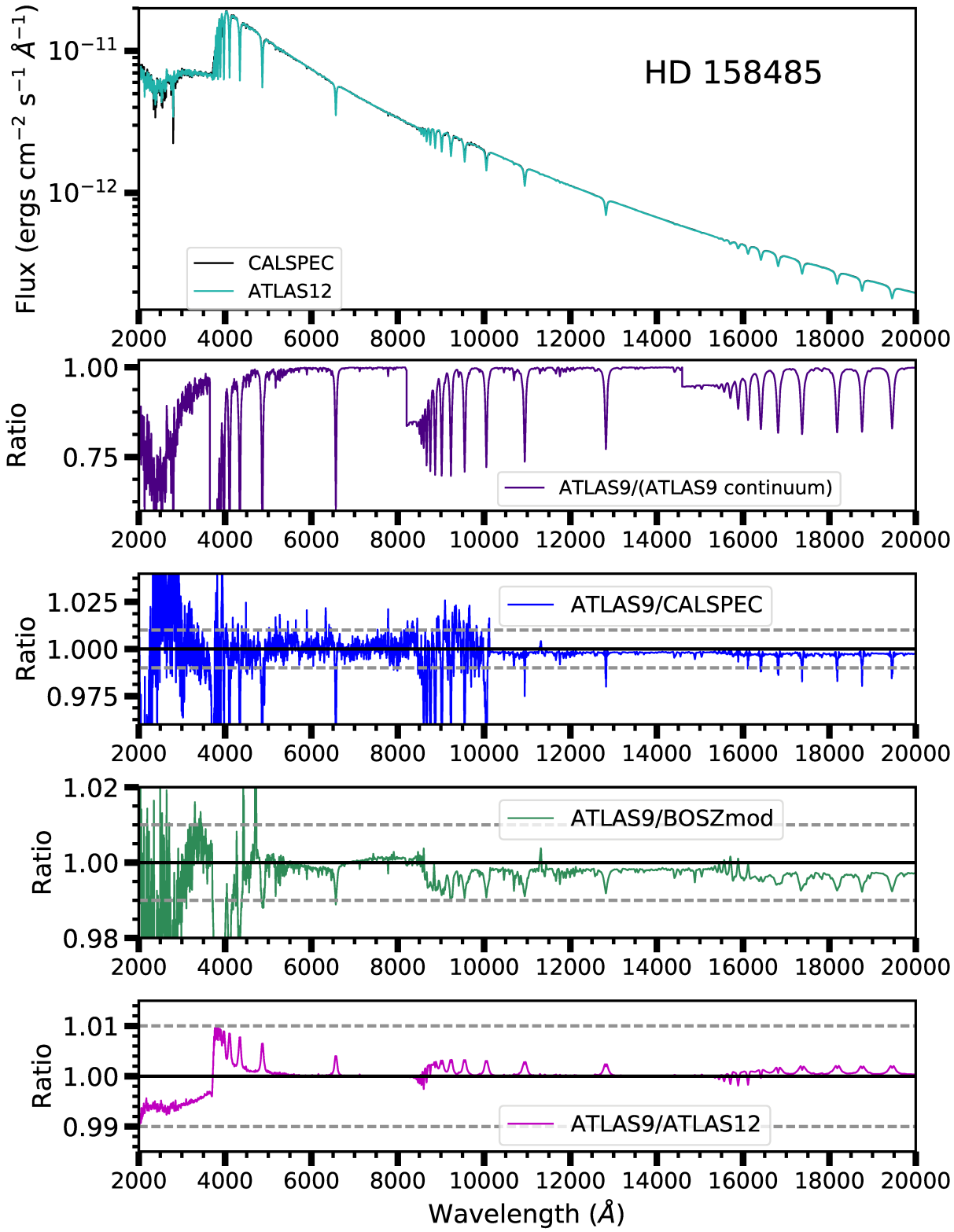

Figure 5.20: Comparison of Model spectra to CALSPEC data, for stellar target HD 158485. From top to bottom: **1.** Overplot of CALSPEC data with best-fit ATLAS9 model. **2.** Best-fit ATLAS9 model, continuum normalized. **3.** Ratio between best-fit ATLAS9 model and CALSPEC data. **4.** Ratio between best-fit ATLAS9 model and best-fit BOSZ model from [Bohlin et al. (2017)]. **5.** Ratio between best-fit ATLAS9 model and best-fit ATLAS12 model.

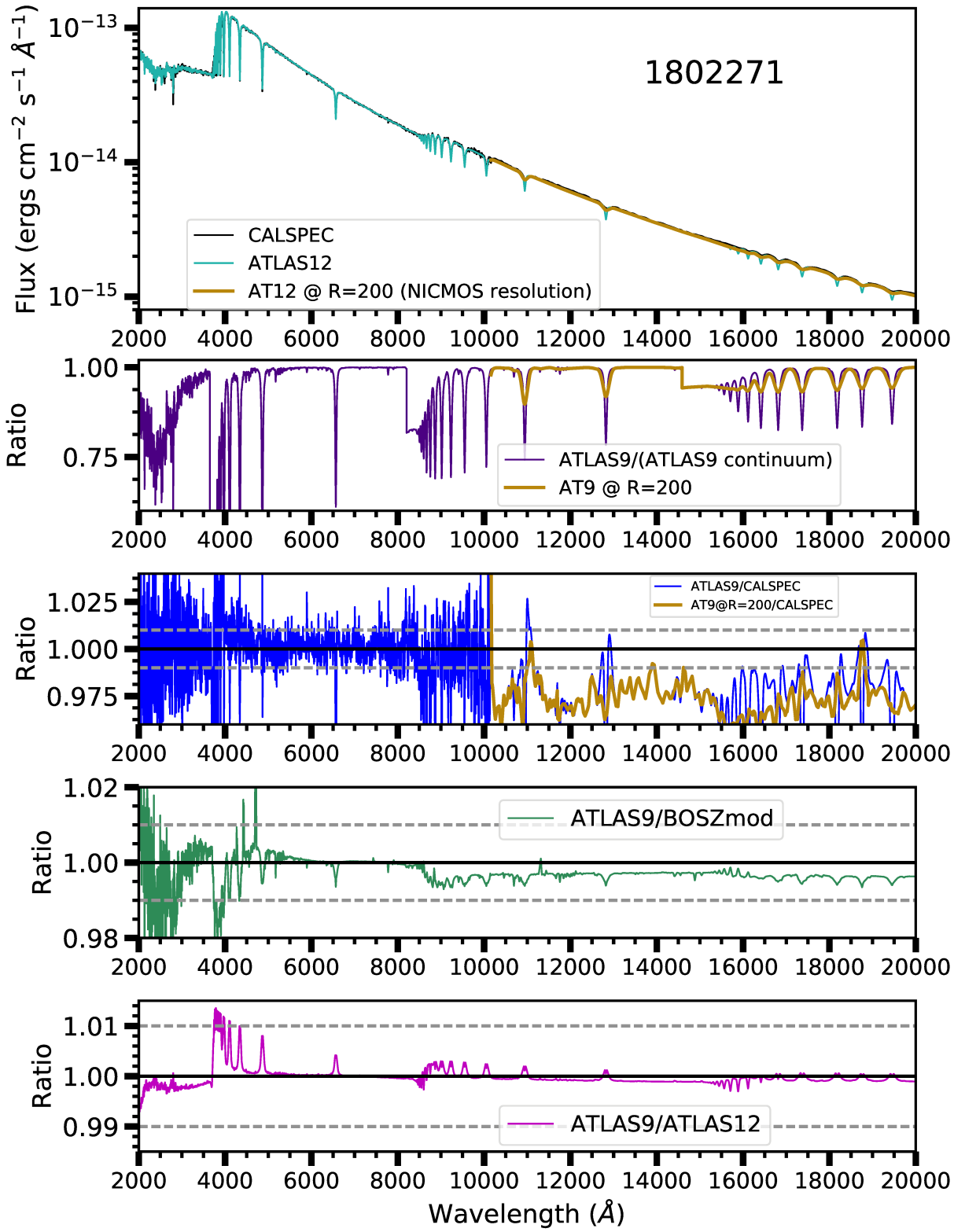

Figure 5.21: Comparison of Model spectra to CALSPEC data, for stellar target 1802271. From top to bottom: **1.** Overplot of CALSPEC data with best-fit ATLAS9 model. **2.** Best-fit ATLAS9 model, continuum normalized. **3.** Ratio between best-fit ATLAS9 model and CALSPEC data. **4.** Ratio between best-fit ATLAS9 model and best-fit BOSZ model from [Bohlin et al. (2017)]. **5.** Ratio between best-fit ATLAS9 model and best-fit ATLAS12 model. **NB:** Gold data in plots 1,2, and 3 are the same dataset smoothed to the NICMOS resolution.

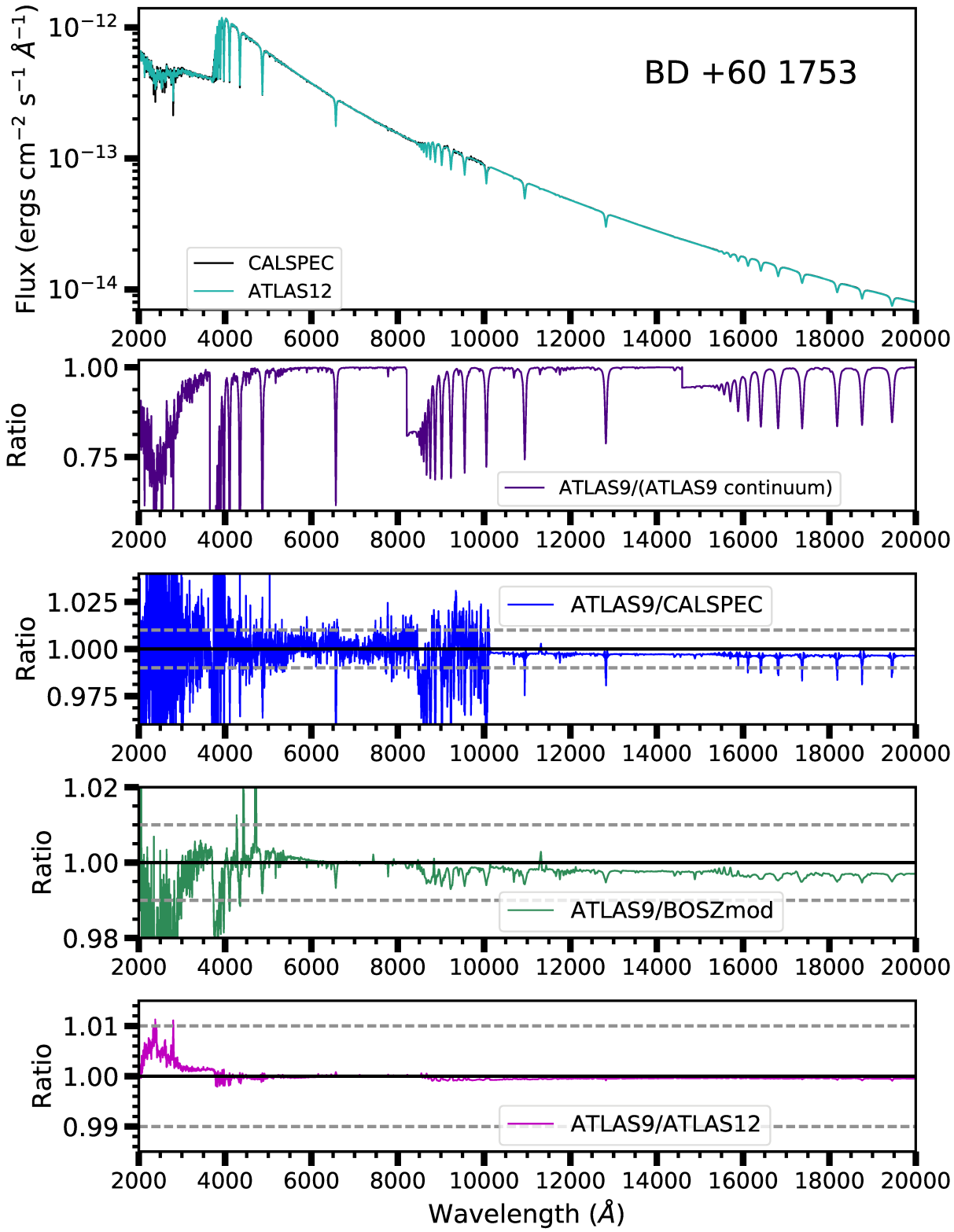

Figure 5.22: Comparison of Model spectra to CALSPEC data, for stellar target BD +60 1753. From top to bottom: **1.** Overplot of CALSPEC data with best-fit ATLAS9 model. **2.** Best-fit ATLAS9 model, continuum normalized. **3.** Ratio between best-fit ATLAS9 model and CALSPEC data. **4.** Ratio between best-fit ATLAS9 model and best-fit BOSZ model from [Bohlin et al. (2017)]. **5.** Ratio between best-fit ATLAS9 model and best-fit ATLAS12 model.

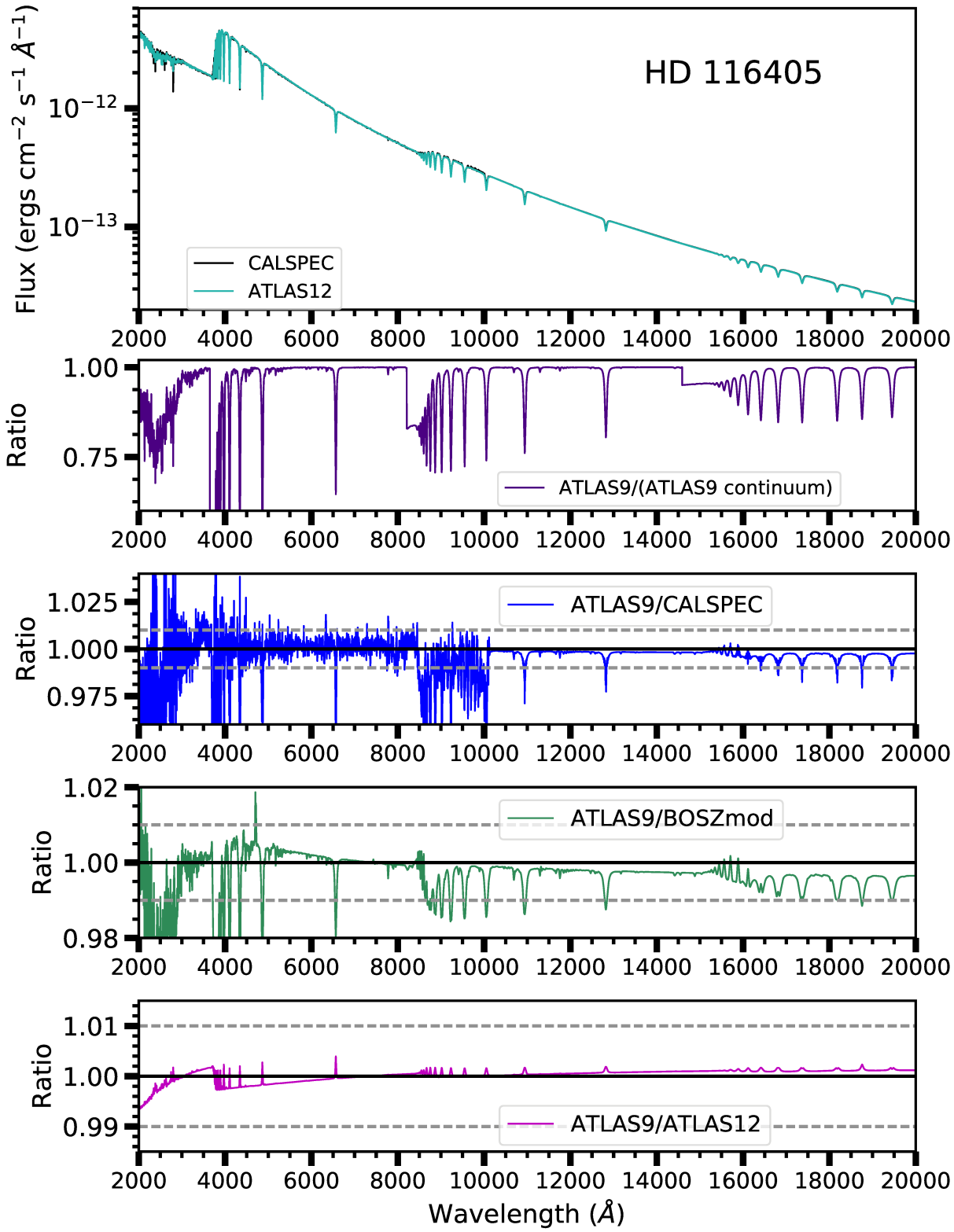

Figure 5.23: Comparison of Model spectra to CALSPEC data, for stellar target HD 116405. From top to bottom: **1.** Overplot of CALSPEC data with best-fit ATLAS9 model. **2.** Best-fit ATLAS9 model, continuum normalized. **3.** Ratio between best-fit ATLAS9 model and CALSPEC data. **4.** Ratio between best-fit ATLAS9 model and best-fit BOSZ model from [Bohlin et al. (2017)]. **5.** Ratio between best-fit ATLAS9 model and best-fit ATLAS12 model.

Chapter 6

The ACCESS Payload

My contributions to the ACCESS payload and ground experiment consist of software development for the detector controller data acquisition and the data pipeline, integration of segments of the payload telescope and spectrograph, modification to the flight computer housing module that contains the detector controller interface board, design of an electronics housing for the battery charger circuit board, thermal vacuum testing of the detector controller and flight computer, thermal monitor module Labview interface and control for ground tests, modification to the blank-off shutter and the addition of a baffle for the cryogenic laboratory dewar, operation or test of various ground support equipment items (e.g. monochromator, filter wheel, Quartz Tungsten Halogen lamp with its radiometrically controlled power supply), contributions to the ACCESS Lab's Labview control program,and implementing the ACCESS wiring harness design ([Kaiser et al. (2017)], and private communication) as an AutoCad drawing.

These contributions are described more fully in Chapters 6, 7, and 8.

As mentioned briefly above, I made the following contributions to the ACCESS payload development:

- The development of flight software for the detector to enable specifying exposure patterns, reading out the detector and writing the data to an on-board flight computer (Sec. 7.1).
- Making modifications to the flight computer housing module (Sec. 6.6), that contains a detector controller printed circuit board.
- Designing the electronics housing for the battery charger printed circuit board (Sec. 6.7).
- Thermal vacuum testing for the detector controller and flight computer (Sec. 6.5, 6.6, & 7.4)

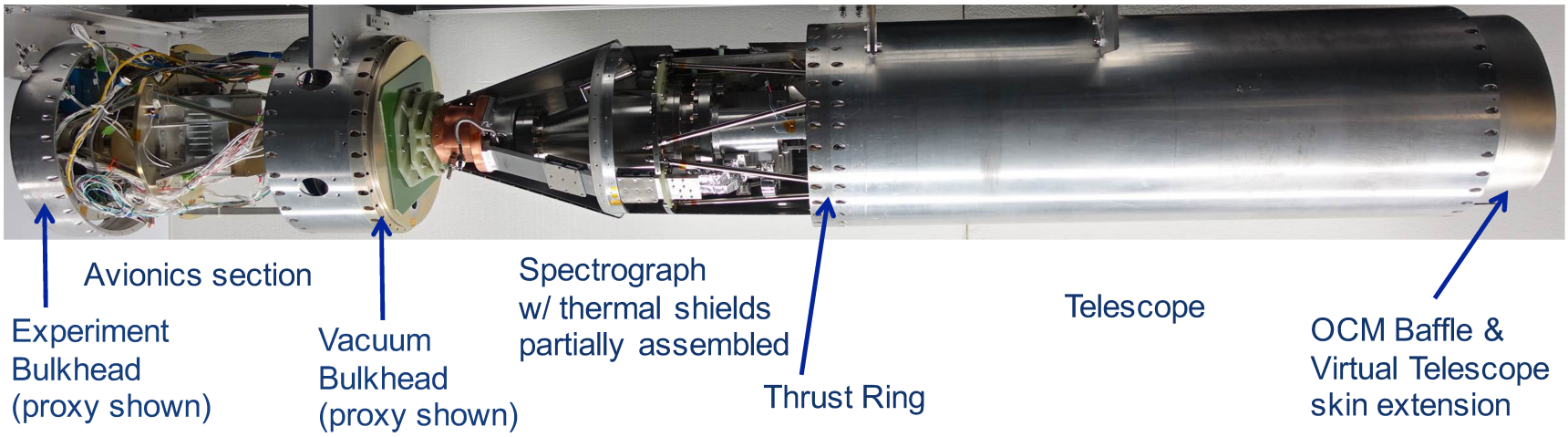

Figure 6.1: The ACCESS payload.

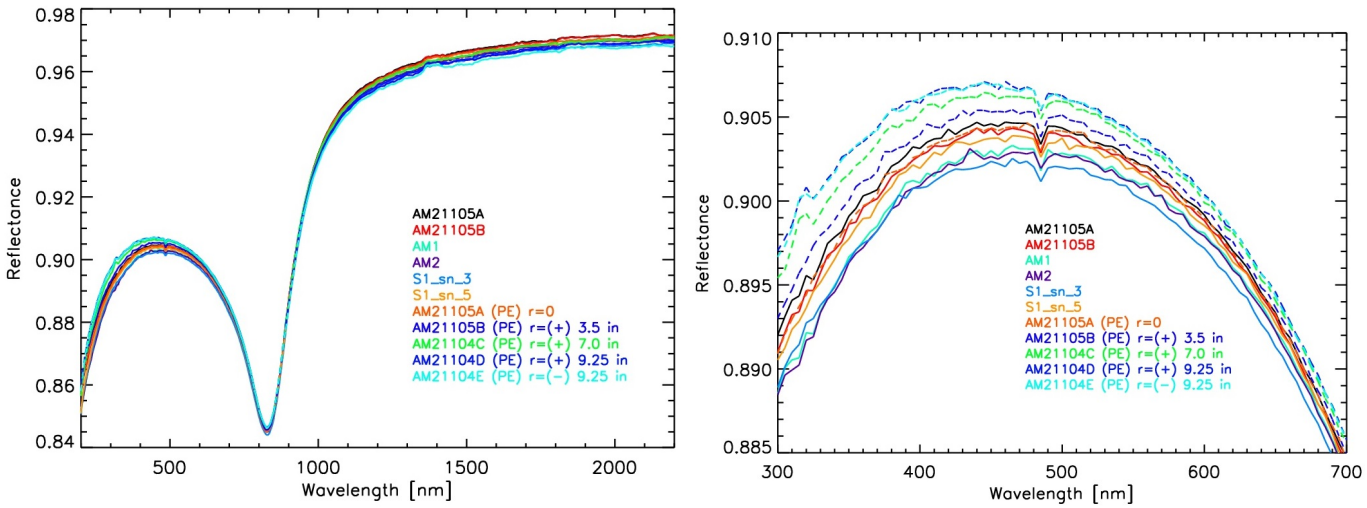

Figure 6.2: Reflectivity measure of Primary mirror coating, measured at various radii [Kaiser et al. (2012)]. Feature at 800 nm is aluminum absorption feature

6.1 Telescope

The ACCESS telescope is a f/15.7 Dall-Kirkham Cassegrain design, with an ellipsoid primary and a spherical secondary. The primary mirror is coated with magnesium fluoride over aluminum. The primary mirror is composed of Zerodur, a form of glass with a very low coefficient of thermal expansion. The telescope mirrors and optical bench have flown on previous rocket flights. The ACCESS program examined the primary and secondary mirror figure, stripped the old coating, and had the mirrors recoated with Al with a MgF_2 overcoat (see Fig. 6.2). The primary mirror has a 15.5 inch diameter.

6.2 Spectrograph

The ACCESS spectrograph is configured as a low order echelle. The ACCESS echelle instrument is composed of two diffractive elements, a grating and a cross-dispersing prism. The light dispersed by the grating is imaged onto the detector, but the spectral images overlap according to the grating equation where $m\lambda = constant$. The prism disperses the spectra perpendicular to the grating dispersion, separating overlapping orders of light and enabling multiple spectra to be imaged without confusion upon a single detector. Thus three spectral orders (m) of light spanning the wavelength region extending from 0.350 to 1.7 μm are dispersed and imaged on the detector. These three orders span the following wavelength ranges: 0.9 to 1.9 μm, 0.45 to 0.95 μm, and 0.3 to 0.63 μm [Kaiser et al. (2008)]. Each image receives the full spectral data from 0.35 to 1.7 μm. The signal overlap provides a crosscheck and ensures spectral continuity.

The telescope focuses the star field onto an angled mirrored plate, with a 1mm aperture at the center. The aperture itself sits at the telescope focus. The region surrounding the target reflects off the angled mirrored plate and transfer optics relay the starfield to a Xybion video camera. The surrounding star field is used for maintaining the pointing direction of the telescope guiding, keeping the target star in the aperture. The aperture structure is housed within a cold baffle box, to minimize the thermal background. A motor positions a cold flag shutter in front of the spectrograph to acquire blank-off exposures of the thermal optical (dark) background.

Downstream of the target aperture plate, at the telescope focus, is a fused silica window that provides the vacuum seal for the spectrograph.

After passing through the window, the light is incident upon a concave diffraction grating. The grating is a Rowland circle grating, diffracting the source into a wavelength-dispersed image along a defined radius [Rowland (1882)]. The grating has a Rowland circle of 400 mm diameter, and has a

ruling density of 45 lines per millimeter. It is coated with Silicon oxide. The grating is mounted to the spectrograph optical bench using a modified hexapod structure within the spectrograph vacuum housing. It is held within a kinematic mount, via a flexing retaining ring [Kaiser et al. (2017)].

The final optical element before the detector is a cross-dispersing Fery prism, composed of LLF1 glass. A Fery prism is different than conventional prisms in that one or more surface is curved [Fery (1911)]. In this manner, the prism provides both dispersion, and imaging. The prism separates the overlapping orders of light from the grating in the cross-dispersion direction. This cross-dispersed spectra is then incident on the detector.

The spectrograph optical components are contained within the spectrograph housing. The housing is evacuated and this evacuated housing is mounted to the rear of the primary mirror mount. The telescope and spectrograph housing are mounted inside a rocket skin. The entire interior of the rocket skin housing the telescope and spectrograph is also evacuated.

6.3 Spectrograph Cooling System

In order to maintain a low thermal background, the ACCESS spectrograph is cooled by trickle-feeding liquid nitrogen through a large copper thermal mass. This mass is connected to a set of pure aluminum cold arms, straps, and block, which cool the detector, detector housing, and baffle box.

The detector itself is also connected to a Stirling cooler coldfinger via a flexible cold strap, for cooling the detector. The cooler, made by Ricor, is a K508N integral Stirling cooler that can provide 1/2 watt of cooling power. The Stirling cooler motor is connected to a container of phase change material, to prevent thermal runaway of the cooler motor.

Two layers of conical and cylindrical shielding composed of thin sheets of aluminum will surround the entire spectrograph, to further protect the detector from thermal radiation. The inner heat

shields are connected to the spectrograph support structures and cooled, but the outer heat shields are thermally separated by G10 washers [Kaiser et al. (2013b, 2017)].

Thermal modeling has been performed for the spectrograph system yielding a temperature less than 160 K for the detector radiation shield and validating the thermal design [Kaiser et al. (2013b, 2017)], so as not to add thermal noise to the science data.

Connected to the two aluminum cold arms are four pairs of wire mesh boxes containing a zeolite cryogetter. Zeolite is a highly porous material. As a result, it has a very large surface area per unit volume that readily adsorbs gas. Heating zeolite will cause it to release the gas that is adsorbed. Once the zeolite is once again brought to cryogenic temperatures, it will again adsorb gas, and bind it to its own structure. In this manner, it behaves as a sorption pump, which complements the pumping systems already being used on the spectrograph.

The cooling system is described in greater detail in [Kaiser et al. (2013a)].

6.4 Detector

The detector is a 1024X1024X18 µm FPA (focal plane array) composed of mercury cadmium telluride (HgCdTe), known as a HAWAII-1R (H1R). In a typical CCD, an image is read out by moving the charge from the pixels out to a circuit, which will read each pixel's charge sequentially, as the charge passes through the circuit. However, because the pixel charge is moved as it is read, a CCD's image information is destructively read, removing the image information from the detector as it is read. The flux rate must then be inferred from the exposure time and the count of the pixel. In an H1R, each pixel is connected to a multiplexer (MUX) array individually, so that to read the pixel data, the charge does not need to be moved along the detector to be read out. Detectors configured in this manner perform non-destructive readouts. The ACCESS detector can therefore observe a target,

reading out the image multiple times during a single observation, and calculating the flux from the count rate between successive images.

The pixels read out 16 bit data, running from 0 to 65535. 65535 is the measurement of DN's (data numbers) at which the pixels are said to be saturated, i.e. the signal viewed is brighter than the detector can process. Even below saturation levels, high signal rates can damage the detector and produce residual signal in later images (this phenomenon is known as "persistence", and has been measured and quantified for this style of detector). DN's are electronic units, and are a measure of electrons produced by the photoelectric effect, and must be converted to a physical unit to express the signal in terms of flux.

Built by Teledyne Imaging Sensors, the ACCESS H1R flight detector is from the same flight build procurement as the detector installed in the Hubble Space Telescope, as part of the Wide Field Camera 3. It has 1024X1024 pixels, with pixel height and width of 18 μm. The outer 5 columns and rows are reference pixels, so as to monitor thermal drift and low frequency noise. The cadmium zinc telluride growth substrate has been removed from these detectors, as it causes proton induced luminescence near 8000 Å. The substrate was designed to block visible light. Its removal provides the detector sensitivity to 3500 Å. The WFC3 Hawaii IR detector has a nominal operating temperature of 145 K [Hartig (2008)]. The ACCESS detector will be operated at 140 K.

The flight, flight spare, and qualification units were all obtained from Goddard Space Flight Center. They have been measured by Goddard's Detector Characterization Lab, with respect to dark current, quantum efficiency, and linearity, over a five year baseline, before being delivered. These measurements informed the selection of detectors for flight. The detector is controlled by a Leach controller, purchased from Astronomical Research Cameras.

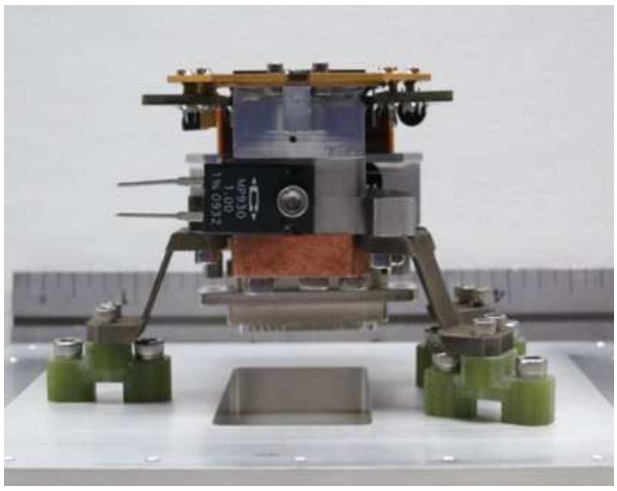

Figure 6.3: Detector view 1

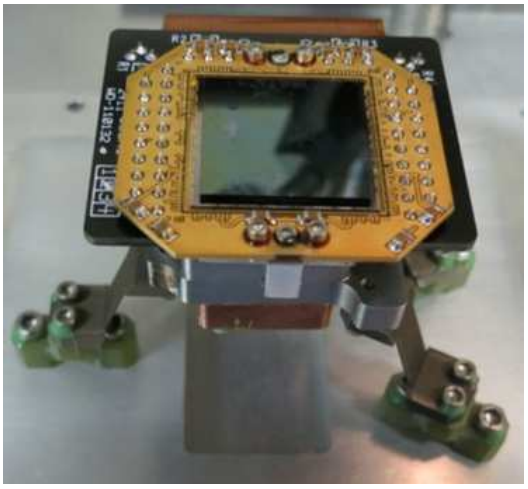

Figure 6.4: Detector view 2

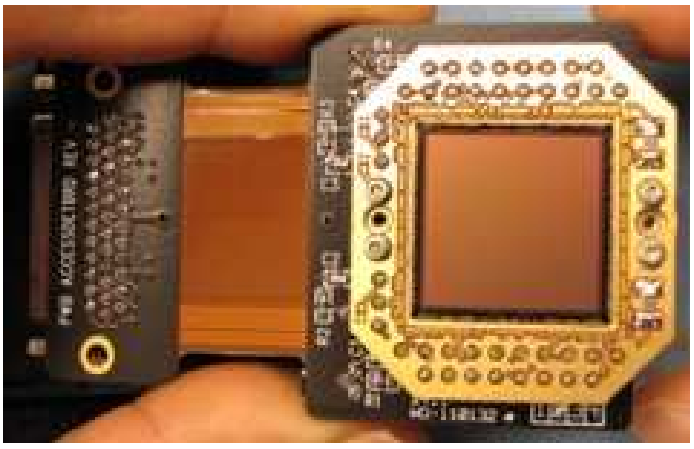

Figure 6.5: Detector view 3

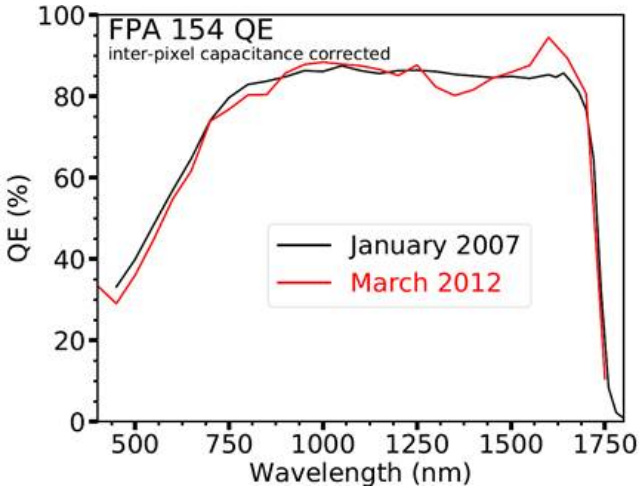

Figure 6.6: Quantum efficiency of FPA 154, as measured by the GSFC DCL

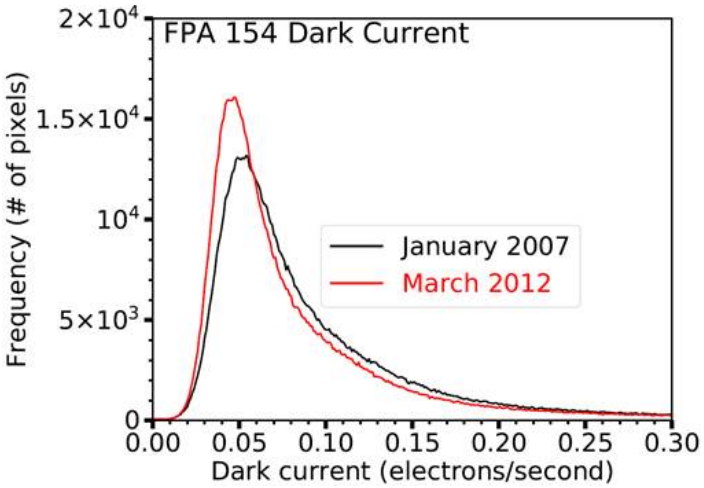

Figure 6.7: Dark current of FPA 154, as measured by the GSFC DCL

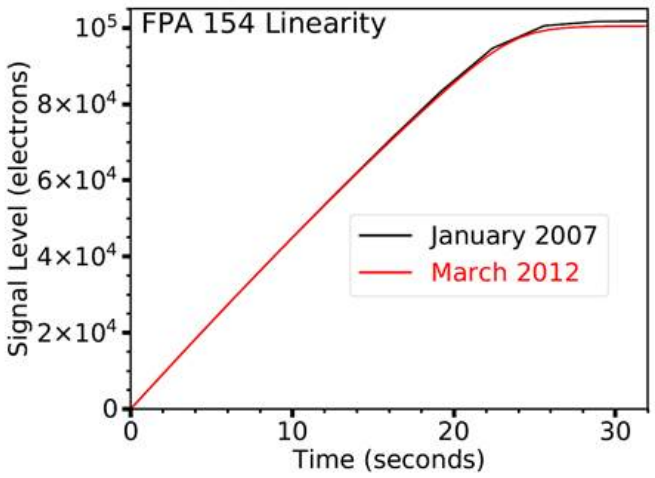

Figure 6.8: Count-rate linearity of FPA 154, as measured by the GSFC DCL

The detector is mounted on a structure tilted with respect to the telescope's axis, normal to the optical path at the spectrograph image plane. The backplane of the detector is connected to a block of molybdenum, which has a very low coefficient of thermal expansion. The detector is mounted on three titanium flexures, with g10 feet, to provide thermal isolation and accommodate the difference in coefficient of thermal expansion between the detector and the g10 feet. It is housed in several layers of shielding, with feedthroughs for cooling and electronics. Three two-phase vacuum stepper motors provided by Physik Instrumente are installed on the detector mount, to provide tip-tilt and focus for the detector. As the spectrograph cools, the distance between objects will shift, and the focus at room temperature will no longer hold at cryogenic temperatures. The detector cannot be adjusted manually once it is pumped to vacuum and cooled, and so these motors will allow automated adjustment for the detector over a limited temperature range.

6.5 Detector Controller

The ACCESS program has obtained two Gen. III Leach Controllers, a flight and flight spare. These are and will be used to power, address, and readout the HgCdTe Hawaii-1R detector in the ACCESS payload, during testing and in flight. The flight controller housing has been ruggedized and successfully tested in vacuum and in air at lengths of time greater than flight conditions (See Sec. 7.4).

The detector controller itself consists of five boards within the controller housing, and one additional board within the operating computer. The ARC-46 Video Board is an IR video processor board the provides power to the detector and reads out the array, when queried. Capable of holding eight channels total, the ACCESS boards have only four channels populated with circuitry, to interface with the four quadrants of the ACCESS detector. The ARC-32 Clock Driver Board provides the analog output clocking signal necessary to read out the array properly. The ARC-22 Timing Board provides several functions, providing communication to the host computer, generating waveform signals for the clock driver board, and monitoring the overall controller system. The ARC-22 houses an on-board digital signal processor (DSP) that performs many of the complex functions of the controller. The ARC-78 Power Control Board monitors the incoming power supply for the controller, shielding the rest of the system from over and under voltages, as well as providing the necessary voltages to the other boards. The ARC-75 Backplane board is a board used simply to interconnect the other four boards.

The final board, within the computer, is the ARC-64 PCI Interface Board. This allows the host computer to communicate with the detector controller, and allows the detector controller to transfer data back to the computer for storage. Communication between the ARC-64 and the ARC-22 is done with two 250 MHz fiber optic links, a “transmit” and “receive” on each board. These allow for a

sustained data transfer rate of 12.5 Megapixels per second. The board mates to the host computer using a traditional PCI connector.

Initially, the detector controller was operated using a GUI-based software called "IRCAM3" that was given to the ACCESS program by Goddard Space Flight Center's Detector Characterization Lab. This program is a Visual Basic based code, interfacing with the ARC PCI Controller Application Interface code, version 1.7, written by Astronomical Research Cameras, the company that produces the detector Controller. It uses the version 1.7 PCI board device driver, for Windows XP.

In flight, ACCESS will perform data acquisition, store science images in an on-board flight computer, and send the science images to the ground by telemetry with minimal user interaction. This required a rewrite of the software interface for the detector controller, and the data acquisition interface (see Ch. 7). I ported the APIs for the detector Controller from those used by IRCAM to the ACCESS lab and flight computers.

6.6 Flight Computer

For flight, ACCESS will be using an RTD IDAN model for its flight computer. This is a ruggedized, modular computer system designed to fly in harsh environments. All boards are designed in the PCI-104 format, so that they are stable, and are stacked closely together. Four IDAN modules will be flying on board.

The IDAN system contains a power supply module, to convert the battery power into several different voltages. It is designed to take an input voltage of 8-32 volts, and output power to the various computer boards. In addition, the power supply can provide output voltages of +3.3V, +5V, +12V, and -12V, through a 9-pin dsub connector.

The CPU module that is onboard is a dual-core processor running at 1.20 GHz, with a 32 Gb

flash drive onboard. The CPU is running scientific Linux, and a command-line-interface environment. This will be used to send signals to the detector controller, perform basic image processing, and store science data. Science data will be stored onboard, and sent to ground via telemetry, while the ACCESS payload is observing a target.

In order to transfer the detector data to the telemetry stack, and subsequently the ground, the last IDAN module onboard is an FPGA processor. An FPGA processor is encoded to perform one specific function with high speed and minimal user input. In this case, an embedded systems engineer programmed the FPGA to receive science data, convert it into data packets, and send the data, via a serial stream, to the payload's telemetry system. In this way, we have two systems of data retrieval, onboard and telemetry, so that data will still be recovered if one system fails.

In order to communicate with the detector controller, the ARC-64 PCI Interface board is mounted on a PCI/104 to PCI adapter bridge, mounted on the bottom of the IDAN system. It was found through testing, that the board will not operate when placed on the top of the CPU stack. The PCI form factor is different than the PCI/104 form factor, so the ruggedized housing module design was modified by me and built to house the ARC-64 board.

Tests have been performed on the CPU system and detector controller with continuous data acquisition. Both systems operate in vacuum without error for up to 4 hours, much longer than actual flight times (see fig. 7.7).

6.7 Battery and Charger

In order to power the electronic systems while in flight, the ACCESS avionics section contains a UBBL13 smart battery, made by Ultralife industries. This battery is a two cell battery, capable of providing 33 volts to the payload. In addition, a Linear Technologies smart charger board is contained

within the payload, to allow for the battery to charge while still within the payload. The battery can also be charged external to the payload.

6.8 Thermal Monitor Modules

The thermal performance of the payload is crucial to the quality of science data obtained by the ACCESS payload. To this end, two 16-channel thermal monitor boards are housed and mounted in the avionics section. These two modules are connected to 22 thermal diodes, and 10 thermistors. Thermal diodes will be used to monitor the cooled sections of the spectrograph, such as the cold arms, detector, and cold shutter. Thermistors, however, are designed to be used in positions that will reach temperatures above room temperature (thermal range of -90 to 130 Celsius). The thermistors will be placed on outer heat shielding, and components expected to heat up from flight. Combined, the thermal diodes and thermistors will monitor the payload to determine if the cooling systems operate as predicted. The thermal monitor boards will condition these measure voltage for transmission to the onboard telemetry stack, and then these signals are subsequently transmitted by the on-board antenna to the ground.

6.9 Onboard Calibration Monitor

An important factor to consider is how much the telescope's sensitivity will change from the time the telescope was calibrated until it observes its targets. To correct for any calibration drift that may occur over this time period, the ACCESS payload is outfitted with an Onboard Calibration Monitor (OCM). The OCM consists of a ring of 16 LEDs spanning the ACCESS bandpass. Two LEDs of eight different colors are mounted around the star tracker system, which is mounted at the

rear of the secondary mirror in the telescope section. The LEDs were chosen for their wavelengths, brightness, and wide angle of illumination. The power output of the LEDs will be measured by a monitoring photodiode while in use. These LEDs illuminate a teflon diffuser mounted on the interior of the telescope (payload) vacuum shutter door [Kaiser et al. (2017)]. The diffuser was designed to be completely out of the optical path of the telescope (so as not to vignette any stray light) during stellar observations, and not interfere with the opening and closing mechanisms of the shutter door.

While the payload is parachuting to the ground with the shutter door closed, the LEDs will illuminate the diffuser. The light will scatter off the diffuser through the telescope and spectrograph and be imaged on the detector. By simultaneously taking detector data, and controlling the brightness of the LEDs with the photodiodes, it is possible to determine whether sensitivity of the payload has changed. Because the LEDs span the ACCESS bandpass, it will be possible to determine if any changes are wavelength dependent as well [Kruk et al. (2008)].

6.10 Telemetry

Communication with the payload, while in flight, will be performed by a Physical Science Laboratory (PSL) Model WFF93 Pulse Coded Modulation (PCM) Encoder. This encoder is provided by Wallops Flight Facility. It includes several modules:

1. A video downlink module will transmit data from the Xybion video camera.

2. A synchronous serial deck with four LVDS (low-voltage differential signaling) input ports will be used to receive science data from the flight computer.

3. A command deck will transmit command words sent from the ground station to the flight computer.

4. Two analog-to-digital converter modules will receive analog housekeeping signals and convert them to digital signals for transmission to the ground. The analog housekeeping includes voltage signals from the LEDs/OCM

5. A timer deck is used to operate the flight battery, cryo-shutter, and OCM

6. Additional power and timing decks for NSROC subsystems (shutter door, star tracker).

6.11 Coarse and Fine Guidance Systems

Provided by NSROC, the ACCESS payload will be outfitted with an ST5000 Star tracker, sitting ahead of the secondary mirror, and co-aligned with the telescope. This star tracker has a field of view of 5.4 X 7.4 degrees. It is initially used to determine the location of the telescope and identify the starfield prior to science observations. During observations, the star tracker will be used to maintain the pointing of the telescope. The noise equivalent angle of the star tracker is 0.8 arcseconds.

For fine guidance, the mirrored aperture plate at the telescope focus reflects the starfield about the target star to reimaging optics which relay the image to a Xybion video camera, which then transmits a live feed of the target field to a user on the ground, who can provide real-time guidance of the target in the aperture and manually correct any tracking drift.

Chapter 7

Detector Software & Data Acquisition

7.1 Detector Control

When the detectors were delivered to ACCESS, the main program used to run tests was a GUI-based Visual basic program, developed by Yiting Wen at the Goddard Space Flight Center's Detector Characterization Lab. This code was used to interface with the detector controller's native assembly code. This software was initially used to test the detectors within the ground characterization dewar, and confirm that signal could be received, and the dewar could provide sufficient thermal radiation shielding for the detector. Though very useful for diagnostic tests, this code was not usable for flight, as it was developed for Windows XP, a different operating system than the flight computer. Additionally, the flight computer operates purely from a command line interface version of Scientific Linux, and so new code needed to be developed. The flight computers require two different programs. The first is a command line software with high versatility, for usage in the lab. This program is used to perform tests and determine the optimal exposure pattern for flight. In flight, however, the software needs to operate with high automation, as it is critical to send as few commands as possible to the flight computer while in flight. This second program will also require any and all exposures to

be saved to the flight computer and sent to the ground station via telemetry, and therefore will need to interface with the flight computer's FPGA.

The detector is controlled and images are obtained using a C++ program, incorporating the controller application library, which was also written in C++. This program is capable of loading code into the controller's DSP, modifying voltage settings to optimize performance (such as the bias voltage for individual detector quadrants, and the detector reset voltage), varying exposure time and specifying the exposure pattern (e.g. sampling up-the-ramp) for the detector, deinterlacing the serial datastream sent from the detector into a four quadrant image, and saving the images to FITS files in a data-cube format.

Initially, before any complex operations with the detector controller can commence, the controller must be connected to the PCI board. Commands are sent and data received using a pair of fiber optic cables. Before communicating with the detector, the controller draws ~ 0.45 amps at 24 V.

Then, the PCI board must be addressed, and two ".lod" files must be uploaded to the ARC-64 and the ARC-22. These are programs, initially written in assembly language, tell the board how to decode basic commands from the user, and how to perform those commands. These ".lod" files are also provided by GSFC DCL. Once uploaded, the detector controller draws approximately 1.1 amps.

The ".lod" file being used for the ARC-22 timing board, when uploaded, requires a few values to be updated upon controller setup. Firstly, the detector's dimensions must be sent; in our case, the H1R detectors are 1024 rows by 1024 columns. These are coded into the "NCOLS" and "NROWS" variable definitions. Additionally, the controller must know the dimensions of each section that an individual Video Board channel addresses, so that it may loop through the rows at the proper points. Because the Video Board loops over one quadrant per channel, the "LCOLS" and "LROWS" variables must be set to 512. These can be hard-coded within the ".lod" files, by modifying a set of provided

".asm" files, and running a batch command that encodes them into an updated ".lod" file for the timing board.

Memory within the host computer must be allocated to hold the image buffer after it is readout, but before it is saved to file. For our purposes, we typically allocate 2 or more frames worth of data for the image buffer; as one frame is read out, it is saved to file, and overwritten by the next frame, but additional buffer space provides as a safeguard in case the computer does not read the data into file quickly enough (to date, this has not happened). Pixel data from the detector controller are 16 bits each, and thus the memory required to hold a frame of data is: 16*1024*1024 = 16777216 bits, or ∼2.1 Mb.

The final step in setup is to ensure that the controller is operating in "reset/read" mode. That is, the detector, upon being given exposure commands, will reset the array before integrating and reading out. Now that the controller is set up, there are many functions that are used in being able to get data from the detector into the computer memory. One can test whether the controller and computer are communicating properly by command "TDL", or "test data link", which sends a word to the controller, which should be mirrored back to the user upon successful communication.

Two commands which are used often are the "RDM" (read memory) and "WRM" (write memory) commands. These, respectively, will read a defined value from somewhere in the controller DSP or EEPROM, or write a value to this specified destination. "WRM" would have already been used to update the "LCOLS" and "LROWS" variables by this time ("NCOLS" and "NROWS" are instantiated upon upload of "tim.lod"). These two commands are important in querying and updating various bias voltages for the detector.

Though "WRM" can write new bias voltages to a table in the DSP memory, the voltages themselves are not changed until a call to "SBV" (set bias voltages) is made.

Because the ACCESS detector is read out non-destructively, one can specify both the number of frames to be readout in a single exposure ("SUR", set up-the-ramp), and the exposure time between each successive readout ("SET", set exposure time). Because the detector takes slightly longer than 2 seconds to be fully readout, an "exposure time" of 0 seconds with a "frame number" of 4 would take ∼8 seconds. Increasing the exposure time to 1 second would add 1 second between each successive frame, and thus the total time to take the image would be ∼12 seconds. The number of "reset" frames may also be specified. A "reset" frame is one in which the entire detector is reset, and each individual pixel is reset to its initial value. This is only done at the beginning of an image.

The number of samples per pixel in an individual readout can be modified by changing the number of Fowler samples ("SFS", set Fowler samples). This is a noise reduction technique, and for the purposes of initial testing, has remained at a value of one.

After the settings have been updated to the user's desired values, one may then start an exposure, using "CRR" (continuous ramp read), or "SEX" (start exposure), although "SEX" only provides a two frame CDS readout.

The rest of the software is internal to the host computer, as the controller will now perform its functions and send the data to the computer without additional input. A ".fits" file is created for each image, and can be in 3D "data cube" format for up-the-ramp exposures. The FITS file will have pertinent parameters for the image loaded as keywords into the FITS header data.

Once a frame is read into the computer, the image must be deinterlaced, as the data for the four quadrants come in simultaneously. When the data arrives at the computer, it is received as one dimensional data, in the manner of: (quadrant1 pixel1),(quadrant2, pixel1),(quadrant3, pixel1), (quadrant4, pixel1), (quadrant1, pixel2), etc. For the H1R detector, the format for the data is that each quadrants first pixel read is at the outermost corner of each detector quadrant, and is read inwards

in the row direction (see Fig. 7.1). The rows are read successively, with the last pixels readout for each frame being the central 4 pixels of the detector. The one dimensional data is translated into this format, and saved into the newly created FITS file.

These steps can all be implemented multiple times, and when the user is done, the "exit" command is sent, which closes the computer connection to the controller drivers and ends the program.

IRCAM3 can perform all of these steps, and more. However, due to the GUI-based nature of the software, it cannot be operated in flight. In addition, IRCAM3 was developed for Windows XP, a now-obsolete operating system. It was necessary to write a command-line code that could perform on the ACCESS flight computer, and was customized for the payload's particular needs.

The new ACCESS code was developed on a Windows 7 machine, using the 2.0 API and drivers. Initially, effort was made to develop the code using the more recent 3.0 version, but our colleagues at Goddard recommended version 2.0 for greater compatibility with the IRCAM3 software. The new code was written in C++, as this is the programming language that the ARC API code is natively written in, and thus the source code for the API could be used as reference.

A new command line software was developed for ground testing that involved a set of functions that would combine commands from the pre-existing library and send the command words to the controller.

After setup, commands may be run in no particular order, but for the purposes of image acquisition, voltages and readout patterns must be set to properly receive an image.

Prior to image acquisition, the detector reset voltage (VRESET), various power supply voltages (VDDA, VPOWER), a bias gate voltage (VBIASGATE), and detector common (VDSUB) voltages must be configured. Each quadrant has a bias voltage that can be adjusted. These can be modified via command, and run between 0 and 5 volts. For the qualification unit, voltages of 2.76, 2.76, 2.77,

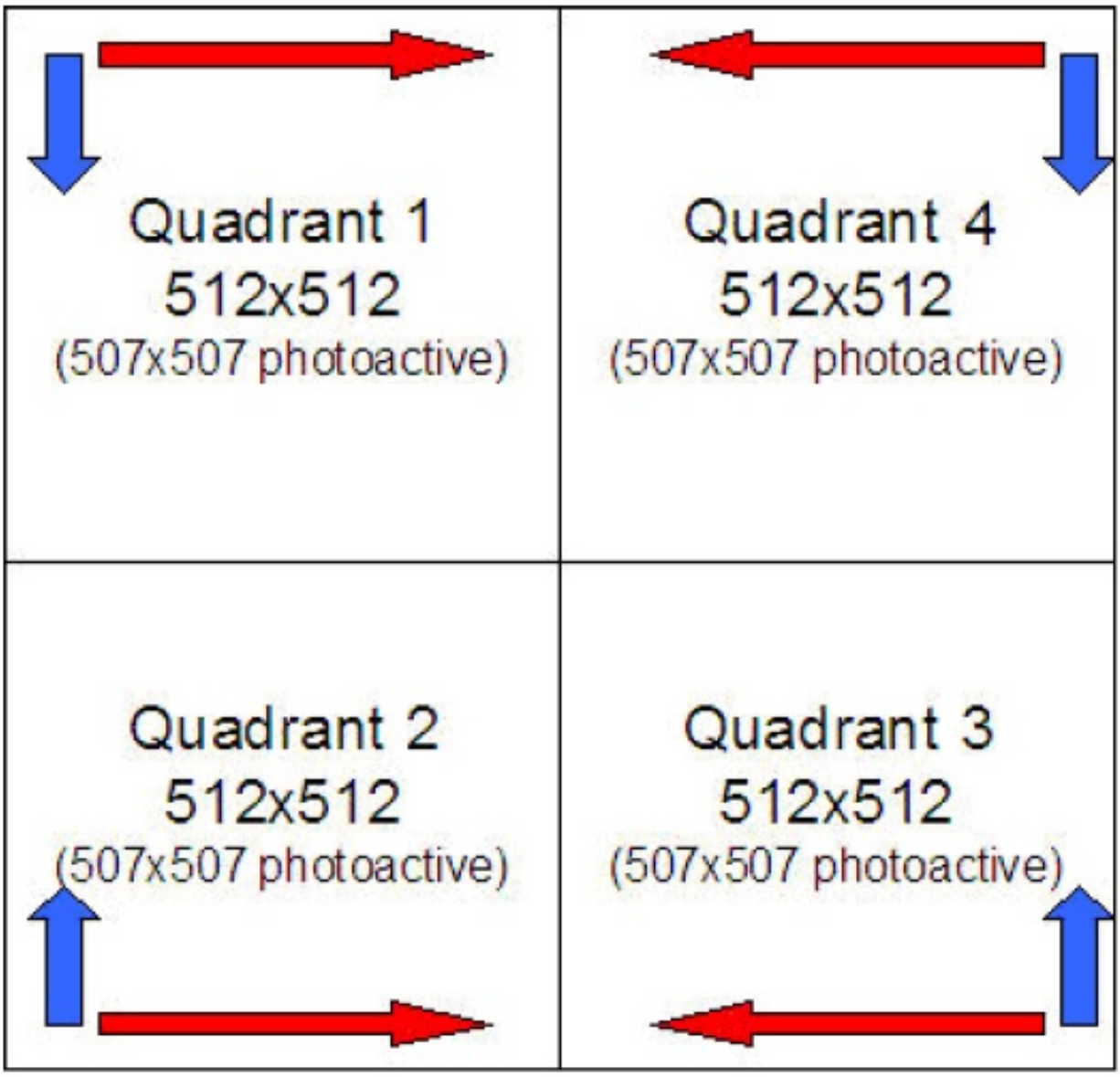

Figure 7.1: Detector Readout Pattern for an H1RG detector [Dressel et al. (2017)], the same readout pattern as the ACCESS detector. Red arrows indicate fast readout direction, blue arrows indicate slow readout direction.

and 2.76 volts for each respective quadrant and typically yielded the best images. If no detector is connected, 0 volts must be set for the bias in each quadrant, or all pixels will read the saturation value of 65535.

Once the voltages are set, the number of frames and dwell time between frames is specified and an image may be taken. After prompting for a filename, an empty FITS file data cube is created. The FITS header populated with the conditions of the image, including the aforementioned settings. As each frame of an image is read into the user computer, it is deinterlaced and saved to the FITS cube.

In the final flight software configuration, this software not only saves a copy of the data to the flight computer's hard drive, but also sends the image through the computer's FPGA, which then serializes the data and sends it to the flight telemetry system, so that the data can be received by the ground while in flight. New software was written, such that it would perform all the previous steps automatically, and continue to take images until a stop command was sent.

The FPGA software was written by Grant Peacock an embedded systems engineer. This software packetizes the data and sends it via serial stream to a ground computer or the payload's telemetry system. Testing in the lab between computers have shown full transmission of image data for tests spanning several hours with no data loss. Tests have been performed at Wallops Flight Facility in Virginia, transmitting the science data to the ACCESS telemetry stack, and error-free transmission and reception has been demonstrated and confirmed by reviewing the images received by the Wallops ground station.

Tests have been successfully performed in which the flight computer and detector controller are controlled by a remote RS422 connection, similar in configuration the ACCESS payload command uplink system. Commands are sent from a host computer through the RS422 connection and received by the flight computer serial port. These operations execute in identical fashion to direct commands

by the flight computer command line.

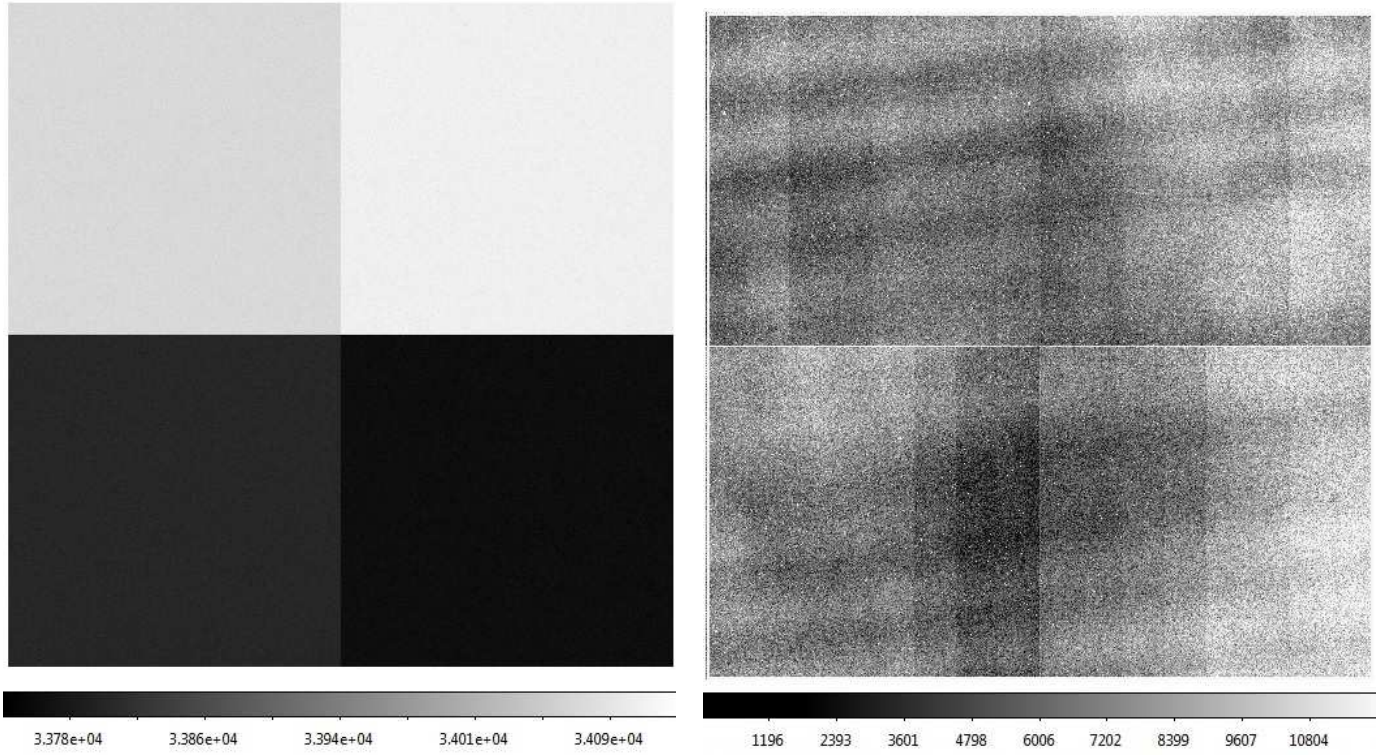

Figure 7.2: **Left:** Image taken by flight computer, with no detector attached, demonstrating variance between quadrants. **Right:** Image taken by FPA 114, qualifying unit. Zeroth frame of dark image, with no processing performed.

The images shown on the left of figure 7.2 are of an image taken with the detector controller by the flight computer, with no detector installed. Though the image looks perfectly flat, each quadrant has noise structure, albeit of a very small spread, around a different peak. The bias voltage is set at zero, as any bias voltage set without a detector in place dominates the noise and all quadrants exhibit either zero signal or instant saturation. The right detector image is of the zeroth frame of a cryogenic dark image. Though this image seems to exhibit a great amount of periodic noise, the scale is greatly contracted to show the detector structure. When the zeroth frame is subtracted from the other frames in the exposure group, this structure is effectively removed from the data. The ACCESS group tested this by taking dark images (see sec. 7.2) with a dwell time between frame reads of 1 second. The median and standard deviation of pixels in the first frame is 8290 and 2855

DN's, respectively. Subtracting the zeroth frame reduces this to a mean of 8.5 DN's and a standard deviation of 520 DN's.

7.2 Ground Characterization Dewar

The detector system must be characterized on the ground prior to flight. Several characterization tests, such as read noise, dark current, and persistence can initially be done external to the spectrograph in a cryogenic dewar. For these characterization tests, a surplus cryogenic dewar was modified to increase thermal radiation rejection and a mount interface to the detector assembly was also fabricated and integrated into this dewar. The addition of the cooled full length radiation shield and a zeolite cryo-adsorber plate permitted the detector to easily reach its flight operating temperature of 130-140 K in this dewar.

The detector itself sits on a cold work surface, mounted on G10 feet above the liquid nitrogen tank. On the underside of the detector is a molybdenum plate. Molybdenum has a very low coefficient of thermal expansion, which prevents the detector from changing dimensions through a temperature. That molybdenum plate is then mounted to a copper block, which is connected to a cold finger on the cold work surface. In the telescope payload, this copper block will be connected to a Ricor Stirling cooler. The detector is affixed to the cold work surface by titanium flexures, with g10 feet, to provide thermal isolation and accommodate the difference in coefficient of thermal expansion between the detector and the g10 feet. This same configuration is used in the spectrograph, and so provides a benchmark for the performance of the system before mounting in the spectrograph. At the bottom of the detector sits a thermal diode, and a heater. To prevent damaging the detector, the thermal diode, heater, and dewar cold finger are used together as a feedback loop, ensuring that the detector is cooled and heated at a constant rate of 1 degree per minute. When the detector reaches 140 K, the

heater can be used to maintain the detector at that precise temperature, within 0.01 degrees kelvin.

Three layers of baffling were installed in the cryogenic dewar, with only the detector surface exposed through each baffle. The outer skin of the dewar is at room temperature, and would appear so bright to the detector, that the image would saturate immediately.

At the top surface, a cold shutter is installed. This shutter is mechanically operated by a slide on the dewar. The slide was originally used for positioning a radioactive source in front of a detector, and was repurposed by ACCESS to provide a cold, dark surface for calibration testing, while allowing an external light source to be used on the detector, while maintaining vacuum. The cold shutter, and its mounting, are connected to a copper braid. This copper braid feeds through the outer baffle, and the cold work surface, and is bolted to the liquid nitrogen dewar. With this system in place, the shutter can be maintained below 130 K. Thus, when the shutter is closed, the detector sees only a dark surface, even in the near-infrared. I improved the cold plate thermal strapping to enable the cold shutter to reach 130 K.

On the top surface of the outer baffle, a plate with zeolite cryo-getter material is placed. This allows the dewar to achieve a higher vacuum. This increases the liquid nitrogen hold time and has the advantage that the dewar does not need to be manually filled with liquid nitrogen as frequently.

Figure 7.4 depicts the additional layers of baffling inside the dewar. Top left is the detector installed on the cold work surface, with G10 feet, and titanium flexures. There is a temporary protective cover pictured, which is removed before adding the baffling. Figure 7.4 top center shows the inner baffle. Figure 7.4 provides a view of the outer baffle (in the lower edge of the image you can see a copper strap, which will be affixed to the cold shutter apparatus). The Kapton tape covering the aperture is removed once the baffling is installed. Figure 7.4 bottom left shows the outer baffle and the cold shutter. The lower right image shows the baffle system with the Zeolite getter installed. The outer

skins are installed. A new dewar extension lid was built to accommodate the inner baffles, and permit the installation and test of the flight Stirling cooler for the detector.

Using the aforementioned dewar modifications, ACCESS has been able to obtain dark rates that are similar to the Goddard Space Flight Center's Detector Characterization Lab. The data in figure 7.3 is for the qualifying unit, which has, over the span of several years, developed a dark current rate of change high enough so as to disqualify it from being considered for flight. The blue peak in the sub-figure (a) shows its initial dark rate, as measured by DCL in August 2005. The red shows the detector's performance, also measured by DCL, in February 2010. The black line signifies the data taken by the ACCESS ground cryogenic dewar system in December 2012, using a cold blank off plate. The detector was read out for 16 frames in an up-the-ramp exposure, for a total image exposure time of 1961 seconds (just over 30 minutes). Subfigure (b) shows the cooldown plot for several measured positions within the dewar. The cold shutter, in closed position, was held at about 140 K for this test. The final subfigure (c) is the dark rate from a cold shutter test, but with extended x axis and compressed y, and separated into respective detector quadrants.

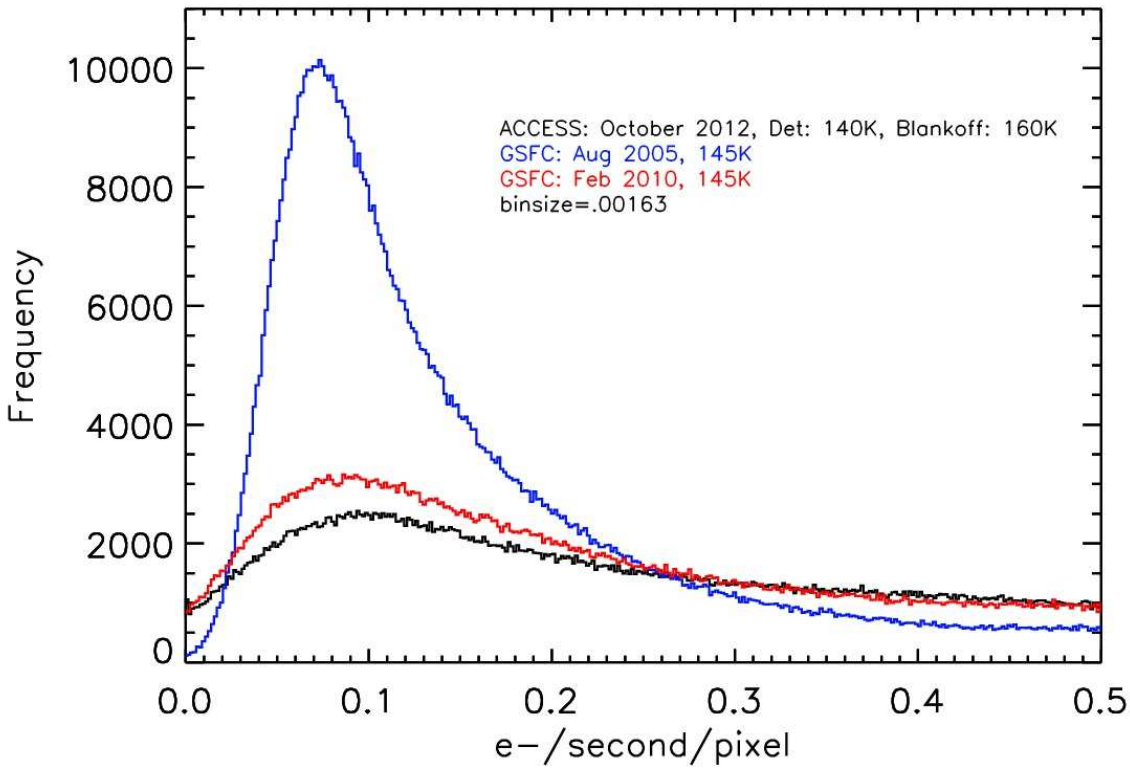

(a) Dark Current results from ACCESS test, compared to DCL tests of same detector, at various epochs.

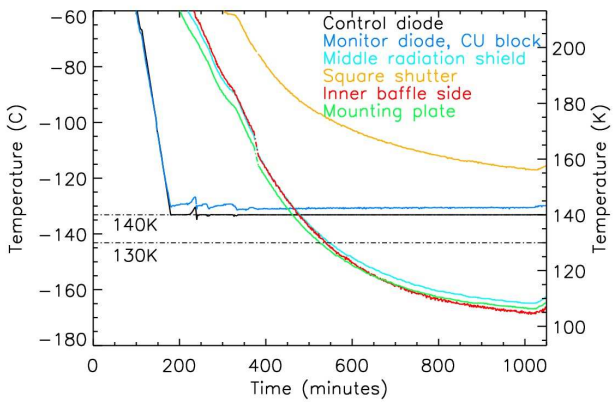

(b) Thermal data from a Detector characterization test, taken in the ground characterization dewar.

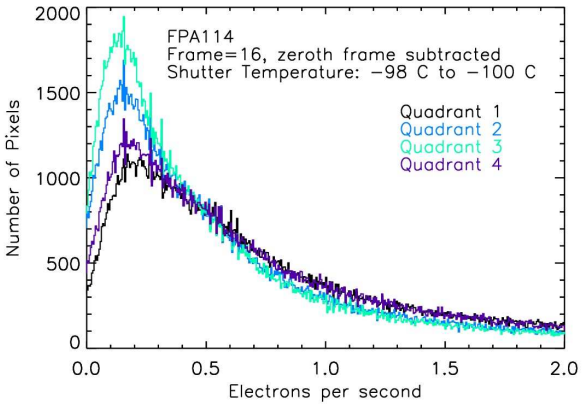

(c) Dark Current results from ACCESS test, broken down by detector quadrant, using cold shutter.

Figure 7.3: Results from dark images using the ground characterization dewar.

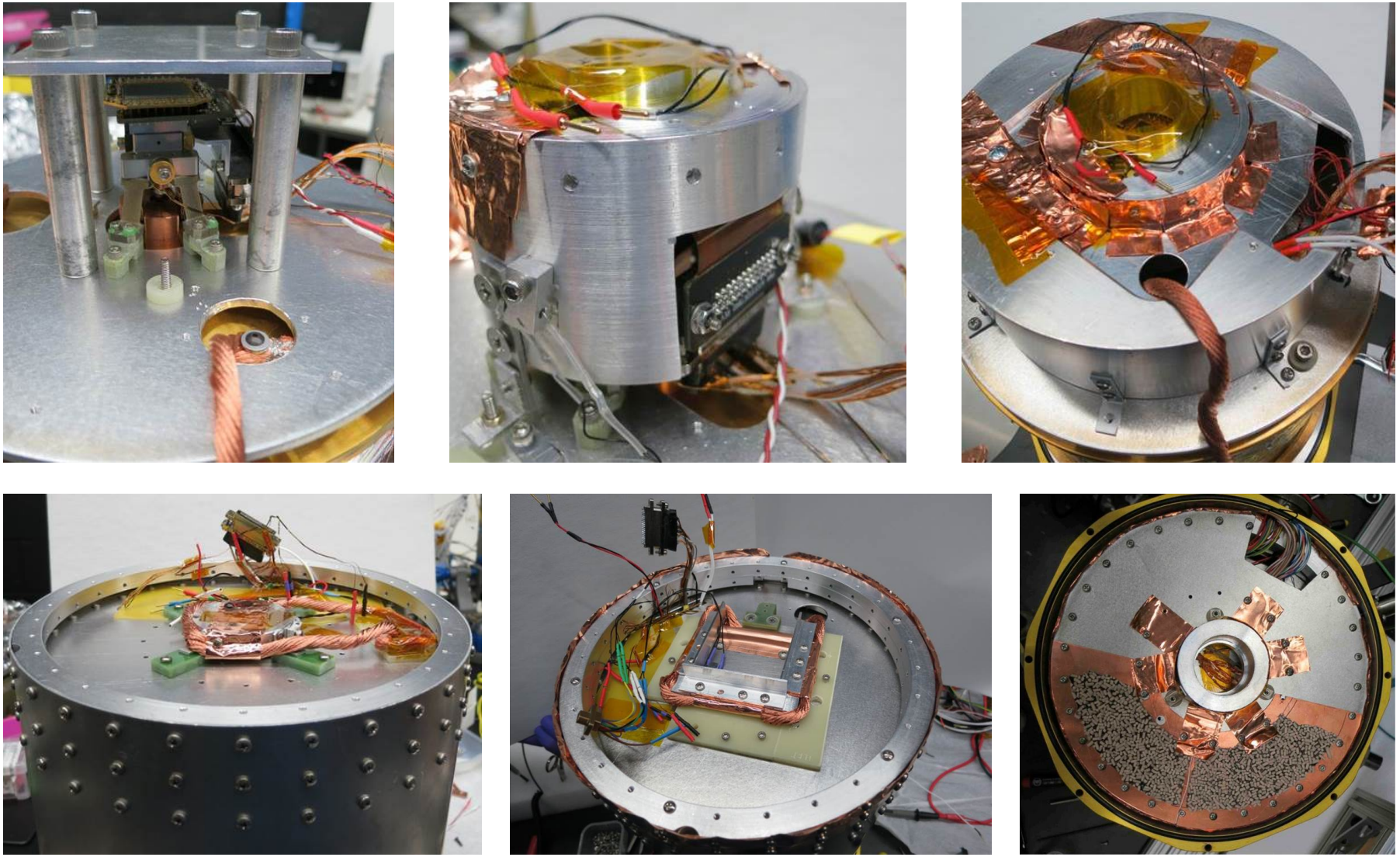

Figure 7.4: Laboratory cryogenic dewar for detector testing. **Top Left:** Detector mounted on cold work surface of ground cryogenic dewar with protective cover. **Top Center:** Inner radiation shield. **Top Right:** Middle radiation shield. **Bottom Left:** Outer radiation shield with cold blank-off plate tied to copper strap. **Bottom Center:** Outer radiation shield with cold shutter installed. **Bottom Right:** Above cold shutter, a cold baffle and Zeolite cryoadsorber plate is installed.

7.3 ACCESS Reduction Pipeline

An image reduction pipeline was written in IDL for the ACCESS payload. The steps are automated, but provide intermediate data for quality control. The ACCESS detector is a WFC3 spare, and therefore the reduction steps mostly follow those outlined within the WFC3 data handbook [Rajan et al. (2010); Deustua & et al. (2016)], for 2-D reduction. The steps are as follows:

1. A data quality array is created that keeps track of bad pixels. Typically, different types of bad pixels are masked by different values, i.e. dead pixels, hot pixels, non-linear response, cosmic rays, etc. This is initialized with an array of known bad pixels, that have been measured during the characterization process.

2. The zeroth frame of an image typically contains no signal, and is an approximate intercept for the calculation of the signal rate in later steps. For this reason, it will be subtracted from the subsequent images, to set the intercept to zero. There may be signal from bright sources in the zeroth read frame, due to the 2.9 second delay between a detector reset zeroth frame readout. This will bias the count-rate calculation if not accounted for. If the signal for a pixel is above the noise level by a factor of 5, that pixel is marked in an array, and the estimated zeroth frame signal is then later fed back into the image (at step 9) [Deustua & et al. (2016)].

3. The bias level is subtracted from a mean that is derived from the reference pixels bordering the detector. The 5 pixels surrounding the detector are engineered to be used solely for the purpose of bias measurement. These pixels have no photoelectric response to light, and therefore only contain signal that comes from the voltage applied across all pixels. The sides are used, as the top and bottom reference pixels have previously been found to be unreliable, showing slight signal responsivity in faint exposures [Rajan et al. (2010); Hilbert (2012)].

4. The zeroth frame signal is subtracted from all frames in the image.

5. At this point, an error array is created. This array will track the pixel-by-pixel error throughout the calibration steps. The error array continues being processed in parallel with the image. Errors inherent in each reduction step and errors from calibration files will be added in quadrature to the error array, on a pixel-by-pixel basis. The initial error array is calculated by a general expression for the total noise in e^- rms of an up-the-ramp readout is [Rauscher et al. (2007, 2010)]:

$$\sigma^2_{total} = \frac{12(n-1)}{mn(n+1)}\sigma^2_{read} + \frac{6(n^2+1)}{5n(n+1)}(n-1)t_g f - \frac{2(m^2-1)(n-1)}{mn(n+1)}t_f f \tag{7.1}$$

Where n is the number of groups sampling up-the-ramp, m is the number of frames per group, $t_g$is the time interval between groups, t_f is the integration time between successive reads, and f is the flux in $e^- s^{-1} pixel^{-1}$. The read noise (σ_{read}) for the ACCESS detectors is computed by taking two identical images, in which the image is read out twice each time, with no dwell time in between the reads. This image is typically known as a correlated double sampling (CDS) integration. A CDS is defined:

$$CDS_0 = READ_1 - READ_0 \tag{7.2}$$

$$CDS_1 = READ_3 - READ_2 \tag{7.3}$$

The read noise for a detector is the noise per CDS:

$$\sigma_{read} = \frac{1}{\sqrt{2}} STDEV[CDS_1 - CDS_0] \tag{7.4}$$

Where STDEV refers to the standard deviation across the image. The read noise for the

ACCESS detectors has been measured to be ∼30-40 DN's RMS in the ground characterization dewar, and will be measured again in the flight configuration.

6. The non-linearity of the detector is corrected, according to a set of correction factors. The detector is designed to be perfectly linear until very close to pixel saturation, but there is still a very small effect of count-rate non-linearity. The correction factors vary from pixel to pixel, and must be calculated accordingly. The corrections take the form of coefficients to a polynomial:

$$F_{corr} = (1 + C_1 + C_2 * F_{init} + C_3 * F_{init}^2 + C_4 * F_{init}^3) * F_{init} \tag{7.5}$$

   The coefficients are found by using a radiometrically controlled light source, and measuring the pixel's non-linear response to the signal.

7. The dark current is subtracted. Dark current is the measure of counts registered in a detector on which no light is incident. This corresponds to the chance that an electron will randomly deposit itself into a pixel. The rate of this effect can be measured by isolating the detector from any thermal background and integrating. A dark image, in this manner, is taken before and after observing with the same observation parameters, and a table of darks is made, for each observing configuration that may be used. Afterwards, this dark image, either individual or averaged with other darks, may be subtracted from the science image, removing the effective dark current from the science data. Dark images have been created for the ACCESS qualification unit using the ground cryogenic dewar (see Sec. 7.2).

8. Cosmic rays are marked in the data quality array, and corrected for in the science data. Cosmic rays are high energy particles, typically bare protons, but may also be in the form of electrons, positrons, muons, or other atomic nuclei [Cronin et al. (1997)]. These particles are energetic

enough to penetrate several centimeters of metal [Burrell & Wright (1972)], penetrating through the payload and hitting the detector. This causes a very sharp spike in the signal detected. This may appear in a single pixel, or a series of pixels, dependent on the angle of incidence of the cosmic ray and the size of pixels. Because the ACCESS detectors are read out in an up-the-ramp fashion, this manifests in a drastic increase in signal rate for a single frame. Pixels contaminated by cosmic rays are replaced with a median of the surrounding pixels. [Offenberg et al. (2005)] provides an algorithm for the identification and removal of cosmic rays in up-the-ramp sampled data.

9. Up-the-ramp fitting is performed, and an array of the slope and intercept are each created for the image. This will yield, rather than total counts, a count rate for the signal seen on the detector. The formula for this fit is done according to the methods in [Rauscher et al. (2007)]:

$$s_{x,y} = a_{x,y} + b_{x,y}t \tag{7.6}$$

In which s is the signal for each pixel in x-y space, and t is the time at which that signal is reached. The fitted slope b for each pixel in x-y space is:

$$b = \frac{n\sum_{i=1}^{n} t_i s_i - \sum_{i=1}^{n} t_i \sum_{i=1}^{n} s_i}{n\sum_{i=1}^{n} t_i^2 - (\sum_{i=1}^{n} t_i)^2} \tag{7.7}$$

and the y-intercept a is:

$$b = \frac{n\sum_{i=1}^{n} t_i^2 \sum_{i=1}^{n} s_i - \sum_{i=1}^{n} t_i \sum_{i=1}^{n} t_i s_i}{n\sum_{i=1}^{n} t_i^2 - (\sum_{i=1}^{n} t_i)^2} \tag{7.8}$$

10. The image is then divided by the flat field. A flat field is a calibration file of the pixel-to-pixel

variation across the detector. In the case of ACCESS and other programs, the flat fields are split up into two regimes: a low frequency flat (how the sensitivity of the detector varies continuously across the detector), and a high frequency flat(the uncorrelated responsivity of each individual pixel). A flat field calibration file is built by illuminating the detector with a spatially uniform light source. The variation is then separated into the high and low frequency variation, and each flat is normalized. The normalization prevents the flat from biasing the image, when the image is divided by the flat. For the error array, error for the flat field and science data are added in quadrature as percent error.

The science error array is added in quadrature with the flat field error array, determined by the formula [Deustua & et al. (2016)]:

$$\sigma_{ir} = \frac{\sqrt{(readnoise)^2 + (counts * gain)}}{gain} \tag{7.9}$$

11. The count rate is converted from DN's to electrons. The gain for the ACCESS detector was measured by the Goddard Space Flight Center's Detector Characterization Laboratory to be 1.9 electrons per DN.

The 1-D processing follows the steps outlined in the STIS data handbook [Bostroem & Proffitt (2011)], and the 1-D calibration pipeline outlined in (ISR 99-03 [McGrath et al. (1999)]), albeit the code here is written in IDL, and not IRAF.

1. The apertures are extracted from the 2-D image. Because there are three orders of light incident on the ACCESS detector, A vertical slice of the image is taken, and three separate gaussians are fit to the individual apertures. Reported back and stored in an array are the peak position and width of each gaussian. This is done for each vertical slice of the image. Taking the peak

positions of each aperture across the image, a polynomial fit is applied to the image, tracing the aperture in the dispersion direction. Using the polynomial fit, the signal is vertically summed at each point. Because the peak position is not an integer value, the summing is done with fractional pixel weighting. That is, the pixel at the end of the extraction aperture is not an entire pixel, so the signal from that pixel is weighted by the amount of pixel within the aperture. For example, if an aperture is defined as ± 2.5 pixels from the peak, the 3rd pixels above and below the peak are multiplied by 0.5, and added to the pixel sum. This is done at the top and bottom of the extraction window. The window height can be set manually or determined from the median width of the signal; images on the ACCESS detector are $\sim$4 pixels (18×18 μm pixels) in the cross-dispersion direction[Kaiser et al. (2010)]. The error array is extracted using the same aperture definitions as the science data

2. The background signal is then subtracted from the summed apertures. The aperture, in which science data enters the spectrograph, may allow light through that comes not from the science target but the background light seen around the target. Additionally, thermal background seen from the detector's surrounding environment can contribute to this background. This light will be seen offset from the aperture trace, and thus can be subtracted from the signal. Using the same aperture trace, offset above and below the signal, background signal is summed in the same manner as the science data. Apertures are 4 pixels tall and separated by a minimum of 24 pixels on the ACCESS detector [Kaiser et al. (2010)], and so the background apertures are defined as 8-12 pixels from the aperture peaks. If the background signal is symmetric, then the average of the two backgrounds is taken and subtracted from the science data. Otherwise, the subtraction algorithm interpolates across the upper and lower background and subtracts the interpolated signal summed over the apertures. No background subtraction is performed on the

error array.

3. The data is then dispersion corrected, and its wavelength scale is applied to the image. The wavelength scale and dispersion non-linearity is measured by using monochromatic light from the artificial star system (see Sec. 8.1). Applying this system to the ACCESS payload, we measure where each wavelength across the ACCESS bandpass is incident on the detector. This calibrated wavelength scale can then be applied the science data and the error array.

4. After this, the count rate seen by the telescope is converted to absolute flux units, from the ground calibration performed prior to observations. The artificial star calibration (see Sec. 8.1) provides a conversion from electrons to ergs cm^{-2} s^{-1} $Å^{-1}$ from, and this conversion can then be applied to the science data.

7.4 Detector Controller Thermo-Mechanical Ruggedization

The detector controller, a Leach controller system built by Astronomical Research Cameras inc., was initially in a housing designed for ground usage. This housing was bulky and contained a fan to regulate temperature. In flight, the detector controller will be in the electronics section of the ACCESS payload, which will be passively evacuated (i.e. it will not be pumped out mechanically, but will be open to the vacuum of space). A compact, ruggedized housing was built for the controller circuit boards to fit within the limited space available, provide thermal strapping and heatsinking for the electronics components in the vacuum environment, and survive the vibrational loads sustained during the rocket launch. These electronics need to be tested in flight-like conditions to identify electronics that require heatsinking, and ensure that all electronic systems will operate properly in flight.

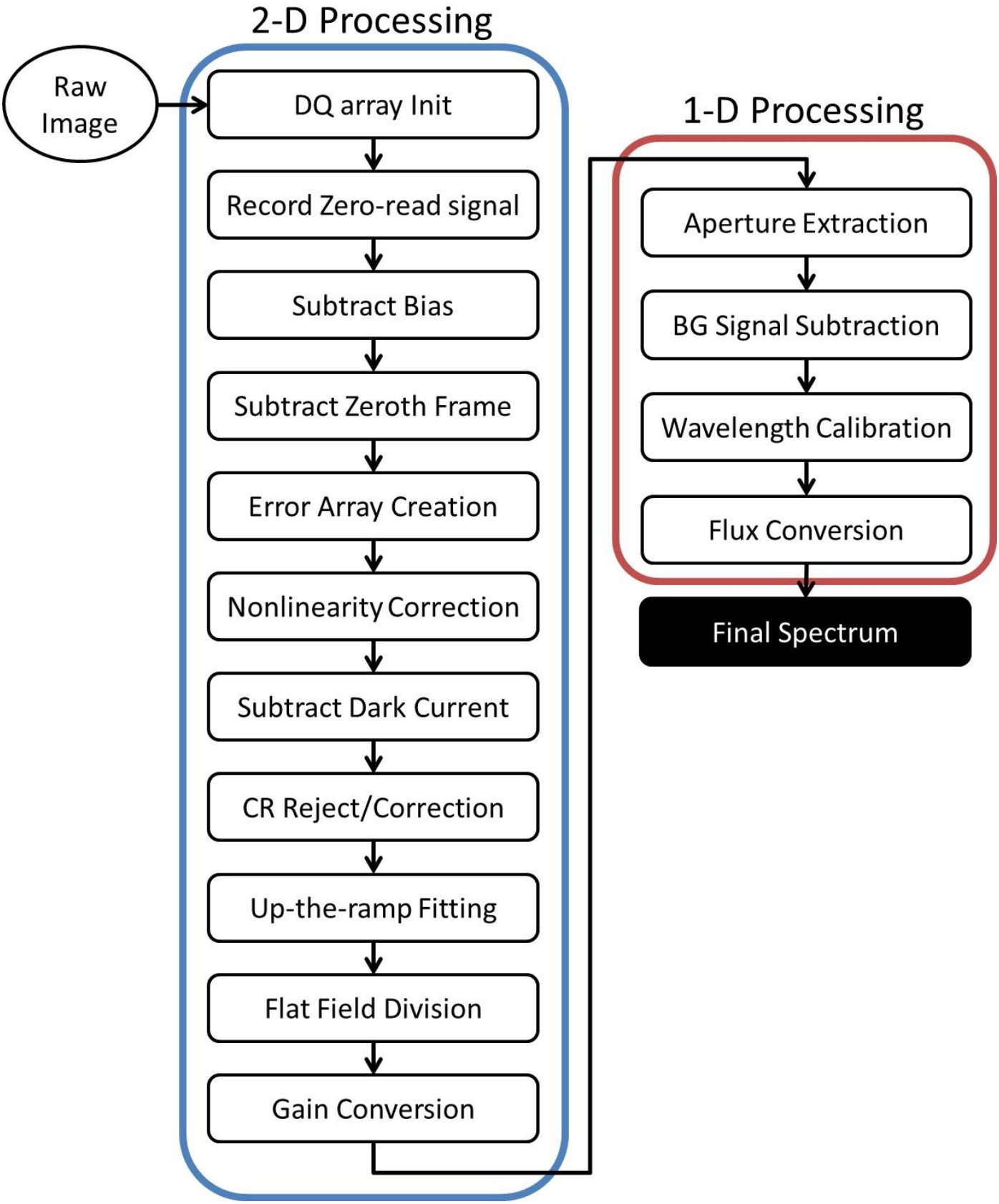

Figure 7.5: A flowchart of the ACCESS data reduction pipeline. The 2-D processes outlined in blue follow the WFC3 data handbook [Rajan et al. (2010); Deustua & et al. (2016)]. The 1-D processes outlined in red follows the STIS data handbook [Bostroem & Proffitt (2011)].

Initial tests were performed to indicate the hottest components, by running continuous image acquisition, and using a laser thermometer to measure the board components individually. Once the hot components were identified, thermistors could then be affixed to those pieces for tests in which the housing is fully closed, to mimic actual conditions more fully. The components which came close to their maximum temperature threshold were then fitted with copper heatsinks. The hottest components were on the ARC-78 Power Control Board, in particular the power regulator. However, the fiber optic communications components, though not the hottest, have a particularly low temperature threshold relative to many other components, and required heat-sinking as well. They are rated to 343 K, and have reached nearly 330 K, before heatsinking. The heatsinks are fed to the housing via copper ribbon, or directly bolted to the housing where possible. The housing acts as a thermal mass, and because of its contact to the avionics base structure, can release heat even in vacuum conditions. Once the heatsinking system was shown to be effective at atmospheric conditions, the system could them be placed under vacuum, to test flight-like conditions.

Though the fiber optics are not the hottest component, they come within the smallest margin of their rated maximum temperature. They are rated to 343 K, and have reached nearly 330 K.

Having heatsunk the components, the detector controller was subjected to the same tests previously performed, both in atmosphere, and under vacuum. The controller was able to continuously operate with the housing closed in a flight-like configuration under vacuum for 90 minutes, and in atmosphere for 8 hours in a sealed volume comparable to the flight avionics dimensions, which are much longer periods than what is required for a rocket flight. A typical rocket flight will last 15 minutes from launch to landing, with about 400 seconds of exposure time above the entire atmosphere.

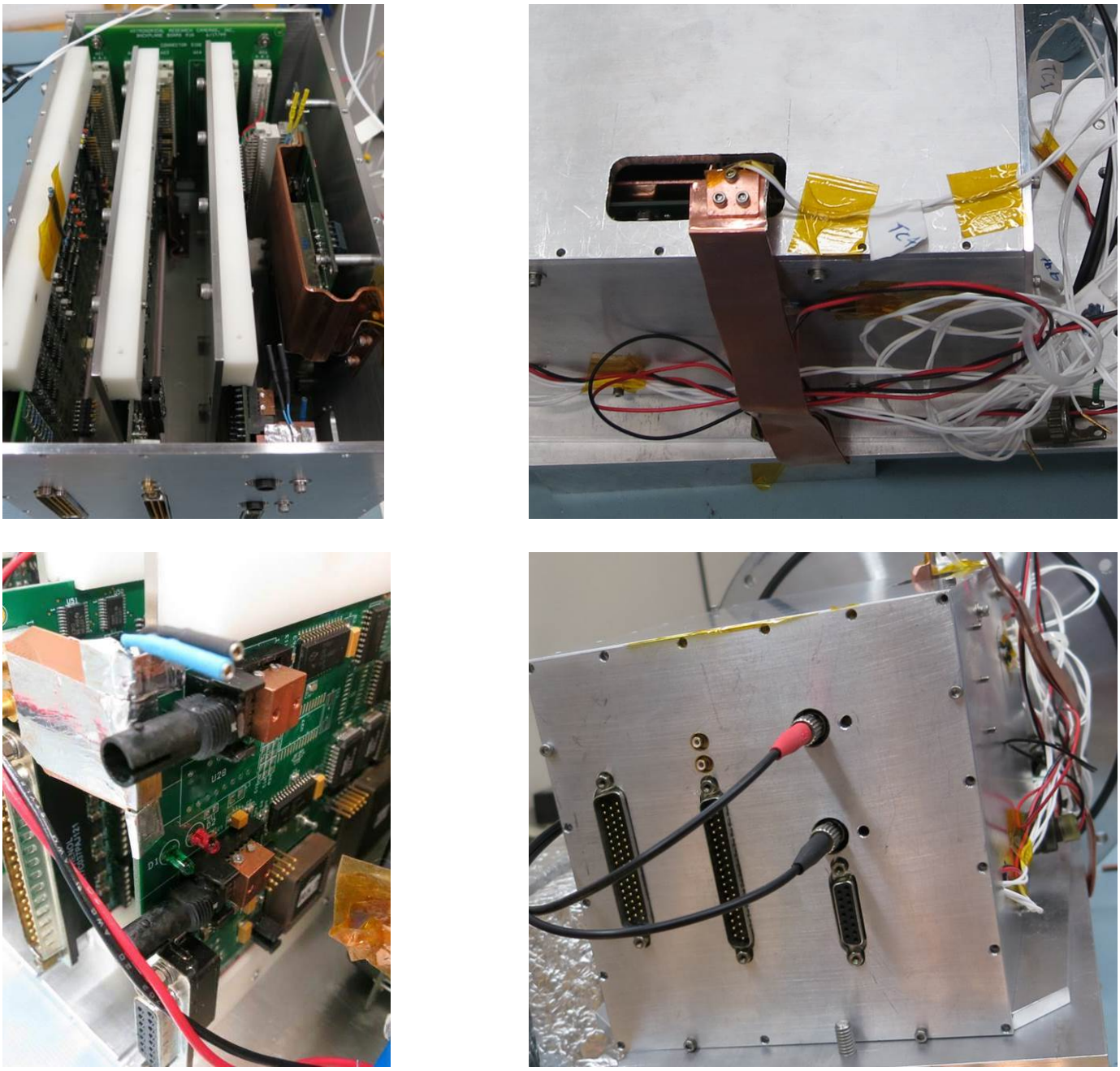

Figure 7.6: **Top Left:** Top view of the detector controller housing with video clocking, timing and power distribution circuit boards. Heatsinks are attached to components high temperatures as initially measured with a temperature "gun". **Top Right:** Copper heat-strap leading from DC power converter to electronics truss structure. **Bottom Left:** Detail view of heatsinks for the fiber optic connections. **Bottom Right:** Front view of detector controller with covers on.

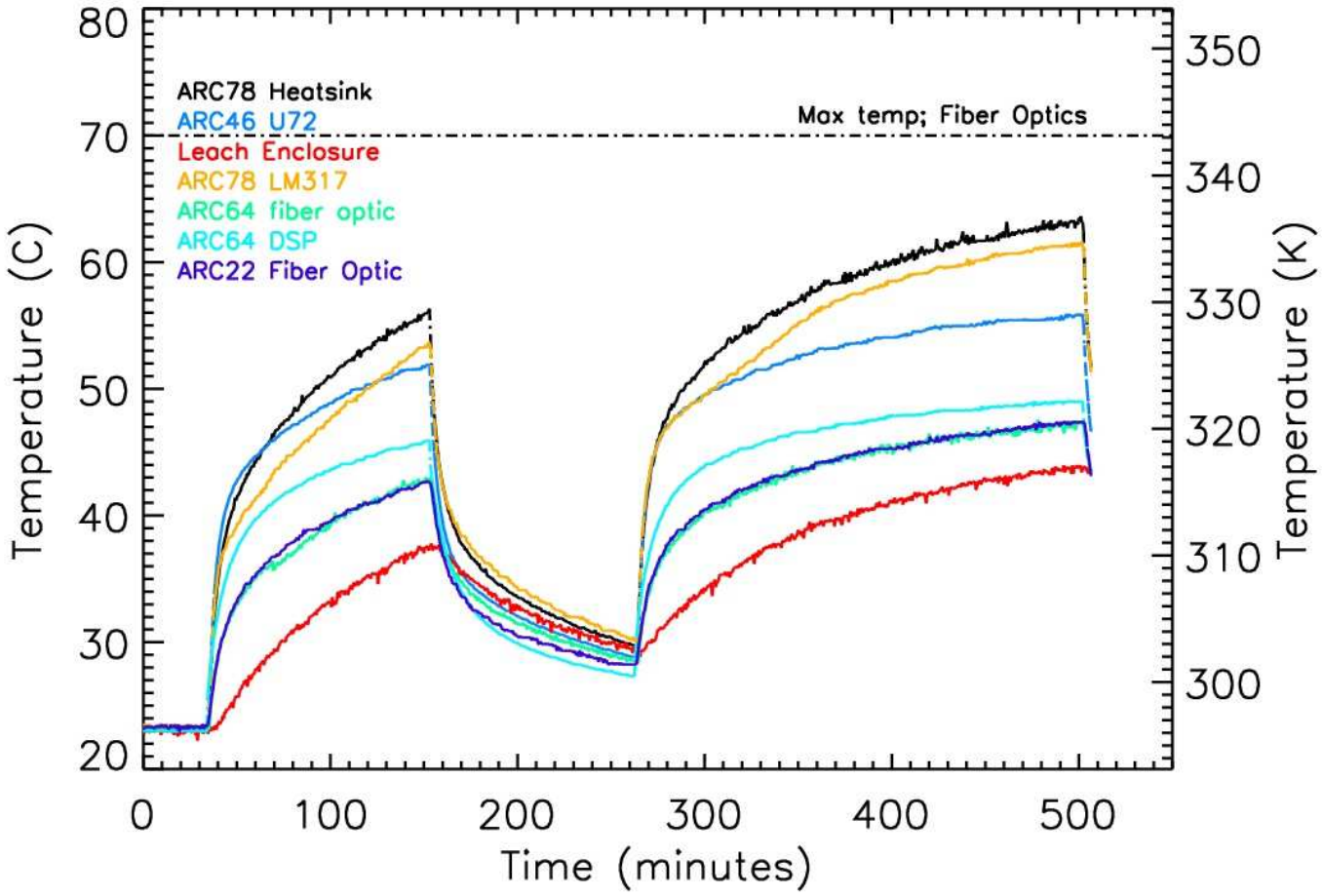

Figure 7.7: Thermal Vacuum test results of CPU and detector controller continuous operation, 2 and 4 hours, with a 2 hour cool-down period between tests.

Chapter 8

Instrument Control for Ground-Based Calibration

A key element of the ACCESS experiment is the ground calibration of the end-to-end efficiency of the ACCESS payload. The calibration, performed in steps, is achieved by the creation of a simulated star that appears to be at infinity (i.e. is a plane wave upon arrival at the telescope aperture), whose absolute flux, measured in ergs cm^{-2} s^{-1} $Å^{-1}$, is established as part of the calibration process. This absolute flux is calibrated against NIST standard detectors and transferred to the ACCESS payload, and ultimately the stars.

A ground based calibration system has been developed and will be tested with the ACCESS payload. In order to ensure that electronic counts observed at the focal plane are accurately converted to physical flux units, a source with known flux must be created in the lab. This source must be stable over long time periods, monochromatic, contain no polarization, and adjustable to many wavelengths.

8.1 Artificial "Star-at-infinity"

In order to perform the calibration steps, a reliable and adjustable light source must be provided. This light source must be a plane parallel set of rays, as it enters the telescope, to emulate the conditions of observing a star, at a distance effectively infinitely far away.

A quartz tungsten halogen (QTH) lamp was chosen as the primary light source, because it provides a stable blackbody spectrum across the entire bandpass of interest, the filament is relatively long-lived and can be easily replaced, and the housed unit can be radiometrically controlled. An Ushio 100W bulb with color temperature of 3300 K is being used in an Oriel lamp housing. The housing contains a back-reflecting mirror, a focusing lens, and a mount for a photodiode that views the filament and is used for radiometric control. An OPS-Q250 power supply is used with the QTH lamp because it is designed to provide a radiometrically controlled power output, with very low current variance when used with a silicon photodiode detector as part of a feedback loop, to ensure the light source outputs a constant flux. The lamp requires approximately 45 minutes after turn-on to thermally settle and operate properly with the Si photodiode feedback loop (see fig. 8.1).

In addition, ACCESS has procured a series of emission line lamps, for the purposes of wavelength calibration of the system. Two styles of lamp were obtained, a Thorium filament/Argon gas (Th/Ar) lamp, and a Platinum-Chromium filament/Neon gas (Pt-Cr/Ne) lamp. These lamps produce features that are very narrow in wavelength space. Using an atlas of lines identified from these elements, one can confirm and correct the wavelength settings of the remainder of the optical system.

Light exits the QTH lamp housing through a circular object aperture. The light then passes through a longpass filter, to block overlapping wavelengths of light from higher spectral orders. Five order blocking filters have been set into a filter wheel, which is mounted on a Newport rotary motor, to allow computerized, automatic selection of the proper filter for the specific application. The cutoff

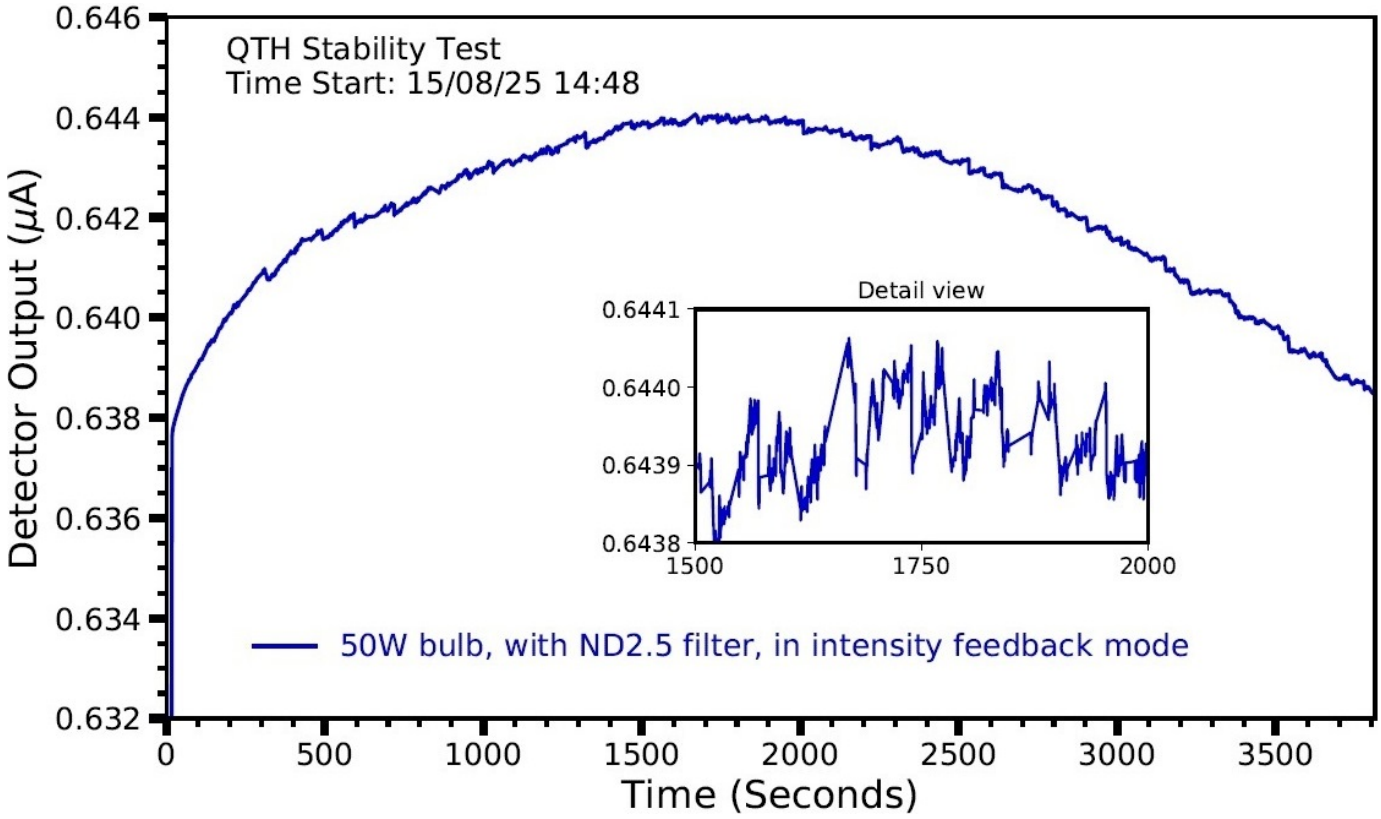

Figure 8.1: The first hour of lamp operations, in which the lamp is settling into stability. Within this hour, the variance does not exceed 1%

wavelengths for these filters are 2800, 4950, 6300, 8500, and 10000 Å.

A lens focuses the illuminated circular aperture onto the entrance slit on the monochromator, an Acton research model VM-505 vacuum monochromator. Two gratings are used within the monochromator: a visible grating (3300-9000 Å) , and a near-infrared grating (6500-18000 Å).

The light then travels from a fiber optic mated to the exit slit of the monochromator to an integrating sphere. The integrating sphere removes all artifacts of polarization introduced by the grating and the multiple scatters of the incident light off the uniform teflon surface interior to the integrating sphere in a uniformly illuminated surface at the output of the integrating sphere.

This monochromatic, unpolarized, diffuse light is then fed through an f/12 baffle box. The baffle box is mounted to a collimator to which the baffle box is matched in f-number. At this point, light exiting the collimator is no longer a point-like source, but is a plane wave with a focus at infinity.

8.2 Flat Mirror Reflectometer

The first calibration step involves the calibration of an auto-collimating flat mirror. The coating of this mirror, as with the primary and secondary mirrors of the telescope, is magnesium fluoride over aluminum.

This mirror is set in a mount within a 22" rocket skin. This mount will later be connected to the ground calibration source, in a skin of the same diameter, and the chamber within purged by vacuum. At the bottom of the mount are two high tension springs and two fine threaded bolts, with each spring and bolt set 90° from the other, to allow for tip-tilt adjustment, as this mount will be used in both horizontal and vertical configurations, and the surface of the mirror must be flat for each configurations. Around the diameter of the mount are standoffs, for witness mirror mounting.

For this step, the mount is not taken to vacuum, but set upright (with the mirror facing upwards),

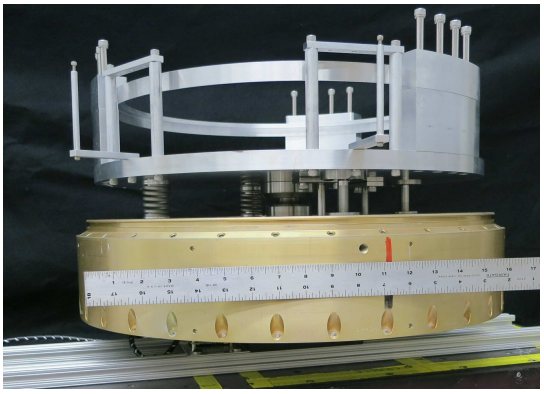

Figure 8.2: Flat mirror side view

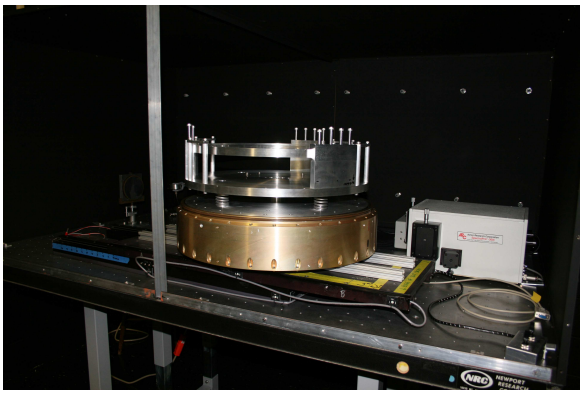

Figure 8.3: Flat mirror mount, on linear and rotary stage

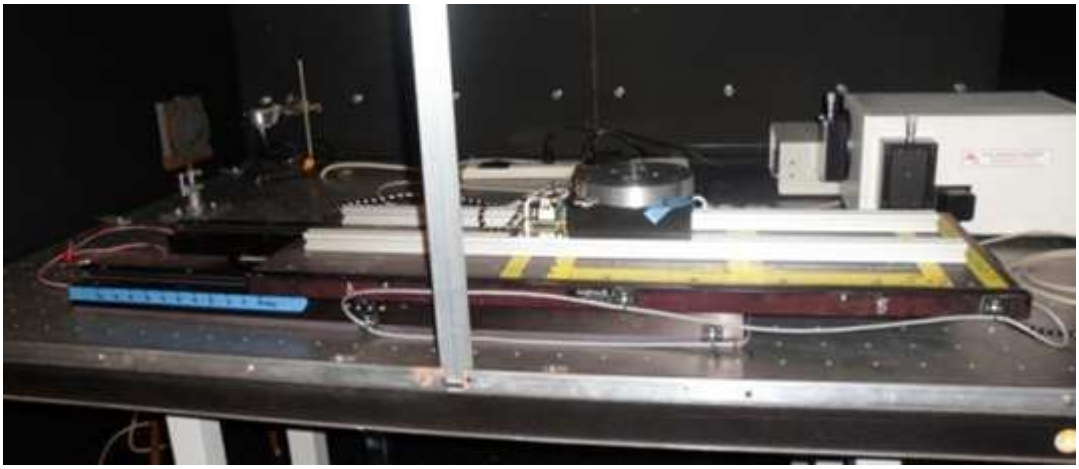

Figure 8.4: Linear and rotary stages, for flat mirror reflectivity measurement

and mounted on a motor stage, with linear and rotary degrees of freedom. A small spot of light, from the aforementioned light source will then be shone on a small section of the mirror. The light beam will be measured, both incident upon, and reflected off the flat mirror. This will be performed for many positions, and many wavelengths. Thus, a reflectance map of the flat mirror can be created, across the ACCESS bandpass. This procedure is automated with the computer controlled monochromator, and a linear and rotary stage that the mirror will be mounted on. In addition, the data is collected from the detector via an electrometer, and is compiled with position, wavelength, and time data, as well as other experiment conditions.

8.3 Autocollimator

Once the reflectivity of the flat mirror has been measured, it will be mounted behind the secondary mirror of the f/12 ground collimator, where the beam will exit the collimator when the flat mirror is removed. At the collimator entrance focal plane is the artificial light source. The light source is at the exit of the baffle box which was matched in f-number to the collimator. The light will travel through the collimator, reflecting off of the secondary mirror, then the primary mirror. It is then reflected off the autocollimating flat mirror, and travel back through the system, reflecting again off the primary mirror and the secondary mirror. A detector will measure the amount of light sent into the collimator system, and coming back out. The incoming light source and return light image at the collimator focal plane are measured with a NIST-calibrated photodiode. The NIST-calibrated photodiode ultimately provides the calibration transfer for the collimator throughput and the ACCESS instrument.

With those two measurements of the input and output from the collimator, we have a reflectivity measurement that consists of five surfaces, in order of the light path: the collimator secondary, the collimator primary, the flat mirror, the collimator primary and the collimator secondary. The flat

mirror's reflectance has already been measured, and thus can be removed. Now the efficiency of the system consists of the square of the total collimator's reflectivity. It is not required to know the primary and secondary mirror reflectivity separately. It is the product of their individual reflectance that is the value of interest. With this information, we now know the sensitivity of the collimator as a function of wavelength and this will be used to determine the absolute flux exiting the collimator for a given input source. The NIST photodiode calibrated output beam is our "star at infinity" that is fed into the telescope. With the knowledge of how much light is incident on the telescope primary mirror, we can then convert the DN counts seen at the detector within the ACCESS payload to a physical unit, i.e. ergs cm^{-2} s^{-1} $Å^{-1}$.

8.4 LabVIEW Instrument Control

In addition to detector control software, many software modules have been written for the ground calibration system. The flat mirror is mounted on a linear and rotary stage, and the mirror must move, and its reflectivity be measured at each spot. A LabVIEW program was written which will take inputs for a start wavelength, end wavelength, wavelength step size, initial and final mirror angle and linear distance from the center, and measured spot size.

This code will then automatically go to the initial wavelength and position, and measure the incoming and outgoing light at that spot. It will then move to the next angular position (calculated by the indicated spot size), and subsequently the next linear position. Once the entire mirror region has been measured, the mirror will then reset to the initial position and step in wavelength. This entire test, depending on initial conditions, can take many hours, and the entire test is written to a file automatically, and includes time stamp, angle position and brightness for each step. In addition, a header is populated with the initial and final test conditions (see Fig. 8.5).

LabVIEW is also used for the detector characterization dewar. A Lakeshore temperature controller provides data to a computer, in terms of the temperature of the detector, in two positions on the backplane. In addition, a heater is controlled by the Lakeshore controller, to provide a feedback loop, in which the detector is brought to 140 K and back at a rate of 1°/minute, preventing any damage to the detector as a result of dramatic temperature shifts. Along with a series of 1n914 temperature diodes placed throughout the dewar, the temperature curve of the detector, baffles, cold shutter, and more are recorded, to ensure that the detector and its surroundings are in thermal equilibrium at temperatures below 160 K to remove any unwanted thermal background.

A similar temperature monitor system, albeit with thermistors rather than temperature diodes, is used for thermal testing of the detector controller, so as to identify components that reach temperatures that require heat sinking.

Within the payload, and as part of the ground calibration system, the LabVIEW program is used to control several motors:

1. A set of three PI micropusher-15 linear actuators within the detector housing in the payload enable an initial focus to be set while the payload is under vacuum. As the payload is cooled, this focus will move, and the motors allow for readjustment of the detector. These are controlled by an SMC-Pollux controller.

2. The filter wheel is controlled by a Newport SR50CC rotary motor with a Conex-CC controller.

3. The linear and rotary stages for the flat mirror are a set of two AutomationDirect SureStep stepper motors, controlled by a set of AllMotion EZ17 stepper motor controllers.

4. Positioning for the NIST calibration transfer photodiode detector is achieved by a series of three Newport LTAHSPPV6 linear motors. The three linear stages are coordinated via an XPS-Q4

motor controller housing an XPS-DRV-01 actuator board for each linear stage.

5. Rotation of the NIST photodiode is controlled using a PI M-116 precision rotation stage with a C-683 Mercury Servo Controller.

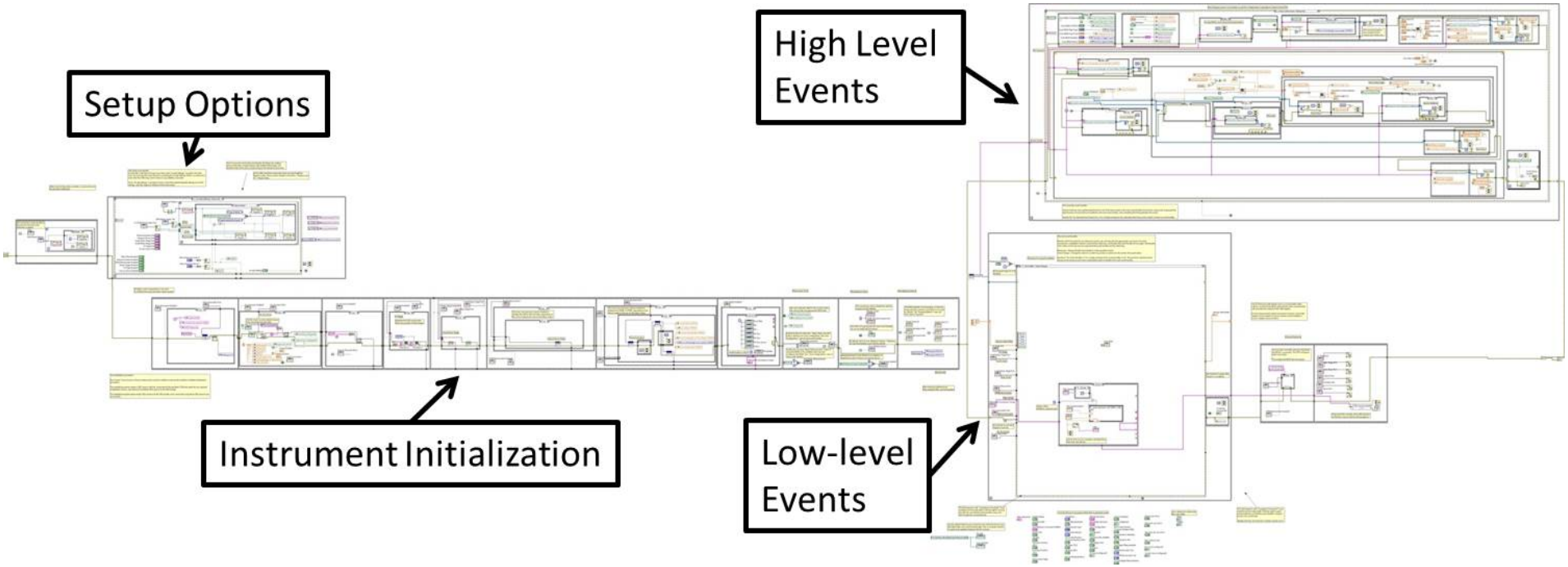

Figure 8.5: Labview Backend for reflectometer instrument control. High-level event handler allows many low-level events to perform in a coordinated, automated manner.

Chapter 9

Conclusions

In this thesis, I have described work I have done with the ACCESS program. I have observed and modeled a selection of the ACCESS candidate stellar targets and the extended sample that includes potential JWST calibrator stars. Using ATLAS9 and ATLAS12 stellar atmosphere model generation codes, I have fit effective temperature, surface gravity, metallicity and interstellar extinction to this stellar sample using a model fitting algorithm built for this purpose. ATLAS12 can produce robust stellar atmosphere models that are in agreement with the models generated by ATLAS9. Therefore, for the purpose of fitting a precise stellar atmosphere model to a standard star, ATLAS12 can provide greater flexibility in parameter space, and allow fine tuning of individual element abundance. However, high resolution data may be needed to break degeneracy between overall metallicity and the abundance of the most common elements.

For studies of large populations of stars, it would be time-consuming to apply this method. There is good agreement between this procedure and interpolation from currently existing model grids, and it is valid to do so in order to determine the primary characteristics of stellar spectra.

Using ground-based data from Apache Point Observatory, I have performed this model fitting

algorithm using on the ACCESS flight candidates, showing that this procedure can be applied to continuum-normalized line data as well as flux calibrated data.

In sum total, more than 11,000 stellar atmosphere models – and their corresponding synthetic spectra – were created throughout this study. They are not evenly spaced throughout parameter space.

9.1 Acknowledgements

Matthew Morris was supported by NASA grants NNX08AI65G, NNX14AH48G, and NNX17AC83G over the course of this research.

This research has made use of the NASA/ IPAC Infrared Science Archive, which is operated by the Jet Propulsion Laboratory, California Institute of Technology, under contract with the National Aeronautics and Space Administration.

Bibliography

Adibekyan, V. Z., & others. 2012, Astronomy & Astrophysics, 543, A89

Ahmed, M. G., et al. 2013, Measurement Science and Technology, 24, 095902

Aller, L. 1971, Atoms, Stars, and Nebulae (Cambridge, MA: Harvard University Press)

Arnett, D. 1996, Supernovae and Nucleosynthesis: An Investigation of the History of Matter from the Big Bang to the Present

Asplund, M., Grevesse, N., & Sauval, A. J. 2005, in Astronomical Society of the Pacific Conference Series, Vol. 336, Cosmic Abundances as Records of Stellar Evolution and Nucleosynthesis, ed. T. G. Barnes, III & F. N. Bash, 25

Aufdenberg, J. P., et al. 2006, Astrophysical Journal, 645, 664

Balmer, J. 1885, Annalen der Physik, 261, 80

Batalha, N. M. 2014, Proceedings of the National Academy of Science, 111, 12647

Beichman, C. A., Neugebauer, G., Habing, H. J., Clegg, P. E., & Chester, T. J., eds. 1988, Infrared astronomical satellite (IRAS) catalogs and atlases. Volume 1: Explanatory supplement, Vol. 1

Bertone, E., et al. 2004, Astronomical Journal, 128, 829

Bessel, F. 1838, Monthly Notices of the Royal Astronomical Society, 4, 152

Bessel, M. 2005, Annu. Rev. Astron. Astrophysics, 43, 293

Bessel, M. S., & Scholz, M. 1989, in IAU Colloq. 106: Evolution of Peculiar Red Giant Stars, 67

Bessell, M. S. 1990, Publications of the Astronomical Society of the Pacific, 102, 1181

Bessell, M. S., & Brett, J. M. 1988, Publications of the Astronomical Society of the Pacific, 100, 1134

Betoule, M., et al. 2013, Astronomy & Astrophysics, 552, 1

Binney, J., & Merrifield, M. 1998, Galactic Astronomy

Blanco-Cuaresma, S., et al. 2014, Astronomy & Astrophysics, 566, A98,1

Bohlin, R. C. 2003, in HST Calibration Workshop : Hubble after the Installation of the ACS and the NICMOS Cooling System, ed. S. Arribas, A. Koekemoer, & B. Whitmore, 115

Bohlin, R. C., & Gilliland, R. L. 2004, Astronomical Journal, 128, 3053

Bohlin, R. C., & Landolt, A. U. 2015, Astronomical Journal, 149, 122

Bohlin, R. C., Riess, A., & de Jong, R. 2006, NICMOS Count Rate DependentNon-Linearity in G096 and G141, Tech. rep.

Bohlin, R. C., et al. 2011, Astronomical Journal, 141, 173

—. 2017, Astronomical Journal, 153, 234

Bohm-Vitense, E. 1992, Introduction to Stellar Astrophysics, Vol. 3 (Cambridge University Press), doi:10.1017/CBO9780511623028

Bostroem, K. A., & Proffitt, C. 2011, STIS Data Handbook v. 6.0

Brackett, F. S. 1922, Astrophysical Journal, 56, 154

Burrell, M. O., & Wright, J. J. 1972, Estimation of galactic cosmic-penetration and dose rates, Tech. rep., National Aeronautics and Space Administration

Cardelli, J. A., Clayton, G. C., & Mathis, J. S. 1989, Astrophysical Journal, 345, 245

Carroll, B. W., & Ostlie, D. A. 1996, An Introduction to Modern Astrophysics

Castelli, F. 2005, Memorie della Societa Astronomica Italiana Supplementi, 8, 25

Castelli, F., & Kurucz, R. L. 2004, ArXiv Astrophysics e-prints, astro-ph/0405087

Catanzaro, G. 1998, Astrophysics and Space Science, 257, 161

Chandrasekhar, S. 1931, Astrophysical Journal, 74, 81

Chandrasekhar, S. 1931, The London, Edinburgh, and Dublin Philosophical Magazine and Journal of Science, 11, 592

Chiar, J. E., & Tielens, A. G. G. M. 2006, Astrophysical Journal, 637, 774

Ciddor, P. E. 1996, Appl. Opt., 35, 1566

Coates, P. B., & Andrews, J. W. 1978, Journal of Physics F: Metal Physics, 8, 277

Cohen, M., Walker, R. G., Barlow, M. J., & Deacon, J. R. 1992, Astronomical Journal, 104, 1650

Colgate, S., & McKee, C. 1969, Astrophysical Journal, 157, 623

Cronin, J. W., Gaisser, T. K., & Swordy, S. P. 1997, Scientific American, 276, 32

Cushing, M. C., et al. 2004, Publications of the Astronomical Society of the Pacific, 116, 362

Cutri, R. M., et al. 2003, VizieR Online Data Catalog, 2246

D'Andrea, C. B., et al. 2011, Astrophysical Journal, 743, 172

Dayton, D., et al. 2010, Spatial and temporal variability of SWIR air glow measurements, doi:10.1117/12.866767

Deustua, A., & et al. 2016, WFC3 Data Handbook v. 3.0

Donnelly, R. F., et al. 1983, Journal of Geophysical Research: Space Physics, 88, 9883

Draper, H. 1877, Nature, 15, 218

Dressel, L., et al. 2017, WFC3 Instrument Handbook v. 9.0

Ducati, J. R. 2002, VizieR Online Data Catalog, 2237

Eisenstein, D. J., et al. 2005, Astrophysical Journal, 633, 560

Engelbracht, C. W., et al. 2007, Publications of the Astronomical Society of the Pacific, 119, 994

Fery, C. 1911, Astrophysical Journal, 34, 79

Fitzpatrick, E. L., & Massa, D. 2007, Astrophysical Journal, 663, 320

Fowler, A. M., & Gatley, I. 1990, Astrophysical Journal, 353, L33

Friedman, E., & Miller, J. 2004, Photonics rules of thumb: optics, electro-optics, fiber optics, and lasers

Fukuda, I. 1982, Publications of the Astronomical Society of the Pacific, 94, 271

Fukugita, M., et al. 1996, Astronomical Journal, 111, 1748

Gaia Collaboration, Brown, A. G. A., Vallenari, A., et al. 2016, Astronomy & Astrophysics, 595, A2

Gandilo, N. N., et al. 2016, in Proc. SPIE, Vol. 9914, Millimeter, Submillimeter, and Far-Infrared Detectors and Instrumentation for Astronomy VIII, 99141J

García Pérez, A. E., et al. 2016, Astronomical Journal, 151, 144

Gogolev, N. L., et al. 1994, Measurement Techniques, 37, 1285

Gontcharev, G. 2006, Astronomy Letters, 32, 759

Gonzalez, G., & Lambert, D. 1996, Astronomical Journal, 111, 424

Gordon, K., & Bohlin, R. 2012, JWST Absolute Flux Calibration II: Expanded Sample of Primary Calibrators, Tech. rep., Space Telescope Science Institute

Gray, D. F. 1992, The observation and analysis of stellar photospheres.

Gray, R. O., Corbally, C. J., Garrison, R. F., McFadden, M. T., & Robinson, P. E. 2003, Astronomical Journal, 126, 2048

Grenier, S., et al. 1999, Astronomy & AstrophysicsSupp. Series, 137, 451

Grevesse, N., Asplund, M., & Sauval, A. J. 2007, Space Science Reviews, 130, 105

Grevesse, N., & Sauval, A. J. 1998, Space Science Reviews, 85, 161

Gustafsson, B., et al. 2008, Astronomy & Astrophysics, 486, 951

Habets, G. M., & Heintze, J. R. 1981, Astronomy & AstrophysicsSupp. Series, 46, 193

Hartig, G. F. 2008, WFC3 IR PSF Evaluation in Thermal-Vacuum Test #3, Tech. rep.

Hauschildt, P. H., Allard, F., & Baron, E. 1999, Astrophysical Journal, 512, 377

Hauschildt, P. H., Baron, E., & Allard, F. 1997, Astrophysical Journal, 483, 390

Hayes, D. S. 1985, in IAU Symp. 111: Calibration of Fundamental Stellar Quantities (Dordrecht: Reidel), 225–249

Hilbert, B. 2012, WFC3/IR Reference Pixel Characterization #1: Comparison of Bias Subtraction Methods, Tech. rep.

Høg, E., et al. 2000, Astronomy & Astrophysics, 355, L27

Houk, N., & Smith-Moore, M. 1988, Michigan Catalogue of Two-dimensional Spectral Types for the HD Stars. Volume 4, Declinations -26deg.0 to -12deg.0.

Howell, D. A., et al. 2009, Astrophysical Journal, 691, 661

Howell, S. B., et al. 2005, Publications of the Astronomical Society of the Pacific, 117, 1187

Hubeny, I., & Lanz, T. 1995, Astrophysical Journal, 439, 875

Husser, T.-O., et al. 2013, Astronomy & Astrophysics, 553, A6

Jha, S., Riess, A. G., & Kirshner, R. P. 2007, Astrophysical Journal, 659, 122

Johnson, H. L., & Morgan, W. W. 1955, The Astrophysical Journal, 117, 313

Jones, D. O., et al. 2013, The Astrophysical Journal, 768, 166

Kaiser, M. E., et al. 2007, in The Future of Photometric, Spectrophotometric and Polarimetric Standardization, ed. C. Sterken (Baltimore: APS Conference Series), 361

Kaiser, M. E., et al. 2008, in Proc. SPIE, Vol. 7014, Ground-based and Airborne Instrumentation for Astronomy II, 70145Y

Kaiser, M. E., et al. 2010, in Proc. SPIE, Vol. 7731, Space Telescopes and Instrumentation 2010: Optical, Infrared, and Millimeter Wave, 77313I

Kaiser, M. E., et al. 2012, in Proc. SPIE, Vol. 8442, Space Telescopes and Instrumentation 2012: Optical, Infrared, and Millimeter Wave, 844246

Kaiser, M. E., et al. 2013a, in American Astronomical Society Meeting Abstracts, Vol. 221, American Astronomical Society Meeting Abstracts #221, 350.08

Kaiser, M. E., et al. 2013b, ACCESS: thermal mechanical design and performance, doi:10.1117/12.2024571

Kaiser, M. E., et al. 2016, in Astronomical Society of the Pacific Conference Series, Vol. 503, The Science of Calibration, ed. S. Deustua, S. Allam, D. Tucker, & J. A. Smith, 221

Kaiser, M. E., et al. 2017, in Society of Photo-Optical Instrumentation Engineers (SPIE) Conference Series, Vol. 10398, Society of Photo-Optical Instrumentation Engineers (SPIE) Conference Series, 1039815

Kalirai, J. S., et al. 2009, WFC3 SMOV Proposal 11451: The Photometric Performance and Calibration of WFC3/IR, Tech. rep.

Kruk, J. W., et al. 2008, in Proc. SPIE, Vol. 7014, Ground-based and Airborne Instrumentation for Astronomy II, 70145J

Kurucz, R. L. 1969, Astrophysical Journal, 156, 235

—. 1970, SAO Special Report, 309

—. 1979, Astrophysical Journal Supplement Series, 40, 1

—. 1993, ASP Conference Series, 44, 87

—. 2005a, Memorie della Societa Astronomica Italiana Supplementi, 8, 14

—. 2005b, Memorie della Societa Astronomica Italiana Supplementi, 8, 73

Lange, A., et al. 2001, Physical Review D, 63, 42001

Lanz, T., & Hubeny, I. 2003, Astrophysical Journal Supplement Series, 146, 417

—. 2007, Astrophysical Journal Supplement Series, 169, 83

Larason, T. C., & Houston, J. 2008, Spectroradiometric Detector Measurements: Ultraviolet, Visible and Near-Infrared Detectors for Spectral Power

Leavitt, H., & Pickering, E. 1912, Harvard College Observatory Circular, 173, 1

Linder, E. V., & Huterer, D. 2003, Physical Review D, 67, 1303L

Lyman, T. 1906, Astrophysical Journal, 23, 181

Mandel, K. S., et al. 2017, Astrophysical Journal, 842, 93

Marinoni, S., et al. 2016, Mon. Not. R. Astron. Soc., 462, 3616

Martínez-Arnáiz, R., et al. 2010, Astronomy & Astrophysics, 520, A79

McGrath, M. A., Busko, I., & Hodge, P. 1999, Calstis6: Extraction of 1-D Spectra in the STIS Calibration Pipeline, Tech. rep.

McWilliam, A., & Rich, R. M. 1994, Astrophysical Journal Supplement Series, 91, 749

Meinel, I. A. B. 1950, Astrophysical Journal, 111, 555

Mészáros, S., et al. 2012, Astronomical Journal, 144, 120

Meyer, M. R., et al. 2006, Publications of the Astronomical Society of the Pacific, 118, 1690

Mishenina, T., et al. 2000, Astronomy & Astrophysics, 353, 978

Neill, J. D., et al. 2006, Astronomical Journal, 132, 1126

Nidever, D. L., et al. 2015, Astronomical Journal, 150, 173

Nomoto, K., Thielemann, F.-K., & Yokoi, K. 1984, Astrophysical Journal, 286, 644

O'Brian, T. R., Johnson, B. C., & Sakuma, F. 1995, Metrologia, 32, 445

O'Donnell, J. E. 1994, Astrophysical Journal, 422, 158

Offenberg, J. D., Fixsen, D. J., & Mather, J. C. 2005, Publications of the Astronomical Society of the Pacific, 117, 94

Oke, J. B. 1974, Astrophysical Journal Supplement Series, 27, 21

Oliva, E., & Origlia, L. 1992, Astronomy & Astrophysics, 254, 466

Palmer, B. A., & Engleman, R. 1983, Atlas of the Thorium spectrum

Pancino, E., et al. 2012, Mon. Not. R. Astron. Soc., 426, 1767

Pascale, E., et al. 2008, The Astrophysical Journal, 681, 400

Paschen, F. 1908, Annalen der Physik, 332, 537

Perlmutter, S., et al. 1999, Astrophysical Journal, 517, 565

Peterson, D. M., et al. 2006, Nature, 440, 896

Planck Collaboration. 2014, Astronomy & Astrophysics, 571, A1

Price, S. D., et al. 2004, Astronomical Journal, 128, 889

Rajan, A., et al. 2010, Version 2.1

Ramirez, I., et al. 2006, A&A, 459, 613

Rauscher, B. J., et al. 2007, Publications of the Astronomical Society of the Pacific, 119, 768

—. 2010, Publications of the Astronomical Society of the Pacific, 122, 1254

Reach, W. T., et al. 2005, Publications of the Astronomical Society of the Pacific, 117, 978

Regnault, N., et al. 2009, å, 506, 999

Rieke, G. H., et al. 2005, Astrophysical Journal, 620, 1010

—. 2008, Astronomical Journal, 135, 2245

—. 2015, Publications of the Astronomical Society of the Pacific, 127, 584

Riess, A. G., et al. 1998, Astronomical Journal, 116, 1009

Rowland, H. A. 1882, Mature, 26, 211

Rybicki, G. B., & Lightman, A. P. 1986, Radiative Processes in Astrophysics, 400

Sbordone, L. 2005, Memorie della Societa Astronomica Italiana Supplementi, 8, 61

Scolnic, D., et al. 2014, Astrophysical Journal, 795, 45

Shapley, H. 1918, Astrophysical Journal, 48, doi:10.1086/142435

Sherwin, B. D., et al. 2011, Physical Review Letters, 107, 021302

Short, J. 1763, Philosophical Transactions, 53, 300

Skinner, C. J. 1996, Flux Units and NICMOS, Tech. rep.

Smith, A. W., et al. 2009, Metrologia, 46, S219

Sneden, C., et al. 2016, Astrophysical Journal, 817, 53

Soubiran, C., et al. 2013, Astronomy & Astrophysics, 552, A64

Sousa, S. G., Alapini, A., Israelian, G., & Santos, N. C. 2010, Astronomy & Astrophysics, 512, A13

Spergel, D. N., et al. 2007, Ap. J. S., 170, 377

Su, K. N., et al. 2013, Astrophysical Journal, 763, 14pp

Su, K. Y. L., et al. 2006, Astrophysical Journal, 653, 675

Teixeira, G. D. C., et al. 2016, Astronomy & Astrophysics, 595, A15

Tinsley, B. M. 1979, Astrophysical Journal, 229, 1046

Trumpler, R. J. 1930, Lick Observatory Bulletin, 14, 154

Truran, J. W., Arnett, W. D., & Cameron, A. G. W. 1967, Canadian Journal of Physics, 45, 2315

Vacca, W. D., et al. 2003, Publications of the Astronomical Society of the Pacific, 115, 389

van Leeuwen, F. 2007, Astronomy & Astrophysics, 474, 653

Voit, M. 1997, HST Data Handbook, Volume I: Current Instruments, Version 3

Wallerstein, G. 1962, Astrophysical Journal Supplement Series, 6, 407

Wang, S., et al. 2003, ARCES: an echelle spectrograph for the Astrophysical Research Consortium (ARC) 3.5m telescope, doi:10.1117/12.461447

Wilson, J. C., et al. 2004, Proc. SPIE, 5492, 1295

Woosley, S. E., & Weaver, T. A. 1995, Astrophysical Journal Supplement Series, 101, 181

Wu, C.-J., et al. 2013, Astrophysical Journal Supplement Series, 208, 29

Yoon, J., et al. 2008, Astrophysical Journal, 681, 570

Matthew Morris

Born January 26, 1988, in Altoona, PA

Education

B.A. - 2010, University of Pennsylvania, Magna Cum Laude in Physics

M.A. - 2012, Johns Hopkins University, Physics

Employment

2007-2010: Undergraduate Research Assistant, Masao Sako, University of Pennsylvania

–Research on determining properties, specifically metallicity, of progenitor galaxies for type Ia supernovae.

2010-2011: Teaching Assistant, Physics for Biology Majors, Johns Hopkins University

2011-Present: Graduate Research Assistant, ACCESS, Johns Hopkins University

–ACCESS - Absolute Color Calibration Experiment for Standard Stars is a rocket-borne payload that will enable the transfer of absolute laboratory detector standards from NIST to a network of stellar standards with a calibration accuracy of 1% and a spectral resolving power of R = 500 across the 0.35-1.7 μm bandpass.

Research Expertise

Image reduction and analysis, optical and near-infrared instrument control, detector characterization, stellar model fitting. **Software Expertise:** Python, IDL, C++, Java, LabVIEW, Bash, Pro-Engineer/Creo, LaTeX, IRAF, Excel

Awards and Memberships

American Astronomical Society, SPIE

Volunteer Experience

2012-2015: Lead Organizer, Johns Hopkins Annual Physics Fair

Organized ∼150 volunteers in a large scale Physics demonstration event, including 4 competitions for K-12 ages, ∼200 demonstrations, 2 30-minute shows, and more. The Physics Fair sees approximately 3,000 attendees per year.